Identification of effective 1D soil models for large-diameter offshore wind turbine foundations based on in-situ seismic measurements and 3D modelling

Versteijlen, Pim

DOI
10.4233/uuid:55e7ff00-02ba-495d-9863-889bb92ee548

Publication date
2018

Document Version
Final published version

Citation (APA)
Versteijlen, P. (2018). *Identification of effective 1D soil models for large-diameter offshore wind turbine foundations based on in-situ seismic measurements and 3D modelling*. [Dissertation (TU Delft), Delft University of Technology]. https://doi.org/10.4233/uuid:55e7ff00-02ba-495d-9863-889bb92ee548

Important note
To cite this publication, please use the final published version (if applicable).
Please check the document version above.

IDENTIFICATION OF EFFECTIVE 1D SOIL MODELS FOR LARGE-DIAMETER OFFSHORE WIND TURBINE FOUNDATIONS BASED ON IN-SITU SEISMIC MEASUREMENTS AND 3D MODELLING

IDENTIFICATION OF EFFECTIVE 1D SOIL MODELS FOR LARGE-DIAMETER OFFSHORE WIND TURBINE FOUNDATIONS BASED ON IN-SITU SEISMIC MEASUREMENTS AND 3D MODELLING

Proefschrift

ter verkrijging van de graad van doctor
aan de Technische Universiteit Delft,
op gezag van de Rector Magnificus prof. dr. ir. T.H.J.J. van der Hagen,
voorzitter van het College voor Promoties,
in het openbaar te verdedigen op dinsdag 12 juni 2018 om 12:30 uur

door

Willem Geert VERSTEIJLEN

Master of Science in Offshore Engineering,

Technische Universiteit Delft,

geboren te Sint-Lambrechts-Woluwe, België.

Dit proefschrift is goedgekeurd door de

promotor: prof. dr. A.V. Metrikine
copromotor: dr. K.N. van Dalen

Samenstelling promotiecommissie:

Rector Magnificus,	voorzitter
Prof. dr. A.V. Metrikine,	Technische Universiteit Delft, promotor
Dr. K.N. van Dalen,	Technische Universiteit Delft, copromotor
Onafhankelijke leden:	
Prof. dr. K.G. Gavin,	Technische Universiteit Delft
Prof. dr. L.V. Andersen,	Aarhus University, Denemarken
Prof. dr. N. Gerolymos,	National Technical University of Athens, Griekenland
Prof. dr. G.R. Eiksund,	Norwegian University of Science and Technology, Noorwegen
Dr. D.P. Molenaar,	Siemens Gamesa Renewable Energy
Prof. dr. S.G.J. Aarninkhof,	Technische Universiteit Delft, reservelid

Keywords: Soil-structure interaction, Rigid monopiles, Small-strain soil reaction, In-situ seismic soil characterisation, Fundamental natural frequency of offshore wind turbine, Soil damping, 3D to 1D modelling translation, 1D effective stiffness, In-situ shaker validation measurements, Non-local (dynamic) stiffness

Printed by: Gildeprint

Cover design: Anouk van Alphen

Author email: pimversteijlen@gmail.com

ISBN 978-94-6233-989-7
An electronic version of this dissertation is available at
http://repository.tudelft.nl/.

CONTENTS

NOMENCLATURE

SYMBOLS

The meaning of the most often used symbols are listed in the table below:

A	Cross sectional area of the pile	$D_m(\omega)$	Modal material damping ratio
A	Geometric damping (Section 2.3.4)	ΔL	Step size of integrals, local method
$A_{sch}(\omega)$	Scholte wave attenuation coefficient	Δz_{an} or z_{an}	Vertical component of wave path of upper or lower ray in layer n
A_p	Acceleration amplitude measured at the top of the pile	Δz_n	Vertical component of wave path in layer n
A_{sh}	Acceleration amplitude measured at the shaker	E	Young's modulus of steel
α	Coefficient for stress dependency of G (Chapter 2)	E_s	Young's modulus of soil
α	Damping tuning factor towards stiffness	e	Void ratio
C_s	Shear wave velocity	ϵ	Steel strain
$C_{sch}(\omega)$	Scholte wave phase velocity	ϵ	Modification factor for half-power bandwidth method (Section 2.3.4)
C_p	Pressure wave velocity	ε	Relative height of the energy peak taken in the modified Q-factor method
$C_{u,u',\psi,\psi'}$	Misfit of the sum of displacements, slopes, rotations and curvatures	η	Soil added mass factor
$C_{\mathrm{Im}(..)}$ & $C_{\mathrm{Re}(..)}$	Misfit of the imaginary and real part of the complex-valued response, respectively	η	Loss factor (Section 3.2)
$c_{eff}(z)$	Effective 1D damping profile	F	Horizontal force
c_n	Shear wave velocity in layer n	F_T	Tangential force
D	Pile diameter	F_R	Radial force
D_r	Relative density of soil	F_V	Vertical force

$\mathbf{F}_{\mathrm{x}}$	Matrix of horizontal reaction forces from soil continuum	K_g	Granular bulk modulus
$\mathbf{F}_{\mathrm{z}}$	Matrix of vertical reaction forces from soil continuum	$\mathbf{K}^{\mathrm{x,x}}$	Global (non-local) stiffness matrix, $x = u, \psi$
f	Frequency	k	Modulus of subgrade reaction
f_1	Fundamental natural frequency	k	Wave number (Section 2.3)
f_s	Cone sleeve friction (Chapter 2)	$k_{eff}(z)$	Effective 1D stiffness profile
$f_{s,n}$	Soil resonance frequency of mode n	k_s, $k_{s,0}$ or E^*_{py}	Initial subgrade modulus (stiffness) as denoted in the p-y curve method
ϕ	Internal angle of friction	$\mathring{k}$	Complex wavenumber
Φ	Angle of SCPT cone rotation around its vertical axis	k_{sch}	Scholte wavenumber
Φ_p	Porosity of soil	κ	Timoshenko shearing coefficient
G	Shear modulus	L	Pile embedment length
G^*	Complex valued shear modulus	L	Pile embedment length
γ	Stiffness correction factor	L/D	Pile embedded length over diameter ratio
γ_s	Soil strain	M	Overturning moment
γ_{el}	Elastic threshold soil strain	M_s	Distributed resonator mass
H	Soil layer thickness	m	Rotating mass of the shaker
$H(f)$	Transferfunction amplitude	n	Number of nodes used for discretisation
H_g	Gassmann modulus	n	Layer number in C_s inversion scheme (Section 2.2.2)
h	Discretization length	n	Geometric decay factor (Section 2.3.4)
I	Second moment of area of the cross section of the pile	ν	Poisson's ratio
I_p	Plasticity index	p_a	Atmospheric pressure
i and j	Discretization points	p	Lateral soil pressure on the beam (in p-y curve method)
K_0	Coefficient of effective lateral earth pressure at rest	Q_m	Quality factor for modal material damping
K_r	Relative pile stiffness	q_c	Cone tip resistance
K_b	Bulk modulus	q_t	Corrected cone tip resistance
K_f	Fluid bulk modulus	R	Resultant direction of wave propagation (Chapter 2)
$K_{f,eff}$	Effective fluid bulk modulus	R	Radius of the pile (Section 3.2)

R	Effective arm for the shaker centrifugal force (Chapter 5)
R_f	Cone friction ratio
r	Radial distance (Section 2.3.4)
ρ	In-situ mass density
ρ_w	Mass density of water
s_{an} or s_{bn}	Wave path length of upper or lower ray in layer n
s_f and s_g	Water and gas saturation degree
σ'_h	Horizontal effective stress
σ'_m	Mean effective confining pressure
σ'_v	Vertical effective stress
$T(f)$	Internal transmissibility function amplitude - measured
$\overline{T}(f)$	Internal transmissibility function amplitude - modelled
t	Pile wall thickness
t	Time (Section 3.2)
t_{n1} and t_{n2}	Arrival times at respectively the upper and lower geophone
$\mathbf{U}$	Matrix of displacements imposed on the soil continuum
$\tilde{\mathbf{U}}$	Auxilary matrix incorporating the Trapezium rule for integration on $\mathbf{U}$
$u(z)$	Lateral pile displacement (depth (z) dependent)
$u'(z)$	Lateral pile slope (derivative of $u(z)$)
u_p	Amplitude of displacement at the top of the pile, derived from A_p
v_x, v_y and v_R	Particle velocity in x, y and resultant direction
Ψ	Matrix of rotations imposed on the soil continuum
$\tilde{\Psi}$	Auxilary matrix incorporating the Trapezium rule for integration on Ψ
$\psi(z)$	Lateral pile rotation (depth (z) dependent)
$\psi'(z)$	Lateral pile curvature (derivative of $\psi(z)$)
σ_0	Confining pressure
ω	Angular frequency
ω_c	Central frequency
x_{an} or x_{an}	Horizontal component of wave path of upper or lower ray in layer n
y	Lateral displacement of the beam (in p-y curve method)
z	Vertical axis
$z^{(1)}_{f,t}/z^{(2)}_{m,t}$	Integration boundaries; 'f' for force, 'm' for moment) and (1)/(2) for the lower/upper integration bound
ζ	Soil material damping ratio
$\zeta_g(r,\omega)$	Amplitude term related to geometric damping

ABBREVIATIONS

The following abbreviations are used throughout this thesis:

1D/3D	One and three dimensional
AEP	Annual electricity production
BHawC	Bonus Horizontal axis wind turbine code
CPT	Cone penetration test
CO_2	Carbon Dioxide
DOF	Degree of freedom
EUR	Euro
FE	Finite element
FD	Finite difference
FLS	Fatigue Limit State
FW	Full waveform
GW	Gigawatt
LFCPT	Low frequency CPT
LCOE	Levelised cost of energy
MASW	Multichannel analysis of surface waves
MW	Mega Watt
MP	Monopile
MP45	Monopile number 45 of the WMW wind farm on which the shaker tests were performed
MWh	Mega Watt hour
MP	Monopile
MSW	Modal surface wave method
NGI	Norwegian Geotechnical Institute
OWT	Offshore wind turbine
PSD	Power Spectral Density
R&D	Research and development
RMS	Root mean square
RnA	Rotor-nacelle assembly
SASW	Spectral analyses of surface waves
SCPT	Seismic cone penetration test
SCPT45	SCPT performed at MP45
SDoF	Single degree of freedom
SSI	Soil-structure interaction
ULS	Ultimate Limit State
UN	United Nations
UK	United Kingdom
US	United States of America
W27	Name of turbine placed on MP45
WMW	Westermeerwind

SUMMARY

Offshore wind generated electricity is currently one of the most promising sources of energy to contribute in creating a sustainable global energy mix. The latter is essential for minimising the detrimental impact of human-induced accelerated climate change. The cost of offshore wind power has strongly decreased over the past years due to (amongst others) progressive R&D, the increased capacity of the plants and due to a lower perceived risk (i.e., interest rates). The current thesis contributes to further lowering the cost of this energy source; it justifies the application of less steel in the design of the most often applied monopile (MP) foundation, by providing a more accurate and less conservative design method for the soil-structure interaction (SSI) of rigidly behaving MP foundations.

More specifically, this thesis addresses the lateral *small-strain* soil response towards rigidly behaving piles that typically have a relatively low ratio of embedded length L to diameter D: $L/D < 7$. It is the small-strain regime that governs the overall dynamic properties of the offshore wind turbine (OWT), which in turn define the accumulation of steel fatigue damage - most often the main design driver in dimensioning the support structure (foundation and tower). The work aims to improve both the currently applied in-situ characterisation of the soil properties and the design model used for simulating the complex SSI of MP foundations.

For capturing the in-situ small-strain soil properties, it is suggested to add seismic measurements to the standard site characterisation scope. The currently applied geotechnical Cone Penetration Test measures the very local, large-strain *strength* parameters, whereas the output of a geophysical method like the Seismic Cone Penetration Test reflects the more global, small-strain *stiffness* properties of the soil.

Regarding the design model, it is suggested to benefit from the accuracy of a 3D model, as it automatically captures the various soil reaction mechanisms that dominate the SSI of rigidly behaving piles. The soil in interaction with the small pile displacements of the fatigue-limit-state load case can be idealised to behave as a linear elastic material. The basic soil stiffness parameters captured by the seismic measurements can be directly used to fully characterize a linear elastic continuum of a 3D model. This physics-based approach, which first identifies the stiffness of the soil and subsequently that of the soil-pile system, is a more versatile and accurate method than the most often applied semi-empirical p-y curve method. The latter method employs the depth-dependent modulus of horizontal subgrade reaction $k(z)$ to quantify a particular soil-pile initial lateral stiffness, to be used in a 1D Winkler foundation model. The Winkler model is the all-time favourite engineering model due to its simplicity and intuitive representation of the main involved physics in the SSI, and the subgrade modulus is a very useful SSI

parameter. However, $k(z)$ is an empirical tuning parameter, depending not only on the properties of the (stratified) soil, but also on those of the pile. As the currently used p-y curves were calibrated on small-diameter, flexible piles, they are not representative for the soil reactions to short, rigidly behaving MP foundations. In only assuming a lateral, uncoupled soil reaction - being the dominant restoring force for flexible piles, and hence the assumption in the p-y curve method - one underestimates the complete restoring reaction of the soil, which is induced by additional, more complex soil mechanisms.

To become truly useful for design, the 3D model should not only serve as a design check, but its accuracy should be directly integrated into the design models. Similar to various other engineering design procedures, the thousands of load simulations required in the design of offshore wind support structures, make the 3D model computationally too expensive to replace the simple, 1D design model. To employ the speed and simplicity of the 1D model with the accuracy of the 3D model, the current thesis presents - as its main contribution - 2 methods to obtain a 1D effective model that mimics the 3D modelled response.

The first, 'local' method establishes an effective 1D stiffness $k_{eff}(z)$, by optimising the profile of the uncoupled (local) lateral springs that renders the response of the 1D Winkler model of a rigid pile in stratified soil the same as that of the static response of the 3D model in terms of displacement, slope, rotation and curvature along the full embedded length of the pile. Accurate matches can be obtained for quite a broad range of pile geometries and soil (stiffness) profiles, however, this local method seems to perform worse for piles with $L/D < 4.5$, softer and/or very irregular soil stiffness profiles. The same methodology was found to be able to also generate an effective damping profile $c_{eff}(z)$ to additionally mimic the energy dissipation in the SSI - provided that a previously found static stiffness profile $k_{eff}(z)$ accurately captures the static response.

In the second, 'non-local' method, effective 1D global stiffness kernels are computed which fully capture the coupled 3D reactions of the stratified soil to the pile, for both the static and the low-frequency dynamic SSI. With the use of the stiffness kernels for the lateral and rotational degrees of freedom, the need of searching for various separate 1D stiffness elements, like distributed lateral and rotational springs along the pile or similar discrete springs at the pile tip, has become obsolete; such mechanisms are all automatically incorporated in the non-local stiffness kernels. The non-local method was shown to be very versatile, irrespective of pile geometry and soil stiffness profile, providing accurate matches of the 3D simulated response of the embedded pile.

Finally, for increased confidence, methods and models should be validated - preferably by measuring the response of a realistic and representative version of the structure of interest. As no measurements of the dynamic response of a large scale MP foundation were reported in literature, an extensive measurement campaign was designed and executed on a 'real' MP foundation of a near-shore wind farm. The setup involved a large amount of sensors on the pile and in the adjacent soil distributed over the full length of the pile, applying a steady-state excitation with a custom-made hydraulic

shaker. The structure being a stand-alone pile, excluding dynamic disturbance of the to-be-installed super structure of tower and turbine, and the test comprising a controlled (known) loading, this campaign was shown to yield a much lower uncertainty regarding the soil response than for the commonly applied monitoring of the operational full OWT structure. Together with the inclusion of realistic saturated, nonhomogeneous sandy soil conditions and installation effects, a 'first-off' opportunity was created to validate a model for the lateral, dynamic response of rigidly behaving monopiles.

In the presented analyses of the measured response, the predicted effective stiffness was employed as an initial guess in a model-based identification of the stiffness, damping and fundamental frequency of the soil-pile system. It was shown that the proposed design procedure yields a 7 times higher accuracy in predicting the in-situ initial stiffness than the best-estimate p-y curve model. Furthermore, 2 adaptations of the 1D model were employed to investigate the presence of soil-added mass effects in the higher-frequency response of the system. Finally, the stiffness and damping of the pile-only system were related to those observed for the full OWT system, and the assumption of linear elastic soil response was validated using the observed pile response.

An initial estimation of the possible benefit of the developed stiffness method, showed a 8% saving potential for the primary steel (shell) mass of the complete support structure (MP, transition piece and tower). This exercise was performed for a contemporary soil-pile case, for which (only) the fatigue-driven wall thickness was optimized and compared to the thickness needed when applying the conventional (softer) p-y curve profile. As the cost for MP support structures typically constitute more than 20% of the total capital cost of an offshore wind farm, the presented and validated work is foreseen to have a significant beneficial impact on the feasibility of future offshore wind projects.

SAMENVATTING

Offshore windgegenereerde elektriciteit is op dit moment één van de meest veelbelovende energiebronnen voor het creëren van een wereldwijde duurzame energiemix. Dit laatste is essentieel voor het beperken van de schadelijke gevolgen van de door de mensheid versnelde klimaatverandering. Door een combinatie van (onder meer) voortschrijdend onderzoek, de toename van turbinecapaciteit en door een lagere risicoperceptie (ergo rentepercentages), zijn de kosten van stroom vanuit wind op zee de laatste jaren aanzienlijk gedaald. Dit proefschrift draagt bij aan een verdere verlaging van de kosten van deze energiebron. Het rechtvaardigt het toepassen van minder staal in het ontwerp van de meest gebruikte monopile (MP) fundering. Dit werk presenteert een nauwkeurigere en minder conservatieve ontwerpmethodiek voor de grond-constructie interactie (GCI) van 'star-gedragende' MP-funderingen.

Meer specifiek: dit onderzoek behandelt de laterale grondreactie voor *kleine rekken* in de interactie met star-gedragende palen die een relatief lage verhouding van inbeddingsdiepte L tot diameter D hebben: $L/D < 7$. De grondeigenschappen bij kleine rekken dicteren de dynamische eigenschappen van de offshore windturbine (OWT). Deze eigenschappen bepalen op hun beurt de hoeveelheid staalvermoeiing, en staalvermoeiing is meestal de drijvende factor in het dimensioneren van de ondersteuningsconstructie (fundering en toren). Het gepresenteerde werk heeft als doel verbetering te brengen in zowel de huidig toegepaste in-situ karakterisering van grondeigenschappen, als in het ontwerpmodel dat wordt gebruikt voor het simuleren van de complexe GCI van MP-funderingen.

Om de in-situ grondeigenschappen bij kleine rekken te identificeren, beveelt dit onderzoek aan om seismische metingen toe te voegen aan de standaard set van grondmetingen. De geotechnische sonderingstest die nu wordt toegepast meet de zeer lokale, *sterkte* parameters bij grote rekken. Maar het is juist de uitkomst van een geofysische test zoals de seismische sondering die de meer globale, *stijfheids* eigenschappen bij kleine rekken reflecteert.

Met betrekking tot het ontwerpmodel, stelt dit proefschrift voor om te profiteren van de nauwkeurigheid van een 3D-model. Zo'n model neemt namelijk automatisch de verschillende grondreactiemechanismes mee die bepalend zijn voor de GCI van starre palen. Voor de kleine paalverplaatsingen die typisch zijn voor vermoeiingsbelastingen, kan de grond worden geïdealiseerd zich te gedragen als een lineair elastisch materiaal. De fundamentele grondstijfheidsparameters die worden verkregen met seismische metingen kunnen we direct gebruiken om een lineair elastische continuüm van een 3D-model volledig te karakteriseren. Deze meer fundamenteel fysische benadering, waarin eerst de stijfheid van de grond en vervolgens die van het grondpaalsysteem wordt geïdentificeerd,

is een universelere en nauwkeurigere methode dan de meest toegepaste semi-empirische p-y-curve methodiek. De p-y-curve methode gebruikt de diepteafhankelijke modulus van horizontale grondreactie $k(z)$ om een bepaalde initiële grond-paal laterale stijfheid te kwantificeren. Deze stijfheid is vervolgens te gebruiken in een 1D-Winkler funderingsmodel. Het Winklermodel is bij uitstek het favoriete model in het ingenieurswezen vanwege zijn eenvoud en intuïtieve weergave van de belangrijkst aanwezige fysica in de GCI. Daarbij is de modulus van horizontale grondreactie een zeer nuttige GCI-parameter. Echter, $k(z)$ is een empirische stel-parameter, die niet alleen afhankelijk is van de eigenschappen van de (gelaagde) grond, maar ook van de eigenschappen van de paal. Aangezien de huidig gebruikte p-y-curves zijn gekalibreerd op flexibele palen met een kleine diameter, zijn ze niet representatief voor de grondreacties op korte, starre MP-funderingen. Door enkel een laterale, ongekoppelde grondreactie te veronderstellen - hetgeen de dominante herstellende kracht geeft voor flexibele palen, en vandaar de aanname is in de p-y-curve methode - onderschat men de complete reactiekracht van de grond. Een reactiekracht die feitelijk ook nog door andere, meer complexe grondmechanismes wordt veroorzaakt.

Om werkelijk nuttig te zijn in het ontwerpproces, moet het 3D-model niet alleen dienen als een ontwerpcontrole, maar moet de nauwkeurigheid van het model rechtstreeks in de ontwerpmodellen worden geïntegreerd. De duizenden belastingsimulaties die nodig zijn in het ontwerp van offshore wind funderingen maken het 3D-model rekentechnisch te duur om het eenvoudige, 1D-ontwerpmodel te vervangen. Dit is ook het geval bij diverse andere technische ontwerpprocessen. Om de snelheid en eenvoud van het 1D-model te gebruiken met de nauwkeurigheid van het 3D-model, presenteert dit proefschrift - als zijn belangrijkste bijdrage - 2 methodes. Met deze methodes verkrijgen we een 1D-effectief model dat de 3D-gemodelleerde reactie reproduceert.

Met de eerste, 'lokale', methode verkrijgen we een effectieve 1D-stijfheid $k_{eff}(z)$. Deze vindt men door het profiel van de ongekoppelde (lokale) laterale veren te optimaliseren zodat het Winkler-model voor een starre paal in gelaagde grond dezelfde statische respons geeft als het 3D-model in termen van verplaatsing, helling, rotatie en kromming langs de volledige lengte van de paal. Nauwkeurige overeenkomsten kunnen worden verkregen voor een vrij breed spectrum aan paalgeometrieën en grond(stijfheids)profielen. Deze lokale methode lijkt echter minder goede resultaten te leveren voor palen met $L/D < 4.5$, zachtere en / of zeer onregelmatige grondstijfheidsprofielen. Dezelfde methodologie bleek in staat om ook een effectief dempingsprofiel $c_{eff}(z)$ te kunnen genereren. Hiermee kunnen we zodoende ook de energiedissipatie in de GCI imiteren - op voorwaarde dat het eerder gevonden profiel van de statische stijfheid $k_{eff}(z)$ nauwkeurig de statische respons reproduceert.

In de tweede, 'niet-lokale', methode worden 1D-effectieve globale stijfheidsmatrices berekend die de gekoppelde 3D-reacties van de gelaagde grond op de paal volledig ondervangen. Dit voor zowel de statische als de laagfrequente dynamische GCI. Door de stijfheidsmatrices voor de laterale en rotationele vrijheidsgraden te gebruiken, is het zoeken naar afzonderlijke 1D-stijfheids elementen, zoals gedistribueerde laterale en roterende veren langs de paal of soortgelijke discrete veren aan de paalpunt, niet meer

noodzakelijk. Dergelijke mechanismes worden allen automatisch meegenomen in de niet-lokale stijfheidsmatrices. De niet-lokale methode heeft aangetoond zeer veelzijdig te zijn wat betreft de paalgeometrie en het stijfheidsprofiel van de grond, en levert nauwkeurige overeenkomsten met de 3D-gesimuleerde reactie van de paal.

Tot slot, om meer vertrouwen te creëren, moeten de methoden en modellen gevalideerd worden - bij voorkeur door het meten van de respons van een realistische en representatieve versie van de constructie in kwestie. In de literatuur werden er geen metingen gerapporteerd van de dynamische respons van een grootschalige MP-fundering. Daarom is er binnen dit onderzoek een uitgebreide meetcampagne ontworpen en uitgevoerd op een 'echte' MP-fundering van een nearshore windmolenpark. De meetopstelling betrof een aanzienlijke set sensoren verdeeld over de volledige lengte van de paal en in de aanliggende grond. Daarnaast is er gebruik gemaakt van een op maat gemaakte hydraulisch shaker voor het toepassen van een steady-state excitatie. De constructie betrof enkel een opzichzelfstaande paal, zonder de dynamische verstoring van de te installeren topconstructie van toren en turbine. Bovendien werd er een gecontroleerde (bekende) belasting toegepast. Deze meetcampagne bleek daardoor een veel lagere onzekerheid te geven wat betreft de grondreactie dan voor de algemeen toegepaste monitoring van operationele, volledige OWT constructies. Samen met de aanwezigheid van realistische verzadigde, niet-homogene, zandige grondcondities en realistische installatie-effecten, werd een 'first-off'-gelegenheid gecreëerd voor het valideren van een model voor de laterale, dynamische respons van star-gedragende monopiles.

In de gepresenteerde analyses van de gemeten respons werd de voorspelde effectieve stijfheid gebruikt als een eerste schatting in een model-gebaseerde identificatie van de stijfheid, demping en fundamentele frequentie van het grond-paalsysteem. De analyses tonen aan dat de voorgestelde ontwerpprocedure een 7 keer hogere nauwkeurigheid levert bij het voorspellen van de in-situ initiële stijfheid dan het best-geschatte p-y-curvemodel. Verder zijn er 2 aanpassingen van het 1D-model gebruikt om de aanwezigheid van toegevoegde-massa effecten vanuit de grond te onderzoeken voor de reacties van het systeem bij hogere frequenties. Ten slotte werden de stijfheid en demping van het paalsysteem gerelateerd aan die waargenomen voor het volledige OWT-systeem. Verder werd de aanname van lineair elastisch grondreacties gevalideerd met behulp van de waargenomen paalrespons.

Een eerste schatting van de mogelijke baten van de ontwikkelde stijfheidsmethode, toonde een 8% besparingspotentieel voor de primaire staalmassa van de volledige ondersteuningsconstructie (MP, overgangsstuk en toren). Deze schatting werd uitgevoerd voor een hedendaags grond-paal-systeem, waarvoor (alleen) de vermoeidheidsgedreven wanddikte is geoptimaliseerd en is vergeleken met de dikte die nodig is wanneer men het conventionele (minder stijve) p-y curveprofiel toepast. Aangezien de kosten voor MP-ondersteuningsconstructies doorgaans meer dan 20% vormen van de totale kapitaalkosten van een offshore windpark, zal het gepresenteerde en gevalideerde werk naar verwachting een aanzienlijk gunstige invloed hebben op de haalbaarheid van toekomstige offshore windprojecten.

PREFACE

It's done! I'm writing these words with a mix of early post-doctoral depression and some disbelief, but fortunately also happiness for soon throwing off the subconsciously ever-present PhD burden. Like most 'great endeavours', this solo-project has leaned upon shoulders of numerous giants. Starting with David-Pieter Molenaar and prof. Andrei Metrikine who created the possibility; somehow you saw the doctoral candidate within me - that on itself is worth a compliment. David (and Siemens Wind Power as a whole), I'm grateful for having been given the opportunity to combine work at Siemens with a doctoral study. Although load engineering and the subject of this thesis turned out to be a challenging combination, I hope an overall positive contribution was perceived. David's nose for opportunities has presented my thesis with various unique features like the in-situ seismic measurements and the DISSTINCT project. I would like to also thank Jan-Bart van der Steen and Sven Voormeeren to have extended the support for this project. The fun, high-performance and academic atmosphere that was created in the engineering department in The Hague is really admirable and is to be cherished.

Then Andrei, after all these years the admiration that I developed for you during my MSc thesis did not diminish. The depth of your theoretical knowledge, creative ideas and mathematical skills are astonishing. Your own ambitious attitude has always inspired me to reach for the top, and although we did not produce "4 to 5 journal papers and a thesis within 3 years part-time PhD", I hope you are still satisfied with the results. Thank you also for appointing another math wonder as my daily supervisor: Karel van Dalen. Karel, it was great to have worked with you, enjoying your personality, energy and patience in helping me along the different mechanical and mathematical hurdles which we encountered. Also your excellent writing and (tough) reviewing skills have greatly smoothened the publishing process. This piece of text being unreviewed, you will probably find a couple of improvement opportunities - but from experience we know such is always the case, and is independent of the amount of your reviews that have already been implemented.

Winning the TKI Wind op Zee subsidy for our DISSTINCT project was a real highlight; David, thank your for the idea and support, and Sven, writing the proposal together was a much appreciated first cooperation! Afterwards Jeroen Bongers became the great 'rock in the surf'; your contribution to this project was one of the main reasons for its success. Paul van der Valk, besides being, together with Sven, my structural dynamics sounding board, your work in purchasing Shakira and arranging the measurements were vital. And of course Frank, thank you for your contribution in the shaker measurements and for being a good SSI-roomy (and that also counts for you Petertje!).

This thesis being long and wordy enough as it is, I cannot individually treat every colleague at the TU Delft and Siemens, but you know who you are; it has always been great fun and very inspirational to have been able to work with such knowledgable and nice people. To all of the students whom I had the pleasure to supervise: Jelle, Ouiam, Ying, Anneke, Christina, Thijs, Gerben, Nina, Corine, Marjolein, Stavros, Ingmar, Olivier, Michael, Evangelos, Matteo and Theofanis; thank you for the interesting and fun times and all of your good work! And thank you Anouk, for a very nice cover design!

Mom & dad, needless to say, 'a good beginning is half of the work'. Bart & Manon thank you for your lasting interest and support. And then of course, my love and personal coach, Eliz-Mari; thank you for all your support, the requested and unrequested advice and your rock-solid realism in countering my and Andrei's overly ambitious plans. Let's now try to keep the peace with 2 doctors in the house.

Pim Versteijlen
Delft, February 2018

1

INTRODUCTION

The motivation for this thesis originates from the offshore wind industry. More specifically, its eventual aim is to decrease the cost of the foundation structures that support the wind turbines, by enabling a smaller dimensioning of these structures - resulting in a reduced application of structural steel. This goal is sought to be achieved by establishing an improved design procedure for characterising the small-strain soil-structure interaction for rigidly behaving monopile foundations.

In this introductory chapter we will first reflect on the motivation for and the role of offshore wind in the global energy mix, listing some of the latest facts of this relatively young, fast growing industry (Sections 1.1.1 and 1.1.2). Afterwards, in Section 1.1.3, we sketch the main geotechnical challenges regarding the design of offshore wind monopiles, to then further zoom in on the main topic of this work: the state of the art in characterising the small-strain soil-monopile interaction in Section 1.2. Finally, the objective, contributions and organisation of this dissertation are outlined in Section 1.3.

1.1. OFFSHORE WIND: SCALING UP TO MATURITY

With the first erection of a wind turbine on an offshore foundation in Nogersund, Sweden, in 1990 and the first actual wind farm in 1991 at Vindeby, Denmark, the offshore wind industry can still be considered quite young. It is nonetheless maturing and growing at an ever-increasing pace. The Danes, the pioneers in industrialising wind-generated electricity, have led Northern Europe to become the cradle of this promising source of energy. The so-far unlimited possibilities to increase the scale of the turbines and farms at sea, together with the favourable wind conditions are the main motivations for undertaking the extra challenge of installing wind turbines offshore.

The industry, having the clear beneficial gain of providing a clean and abundant energy supply but being young and underdeveloped, needed (similar to, for instance, aviation when it was considered an 'infant industry' [1]) governmental support to financially

compete with traditional sources of electricity production based on (burning) fossil fuels. The seemingly high monetary cost of offshore wind generated electricity has formed the main topic of criticism over the last two decades. Despite the seemingly endless supply of renewable energy, their extraction process is generally underdeveloped due to the larger profits available in the fully developed extraction of highly energetic carbon fuels. Such a status-quo is not fastly broken by the plain laws of capitalism, but needs a (steady) visionary government and a broad evaluation of the long-term impact. Renewables lacking the financial vigour, need to cope with - besides a yet unequal economic playing field - a dwarfing lobbying effort of the oil & gas sector [2, 3]. Besides governmental influence, the consistent spread of alternative facts by the oil-oriented International Energy Agency undermined the perceived potential and installed power of renewable energy [4–6] and motivated the creation of the International Renewable Energy Agency as an alternative. The truth lies in the eye of the beholder, but as the motivation for the current research originates from a strong believe in the necessity of renewable energy in general, and wind power as one of the currently most promising applications, this chapter will list some of the published facts that confirm the confidence in the possibility of replacing polluting fuels by sustainable alternatives.

1.1.1. THE VALUE & COST OF OFFSHORE WIND GENERATED ELECTRICITY

With the progressive evidence of accelerated climate change, the necessity of engaging more sustainable, non-polluting energy sources becomes more evident every day. The 2015 Paris UN Climate Change conference [7] was a great success in clearing some of the 'fog' and alternative opinions on climate change by reaching an almost global consensus in formulating a concrete goal (and necessity): limiting average global temperature rise well below 2 degrees Celsius (°C) with respect to pre-industrial times, and aiming to keep this to 1.5 degrees. We are indeed experiencing a steady temperature rise, and it has become clear that this rise is accelerated by man-made emissions. 2016 was the third year in a row to set a new record on highest average global surface air temperature. Climatological modelling and collecting in-situ data (for instance quantifying the global ice melt) is highly challenging, so predictions always show a scatter, but many specialists predict that even with 'Paris measures', the world is still heading for a 2.9 to 3.4 °C increase within this century [8]. It has been shown [9] that a correlation exists between atmospheric CO_2 concentration, global temperature variation and sea water level, see Fig 1.1. Climatological changes are very slow ('inertial') processes, and the main challenge is to predict *when* things will change, rather than *if*. It is for instance expected that due to this climatological inertia, the sea level would continue to rise for the next 500 years, even if all our CO_2 emission were halted today. Historical (glacial/geological) data shows that every degree Celsius variation in the global mean temperature, has resulted in a sea level variation of about 20 meters [10]. According to the leading climate specialist James Hansen (for instance [11]) the Earth has warmed up 20,000 times faster over the last century than during the last abrupt change 65 million years ago (an asteroid impact), making it hard to predict when drastic effects will impact our living environment. However, by noting that the green line in the middle panel of Fig. 1.1 reflecting the CO_2 concentration, dramatically increases (overshoots) in the current century, one might become worried of what lies ahead of us. As can be

seen in that figure, a period which knew only slightly higher temperatures (about 1 °C higher) than currently measured, was the Eemian period. It is interesting to know that the average sea water level back then was 5 to 9 m higher than is currently the case [11]. Sadly however, still many people, companies and organisations, being motivated by short-term financial gain, continue to pursue the easy, conventional track of sustaining our society's carbon addiction - whilst employing a strong lobbying power in their defence in the public debate.

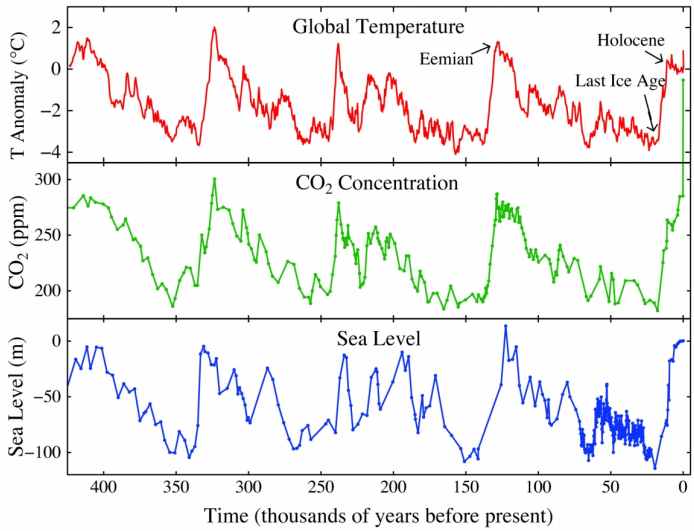

Figure 1.1: Historic variation (with respect to current (2012)) of global (from top to bottom) average temperature T, CO_2 concentration [parts per million (ppm)] and average sea level [9]. Note that the current (2017) CO_2 concentration is 405 ppm, which is substantially higher than indicated in this figure.

Having reflected on the necessity (or value) of limiting climate change, let us reflect on the cost of a measure we can exploit to limit further climate change as much as we can: offshore wind generated electricity. Clearly, this is only one amongst many measures that will contribute to that goal, but as discussed and what might become clear, offshore wind is currently amongst the most promising sources in sustainable energy generation. The noted main criticism on offshore wind (or renewables in general) - the seemingly high monetary cost - can be retorted at three levels of abstraction, depending on the definition of 'cost'. Namely, i) the broad-scale and long-term cost for society as a whole, ii) the cost for an economy, or iii) the direct monetary cost of the product (offshore-wind generated electricity). Obviously, the latter of the 3 is the most popular and convenient definition to focus on in criticising sustainable energy. Therefore we will here also shed some light on the other 2 definitions of cost before reverting to the monetary cost.

In the first definition, one takes into account the entire eventual chain of impacts the use of a certain energy source has on our society. The limited horizon of human nature

having a maximum length in the order of a lifetime, combined with a lack of awareness, has led the post-war Western world to unboundedly exploit natural resources and pollute the environment. It seems that only due to visual, concrete evidence and related living inconvenience [12], slowly a change of mind-set is observed [13]. Now it might be conceived too extreme (but arguably not unfair) to add to the cost of burning fossil fuels, part of the cost of, for instance, raising the Dutch dikes that will be required due to the rising sea level, but there are other, more direct, shorter-term, cost involved in these polluting activities; e.g., the extra health cost involved due to air pollution can nowadays be quantified quite well [12]. Advanced meteorological models can estimate the required measures for reaching a goal such as 'Paris' (temperature rise < 2 °C). One of those is the interesting fact that we can simply not extract the remaining explored (and let alone unexplored) fossil reserves from the ground, due to the involved detrimental effect on our climate. This makes a previously used argument for sustainable energy - depleting resources - obsolete, and sheds new light on the future of the oil & gas industry [14] that currently have 14 times more reserves than we can burn to stay below 1.5 °C temperature rise. Active divestment in this industry might be necessary to avoid a major global financial crisis once it is comprehended that those reserves - being the largest assets comprising the value of those companies (and our entwined economies) - are in fact not to be exploited.

On the second level, the macro-economic scale, numerous studies have already shown that - even for the higher prices of offshore wind a few years ago - when incorporating associated impacts such as employment opportunities, tax revenue, social cost, geopolitical risks, subsidies[1], transmission cost, etc., much more favorable outcomes are obtained for renewable energy than often stated [16, 17].

Then, the third, most common cost evaluation: the levelised cost of energy (LCOE); this is the sum of the total monetary cost of an energy plant throughout its lifetime (both capital and operational cost), divided by the total energy output [Euro per megawatt-hour (MWh)]. The shift of moving the turbines offshore comprised a significant increase of capital and also operational cost, and one of the main goals of the industry has been to decrease these cost in order to become also competitive on this direct monetary level (LCOE). Fortunately, many areas were identified where 'cost-outs' could be achieved, the current research being one of those. Due to progressive R&D, increasing the size of turbines and farms and due to obtained experience resulting in higher efficiency throughout the product-chain, the LCOE of offshore wind electricity has decreased over the last years - in line with the target that the industry set in 2013: a LCOE of 115 EUR/MWh in 2020. However, more recently, a breakthrough seems to have occurred in the bidding prices offered at the Dutch and German governmental auctions for wind farm permits and subsidies. In 2016, the Dutch Borssele I-II wind farm was conceded at a historic

[1] It is often assumed that fossil energy is not subsidized, whereas it in fact receives much more public support than renewable energy. Of course it has to be noted that these sources are still very important for our current economies, but factually, in the G20 countries they receive 4 times more public funding than renewable sources, often in the form of indirect subsidies like tax cuts, soft loans etc. [15]. Interestingly, also other industries that are perceived to be 'grown up' and economically viable are actually subsidized, the aviation industry being another example [1].

low price of 87 EUR/MWh (including costs for the grid connection). Figure 1.2 shows the development and prediction of the LCOE of offshore wind power from 2008 to 2020 [18]. Apart from the reasons named above, one of the main drivers causing such a shock effect were the clear policy and plans outlined in Denmark, the UK, the Netherlands and Germany, providing a healthy investors climate. Another game-changer was the auction type system introduced by the Danes and further developed in the Netherlands; the government executed the spatial planning, arranged the permits and collected the required environmental data beforehand, consequently reducing the perceived risk (resulting in lower financing cost) and time to first power production. In actual fact, financing cost were previously one of the main cost drivers for offshore wind projects, as very high interest rates were called for, stating that the application was one of high risk[2]. With about 12 gigawatt (GW) of installed power without any severe failures, the high-risk allegation is not accepted anymore. Moreover, the current low interest rates further helped reducing financing cost. Fortunately, Borssele I-II was not a single occurrence; since then, also historically low striking prices were reached in the UK, Denmark and some 'zero-subsidy' (grid-parity) bids in Germany. Finalizing this discussion, it should be noted that the competition in turbine manufacturing is high, and that these bidding prices are promised prices, not actual cost; the coming years will reveal whether still sustainable profits are realized, or whether the bids were too ambitious, leading to infeasible business cases.

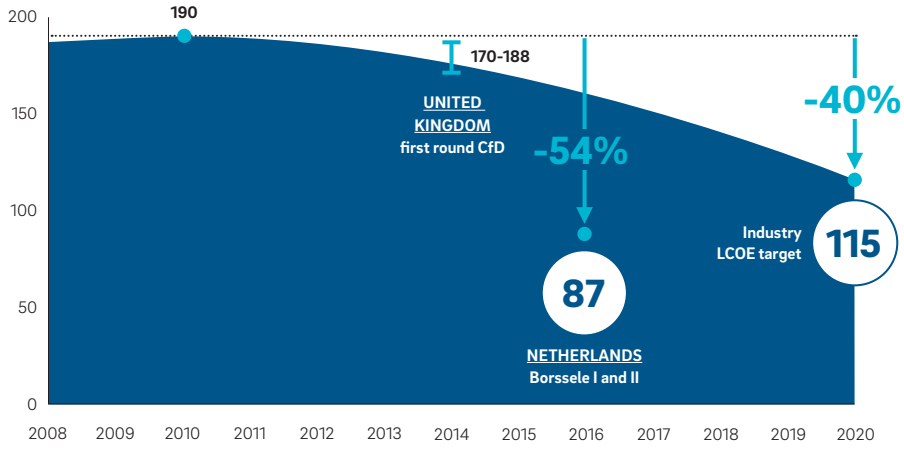

Figure 1.2: LCOE development and prediction (assumed in 2013), and actual bidding prices for the UK 'Contract for Difference' (CfD) round and the Borssele I-II wind farm. Prices include the cost for the grid connection [EUR/MWh] [18].

[2] McKinsey analysis have showed that a one-percentage-point decrease of capital yields a 5 to 10 percent decrease of the LCOE of renewables [19].

1

1.1.2. SOME RECENT FACTS

Offshore wind turbines (OWTs[3]) are growing to become amongst the tallest structures in the world, and the capacity of current farms are reaching the 1 GW power level, which is similar to an average coal-powered station. The turbine size and challenging offshore environment make them a very interesting engineering application where the fields of structural dynamics, geo-engineering, electrical engineering, aerodynamics, hydrodynamics and logistics all come together. The previously explained need of cost-effectiveness and the serial-production aspect (as opposed to the oil & gas industry where a 'once-off' and very safe, conservative design is typical) increase the design challenge, making it a popular topic for current research.

Figure 1.3 shows the cumulative and annually installed offshore wind power in Europe over the last 16 years. As can be seen, a vast growth has occurred; the total installed capacity has doubled about every 3 years, and projections indicate another doubling by 2020. These numbers can be considered representative for the globally installed capacity, as so far about 90% of offshore wind was developed in Europe: 12.63 GW versus 14.38 GW globally. Other markets are however emerging, the Chinese, Taiwanese and US markets being the first followers of the European example. It is estimated that a global capacity of 150 GW can be reached by 2030.

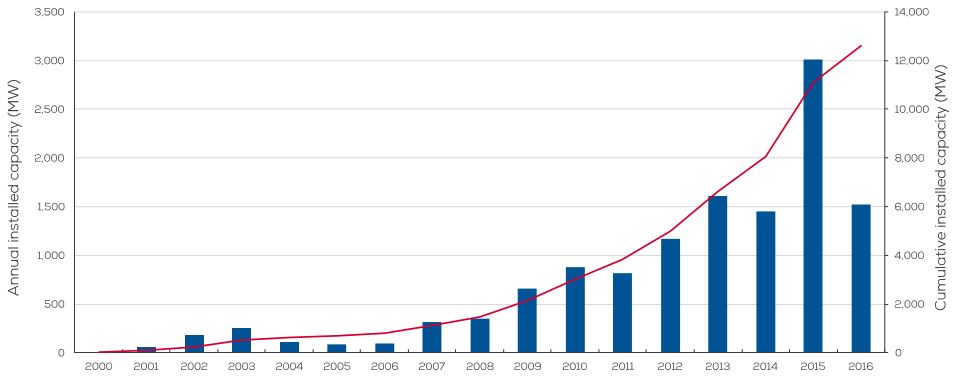

Figure 1.3: Cumulative and annually installed offshore wind power in Europe [20].

As mentioned in the previous section, one of the key drivers increasing the cost effectiveness of wind power is scaling up the rotor size; a quadratic relation exists between the power production and the radius of the rotor (the blade). Therefore, rotor sizes, rated power capacities and support structures of the turbines have increased dramatically over the years. Turbines of 7 - 8 MW with rotor sizes of 154 - 164 m are currently being installed, and the 'double digit' capacity turbine is expected to be available soon. As for

[3]In this thesis, 'OWT' indicates the total of support structure and rotor-nacelle assembly.

wind farm sizes, similar economies of scale have led to increased wind farm capacity, the current largest being the London Array wind farm with 630 MW and larger ones coming operational soon. In 2012 the Greater Gabbard wind farm (504 MW) produced 4,195 GigaWatt-hours of electricity, saving 2.3 million tonnes of CO_2 emission[4], and covered a bit more than 10% of the Greater London area electricity consumption.

From the discussed recent price-level successes and the agendas of current policy makers around the world, offshore wind appears to have a bright and ambitious future as one of the sources in the energy mix. As stated in the beginning of this chapter, the monopile (MP) is currently by far the most applied foundation type; more than 80% of the installed foundations are MPs [20]. The reason for its popularity is the cost effectiveness of the MP; it is a single, thin walled tube, making the fabrication and installation cheaper than for instance a truss, jacket-type foundation. Due to progressive R&D, its applicability has been stretched to much deeper waters and more unfavourable soils than initially anticipated, and it is expected that many more MPs will be installed in the future wind farms across the globe. Although the MP is a relatively simple structure, its interaction with the harsh offshore environment is not yet entirely understood, leading to conservative designs. However, as will be discussed in the next section, it is expected that many of the thus far installed MPs were in fact over-designed in terms of pile geometry - meaning that too much structural steel was applied. Since around 20% of the construction cost of an offshore wind farm are related to foundations [21, 22], reducing the conservatism applied in design by a better understanding of the interaction of the MP with the offshore environment, is an obvious step in further reducing the LCOE of offshore wind.

1.1.3. IMPROVEMENT OPPORTUNITIES IN GEOTECHNICAL DESIGN

The highest modelling uncertainty in the design of monopiles is related to the characterization of the soil and its interaction with this type of foundations [23]. Due to its variability in properties and the dependency on numerous condition factors, the understanding and modelling of soil reactions is in general a notoriously challenging exercise. Furthermore, as will be discussed later, the specific character of the soil-structure interaction (SSI) of rigidly behaving monopile foundations conveys complicated soil reaction mechanisms that require advanced modelling techniques. Various aspects and operational regimes of the SSI of MPs are currently not yet fully understood and are hence the topic of ongoing research. These can be roughly categorized in

- the small-strain regime, displacements resulting from fatigue limit state (FLS) loading, soil initial stiffness characteristics dictating the dynamic properties of the structure - the topic of this thesis,

- the large-strain regime, displacements resulting from ultimate limit state (ULS) loading, soil stiffness and strength characteristics dictating overall lateral stability of the structure,

[4] To put this in perspective, the US emission for 2016 was around 5.18 gigatonnes and the global emission of 2014 was 32.75 gigatonnes of CO_2 [8].

- soil stiffness degradation or increase and permanent displacements of the pile due to cyclic loading,
- installation-related problems like pile driveability, acoustic disturbance of sea life due to hammering of the pile and the influence of the installation on the properties of the soil.

As previously mentioned, a lack of knowledge on these topics, most often results in conservative designs of the MP foundations. At least, this is the expectation; the knowledge gap or measurement uncertainty does not always permit such a statement. For instance, the modelling of short-term stiffness evolution during cyclic loading is a challenging task, and where often a degradation of the stiffness is assumed, sometimes an increase is observed [24, 25]. Coupling this short-term evolution to the longer-term (accumulated) displacement and effective stiffness is then another topic requiring extensive research [26, 27]. Furthermore, pile-driveability analyses are known for their inaccuracy, resulting in undesirable in-situ surprises like pile refusals or run-aways.

In general, as the wind and wave loading act in the horizontal direction, only the lateral stiffness and strength of the MP are considered for the operational load cases and design checks. The lateral stability being design-driving for quantifying the diameter and the pile embedment length, the vertical capacity is always assured. The large-strain regime (relating to the strength of the soil) and the small-strain regime (stiffness) are often separately assessed in design checks, and such a split is also frequently observed in research scoping.

Concerning the large-strain regime, this involves the characterisation of the nonlinear part[5] of the soil force-displacement curve. The currently adopted p-y curve method for modelling the soil reaction (on which we will elaborate in the next section) describes this regime for both sand and clay. However, researchers claim that the method underpredicts the ultimate capacity of clay towards typical monopiles [28], and others have claimed that the ultimate capacity of sand is over-predicted by the p-y curve method [29] -[31], but the paper of Byrne [32] seems to suggest differently. As mentioned, the ultimate strength of the soil dictates the stability of the structure and mostly drives the design in terms of embedment length and also diameter. The ultimate displacements occur under the ULS loading which is obtained from the design load case simulations.

During most of its lifetime however, the OWT support structure endures small vibrations that cause cumulative fatigue damage in the structural steel. It is the soil-initial stiffness that governs the natural frequencies and the dynamic characteristics of the OWT. In monitoring the fundamental natural frequencies of installed OWTs, a quite consistent discrepancy is found between this measured frequency and the design-aimed frequency; up to 20% higher frequencies are measured, with most turbines within the 5% higher range [33]. This frequency corresponds to the first bending mode of the

[5] The stress-strain behaviour of soils is nonlinear, nevertheless, the initial part of this softening curve is often assumed to be linear - as is also assumed in this work. Section 2.1 contains more discussion on this topic.

support structure (MP + turbine tower). Due to the symmetry of an MP-based OWT, the structure has in fact 2 closely spaced first bending modes, vibrating in perpendicular directions: the fore-aft bending mode and the side-side mode. The frequencies of these 2 modes are key design parameters, as they need to be placed outside the resonance regimes of the wind and wave loads and the blade-passing frequencies. The fact that the true frequency is often higher than the one designed for is expected to be caused by underestimation of the initial soil stiffness. The resulting over-dimensioning of the support structure is mainly a waste of steel as the diameter and also the wall thickness[6] of the support structure are often increased to reach the desired fundamental natural frequency. It can however also justify an extended life time, as less amplification of the low-frequency wave loading takes place, resulting in less fatigue damage. In any case, a correct prediction of the fundamental frequency is desirable. The FLS loads, being related to the small-strain soil stiffness, currently most often determine the overall steel mass of the support structure.

Finally, although not explicitly mentioned in the above topics, there is another very important aspect in all the discussed SSI regimes which is not well understood and indeed has a very large impact on the structural response: soil damping. Damping reduces the amplitude of vibration, therefore, the more damping, the lower the accumulated fatigue damage and the lower the ultimate-loading response. As is often the case in structural dynamics, the damping in SSI is the most challenging property to identify and most challenging mechanism to model. Nevertheless, besides aerodynamic damping, the largest damping contribution is believed to stem from the soil. Most published attempts on modal identification [35–42] report values larger than assumed in the design models for the OWTs, which is often assumed to be around 1% of critical damping for the total support structure damping (excluding aerodynamic damping).

1.2. STATE OF THE ART IN SMALL-STRAIN SOIL-MONOPILE INTERACTION

The previous section sketched the wider background of geotechnical design of MP foundations. The current research focussing on the initial soil stiffness, this section elaborates on the state of the art within the industry and research community regarding modelling, soil characterisation and reported validation tests of the small-strain SSI for monopiles.

1.2.1. MODELLING

To model the lateral pile response, the industry has adopted the p-y curve approach from the oil & gas industry. This is a very intuitive, semi-empirical method that yields curves describing the local (uncoupled), nonlinear relation between the soil resistance p and the pile displacement y at specific depths and soil layers along the pile. The derivative of the p-y curve yields the (tangent) spring stiffness, which is used in a 1D

[6] A larger diameter stiffens the support structure, resulting in a higher natural frequency. This generally yields lower wave-induced fatigue damage as the natural frequency is shifted towards the less energetic, higher-frequency tail of the wave spectrum [34]. An increased wall thickness also stiffens the structure, and creates more contingency against fatigue-failure.

(Euler-Bernoulli) Beam-on-Winkler-foundation model. The method was developed for both clay [43] and sand [44, 45]. It contains a theoretical basis of soil reaction and failure mechanisms towards slender, flexible piles, which was subsequently calibrated using field tests on such flexible piles. The method has allowed the safe design of numerous MPs so far, but the p-y method, being calibrated for flexibly behaving piles, does not capture all the reaction mechanisms involved in the SSI of the currently employed rigidly behaving monopiles [46]. An often used parameter to aid in predicting the pile behaviour is the ratio of embedment length L and diameter D; piles with a higher L/D ratio behave in a more flexible manner. The displacements of flexible piles are primarily caused by bending of the pile. For piles with a low L/D ratio, the displacements, apart from bending, also result from shearing and overall rigid rotation of the pile. While a flexible pile evokes a more local reaction of the soil, a rigid pile makes the soil react in a global (i.e. non-local) way; a larger part of the continuum is mobilized to counteract the rigid pile [47]. Fig. 1.4 shows an example of the typical response shapes of a flexible versus those of a rigidly behaving pile[7]. The large shearing forces due to displacements of the rigid pile tip, and the distributed restoring moment caused by shear forces along the pile wall working at a large lever arm (the radius of the pile), are extra soil reactions that generally cause rigid piles to behave stiffer than flexible piles. A local 1D Winkler foundation containing only lateral springs (as assumed in the p-y method) may therefore suffice for flexible piles, but a 1D model for rigid pile behaviour needs additional features to capture the complex SSI [48]. The piles used for calibrating the p-y curves had L/D ratios larger than 20 and the MPs that are currently being designed have a L/D as low as 3. Furthermore, although the often employed DNV GL design standard [49] advises not to use the p-y curves for small-strain analyses, in practice the curves are used for all load and design simulations.

Regarding the small-strain modelling, the p-y initial 1D stiffness k_s [N/m^2][8] is assumed linear, and it is often referred to as the initial subgrade modulus $k_{s,0}$ or E^*_{py}. In the p-y curve formulation for sand, k_s is calculated by multiplying k, the modulus of subgrade reaction [N/m^3] (first described by Terzaghi [50]), with depth z. k is only determined by the angle of internal friction of sand ϕ. Note that this k is a soil-structure interaction (SSI) modulus (as opposed to a 'pure' soil property like for instance the shear modulus G); it was once calibrated on the way slender piles react when embedded in specific soil types. As the same value for k is currently still adopted for large-diameter piles, and no geometric pile effect is taken into account in establishing the initial stiffness, a modelling error seems apparent. Furthermore, the assumption that this stiffness increases linearly with depth for any type of sand, is expected to be incorrect [51]. The p-y curve for clay is described using a 3$^{\text{rd}}$ order polynomial, resulting in infinite initial stiffness (an infinite slope of the curve near the origin at y=0) [49]. To overcome such unphysical behaviour for small-strain dynamic simulations, rules have been established

[7] The details of the shown SSI: the length L of both piles is 30 m, and they are embedded in homogeneous, linear elastic soil with a Young's modulus of 200 MN/m^2. The diameter D of the flexible pile is 1 m ($L/D = 30$) and that of the rigid pile is 8 m ($L/D = 3.75$). The wall thickness is 1% of the diameter for both piles. The piles were loaded with an overturning moment of 45 Nm and 1 N horizontal force at mudline.

[8] The stiffness k_s is computed per unit vertical length of the pile, explaining the dimension [N/m/m].

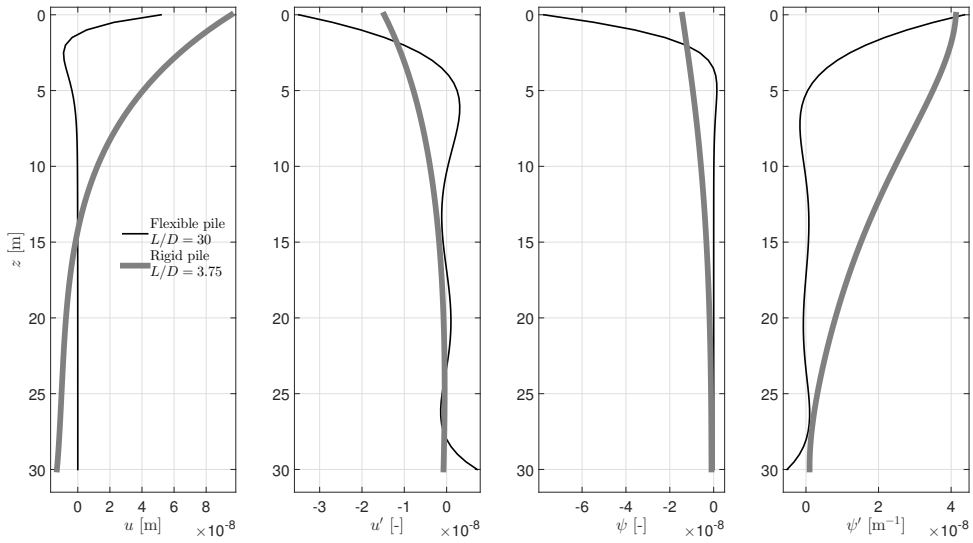

Figure 1.4: Typical embedded pile response of a flexible and a rigidly behaving pile, showing from left to right the (modelled) displacement u, slope u', rotation ψ and curvature ψ' profiles. To enable visual comparison, the displacements, slopes and rotations of the rigid pile were multiplied by a factor 80, and the curvature by a factor 3200.

.

that yield a linear (finite) initial stiffness by placing the first discretization point near the origin. Because of the shortcomings and because of its relevance, the modelling of initial stiffness for both sand and clay has been critically studied by several researchers [51–56]. Seemingly contradictory to what is measured in the field, it was found in some of these studies that the p-y curve method actually over-predicts the initial stiffness of the soil for larger depths. If this were generally the case, it would not explain the higher natural frequencies that are measured, or it would indicate the crucial contribution of the shallow-layer stiffness to the overall stiffness of the soil-pile system. As the stiffness depends on the soil type, the geometry of the structure, and the loading type, it remains challenging to find a generally valid design method for this problem. Depending on the focus of the researchers, and possibly the applied advanced modelling techniques, different methods have been suggested. In geotechnical design, empirical tuning factors are often used to capture the complex interaction of the soil with different structure types. For instance, in the OWT-related research, large diameter-effect tuning factors were suggested to improve initial stiffness predictions [52, 54, 57]. More recently however, some of these tuned p-y relations were said to be incorrect or at least not generally applicable, and yet another method was presented [31].

Impressive work has been performed on dynamic SSI modelling over the past decades. The engineering [58–60] as well as the rigorous models, [61–63], however, all have in common that they were - similar to the p-y curve method - mainly focussed on describing the SSI of slender, flexible piles. Therefore the engineering methods and tables, in

some of these cited works, linking stiffness and damping coefficients to soil and structure type, are not directly applicable to current OWT foundation dimensions and typical frequencies.

More recently, some of the referenced researchers proposed the use of a 3D model to more accurately capture the global soil reactions towards rigidly behaving piles [48, 54, 55, 64]. A 3D model automatically captures the additional soil reaction mechanisms and non-local behaviour invoked by rigid piles. Other than only employing these more advanced models to serve as a check (validation) of the 1D design models, it is desirable to incorporate their accuracy directly into these design models. However, the computational time involved in solving 3D models, makes them only appropriate for 'once-off' simulations. Simpler models are required for application fields needing thousands of design simulations. Due to the stochastic nature of the loading environment of offshore wind turbines, currently about 120,000 10-min time-domain (for capturing the nonlinear aeroelastic interaction) simulations are performed for an average design case. This simulation demand has steadily grown over the last years, and is expected to keep increasing with progressive certification demands. The gain in computational efficiency due to the significant reduction of the number of degrees of freedom in the transition from a 3D model towards a 1D model, becomes substantial for such simulation requirements.

Concerning the modelling of damping, as no proper or relatively low-threshold alternative is available, most foundation designers refer to a paper of Cook from 1982 [65] on the modal identification of a single-pile platform in the Gulf of Mexico. Herein, the modal soil damping is computed based on the material damping of the specific soil, the stiffness profile and the mode shape and modal mass of the structure. A conservative total 'support structure damping' is estimated as the sum of the structural steel hysteresis, damping from the interaction with the water, the inclusion of a passive damper in the tower (if present) and the soil damping - the contribution of the soil often being estimated to comprise at least half of this support structure damping. For operational turbines, by far the largest contribution of damping is generated by the aerodynamic interaction of the rotor and the wind, and this damping is quite successfully captured by the currently employed aeroelastic simulation codes. Clearly, however, this damping is mainly activated for the fore-aft vibration mode, aligned with the wind direction. In case the wind and wave directions are not aligned, or in case the turbine is idling (out of production with its blades pitched out to feathering position) the structure fully 'relies' on the support structure damping. The soil damping is attributed to the (hysteretic, displacement-dependent) material damping, and the geometric damping in the soil is generally said to be negligible for the low frequencies typical for relatively flexible offshore monopile structures. The damping in design models is typically included using the Rayleigh method; the damping matrix is made proportional to the stiffness and mass matrices, tuning the proportionality factors so to reach a total damping percentage that has been established based on Cook's (or a similar simple) procedure. More rigorous methods are available, however, similar to the challenge of improving the stiffness in the design method, the advanced modelling techniques can be used to more accurately

capture the damping. However, subsequently extracting the obtained results to be used in simpler models is as yet another major challenge [66]. In the saturated offshore soils, damping is expected to not only be caused by material hysteresis, but also by viscous effects related to pore-water flow [67]. Such viscous damping is thus related to the permeability of the soil, the frequency and amplitude of vibration of the pile, but also to the geometry of the pile (relating to the water-pressure dissipation path). This porous effect and the resulting damping is present in the small-strain (linear) SSI [67], but was also shown to influence damping levels in a more indirect way for large displacements in the nonlinear dynamic SSI, where the damping stems from plasticity caused by liquefaction [68]. In actual fact, a realistic simulation of the nonlinear unloading-reloading behaviour of soils [69] will inherently include the hysteretic behaviour of soils. The 'Masing rule' is a well-known and established soil model describing such hysteretic behaviour, however, only recently have researchers started employing it for the offshore wind application [70, 71]. Nevertheless, capturing and subsequently simulating the correct shapes for the virgin backbone curve and the subsequent cyclic force-displacement paths of the 1D macro elements along the depth of the 1D pile is highly challenging. Finally, it is good to note that - as will also be shown in this work - independent of the modelling method, a correct representation of the soil stiffness is a requisite for an accurate approximation of the soil damping. Moreover, the quality of the predictions of any (advanced) SSI method is highly dictated by the success in characterising the input soil parameters.

1.2.2. SOIL CHARACTERISATION

The most applied soil measurements in the OWT industry are conventional geotechnical tests like the in-situ Cone Penetration Tests (CPT) and laboratory testing of borehole samples. In that sense, the soil characterisation is also similar to that in the oil & gas industry, as these tests provide the geotechnical strength parameters that are input to the p-y methodology. These testing techniques are large-strain, soil-disturbing measurements, and one may question whether they allow to assess the small-strain behaviour of the soil. As previously discussed, it is the small-strain stiffness that dictates the dynamic behaviour of the structure, therefore, characterisation techniques are required that can identify this initial soil stiffness directly - as apposed to indirect empirical methods that aim to correlate the measured soil strength properties and stiffness properties for a certain type of SSI.

1.2.3. EXPERIMENTAL VALIDATION

Most published experimental validation of the SSI of rigidly behaving MPs comprise scaled lab tests, either simple direct ('1 g') testing [72], or involving a centrifuge to additionally scale the gravitational force (confining pressure) [25]. These tests can yield valuable insight, especially in the qualitative difference in response between different structures. However, as a correct simultaneous scaling of all of the involved properties is very challenging [73] and due to the need of substantial idealization of the in-situ conditions, caution has to be exercised in establishing direct links between these lab tests and the SSI of the real-sized structures in the field.

In the attempt to relate the response predicted by design models to that of the actual foundation response in the field, many researchers have identified the modal (dynamic) properties of the installed turbine and support structure [36–42]. Not all of these researchers necessarily focus on a detailed identification of the soil response, but more on the fundamental frequency and - if successful - the total damping of the structure as a whole. For installed operational OWTs, such modal identification based on monitoring of the full system (i.e. foundation, tower and rotor-nacelle assembly (RnA)) strikes a good balance in yield of knowledge and cost level; the structure being placed in the offshore environment and it being loaded by highly variable wind and wave loads, it is challenging to establish a clear force-response relation. However, as such load-validation is strongly desired within the industry, more advanced measurement campaigns involving lidar wind and turbulence measurements and recording of the wave characteristics are coming online. In most of the current modal identification techniques, the structure is in fact assumed to be unloaded. This is practically the case when the turbine is in idling state [40], or when the turbine exerts a free decay after being excited by for instance a rotor stop [36, 38] or after a boat impact [42]. In judging the contribution of the soil to the total system stiffness, it is generally assumed that the stiffness and mass of all the structural components are correctly modelled, and that any discrepancy between the observed and simulated (design) fundamental frequency can be attributed to a soil modelling error. Nevertheless, as will be shown in this thesis, for stiff soil-pile cases, the frequency can prove to be rather insensitive to variations of the soil stiffness. Furthermore, uncertainties do actually exist regarding the mass and stiffness of the installed structure; the exact RnA mass and that of all internal components are not always exactly known, and for instance the stiffness of a grouted connection between the MP and the transition piece is not trivially obtained. In addition, due to the occurrence of scour holes and migrating sand banks, the seabed level is a variable parameter that is not easily monitored and which influences the structure's natural frequency. As previously mentioned, identification of the damping is challenging and outcomes show a higher scatter than for the natural frequency. The soil damping is estimated by subtracting from the total support structure damping (mostly identified for either the idling state or free-decay state[9]), the damping contributions of the structural steel hysteresis, damping from the interaction with the water and the damping caused by an installed passive tower damper - thus assuming that these latter 3 damping contributions are well-known, and that the different contributions can be linearly superimposed to form the total damping.

Clearly, it is most desirable to directly measure the force-response relation of the system of interest: a real-sized, installed offshore monopile. To exclude the dynamic disturbance of the tower and RnA (and the related modelling uncertainties), such a super structure should preferably not be present during identification of the SSI. As will be shown in this thesis, the sensitivity of the structural response of a MP-only system to the properties of the soil is much higher than that for a full OWT system. We aim to predict the SSI of real offshore MPs, therefore, the presence of pile-installation effects and pore-water pressures and the absence of scaling issues are great benefits of measuring (on) in-situ

[9] Note that the idling and free-decay state in fact involve different vibration amplitudes, for which we may expect different damping values.

piles. To establish the force-response relation of the SSI system, a load needs to be applied in a controlled way, which is a challenging task in the offshore environment. Furthermore, to truly capture the SSI, measurement sensors need to be installed on both the embedded part of the structure and in the soil. The combination of controlled loading, the need of an extensive sensor array and the desire of identifying the SSI for a real-sized offshore MP-only system, make such a measurement campaign a costly and ambitious operation. Maybe for that reason, only few publications are available on controlled ('known input') dynamic testing of laterally loaded, in-situ, rigidly behaving MPs. The few available attempts of using a shaker as an excitation source were on very slender piles in onshore conditions [74, 75] or on an onshore wind turbine which is not supported by an MP [76]. Research on lateral pile-resistance has been performed by Byrne et al. [77], but these experiments mainly focused on monotonic (static) loading, and to a lesser extent also one-way cyclic (i.e., not harmonic) loading was applied. Piles varying from 0.27 m to 2 m in diameter were tested at two onshore sites (one with mainly clay, the other sand). By also varying the embedded length, L/D ratios were obtained that are characteristic for current MP foundations. All in all, we can conclude there is a lack of reported test data of in-situ, rigidly behaving piles with which we can validate the models that simulate the dynamic SSI of these structures.

1.3. THESIS OBJECTIVE & OUTLINE

In this section we shortly recap and reflect on the discussed state of the art, and extract the research gaps and requirements from the design community, to formulate the objective of this thesis. The original contributions and outline of the thesis are given in Sections 1.3.2 and 1.3.1, respectively.

From the previous paragraphs it became clear that both the modelling and the soil characterisation for capturing the small-strain soil-structure interaction for relatively short, large-diameter, rigidly behaving monopiles needs to be improved. Moreover, there is an absence of measurements of the response of realistic in-situ piles to controlled lateral loading, which can validate any of the newly developed SSI models.

Besides measuring the large-strain properties of soil, we should aim to directly capture also the in-situ small-strain, dynamic characteristics of the soil. On the modelling front, it is widely accepted that the SSI of rigidly behaving piles can be best simulated using 3D models; the extra soil reactions (with respect to flexible piles) and the non-local, coupled response of the soil continuum towards rigid piles cannot be captured using merely uncoupled, lateral springs as used in the 1D Winkler model.

Nonetheless, a 1D model is currently still required in the design process. 3D models are computationally too expensive to run the thousands of time-domain simulations that are needed to capture the stochastic wind and wave loads. Apart from being fast, the 1D Winkler model is an all-time preferred concept of the engineering community, due to the related intuitive visualisation of external forces and internal stresses and overall response of the pile. To combine the accuracy of a 3D model and the speed of a 1D model, a method is required that yields the properties of an equivalent 1D model

so that it mimics the 3D model. This translation method is therefore a necessary third step in improving the current design methodology for the SSI of monopiles.

Finally, after having established the three-fold improvements of the a priori in-situ small-strain soil characterisation, 3D modelling and 3D to 1D translation, the research cycle should be closed by performing a posteriori in-situ validation measurements on an installed monopile. As no such tests have yet been reported in the offshore wind industry, newly developed SSI methods for monopiles could so far only be validated in a limited way. For these reasons the aim of the current thesis is to

provide a method for identifying an effective 1D soil-structure interaction model for rigidly behaving monopiles that mimics the small-strain response of a 3D model, of which the dynamic soil properties are characterised using in-situ seismic measurements.

Moreover, the success of this **effective stiffness method** in predicting the SSI should be **validated** by comparing the recorded response of an **in-situ installed monopile** with that predicted by the effective 1D model.

1.3.1. ORGANISATION OF THE TEXT

The thesis is structured in line with the sequential steps that are to be followed to establish an effective 1D, small-strain model for a rigidly behaving monopile.

The initial step concerns the characterisation of the relevant in-situ soil conditions - this is the topic of **Chapter 2**. The design of OWT support structures is often driven by fatigue loads. As the accumulation of fatigue damage is strongly effected by the dynamic properties of these offshore structures, and as in turn these properties are governed by the initial, small-strain soil reactions, this chapter is focussed on acquiring the in-situ dynamic soil characteristics. After a brief reflection on the small-strain regime and the assumption of linear elasticity, some measurement setups are described for both laboratory and in-situ testing. Subsequently, the chapter presents the 2 in-situ tests that were performed in the course of this thesis: the Seismic Cone Penetration Test (SCPT) - used for acquiring the stiffness (i.e., the shear modulus) profile, and the Multichannel analysis of surface waves (MASW) - used for acquiring both the stiffness and the material damping profile. Methods are described to invert these seismic data, and the generated stiffness profiles will be used throughout the next chapters of the thesis.

The identified small-strain soil properties are employed in **Chapter 3** to define the linear elastic continuum of a 3D SSI model. As was discussed, incorporating the 3D soil effects is essential for capturing the rigid SSI typical for monopile foundations. This short chapter presents the two 3D models employed in this thesis: a finite-element (FE) model developed using ANSYS software to simulate the static SSI, and a MATLAB based model for capturing both the static and the steady-state dynamic SSI of rigidly behaving monopiles.

For the 3D simulations to become (even) more valuable to the engineering design community, the complex 3D soil mechanisms should be translated into a simpler, faster model that can be used in the design process. **Chapter 4** presents the 2 novel techniques that were developed for computing a 1D effective soil stiffness profile for the Winkler-type model, so that it mimics the 3D simulation of both the small-strain static and the steady-state dynamic SSI of large-diameter piles.

In **Chapter 5** the performed in-situ validation pile tests are described and analyzed. The pile head of a stand-alone MP was excited with a shaker, applying a lateral steady-state excitation, and measuring the response of both pile and soil at multiple vertical levels. The performance of the 2 effective stiffness methods in predicting the stiffness profile for the test pile (which were identified in Chapter 4, based on the 3D models established in Chapter 3, using the input parameters identified in Chapter 2) are assessed based on a comparison of the modelled and measured pile response. Furthermore, the response of the 1D effective model is compared with the response predicted by the p-y curve design model. A single stiffness-profile correction factor is extracted so that the modelled response best matches the internal transmissibility functions as obtained for the shaker-excited pile response. In subsequently fitting the measured transfer function, also the soil damping of the stand-alone pile is estimated. Two adaptations of the 1D model are considered to investigate the presence of soil-added mass effects in the higher-frequency response of the system. The identified effective stiffness and damping properties of the stand-alone pile are related to the fundamental frequency and damping as observed for the full OWT structure (of which the tower and RnA were installed soon after the experiments). The benefit of stand-alone pile testing for validating a soil model is demonstrated in light of the much higher sensitivity of the response of this system to the soil properties compared to the response of a complete OWT structure. Finally, the linear elastic soil assumption is validated for the observed SSI.

Finally, the main conclusions of the thesis and recommendations for extended research are given in **Chapter 6**.

1.3.2. THESIS CONTRIBUTIONS

This thesis comprises the following academic and practical contributions:

- A method was established to compute an effective 1D local stiffness $k_{eff}(z)$, optimising the profile of the uncoupled lateral springs so that the response predicted by the 1D Winkler model mimics the static response of the 3D model of a rigid pile in stratified soil in terms of displacement, slope, rotation and curvature along the full embedded length of the pile. Accurate matches can be obtained for quite a broad range of pile geometries and soil (stiffness) profiles. However, this 'local' method seems to perform worse for piles with $L/D < 4.5$, softer and/or strongly irregular soil stiffness profiles. The same methodology was found to also be able to generate an effective 1D damping profile $c_{eff}(z)$ to additionally mimic the SSI damping at low frequencies - provided that the previously found static stiffness profile $k_{eff}(z)$ accurately captures the static response. See Section 4.2 and [78].

→ A second method was established to compute effective 1D non-local stiffness kernels which fully capture the coupled 3D reaction of the stratified soil towards the rigid pile, for both the static and the low-frequency dynamic SSI. By implementing the complex-valued stiffness kernels in a 1D Winkler-type model, both the real and the imaginary part of the steady-state 3D dynamic response in terms of displacement, slope, rotation and curvature along the full embedded length of the pile are matched by the 1D model. This 'non-local' method was shown to be applicable for a large range of pile geometries and soil stiffness profiles. See Section 4.3 and [79].

With these 2 methods, the engineering design community is served with the accuracy of a 3D model, and the speed of the (effective) Winkler model. The choice of condensing to a full Winkler-type model instead of for instance a lumped parameter model, stems from the strong desire of the engineering community to employ such 1D models. Winkler-type models have the advantage of increased physical insight as they directly yield a simple representation of the soil reaction and the distribution of stresses within, and displacements of the pile.

→ At the start of the thesis, only conventional geotechnical measurements (CPTs and borehole sampling) were reported to be performed to characterise the in-situ soil conditions of OWT foundations. At an early stage it was advocated [80] to additionally perform geophysical measurements like the SCPT to truly capture the small-strain, dynamic soil properties that are relevant for the small vibrations of offshore monopile foundations. The SCPT, although not new in other fields, was so far not reported in the OWT related literature. Therefore a thorough inversion of in-situ measurements (performed by the author) is reported, showing common pitfalls and presenting an improved inversion method with respect to more commonly applied techniques. See Section 2.2 and [78].

→ A new seismic cone test setup was developed together with Fugro, aiming to capture the in-situ soil damping. Nevertheless, no meaningful damping values could be extracted from this data - nor from the SCPT data [81]. For that reason, an investigation track was set up focussing on the inversion of surface wave measurements; the author co-supervised numerous MSc theses on developing inversion methods to extract the shear-modulus profile and subsequently the damping profile. Actual MASW were performed by the author at the same site (turbine position 'W27' at the Westermeerwind wind farm). However, the data quality only allowed for stiffness inversion - not damping. Subsequently a collaboration was setup with the Norwegian Geotechnical Institute, providing us with high-quality data, which should allow for successful damping inversion. This research track is currently ongoing. If successful, the community will be served with a novel step-wise approach for capturing also (apart from stiffness) the effective damping profile, by performing (1) in-situ MASW measurements yielding an accurate material damping profile which is used as input for the 3D model (2), of which the effective 1D damping (dashpot) profile can be extracted using the presented methods. See Section 2.3, which is a summary of the guided works of [81–84].

→ To close the scientific loop, the a priori in-situ characterisation in combination with the 3D modelling translated into a 1D effective model, the eventual simulated pile response was validated through unique in-situ measurements performed on the installed foundation piles of turbine W27 and W24. A customized shaker was built to ensure measurable low-frequency pile response. Together with an extensive set of sensors on both the embedded W27 pile and in the surrounding soil, a 'first-off' measurement setup was established [85], yielding the best as yet reported validation opportunity for the lateral, dynamic response of a rigidly behaving monopile, including saturated, nonhomogeneous sandy soil conditions and installation effects. Furthermore, the structure being a stand-alone pile, excluding dynamic disturbance of the (usual) super structure of tower and turbine, and the test comprising a controlled (known) loading, this campaign was shown to yield a much lower uncertainty than for the commonly applied monitoring of the operational full OWT structure. A prompt extraction of the dynamic properties of the system initially proved not to be trivial, being related to the high damping of the structure and the necessity of a detailed modelling of the shaker excitation force. In matching the observed and modelled internal transmissibility and transfer functions, the employed model-based identification approach showed to be successful in estimating the stiffness, damping and fundamental frequency of the soil-pile system. It was shown that the proposed design procedure yields a 7 times lower relative error in predicting the in-situ initial stiffness than the best-estimate p-y curve model. Furthermore, 2 adaptations of the model were employed to investigate the presence of soil-added mass effects in the higher-frequency response of the system. Finally, the stiffness and damping of the pile-only system were related to those observed for the full OWT system, and the assumption of linear elastic soil response was validated using the observed pile response.

A large set of data (of the response of both the pile and the soil) of various shaker-excitation runs is now available for future research. Furthermore, that data can be correlated to the data of the full OWT response, which has been monitored since March 2016 - comprising the MP and soil sensors, strain gauges in the tower and the standard turbine operational-monitoring channels.

→ The developed 'Effective Stiffness Method for small-strain soil reactions' was qualified by DNV GL, through their DNV-RP-A203 Technology Qualification process [86–88]. This involved extensive reviewing of the method and a workshop, which further improved the method for industrial application. The Effective Stiffness Method comprises the 3 described steps of in-situ characterisation of the small-strain soil conditions, 3D modelling and the translation of the 3D effects into a 1D effective model.

→ An initial estimation of the possible benefit of the developed stiffness method, showed an 8% saving potential for the primary steel (shell) mass of the complete support structure (MP, transition piece and tower). This exercise was performed for a contemporary soil-pile case, for which (only) the FLS-driven wall thickness was optimized with respect to the thickness needed for the conventional (softer) p-y curve profile.

2

Small-Strain Soil Characterisation

In this thesis we assume that the occurring soil strains γ_s in the SSI of an OWT monopile foundation belong to the small-strain regime for most of the endured load cases, and that the soil can therefore be idealised to behave as a linear elastic material [66]. It is this linear elastic regime that dictates the dynamic behaviour of the support structure. Determining the occurring strain levels in the soil due to loading of the structure is a challenging task, involving accurate measurements of pile displacements and back calculation of the soil reaction with advanced nonlinear 3D constitutive models that in turn require extensive in-situ soil characterisation. Given the indications of (over-) conservative design of the installed monopiles so far (the higher measured natural frequencies of the OWTs than designed for, as discussed in Section 1.1.3), the assumption of small-strain soil behaviour for these structures could be justified. Simulated pile behaviour indeed shows that for most depths and the majority of load cases the displacements remain within the linear regime of the p-y curves, and these curves are said to be conservative for both small displacements [57] and large displacements [32]. If research like the one reported in the current thesis will remove some of this conservatism, resulting in less stiff SSI systems, more focus on the nonlinear soil behaviour will be required.

For linear elastic soil behaviour, the following relatively simple relations hold between the velocity of shear waves C_s and that of pressure waves C_p in the continuum, and the basic elastic properties: the shear modulus G (also referred to as the initial shear modulus G_0 or G_{max}), the Young's modulus E, the density ρ, and Poisson's ratio ν:

$$C_s = \sqrt{\frac{E}{2(1+\nu)\rho}} = \sqrt{\frac{G}{\rho}}, \tag{2.1}$$

$$C_p = \sqrt{\frac{(1-\nu)E}{(1+\nu)(1-2\nu)\rho}}. \tag{2.2}$$

In modelling soil-structure interaction, the shear modulus G is the most important stiffness parameter, and due to the above simple relation and the high sensitivity of G to C_s, determining the shear-wave velocity of the soil is the goal of most of the developed soil characterisation techniques which will be discussed in the next section (2.1). The stiffness is less sensitive to the density and Poisson's ratio, and, moreover, their values are known to lie within a relatively narrow range [89].

A proper identification of the elastic properties of the foreseen site is the first requisite step for a correct modelling of the SSI. This chapter explains how this can be done; in-situ measured data will be inverted, and the stiffness profiles that are identified will be employed throughout Chapters 3 to 5 to showcase and validate the effective stiffness method. In the next sections we will first shortly reflect on the definition of small soil strains to subsequently provide an overview of some small-strain testing methods, categorized in laboratory methods (Section 2.1.1) and in-situ methods (Section 2.1.2). Afterwards, we focus on the 2 seismic in-situ testing methods that were employed in the course of this thesis for identifying both the stiffness and the damping profile: these are respectively the Seismic Cone Penetration Test (SCPT, Section 2.2) and the Multi Channel Analyses of Surface Waves (MASW, Section 2.3).

2.1. TESTING METHODS

A vast amount of testing methods have been developed over the last decades to characterize soils. They can be categorized in those performed in a laboratory (lab) where soil samples retrieved from in-situ boreholes are tested in a controlled environment, and methods performed directly in the field (in-situ). Here we will only discuss a few small-strain testing methods. Before doing so, it is good to touch upon the definition of small soil strains, the typical strains occurring at different SSI systems and testing methods.

The stiffness of soil is known to be highest at very small strains (hence the indication G_{max}), and to remain relatively constant with increasing strain up to a certain linear elastic threshold strain γ_{et}. The value of γ_{et} depends on the soil type and in-situ condition factors, but a value in the order of $\gamma_s = 5 \cdot 10^{-5}$ [-] is reported in [90] to be a strain level beyond which the stiffness degradation occurs. This seems to correspond quite well with the often referred stiffness-degradation curve for sand of Atkinson & Sallfors [91] shown in Fig. 2.1, where the shear modulus for strains up to roughly $5 \cdot 10^{-5}$ only degrades with a small percentage. Seed & Idriss [92] published a value of $\gamma_{et} = 2 \cdot 10^{-5}$, which was nevertheless argued to be too low by Llambias [93]; a $\gamma_{et} = 4 \cdot 10^{-4}$ would better match site response studies during earthquakes. Other published curves show a slightly different initial degradation; see for instance the more general soil (i.e., both sand and clay) shear modulus degradation curve of Sawangsuriya [94] shown in Fig. 2.2, which in turn is based on various other studies. In this curve, the elastic threshold strain γ_{et} is set at 10^{-5}, but here it is emphasized that other properties of the soil and in-situ conditions influence this threshold location: the plasticity index I_p and confining pressure σ_0. Other properties influencing the shear modulus degradation curve $G(\gamma_s)$ are overconsolidation ratio, void ratio, degree of saturation, aging and cementation. Depending on the foreseen SSI application, a choice has to be made regarding the test-

ing method for characterising the soil at the relevant strain level. Fig. 2.3 shows an overview of occurring strain amplitudes at various testing methods and SSI applications according to Studer & Koller [95]. It can be observed that the smallest strains occur when seismic testing is performed.

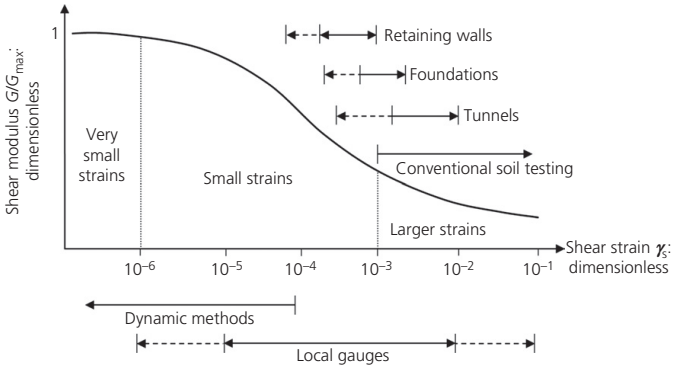

Figure 2.1: Shear-modulus degradation with strain γ_s for sand according to Atkinson & Sallfors [91].

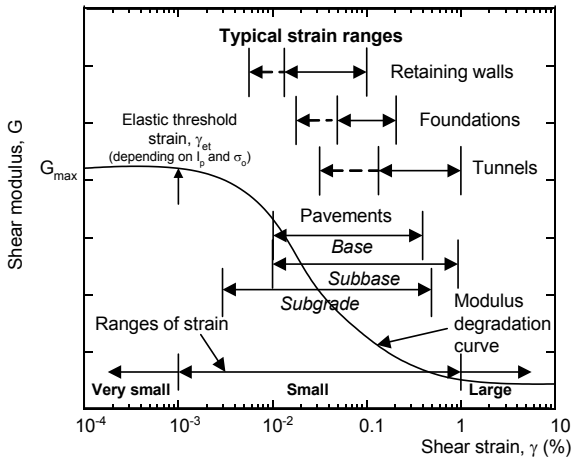

Figure 2.2: Shear-modulus degradation with strain γ (γ_s) according to Sawangsuriya (which is in turn based on various other studies) [94].

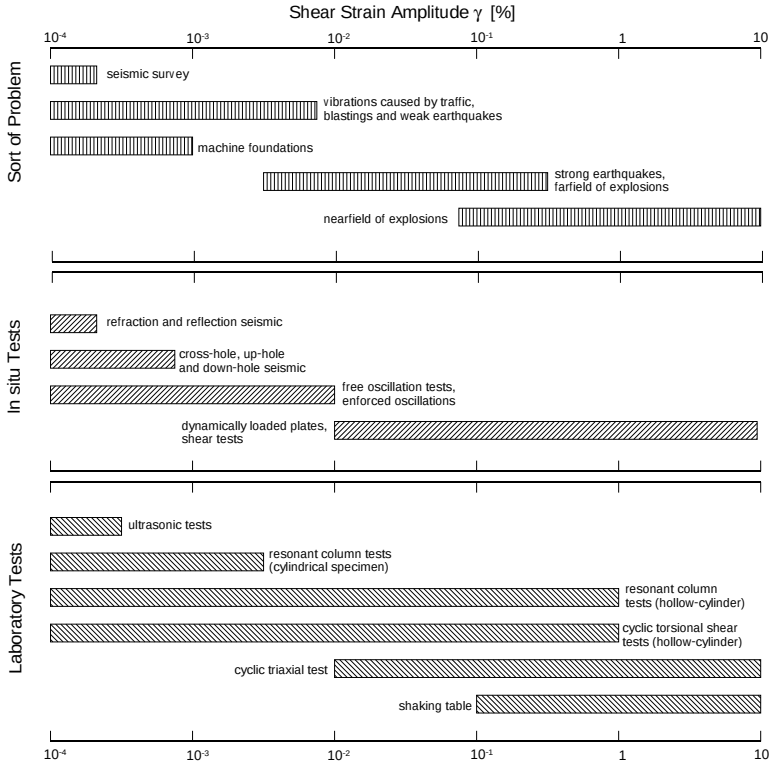

Figure 2.3: Shear strain amplitudes for various testing methods and SSI applications according to Studer & Koller [95].

2.1.1. LABORATORY TESTS

In the subcategory of small-strain lab tests, a wide choice of testing setups is available. Among them are the dynamic tests (i.e., very small strain, harmonic, not cyclic), of which the Resonant Column and Bender Element Tests are well established. The more often applied cyclic triaxial test or cyclic simple shear tests involve larger strains, and are used to study cyclic degradation of stiffness or pore water pressure accumulation. Fig. 2.4 shows the schematics of the Bender Element and Resonant Column Test setups. The goal of the Bender element test is similar to the in-situ seismic tests (as will be discussed in the next section): determining the shear-wave (or pressure-wave) velocity based on the measured arrival time and known distance between a source and receiver. The source and receiver are called Bender Elements; piezoelectric elements that change dimensions when applying an electric pulse (source), or inversely, that generate an electric pulse when they are deformed (receiver). Depending on the orientation of the source, either shear or pressure waves can be generated. In the Resonant Column Test, the soil sample is excited by a harmonic torsional load, of which the frequency is increased until the first resonance is observed. That frequency is referred to as the fundamental frequency of the sample, and a standard relation is used that relates this frequency to the characteristics of the apparatus, sample geometry, and the shear-wave velocity of the soil.

Lab tests are often a preferred choice of geotechnical engineers, as the controlled environment can ensure a high accuracy and repeatability of the results. Nevertheless, a large drawback of these tests is that the samples need to be retrieved from boreholes, always involving deformations (disturbances). Much effort is put in re-establishing the in-situ conditions (for instance consolidation and stress levels). However, it is never certain if the original, undisturbed circumstances have been reached. It can be understood that this disturbance is especially an issue when the small-strain soil characteristics are to be obtained. Therefore, often a lower stiffness is identified using lab tests than when measuring in-situ [96]. Besides the sample disturbance, the limited size of a sample holds the dual disadvantage that (a) it is a local representation of the in-situ soil, and (b) in dynamic testing, the response of the sample is prone to boundary disturbances as the propagating waves can - depending on their wave length - 'feel' the boundaries of the sample. The first point (a) relates to the discussion whether to focus on obtaining a high level of detail of local properties or rather acquiring a proper global representation of the soil stratum. This choice depends on the envisioned structure, but, as discussed in Section 1.2.1, it is believed that large-sized, rigidly behaving structures like OWT monopiles, interact with the soil in a global way. Furthermore, in testing and extracting dynamic soil properties, it should be attempted to simulate the relevant frequencies and wavelengths induced by the foreseen structure.

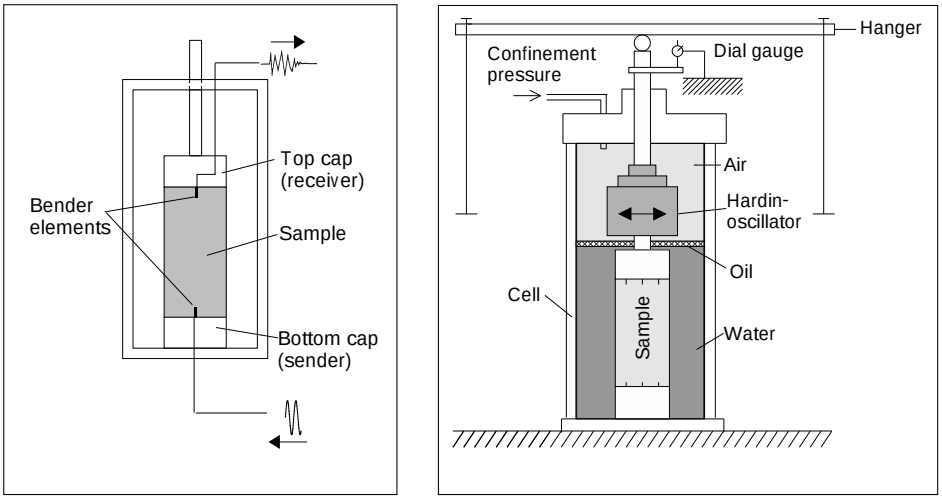

Figure 2.4: The Bender Element (left panel) and Resonant Column (right panel) Test setups [90].

2.1.2. IN-SITU TESTS

In-situ tests have the great benefit that the soil stratum can be characterised under the conditions as will be experienced by the envisioned structure. For the small-strain applications, various seismic testing methods are available, as can be seen in the overview given in Fig. 2.5.

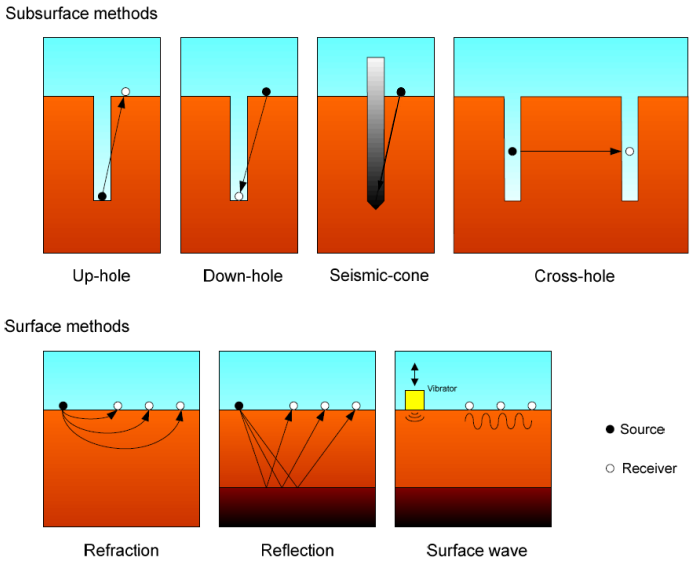

Figure 2.5: Overview of the main in-situ seismic testing methods [94]. The SCPT (discussed in Section 2.2) is indicated by *Seismic-cone*, and the MASW (discussed in Section 2.3) belongs to the *Surface wave* category.

To aid the following description of seismic testing, it is useful to shortly define a few of the main wave types that develop after disturbing (in both time and space) a continuum. Two types of *body* waves will travel in the unbounded domain; these are the previously defined shear wave (or secondary, S-wave) and the pressure, or primary, P-wave. The particle motion in shear waves is polarized perpendicular to the direction of propagation, whereas the particle motion and propagation direction for the pressure (or longitudinal) wave are aligned, resulting in higher propagation velocities than those of the shear waves. The S-wave can be distinguished further in waves having a vertically polarized particle motion (the SV wave) and horizontally polarized particle motion: the SH waves. At the boundary of the soil domain, the P- and S-wave will interact to form *surface waves*. In this case a boundary, or rather interface, can be any (sharp) transition of medium properties; this can be the interface between soil layers, but the sharpest and most accessible (measurable) interface in our offshore-soil application is the mudline. The particle motion induced by surface waves exhibits an elliptical pattern, and as their energy only spreads over a surface (plane) the associated geometric damping (spatial spreading of wave energy) is much lower than that for body waves which spread spherically over space. Perpendicular to the direction of propagation of surface waves, the particle motion amplitude decreases exponentially to zero within a distance of a few wavelengths into the continuum. Depending on the contrast in the properties of the neighbouring domains, different types of surface waves exist; for the offshore case, *Scholte* waves will develop at the interface between soil and water, as a result of the interaction of SV-waves and P-waves (in both water and soil). For onshore soil applications, at the interface of soil and air (vacuum, striktly speaking), the *Rayleigh* wave develops, and can be employed for sub-soil characterisation. If the seismic source also generates SH waves in the layered soil, *Love* waves, having elliptical motion in the horizontal plane, can develop at the surface. An analytical expression similar to the one in Eqs. 2.1 or 2.2 does not always exist for the velocity of surface waves, but they are generally slower than the slowest body wave; often an indicative 90% of the S-wave velocity is used as a rule of thumb, however, a model (and/or measurement) is needed to determine the surface-wave velocity more accurately.

As can be seen in Fig. 2.5, the seismic testing methods can be categorized in *invasive* (or as in the overview *subsurface*) and *non-invasive* (*surface*) methods. In using the invasive methods, the body-wave velocity is determined with the measured arrival time of the wave and the known distance between source and receiver. Although these tests will still disturb the soil by embedding the source and/or the receiver, the ray path of the wave, mostly lies in undisturbed soil. The SCPT is the most cost-effective setup of the invasive tests shown in Fig. 2.5, as the up-, down- and cross-hole test all involve the excavation of a borehole, and the installation of a borehole casing. The SCPT has the added benefit that the used cone, besides holding the geophones, also contains the usual CPT sensors, measuring sleave friction, cone-tip resistance and pore water pressure.

As shown in the overview of Fig. 2.5, non-invasive tests include refraction, reflection and surface-wave methods. These testing setups, in which the source and receivers

are placed at the top interface (on mudline), are the only methods that do not disturb the soil in its bulk. Without going into much detail, the physical basis for the reflection and refraction methods is the phenomenon that when a wave travels away from the source in a first soil layer and encounters an interface with a layer that has different properties, part of the wave energy is reflected, and a part is refracted (transmitted) into the encountered soil layer. The angle of refraction can be calculated using Snell's law, as will be shown in Section 2.2.2. By distinguishing the arrival of the direct waves and the reflected waves, one can determine the layer thickness and the body wave velocities of the different layers [89, 90].

As discussed, apart from the body waves (being the focus of reflection and refraction testing), a source on the mudline also excites surface waves. In the surface-wave techniques, the *geometric dispersion* characteristic of these waves is used to back-trace the stiffness of the soil stratum. A surface-wave field consists of a group of waves with different frequencies and wave lengths. The propagation of a particular surface wave traveling along a surface is influenced by the properties of the adjacent media close to the interface. As discussed, the length of this influence zone extends to a few wavelength depth, beyond which the particle motions become negligible. For soil testing this implies that long waves traveling along the surface are affected by the properties of the soil over a large depth, and short waves only 'feel' the shallow layer(s). Fig. 2.6 aids in visually explaining this concept.

These non-invasive methods often involve solving an inverse problem that has no unique solution. The resulting outcome is an optimum solution, including a certain range of likelihood. This disadvantage is however compensated by the fact that it seems - as will be discussed later - that from the surface wave measurements, also soil damping properties can be extracted. Furthermore, placement of a horizontal receiver array is generally a more cost-effective and flexible solution than the vertical penetration involved in the invasive techniques. In Section 2.3 we will discuss the Multichannel Analysis of Surface Waves (MASW) in more detail.

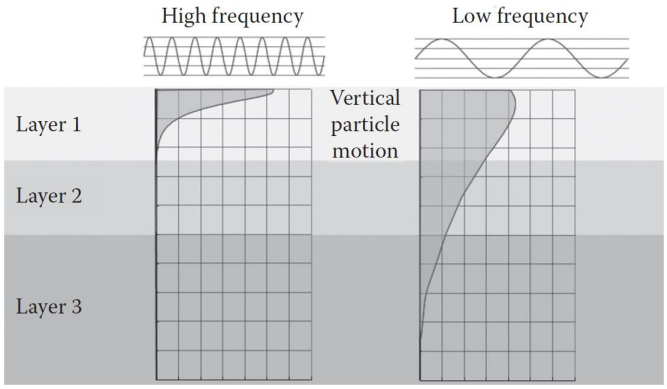

Figure 2.6: Geometric dispersion of surface waves [97]; short-wavelength, high-frequency waves are effected by the properties of only the shallow soil layers, whereas the longer wavelengths (with generally lower frequency content) 'feel' the properties of also the deeper layers.

2.2. STIFFNESS IDENTIFICATION: THE SCPT

This section describes how measured SCPT data can be interpreted to derive the linear elastic input parameters that are needed for 3D SSI modelling[1]. SCPTs were performed by the author in the summer of 2012 as part of the soil measurement campaign carried out by Fugro GeoServices B.V. for the Westermeerwind near-shore wind farm. In the following soil characterisation, we assume that small vibrations of the soil can be described by the classical elastic continuum with frequency-independent parameters.

Seismic data of 2 positions were analyzed: 'SCPT20' and 'SCPT45'. As will be discussed in Chapter 5, a full-scale validation campaign was performed in the summer of 2015, in which the MP of turbine W27 was excited with a hydraulic shaker. SCPT45 was performed at the position of turbine W27, therefore slightly more focus is laid upon deriving a 'best estimate' stiffness profile for this location. SCPT20 will be used for extracting sensitivities of (modelled) pile displacement to choices made in the soil characterisation. For easier reading, we will in this thesis indicate the piles at the 2 discussed locations according to their SCPT number; MP45 for position (SCPT profile) SCPT45, and similar for MP/SCPT20.

In the conducted SCPTs, a hydraulic shear-wave hammer placed on the seabed was used as excitation device, and shear waves were recorded at 1 meter depth intervals with a dual-phone cone, having a 0.5 m interval distance between the geophones. Stacking responses over multiple hits for each depth rendered clear shear-wave patterns. The seismograms of the recorded responses at positions 20 and 45 are shown in Fig. 2.7. The maximum depth that was reached with the SCPTs was limited by a threshold maximum cone pressure to avoid damaging the cone. Reaching such a maximum pressure usually indicates the presence of a stiff soil layer. As can be seen in the seismograms,

[1] Parts of this section have been published in Engineering Structures **124**, 221-236 (2016) [78].

for SCPT20 the maximum depth was 25 m (position of the lowest geophone) and for SCPT45 a depth of 30 m was reached.

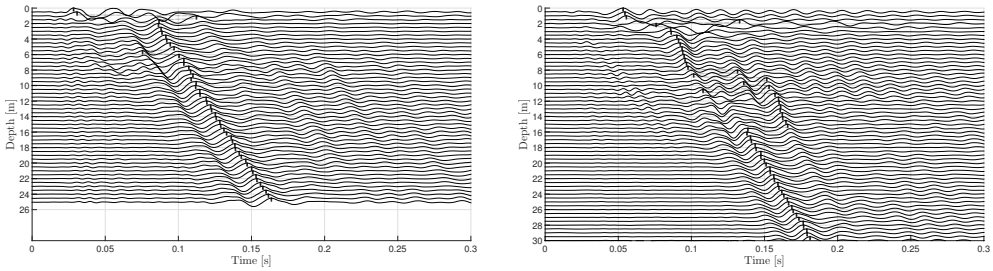

Figure 2.7: Seismograms showing the response traces of the particle velocities in horizontal direction (in-line with the shear-wave hammer) measured at each geophone, for SCPT20 (left panel) and SCPT45 (right panel). When defining the arrival time of the shear-wavefront as the moment of maximum particle velocity, the arrival times can be automatically picked. These auto-picked arrival times are indicated by the black dots. As can be seen and will be discussed, this can lead to erroneous results in case the waveform changes from one depth to another.

We will first discuss how the arrival and interval times of the measured waves are defined (Section 2.2.1), as this choice influences the magnitude of the shear-wave velocity that will subsequently be determined. In Section 2.2.2, a simple model is used to invert the seismic data for the shear-wave velocities based on the previously identified interval times. In Section 2.2.3 all other parameters that are needed to describe the soil continuum are quantified. These parameters are input for Chapter 3, where the 3D SSI model will be discussed. To obtain the sensitivity of the response of the pile to some of the choices made in the soil interpretation, 3 different stiffness profiles based on SCPT20 are defined in Section 2.2.4. Finally, Section 2.2.5 compares the determined shear-modulus profile with an often used empirical relation for calculating the shear modulus based on conventional CPT output.

2.2.1. WAVE ARRIVAL TIMING

To determine the shear-wave velocity, we need to know the length of the path traversed by the wave, and define its arrival time at the measuring sensor, the geophone. The difference in arrival time between two adjacent receivers - the interval time - can then be obtained by subtracting the arrival time of the upper geophone from that of the lower geophone. Taking advantage of the fact that for a dual-phone SCPT, the recordings of two consecutive depths belong to the same measurement setup (the cone has not moved), it is this interval time and distance between the geophones that we use for the shear-wave velocity determination. Different definitions of this 'arrival time' exist. Here we define the moment of appearance of the maximum particle velocity of the soil as the arrival time of the wavefront, as this allows for automated picking. The picked arrival times are indicated with black dots in the seismograms of Fig. 2.7. Nevertheless, these 'picks' have to be visually checked, as the waveform needs to be consistent between the different observations for the picks to be reliable. Especially in the first few meters, the waveform tends to change significantly due to near-field (near to source) effects.

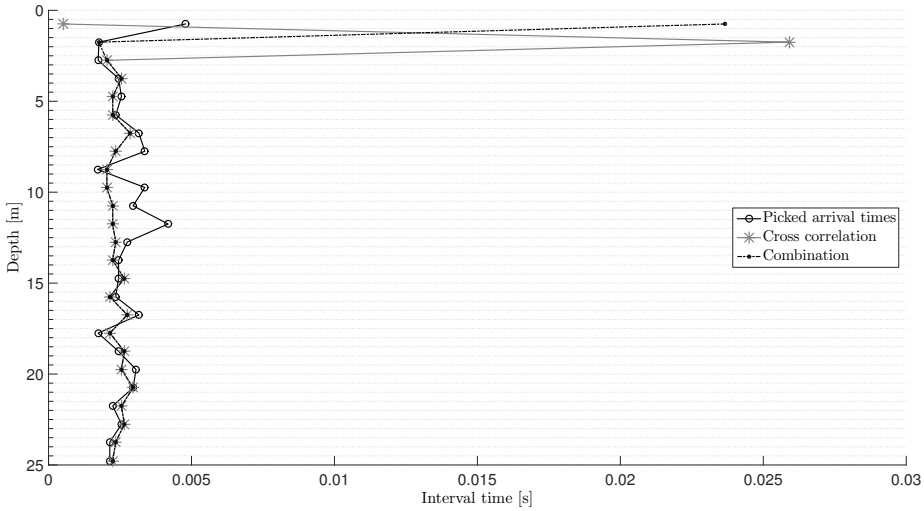

Figure 2.8: Interval times between adjacent geophones of SCPT20. The interval times can be defined as the difference in picked arrival times (black "∘"), or determined with cross correlation (grey "∗"). A combination can also be chosen (black "•"); cross correlation was used for all interval times except for the first layer, where the S-transform technique was used, and the second layer, which was manually picked.

The waveform also changes when the structure of the soil (the soil type) alters; for instance, in SCPT45 (right panel) this seems to occur at around 10 m and 15 m depth. Furthermore, as will be confirmed by the CPT output of this SCPT and laboratory classification given in Section 2.2.3, a soft soil layer around 2-3 m depth causes distortion of the wave pattern. Hence, to derive consistent interval times (positive valued and within a certain expected range), the peaks of the deviating waveforms are to be picked manually.

The interval time between the geophones can also be obtained by cross correlation, which is a more objective technique. The interval times found by both picking (including a few manually picked values) and cross correlation for SCPT20 are displayed in Fig. 2.8. We observe that cross correlation gives more smooth results, especially for depths between 7 to 13 m. The near-field effects within the first 2 m made the use of cross correlation and also the use of manual picking less reliable. A time-frequency analysis proved useful to pick the arrival of the maximum energy peak, as shown in Fig. 2.9. The time-frequency analysis was done using the S-transform [98]. The S-transform also showed that the region of maximum energy in the spectrum of the recording at 2 m depth was shifted in frequency content with regards to those at 0.5 m, 1 m and 1.5 m depth. Altogether, the wave arrival for the first 2 meters remains uncertain, but more consistent results are found for larger depths. A smoother profile is expected to be more realistic, as we expect the soil to be smoothly inhomogeneous. As will be shown in Section 2.2.4, the variability in the interval times for the shallow layers do have a

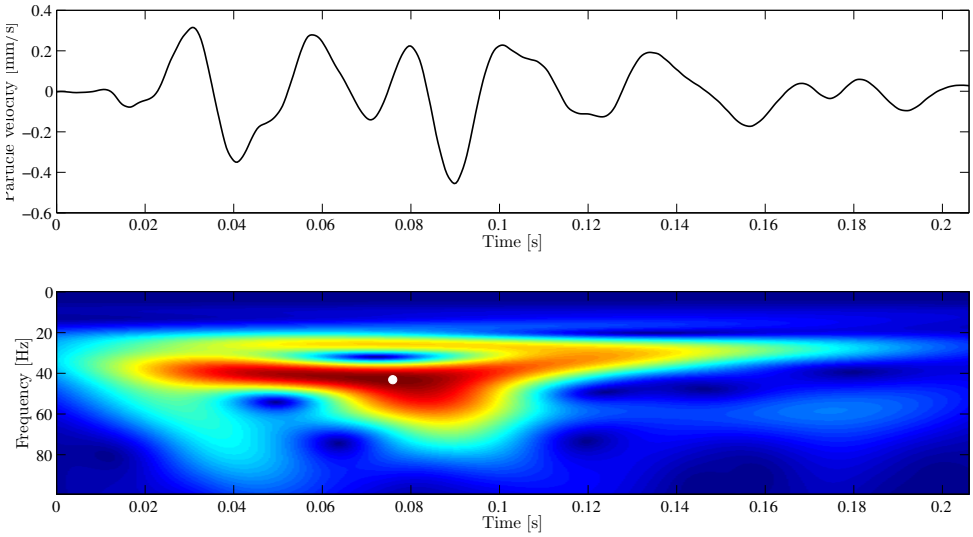

Figure 2.9: Time response of the geophone placed at 1 m depth (upper panel), and the corresponding time-frequency diagram (lower panel). The maximum energy is indicated with a white dot.

significant effect on the stiffness estimation of the upper half of the stratum.

As SCPT45 was conducted at the location where the in-situ pile validation measurements took place (discussed in Chapter 5), we will focus a bit more on this profile, describing another technique to further enhance the reliability of the wave-arrival estimation. This concerns the issue of misalignment between the direction of wave propagation (controlled by the orientation of the shear-wave hammer) and the orientation of the receivers, the geophones in the cone. Each geophone has a sensor recording in x- and another sensor recording in the y-direction. During lowering of the SCPT cone, care is taken to align the x-direction of the geophones with the direction of excitation of the shear-wave hammer. However, during further penetration of the soil, the cone is prone to rotation about its vertical axis. This rotation angle Φ, the angle between the x-directed sensor of the geophone towards the true (resultant) direction of wave propagation R, was estimated by considering the magnitudes of the x- and y-recordings v_x and v_y respectively, for each response trace, see Fig. 2.12. The alignment can be estimated by displaying both recordings, as can be seen in the left panels of Fig. 2.12, in which examples are shown for two shot records at depths of 13 and 21.5 m. The angle Φ was estimated by fitting a linear function through these time samples, and considering the angle of this line with the x-direction. Fig. 2.11 shows the angles Φ determined for each depth (geophone position). The outliers are not considered to be physically realistic; they could be related to the distorted wave patterns occurring at these depths (as previously discussed regarding the seismogram of Fig. 2.7). When interpreting these angles in line with what can be expected regarding the rotation of the cone, it seems that the cone was inserted into the soil at an angle $\Phi = 62°$ and started a rotation of more than 90° around its vertical axis over the depth interval between 9 and 18 m, towards $\Phi = -32°$.

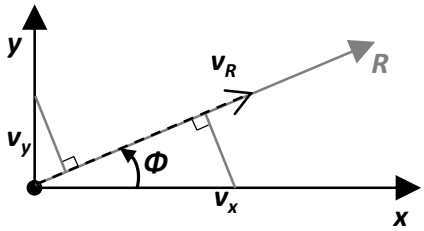

Figure 2.10: The resultant direction of wave propagation v_R in relation to the x- and y-directed response traces v_x and v_y.

Using this 'interpreted' angle Φ, the resultant signal v_R was calculated by considering the axes rotation shown in Fig. 2.10:

$$v_R = v_x \cos(\Phi) + v_y \sin(\Phi). \tag{2.3}$$

Fig. 2.12 shows examples of the estimated angle Φ (left panels), the related v_x and v_y time signals and the calculated v_R signal using the interpreted Φ (right panels). Fig. 2.13 shows the interval times that are retrieved by cross correlating the corrected, v_R signals. For comparison, the figure also shows the interval times that are obtained by directly cross correlating the v_x and v_y signals. It can be seen that using the corrected signals yields a more smooth interval time profile as opposed to directly using the x- and y-directed signals. Still, the third interval time of this profile was based on manual picking, as the deviating waveforms of the shallow weaker soil layer would result in a too high interval time when using cross correlation.

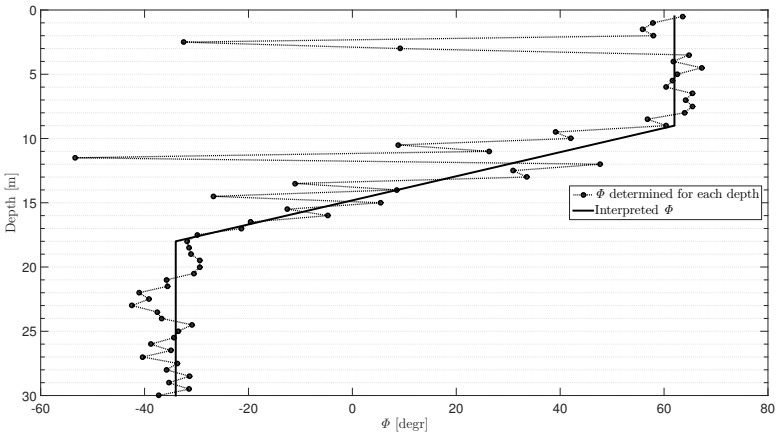

Figure 2.11: The angles of cone rotation Φ around its vertical axis (dotted line), determined for each depth (geophone position). The angle Φ is defined as the angle between the x-directed sensor of the geophone and the true (resultant) direction of wave propagation R, see Fig. 2.10. The 'interpreted' value for Φ, which ignores the outliers, is used for calculating the resultant v_R signals (solid black line).

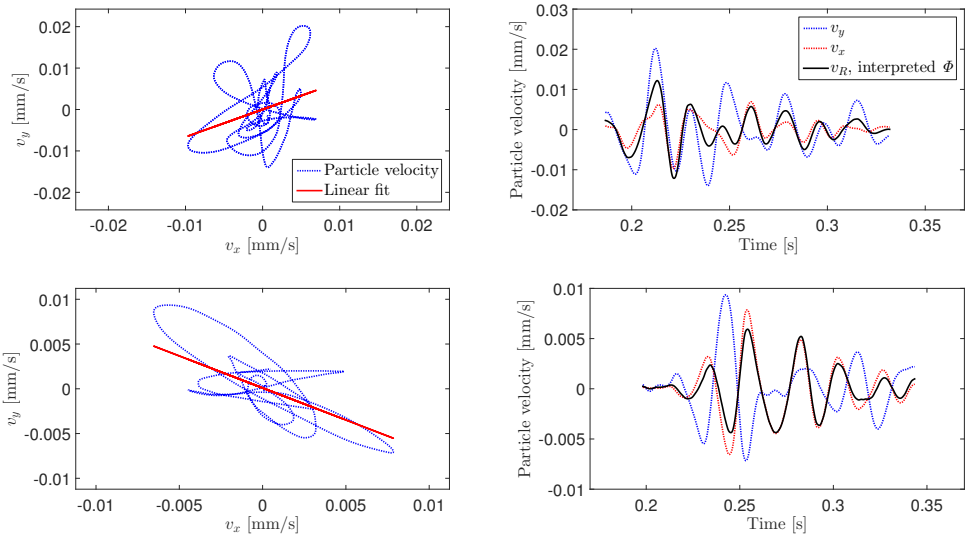

Figure 2.12: Examples of the polarisation of particle velocity in the horizontal plane for SCPT45 and the associated linear fits (left panels), for geophone recording at 13 (upper panels) and 21.5 m depth (lower panels). The right panels show the related time signals of v_x and v_y and the calculated resultant v_R (R-direction) signal using the interpreted Φ (Fig. 2.11).

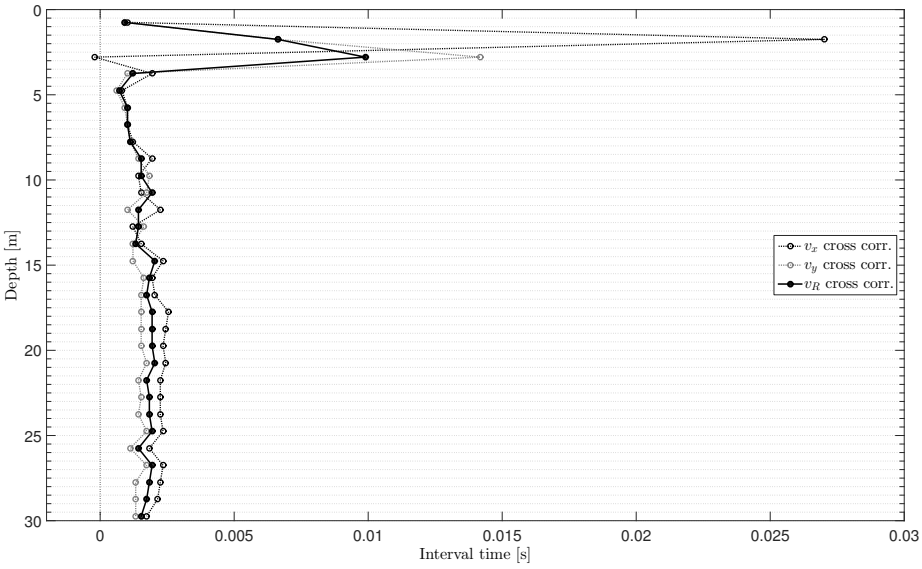

Figure 2.13: Interval times for SCPT45, calculated by cross correlating the seismic response traces of a geophone pair. Three signals are shown: cross correlation of the x-directed v_x signal (black dotted line), the v_y signal (grey dotted line) and the calculated resultant v_R signal using the interpreted angle Φ (see Figs. 2.10, 2.11 and 2.12) is indicated by the black solid line. The third interval time of the latter profile was adjusted, based on manual picking.

2.2.2. SHEAR-WAVE VELOCITY INVERSION

To find the shear-wave velocities, a minimisation problem was formulated. Assuming the soil to be horizontally stratified with homogeneous soil layers of 1 m thickness of which the centre points corresponds to the middle points of the placed geophone pairs, the successive layer shear-wave velocities can be computed by minimising an objective function for the observed arrival times. The method incorporates the effect of wave refraction through Snell's law, which has to be taken into account because of the horizontal offset between the source and the receivers. Especially for shallower layers, this effect cannot be ignored.

The geometry of the minimisation problem is shown in Fig. 2.14, in which an example is given for layer number $n = 3$. The equations of the optimisation problem (for the general case, layer n) are given by

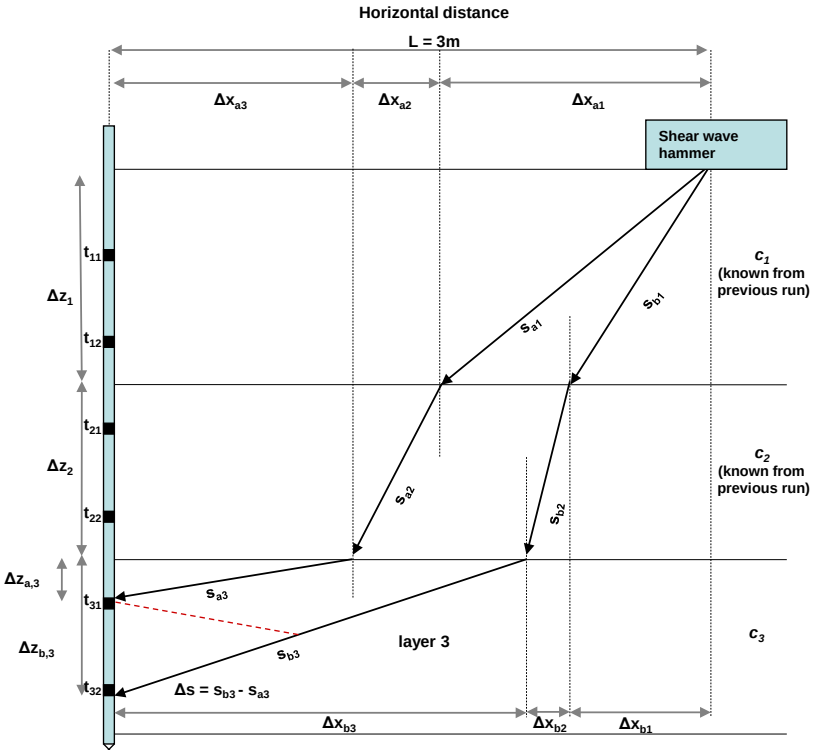

Figure 2.14: Schematic view of the minimisation problem that was used to find the shear-wave velocity, c_n. An example is given for layer number $n = 3$. Through Snell's law, $4n+1$ geometric relations can be formulated to find an optimized solution for the $4n+1$ variables. The variables are explained in the text.

$$\begin{aligned}
\frac{\Delta x_{ai}}{s_{ai}\ c_i} &= \frac{\Delta x_{a(i+1)}}{s_{a(i+1)}\ c_{i+1}},\\
\frac{\Delta x_{bi}}{s_{bi}\ c_i} &= \frac{\Delta x_{b(i+1)}}{s_{b(i+1)}\ c_{i+1}},
\end{aligned} \tag{2.4}$$

$$\begin{aligned}
s_{ai} &= \sqrt{(\Delta x_{ai})^2 + (\Delta z_i)^2},\\
s_{bi} &= \sqrt{(\Delta x_{bi})^2 + (\Delta z_i)^2},\ \ i = 1,..,n-1,\\
s_{an} &= \sqrt{(\Delta x_{an})^2 + (\Delta z_{an})^2},\\
s_{bn} &= \sqrt{(\Delta x_{bn})^2 + (\Delta z_{bn})^2},
\end{aligned} \tag{2.5}$$

$$\begin{aligned}
&\sum_{j=1}^{n} \Delta x_{aj} = L,\\
&\sum_{j=1}^{n} \Delta x_{bj} = L,\\
&c_n = \frac{s_{bn} - s_{an}}{t_{n2} - t_{n1} - \sum_{i=1}^{n-1} \frac{s_{bi} - s_{ai}}{c_i}}.
\end{aligned} \tag{2.6}$$

Here s_{an} is the length of the wave path belonging to the upper ray, and s_{bn} to the lower ray in target layer n. $\Delta x_{an,bn}$ are the horizontal components of the wave path, and Δz_n the vertical component. t_{n1} and t_{n2} are the arrival times at respectively the upper and lower geophone in the last (target) layer n. In the equations, i is the index for the layers above the target layer n. The amount of variables and equations to be solved equals $4n+1$: s_{an}, s_{bn}, Δx_{an}, Δx_{bn} $(4n)$ and c_n (1). As the shear-wave velocities in the layers are sequentially solved, c_1 and c_2 are assumed known in the example of Fig. 2.14.

Matlab's gradient-based 'fmincon' function was used for setting up a nonlinear optimisation, and within this function, the 'Sequantial Quadratic Programming' algorithm appeared most appropriate for our problem. Being a medium-scale algorithm, it stores full (dense) matrices, remaining stable for deeper layers. The amount of equations and variables in this problem is small enough for acceptable computational speed. Furthermore, the algorithm was found to be insensitive of the initial guess. The shear-wave velocity was constraint in between 1 and 1000 m/s. Confidence in finding the global minimum can be reached by visual inspection of the objective function for the first layers. The ray paths of the optimized solution for SCPT45 are given in Fig. 2.15. Here we can clearly see that, due to Fermat's principle of least time, a minimum of ray path length is assigned to the previously discussed shallow soft layer. The found shear-wave velocities for SCPT20 are depicted in Fig. 2.16. As discussed in Section 2.2.1, different choices can be made in defining the interval times, and these choices influence the computed shear-wave velocity profile. Computing the profile using cross correlation only (employing the interval times shown in Fig. 2.8), renders the solid grey profile with "+" markers. This profile is included to assess the effect of neglecting any near-field

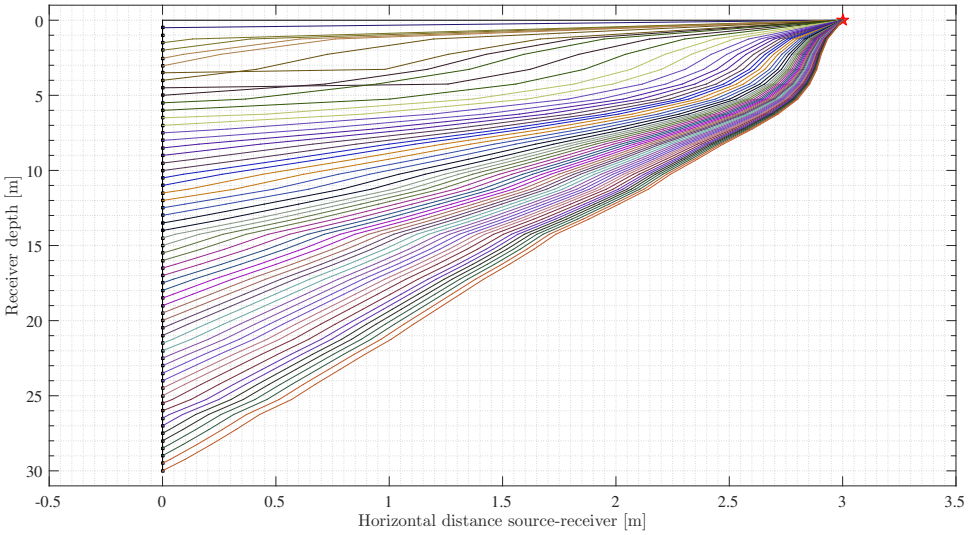

Figure 2.15: The ray paths that belong to the sesimic response traces of SCPT45, according to the optimized solution (corresponding to the shear-wave velocities given in Fig. 2.18).

effects and relying on 'automated' processing. The solid black line with "∘" markers named "Combination" in Fig. 2.16 is the profile linked to the Combination interval time profile in Fig. 2.8; choosing a combination of using the S-transform for the first layer, peak picking for the second layer and cross correlation for the rest of the layers. The only difference between the black and grey profiles is thus the adopted interval time for the first 2 meters. We can see that this difference has a relatively large influence on the first 15 m of the profile. As discussed, the magnitude of the interval time can be uncertain. The black profile (Combination) seems most realistic, but the true profile might lie somewhere in between the black and grey profiles. To determine the effect of these choices on the pile response (which will be calculated in Chapter 3), these 'black' and 'grey' profiles will be used for defining different stiffness cases in Section 2.2.4. As a reference, the profile determined by Fugro is given by the grey dotted "•" line. This profile was computed assuming straight rays from source to geophone (so ignoring the wave refraction), and without taking the wave velocities of previously calculated shallower layers into account.

Fig. 2.17 shows the Combination profile of Fig. 2.16 (which is is deemed most realistic) in combination with the CPT output of the same SCPT cone: the cone-tip resistance q_c and sleeve friction f_s. Additionally, on the right side of the figure, the laboratory soil classification profile is shown which was obtained using borehole samples retrieved at the same location of SCPT20. Differences in the profiles retrieved from these measurement methods are to be expected, as these measurement methods are fundamentally different: the local and static CPT versus the more global, averaged and dynamic SCPT. Nevertheless, it can be seen that in general the agreement in stiffness/strength indications of the methods is quite reasonable; the weaker soil layers

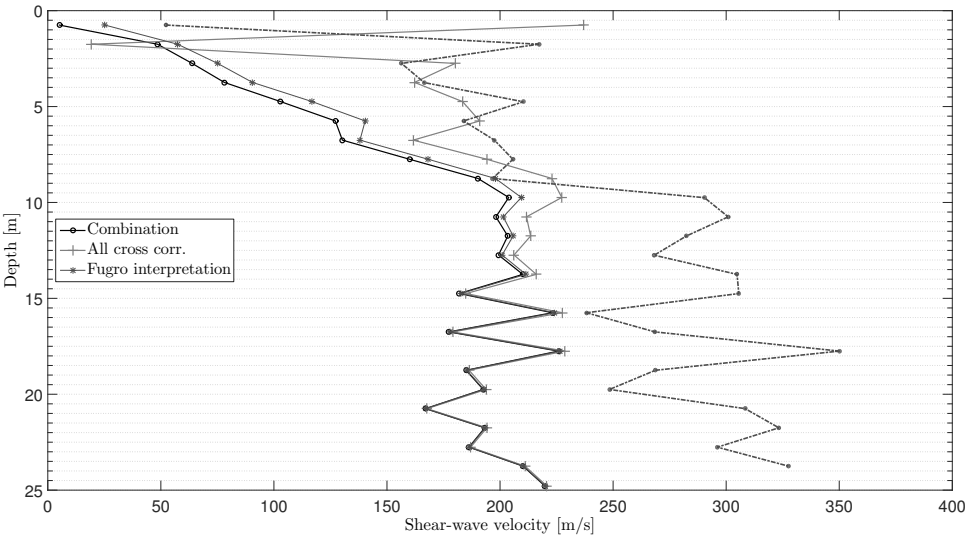

Figure 2.16: Derived shear-wave velocity profiles for SCPT20. The solid black "∘" profile (Combination) is deemed most realistic; it is based on a combination of techniques to compute the interval time (see Fig. 2.8), using cross-correlation, the S-transform and peak-picking. The solid grey "+" profile is based on using cross-correlation only. The dotted grey "•" profile was obtained by Fugro, using the 'straight-ray assumption.

between approximately 15 m and 23 m depth, which are clearly indicated by the CPT output and lab classification, are quite well reflected in the estimated velocities. The velocity jumps in this region can be caused by the thin stiffer layers embedded in the softer layers (as depicted in the laboratory classification). Within this region, a thin stiffer layer is present (at around 18 m depth), which is reflected in both CPT output and the shear-wave velocity profile. Finally, a stiffer sand layer is present beyond 23 m, at which depth the shear-wave velocity also increases. Fig. 2.18 shows the same information for SCPT45 (for which a single 'best-estimate' shear-wave velocity profile is determined, based on the v_R cross correlated interval times shown in Fig. 2.13). Again, the C_s and q_c & f_s profiles seem to correspond quite well in their trend, but there are also some differences. The presence of the soft layer at about 20 m depth, which is visible in the geotechnical output (q_c & f_s and borehole classification), is less pronounced in the geophysical output (C_s). The clay layer is probably thin, stiff and confined enough to not cause any significant decrease of C_s at this depth.

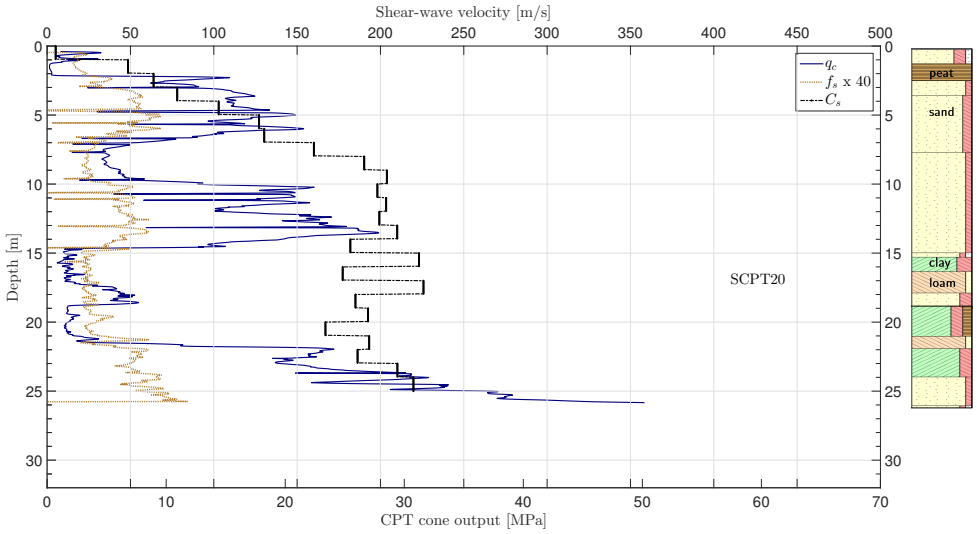

Figure 2.17: The derived shear-wave velocity profile for SCPT20 (Combination profile of Fig. 2.16), in comparison to the CPT output measured by the same SCPT cone. Note that the sleeve friction pressure f_s has been multiplied by 40 in order to share the same value along the horizontal axis as the cone-tip resistance q_c. On the right side, the laboratory soil classification profile is shown.

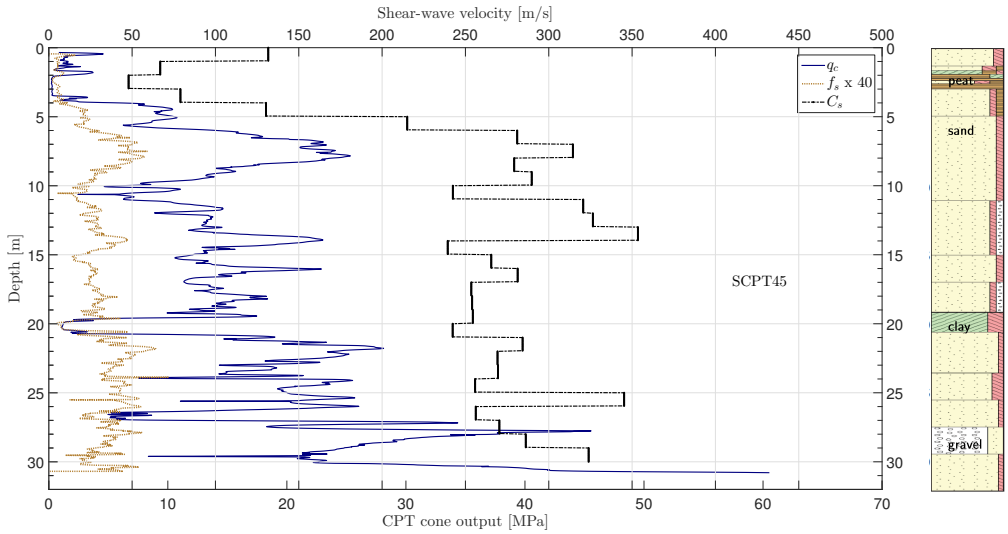

Figure 2.18: The derived shear-wave velocity profile for SCPT45, in comparison to the CPT output profiles measured at the same location. Note that the sleeve friction pressure f_s has been multiplied by 40 in order to share the same value along the horizontal axis as the cone-tip resistance q_c. On the right side, the laboratory soil classification profile is shown.

2.2.3. SOIL DENSITY & POISSON'S RATIO

Having identified the shear-wave velocities, we still need to acquire the in-situ density ρ and Poisson's ratio ν to determine the shear and Young's modulus of the continuum, see Eq. 2.1. This set of input parameters will be employed to characterize the 3D linear elastic continuum in the models discussed in the next chapter.

The in-situ saturated soil densities ρ used and presented in this thesis, were determined by Fugro. For the in-situ density of SCPT20 the relation of Robertson [99] was used. This relation is based on the cone tip and frictional resistance measured by the SCPT:

$$\rho/\rho_w = 0.27\log(R_f) + 0.36\log(q_t/p_a) + 1.236. \tag{2.7}$$

In this equation, q_t is the corrected cone resistance, R_f is the friction ratio (sleeve friction over the corrected cone resistance), ρ_w is the mass density of water and p_a is the atmospheric pressure. For the SCPT45 profile (the position where pile-response validation measurements were performed, Chapter 5), the employed in-situ densities are based on the soil type; the typical in-situ density of the layers encountered across the wind farm were determined with lab tests like unit weight, water content, oedometer and triaxial tests. These densities based on lab tests were verified to be very similar to those determined using Robertson's relation (as described above for SCPT20). Only for the first 2 m, lab tests indicate a density of 1900 kg/m^3, whereas a density of 1600 kg/m^3 is obtained using the Robertson relation. The employed in-situ densities for both positions are shown in the left panel of Fig. 2.19.

The estimation of the effective Poisson's ratio ν is a challenging task, as it is dependent on the type of soil, but for instance also on the occurring strain [100], the degree of water saturation and the loading frequency. In civil engineering practice, the Poisson's ratio is often taken as 0.3 for sand and 0.45 for cohesive material [101]. The small-strain Poisson's ratio can also be estimated from identified pressure-wave and shear-wave velocities. Measurement data acquired with a different cone (the 'LFCPT', discussed in Section 2.3.1) indicated much higher Poisson's ratios for the (saturated) sand at location SCPT20 [81]. In this LFCPT data, we could extract both the pressure and the shear-wave velocities. With the ratio of these velocities and the in-situ porosity estimated from lab tests, the Poisson's ratio can be approximated using an effective two-phase model for wave propagation in a three-phase medium where the pore fluid contains minor gas bubbles (low-frequency limit [102], [103]). In this theory, the Poisson's ratio is calculated by

$$\nu = \frac{3K_b - 2G}{2(3K_b + G)}, \tag{2.8}$$

in which the bulk modulus of the solid frame (drained) K_b is calculated using an effective fluid bulk modulus $K_{f,eff}$ as

$$K_b = H_g - \frac{4}{3}G - \frac{K_{f,eff}}{\Phi_p}. \tag{2.9}$$

Here H_g is the so-called Gassmann modulus (undrained bulk modulus) as extracted from the pressure-wave velocity, and Φ_p is the porosity of the soil, in which the grains are

assumed to be incompressible [102]. The degree of water and gas saturation (s_f and s_g respectively) are incorporated in $K_{f,eff}$ as

$$\frac{1}{K_{f,eff}} = \frac{s_f}{K_f} + \frac{s_g}{K_g} \tag{2.10}$$

in which $s_f = 1 - s_g$.

High Poisson's ratios for marine sediments were also observed by Hamilton [104], [105]. The higher apparent Poisson's ratio is related to the drainage capacity of the sand. Reference [67] addresses the relation between the drainage capacity of the soil, the permeability of the soil and the frequency of oscillation of the structure. The question whether the soil behaves drained or undrained during the vibrations of the installed MP does not belong to the scope of this thesis; however, the higher Poisson's ratio will be considered for SSI stiffness calculations. To obtain the pile stiffness sensitivity to the Poisson's ratio profile, a variation of this parameter will be incorporated in defining different stiffness cases for SCPT20 in the next section. The best-estimate Poisson's ratio profiles for the two locations are given in the right panel of Fig. 2.19. For SCPT20, the best estimate profile is taken as the average of the 3 cases discussed in the next section. For SCPT45, slightly lower Poisson's ratios were assigned to the soil types, as additional measurements with a hydraulic profiling tool and slug testing indicated a high permeability of the sand (around 15 m/day) at this location. With the estimated densities and Poisson's ratios, the Young's modulus profiles were calculated; they are shown in the middle panel of the same figure. To serve as a reference for the soil stiff-

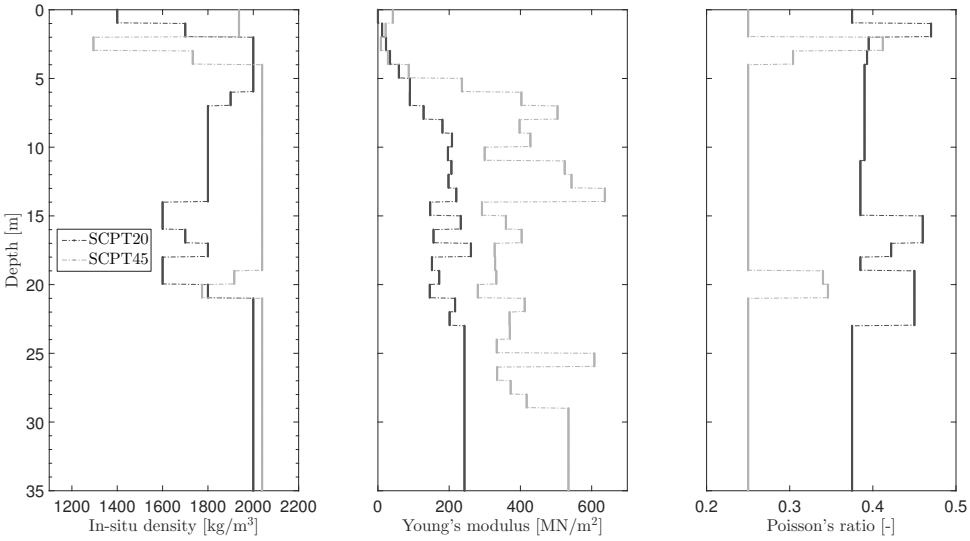

Figure 2.19: In-situ density ρ, Young's modulus E and estimated Poisson's ratio ν for SCPT20 and SCPT45.

ness, Fig. 2.20 shows the internal angle of friction ϕ, also determined by Fugro using

the relation between the initial modulus of subgrade reaction k, the relative density and internal angle of friction for different sand types, as specified in the standards [106]. The obtained values were verified with triaxial tests. It is interesting to note that, when comparing the Young's modulus profiles of Fig. 2.19 and the internal angles of friction ϕ of Fig. 2.20, the stiffness of SCPT45 is clearly higher than that of SCPT20 according to the geophysical results (Young's modulus based on shear-wave velocity), and this difference is hardly reflected by the geotechnical parameter ϕ. Possibly this reflects the fact that caution should be applied in using large-strain, *strength* parameters like the angle of internal friction ϕ for determining the *stiffness* of a profile. We will come back to this in Section 2.2.5.

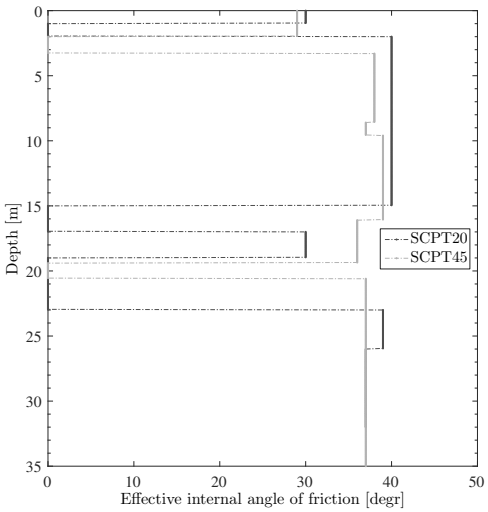

Figure 2.20: Angle of internal friction ϕ for SCPT20 and SCPT45. For peat and clay layers, ϕ is set to 0.

2.2.4. STIFFNESS CASES

To investigate the sensitivity of the pile displacements to the choices made in the soil characterisation, we here define 3 stiffness cases based on SCPT20, ranging from lower (case 1) to higher stiffness (case 3). The choices considered are the Poisson's ratio estimation (due to the related uncertainty discussed in the previous section), and the method used for defining the interval times (the effect of automated processing). An overview of the stiffness cases and the related choices are given in Table 2.1. For the

Table 2.1: Overview of the considered soil stiffness cases for SCPT20. The Poisson's ratio and Young's modulus profiles of the three cases are shown in Fig. 2.21.

	Case 1	**Case 2**	**Case 3**
dT method	Combination	Combination	Pure cross correlation
Poisson's ratio	Engineering practice	Average	Effective medium

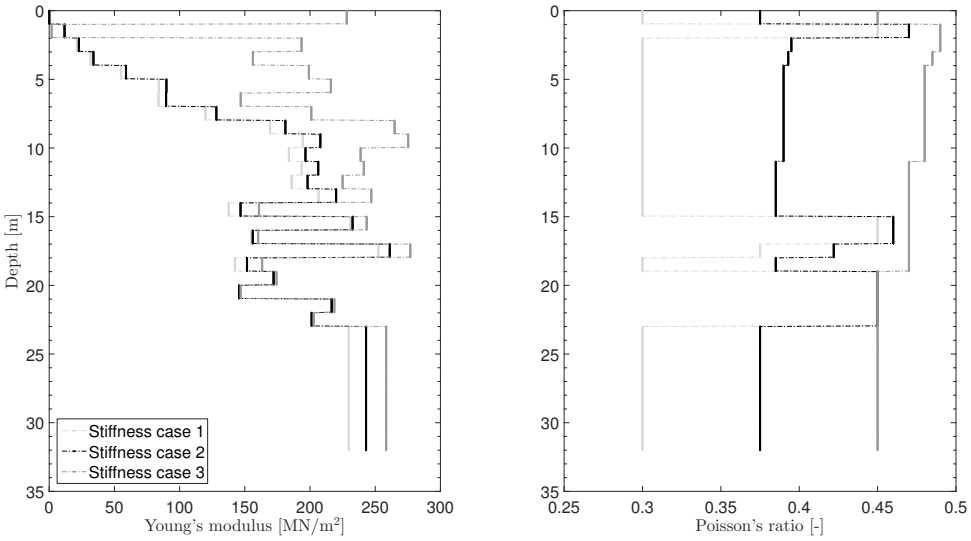

Figure 2.21: Profiles of the different Young's moduli (left panel) Poisson's ratios (right panel) for the 3 stiffness cases considered for SCPT20.

Poisson's ratio the lower bound engineering practice values are used for case 1, and the upper bound 'effective medium' values are adopted in case 3. An average of these two profiles is employed for case 2. The 3 Poisson's ratio profiles are shown in the right panel of Fig. 2.21. For the interval time (dT) methods, the Combination profile (Fig. 2.8) is assigned to cases 1 and 2; the Young's moduli for these cases will thus be calculated based on the Combination shear-wave velocity profile given in Fig. 2.16. This profile is thought to be most realistic; the interval time for the first layer was determined with the S-transform, the second by peak-picking, and the rest by cross correlation. Then, the Young's modulus of case 3 is calculated by combining the solid grey velocity profile in Fig. 2.16, which is based on the automated, cross-correlation-only interval time method (Fig. 2.8). The left panel of Fig. 2.21 shows the calculated Young's modulus profiles for the three cases. The same density profile was used for all cases (shown in the left panel of Fig. 2.19: SCPT20). We can see that the Young's modulus of case 1 is almost equal to that of case 2, as this difference is only caused by the different values of Poisson's ratio. In Chapter 3, we will consider the associated difference in terms of pile displacements.

2.2.5. COMPARISON TO EMPIRICAL G_0 RELATION

Empirical relations between the shear modulus and CPT-output parameters are widely available. The weakness in such relations is that they aim to link local large-strain output of a CPT-cone with the larger scale small-strain characteristics of the soil needed for our analyses. Perhaps for that reason, these relations are often concluded to be site-specific, and coefficients in the relations are then tuned to provide a good match. Nevertheless,

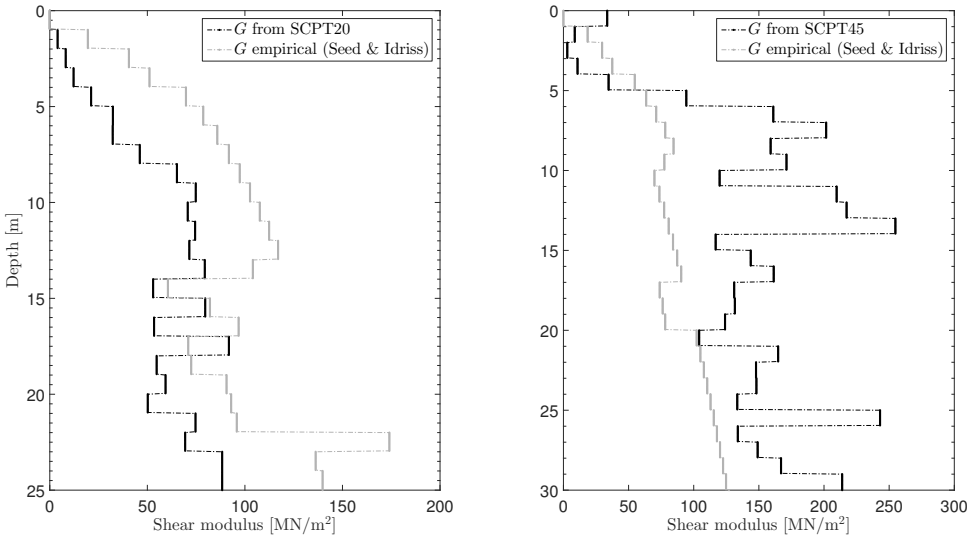

Figure 2.22: Comparison of identified shear modulus and reference empirical relation according to Eq. 2.11 [92], with $\alpha = 0.50$. Left panel: SCPT20 (case 2), right panel: SCPT45.

we check the applicability of such a relation for the data at hand. We compare the outcome with the shear modulus profile of SCPT45 and the best estimate, the case 2 profile, of SCPT20. An often used relation for sand developed by Seed and Idriss [92] is

$$G = 220 K_{2,max} (\sigma'_m)^{\alpha}. \tag{2.11}$$

In this equation, the coefficient $K_{2,max}$ is a function of the relative density D_r or void ratio e, α is a coefficient for the stress (depth) dependency of G and has a value of 0.5 according to the developers, and σ'_m is the mean effective confining pressure. This pressure is related to the vertical and horizontal effective stress by $\sigma'_m = (\sigma'_v + 2\sigma'_h)/3 = \sigma'_v(1 + 2K'_0)/3$. In this equation, K_0 is the coefficient of effective earth stress at rest: $K_0 \approx 1 - \sin(\phi)$, with ϕ the internal angle of friction. Paoletti et al. [107] emphasized the site-specific character of this relation of Seed and Idriss (Eq. 2.11), and found α to be equal to 0.63 for offshore sands in the Adriatic Sea. Fig. 2.22 compares the empirical relation (for α equal to 0.50) with the shear moduli identified using SCPT20 and SCPT45.

Similar relations as equation 2.11 are available specifically for clay; however, because of the limited presence of clay at this site, they have not been included in Fig. 2.22.

We observe that for SCPT20 (case 2), the empirical relation predicts a higher shear modulus for the first shallow layers than that determined with shear-wave measurements. This is most likely caused by the relatively high internal angle of friction of these layers, which pushes up the value of G in Eq. 2.11. The profile of case 2 is conservative in this respect, because a high stiffness in these shallow layers has a relatively large

influence on the pile response. For SCPT45, the difference is more apparent. This is related to the fact that the higher stiffness for this location, which is reflected by the shear-wave measurements, is not evident when considering the values for the internal angle of friction (a large-strain, strength parameter). Note furthermore that the empirical values are quite sensitive to the α parameter. Using an α equal to 0.63 as suggested by Paoletti et al. [107], would yield a factor 3 to 4 higher shear moduli for the deepest two-third part of the layers. This confirms that designers must be cautious when using empirical relations like in Eq. 2.11.

2.3. DAMPING IDENTIFICATION: THE MASW

This section is a summary of the MSc thesis works by de Winter [82], Bolderink [83] and Armstrong [84], all of whom the author co-supervised. These theses were aimed at identifying the dynamic soil properties based on surface wave measurements. The overall goal of these works was to identify the soil material damping, however, as we will see, a prerequisite for doing so is a proper estimation of the stiffness profile. Therefore, most of the performed work focuses on the identification of the stiffness profile based on the Multichannel Analyses of Surface Waves (MASW) setup. Only at the end of the subsequent studies has Armstrong been able to make an initial attempt to invert for the damping profile. The motivation for choosing the MASW setup was partly based on the work by de Groot [81], which is discussed in the next subsection.

2.3.1. FIRST ATTEMPT

An initial attempt to extract the soil material damping from a novel, in-situ seismic setup (the 'Low Frequency CPT', LFCPT) was made in the MSc thesis by de Groot [81]. The LFCPT, which we executed in the same soil measurement campaign on the IJsselmeer in 2012, is similar to the SCPT, but consisted of a second cone placed at a different position and a fixed depth to capture the soil attenuation. Furthermore, to mimic the foreseen SSI frequency and capture the relevant, possibly frequency-dependent, dynamic soil properties, cyclic excitation of the shear-wave hammer was applied at a frequency of 0.275 Hz. However, no low-frequency response was visible in the recorded data. Furthermore, using the Spectral Ratio Slope (SRS) technique to extract the damping from the acceleration spectra yielded unphysical results. Similar attempts reported by S.A. Badsar [108] and L. Karl [90] yielded comparable unsatisfactory results. In the SRS method it is assumed that the geometric damping in a layered medium is the same as for homogeneous soil, and that this damping is frequency independent. It is expected that this assumption is violated for the reported tests.

2.3.2. THE WAY FORWARD: THE INVERSE APPROACH

Instead of the direct identification approach (like the SRS method), the inverse approach was chosen, using a linear elastic continuum model considered in the frequency f [Hz] - wavenumber k [1/m] domain as a forward model, of which the properties are optimized to mimic the measurements. De Winter [82] confirmed the high sensitivity of the surface-wave response spectrum to the shear-wave velocity profile of the stratified soil. Together with the low operational cost and flexibility of the measurements setup, the MASW setup (sometimes referred to as Spectral Analyses of Surface Waves (SASW)) was selected as the focal point of further research. De Winter compared the modelled response with synthetic measurements in the f-k domain, merely based on the locations of the surface-wave modes - the modal surface wave method (MSW), or based on the full waveform (FW); the latter involves matching the full spectrum of the response, including energy distribution over the modes. The FW method was chosen, as this allows for a fully automatic inversion process; the modal method often requires hand picking or a check by an experienced geophysical engineer to ensure the right modes are selected in the measured data (modes can be closely spaced, and modes belonging

to other waves can mistakenly be interpreted as surface wave modes in case automatic picking is applied). The 'genetic algorithm' was employed as an optimisation scheme to find the global minimum of this nonlinear inversion problem. The objective is to maximize the suitability of a candidate soil profile by adapting the shear-wave velocity profile. The suitability is calculated based on the correlation of its response spectrum with the measured spectrum. Based on synthetic data, it is shown that the FW method using the genetic algorithm can determine the C_s profile with a 5% inaccuracy, where the highest certainty is obtained for the shallow layers. In the inversion, the layer thickness, density and pressure-wave velocity are assumed to be known. However, it is shown that a 5% error in these background properties, results in a mostly smaller than 5% error in the identified shear-wave velocities up to a depth of 35 m.

2.3.3. FURTHER DEVELOPMENT & PERFORMING MASW MEASUREMENTS

In-situ MASW measurements were performed on the IJsselmeer lake during the graduation project of Bolderink [83], in April 2015. The suitability function for the FW method was adjusted to become more source-independent. This aids in equal comparison of modelled and measured responses, as a proper signature of the source used in the measurements cannot always be obtained. When using the FW method, the energy distribution, i.e., the width and height of the spectral peaks, is an important additional (w.r.t. MSW) dimension in the objective function. Besides damping, also the finite length of the receiver array ('streamer') in actual measurements influences the energy distribution in the response spectrum. The effect of finite receiver length was incorporated, and it was found that it is most efficient to - instead of directly applying a convolution in the wavenumber domain - use a FFT algorithm to transform the modelled response to the space domain, apply a window to truncate the signal, and back-transform the response to the wavenumber domain. Furthermore, it was shown that, for the synthetic case, an inversion for the pressure-wave velocity is possible by disregarding (cutting out) the surface-wave dominated zone of the response spectrum in calculating the suitability.

In the IJsselmeer measurements, a 47 m streamer was used with a 1 m sensor spacing. The streamer remained on the same position on the mudline (with its center on turbine position W27, MP/SCPT45), and the airgun source was shifted to different positions with respect to the streamer; by concatenating the space domain records, a longer virtual streamer length was created. The MASW in this near-shore application being a fairly new technique, resulted in some teething problems in the execution; the geophone streamer was damaged, leaving only the hydrophone data to be useable for analysis. Furthermore, due to a low accuracy of the positioning system of the boats, the different shot positions of the airgun were not aligned with the streamer. The misalignment angle was estimated to be 15 degrees, resulting in an effective receiver spacing of 0.97 m. The different short records were concatenated towards a total virtual receiver length of 237 m, using the direct arrival of the pressure wave in the water. Several pre-processing techniques were applied to improve the quality of the measured dataset. These included the stacking of multiple shot records (of equal source position) to reduce noise, and the reconstruction of the data using the Radon transform. This transform assumes that the

data consist of a summation of linear and parabolic events, and is used to interpolate the bad or defect traces, and to further reduce noise. Additionally, root mean square (RMS) scaling was applied to each trace, which results in a fairly equal distribution of energy amongst the different modes, thus improving the visibility of the higher modes in the f-k spectrum. The left panel of Fig. 2.23 shows the shot records in the space-time domain after applying these preprocessing steps, and the right panel of that figure shows the same data in the f-k domain.

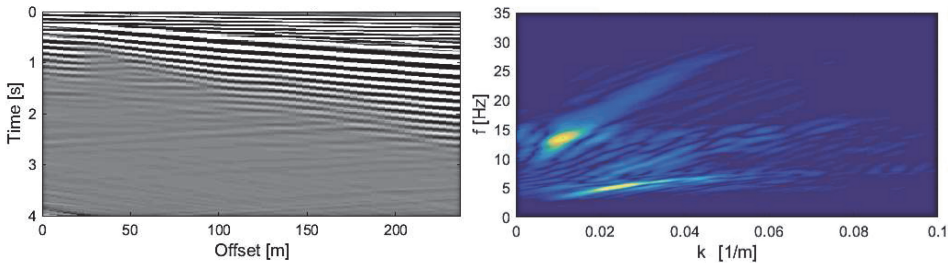

Figure 2.23: Concatenated dataset of the traces centred on position W27 (MP45) in the Westermeerwind wind farm in the IJsselmeer lake. The bad traces have been removed and reconstructed using the Radon transform. Furthermore, to improve the visibility of the higher modes, RMS scaling has been applied. The data is shown in the time-space domain (left panel) and frequency-wavenumber domain (right panel).

The RMS scaling amplifies the far-field response, however, it also creates higher values at the end of the traces, introducing side lobbing or roll-off effects. Hence also a Hanning window was applied. For equal comparison, the same scaling and windowing is applied in the modelled response. With a background model of which the layer thickness and mass density was based on CPT output, the FW method was used to invert the measured data. It was found that also this method is much aided by experienced interpretation of the dispersion spectrum, improving the settings for new inversion runs. For instance, to mimic a high energy event in the measurements at relatively low wavenumbers, the shear-wave velocity settings (initial value and range) for the deeper layers was increased. Nevertheless, despite several runs, a rather low suitability was reached, and the visible match in spectra was also poor. It is expected that the damping has a larger influence on the spectral shape than the truncation of the signals in space and time. Including a correct material damping profile and also incorporating geometric damping (which was not incorporated in this work), should benefit the inversion result.

2.3.4. STIFFNESS & INITIAL DAMPING INVERSION

Apart from being a desired output property, a correct damping profile seems a necessity for successful inversion of the elastic parameters using the FW method. This being the starting point for the MSc thesis of Armstrong [84], it was chosen to split up the inversion for dynamic soil properties in 2 steps. A correct stiffness profile is a requisite for estimating the damping profile. So rather than inverting for these 2 properties simultaneously, it was decided to first apply a damping-independent method to find the stiffness profile, and subsequently estimate the damping profile as a second step. As

the locations of the surface wave modes in the f-k domain are quite insensitive to the damping, the MSW method could be a better alternative (w.r.t. the FW method) to estimate the stiffness profile. It was shown that for an expected soil material damping ratio within 10%, the maximum shift in real part of the complex wavenumber was around 2%.

Improving the inversion method

The next few paragraphs summarize the several improvements of the inversion method that were implemented within this thesis. First of all, as the aim was to eventually invert for the material damping profile, a distinction had to be made in the forward modelling between the 2 major types of damping in the considered wave propagations: these are geometric damping and material damping. To quantify the material damping, the geometric damping needs to be modelled correctly. To include geometric damping in a layered forward model for wave propagation caused by a point source, the governing equations can be formulated in 3D cylindrical coordinates (rather than the previously used 2D cartesian coordinates). These equations can be transformed from the space domain to the wavenumber domain using the Hankel transform. The Hankel transform automatically incorporates an amplitude decay along the radial distance: the geometric spreading of energy. In the Fourier transform, the harmonic basis functions do not decay. As for this work an axisymmetric model was assumed, the circumferential direction could be disregarded, and the problem could still in fact be considered in only 2 dimensions (the radial and vertical directions).

One of the major challenges in the forward modelling of the dynamic response of a stratified continuum, is mapping all the zeroes of the dispersion curves: finding the locations on the f-k grid where the determinant of the system (coefficient) matrix equals zero. The determinant equation is highly nonlinear and therefore contains many local minima. This complexity is already present in an undamped model (in which the wavenumbers of the surface waves remain real valued); by including damping, an extra dimension is added to the problem as the wavenumbers become complex, making the root mapping even more challenging. In this work, the undamped ('elastic') roots are identified by searching (in the f-k plane) along constant wavenumber for a sign switch of both the real part and the imaginary part of the determinant. For identifying the modes of the slow surface waves (occupying the lower right corner of the spectrum), searching along constant wavenumber results in a higher resolution than searching along frequency. The speed of the root finder algorithm was enhanced by first considering a course search grid, and finding the more accurate position by using a local, constraint, non-linear optimisation function (Matlab's *fmincon* function). As previously indicated, finding the damped roots in the complex plane in the same fashion as the elastic roots, is computationally very expensive due to the added dimension along the imaginary axis. Instead, use was made of the fact that the roots start on the real axis (for zero damping) and shift into the complex plane as damping increases. As this shift into the complex plane generally follows a similar path, a small plane around the expected root location was swept with a fine step size to find the minimum. As some roots can still be missed with this approach if a large damping is applied, it was chosen to use intermediate forward models, in which the damping is incrementally increased up to the desired damping

as to map the path of the roots in the complex plane. Nevertheless, sometimes erroneous roots are found and/or roots are missed using this method, especially if a too coarse discretization is used in the search.

Regarding the actual inversion process, the speed of the MSW method was greatly enhanced by using a misfit function based on Maraschini et al. [109], in which the modal peaks (locations) are picked from the measured f-k domain. This is a very efficient approach, as instead of calculating the entire f-k grid, the forward model is only used to calculate the determinant for the few locations along the dispersion curve. The aim is to minimize the value of the determinant at these locations; the determinant should be zero at the root locations, hence the error or misfit of a candidate soil profile is calculated as the sum of the (residual) determinant values at these locations. Note that this also implies that no roots need to be found during the inversion process. However, a challenge in this method is that the value of the determinant varies greatly over the f-k spectrum; it decreases by multiple orders with decreasing phase velocity. This is a disadvantage when using a misfit function which is based on the summation of the determinant values. For such a misfit function to work, the determinant should be quite comparable over the f-k grid, except at the root locations, where it becomes small. Therefore, the determinant was normalized over a desired f-k grid by the (mean) determinant - phase velocity relation. This was found by determining the moving average of the determinant along a few arc lines (moving from low to high phase velocity) in the f-k grid at different (randomly chosen) radial distances from the origin, see the left panel of Fig. 2.24. The (smoothed) average relation of these lines (the determinant value - phase velocity relation, see the right panel of the same figure) is subsequently used to normalize the determinant. The resulting normalized determinant can be seen in Fig. 2.25.

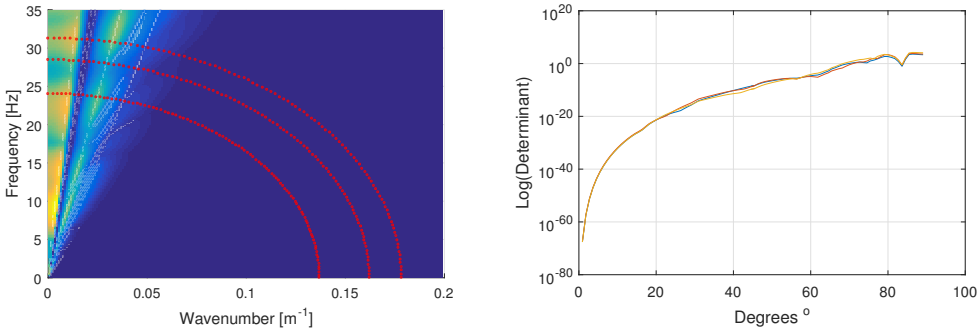

Figure 2.24: Left panel: arc lines drawn in a (non-normalized) spectrum, along which the determinant-phase velocity is determined. Right panel: the determinant versus the angle in the f-k spectrum for the same arc lines, where 0 degrees corresponds to a position on the horizontal (wavenumber) axis and increases counter-clockwise.

In further preparation for inverting in-situ measured data, model sensitivity studies were performed, indicating that besides the shear-wave velocity profile, also the layer thickness

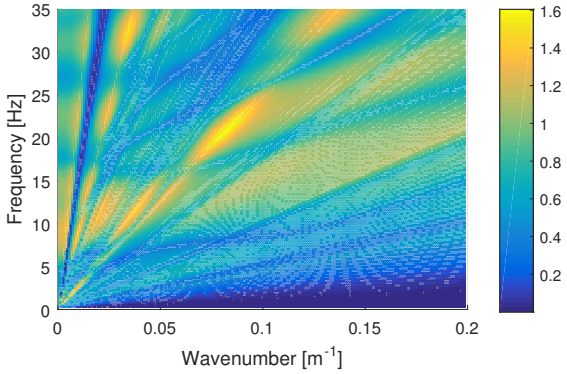

Figure 2.25: The determinant after normalisation; the range of values along the spectrum has much reduced.

has a large effect on the root locations. Related to this, it was shown that for a correct determination of the dispersion curves, the layer discretisation should be at least 2-4 times smaller than the smallest considered wavelength. The density and pressure-wave velocity seem to have only minor influence on the root locations. In general, the sensitivity of the fundamental mode to the profile properties decreases with depth - which is not surprising when considering surface waves. The higher modes, propagating at higher phase velocity, having generally larger wavelength, are more sensitive to the deeper soil deposits. Even for waves of equal wavelength belonging to different modes, the shape of the waves shows that the main energy (amplitude) of the waves of the higher modes will be more contained in the deeper layers. Finally, aiding further in understanding the spectral results of the measurements and inversion runs, it was found that the smaller the contrast between the soil layers, the smoother the dispersion curves; sharp bends or kinks in the curves can indicate the presence of discontinuities or sharp boundaries in the soil deposits.

The genetic algorithm as implemented by de Winter [82] was enhanced to be more versatile during an inversion run, by including options for dynamic re-ranging, layer-stripping, and phased settings. In dynamic re-ranging, the search ranges for the soil properties can be decreased based on the progress (convergence) of the inversion. It was found that this has a large positive impact on the inversion success. In layer-stripping, the shallow layer-properties (having highest influence on the root locations) are fixed after some convergence of the inversion, so that the focus is switched to finding the deep layer properties. The phased settings option allows for changing the settings during the run. For instance, an additional set of modes can be introduced after that the location of the fundamental mode has converged in the forward models. In general, the inversion tool was greatly improved in efficiency. A regular computer could be used for more intensive inversion runs than previously done on a computer cluster with 32 processors [83].

Inversion for stiffness

With the obtained knowledge and tools, a new effort was made in inverting the IJsselmeer data to find a best fit shear-wave velocity profile. The SCPT45 inversion result discussed in Section 2.2, Fig. 2.18, was used as a reference, as in fact, SCPT measurements are deemed to yield a higher level of certainty regarding the stiffness (shear-wave velocity profile) than the MASW, for the dual reason that i) the SCPT is a more direct, vertical measurement of the profile, and ii) a higher certainty is thought to be involved in the 'layer stripping' measurement and inversion approach. This line of thought is shared by Noorlandt et al. [110], who found that the MASW gives a more averaged C_s profile along the length of the array, and the SCPT renders more precise C_s values of the profile at the position of the cone and source. Nevertheless, the MASW provides a valuable confirmation of the values retrieved by the SCPT, and, as previously mentioned, in using the MASW measurements for damping estimation, the estimation of the stiffness profile is a prerequisite step. The reasons for this being that the forward model should have its (undamped) roots at the right locations. Furthermore, the geometric damping is sensitive to the stiffness profile.

Several inversion runs were performed, all of them having a closer resemblance to the SCPT profile than the best output of the FW results of Bolderink [83]. Therefore, the damping-insensitive MSW method seems to be the right choice for stiffness inversion. The best forward model was found to be a 21 layer model (reflecting the importance of small layer discretisation) including a large stiffness range for the halfspace. The input (objective) roots for the best run were semi-automatically selected from the measured spectrum, see Fig. 2.26. In selecting these roots, the large-energy event between 12 - 15 Hz and 0.01 m^{-1} wavenumber was neglected, as this event was not visible in the output spectra of previously performed simulations. It is not fully understood what the origin of this large phase velocity and wavelength event could be. However, analyses of the geometric decay factor n, fitting the relation $A = \frac{c}{r^n}$ (with A the geometric damping term, c a constant and r the radial distance) to the data in the frequency-space domain, showed that this event, having n almost equal to 2, is not related to surface waves (which have a decay factor of $n = 0.5$). Fig. 2.27 shows the ranges and mean C_s profiles of the best top 15% of the final populations; due to the non-unique character of the inversion, it is best to express the results in a mean and range of the values, as multiple soil profiles have comparable suitability (misfit). The figure also includes the C_s profile found with SCPT45 (Fig. 2.18), showing that comparable values are found with both techniques; this increases the confidence in the obtained solution. Furthermore, the left panel of Fig. 2.28 shows the correspondence between the selected objective modes and the response spectrum of the best candidate and vice versa for the right panel; the roots of the best candidate are drawn on top of the measured response. Finally, Fig. 2.29 compares the objective modes and the theoretical modes of the best candidate; it can be seen that the fundamental mode is matched well by the forward model, whereas a poorer fit is obtained for the 2 higher modes. The latter could be associated with the choice of the objective higher modes; assuming more straight lines for the picked modes, could improve the results of a next inversion run.

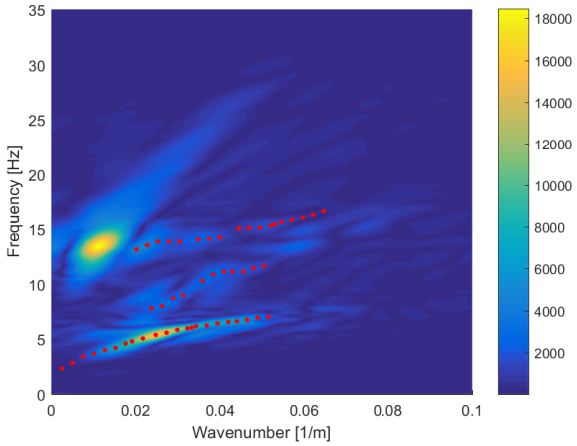

Figure 2.26: The objective root set that was picked from the IJsselmeer (position W27/SCPT45) response spectrum containing the 3 lower modes.

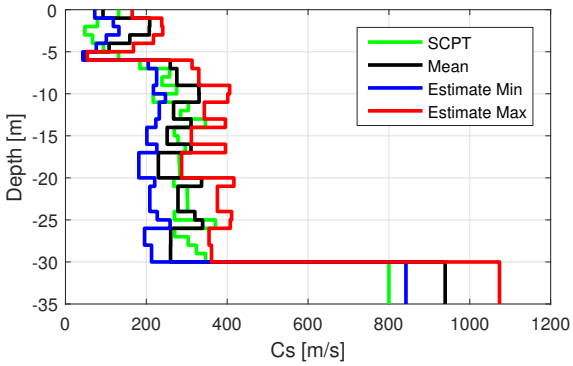

Figure 2.27: The mean and ranges of the top 15% C_S profiles of the final candidate profiles, IJsselmeer data inversion, position W27.

Apart from the data of the IJsselmeer (Westermeerwind wind farm), we got the opportunity to work with another, higher quality dataset; a collaboration was set up with the Norwegian Geotechnical Institute (NGI), who granted access to their data which was shot at the Gjøa oil field, offshore Norway at a water depth of 364 m [111]. NGI developed a shear wave vibrator for these tests which consisted of a 3.25 m diameter suction caisson (2.5 m embedment length) containing a hydraulic actuator which moves a 3700 kg mass, producing a maximum force of 250 kN, see Fig. 2.30 for an impression. By rotating the actuator, either Love or Scholte waves can be produced. The source could excite at frequencies between 2 and 60 Hz, and produce a flat power spectral density between 10 and 55 Hz. A 1 km long cable was used with 42 accelerometers

spaced at 25 m distance. By dragging the cable, an effective receiver spacing of 2.5 m was reached. In the end, a 600 m long effective streamer length could be used, with the source at about 160 m from one side. The recorded vertical velocities that will be used for the inversion are shown in the time-space domain in Fig. 2.31, and Fig. 2.32 shows the same record in the frequency-wavenumber domain.

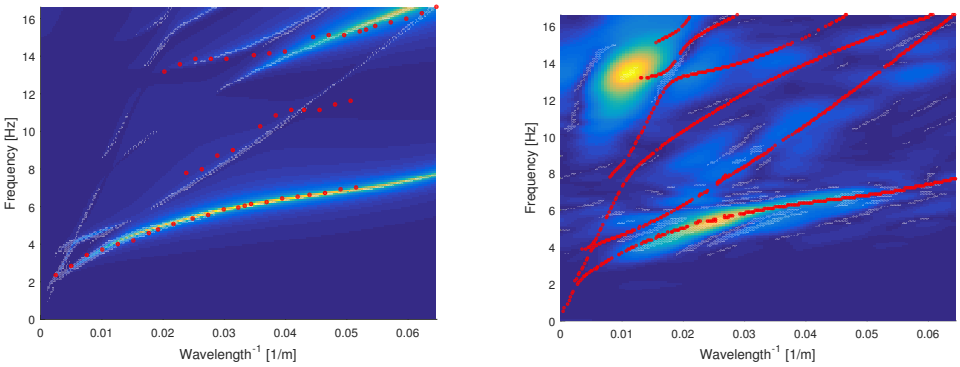

Figure 2.28: Left panel: the objective measured modes plotted on the response spectrum of the best candidate. Right panel: theoretical modes of best candidate plotted on the measured response spectrum.

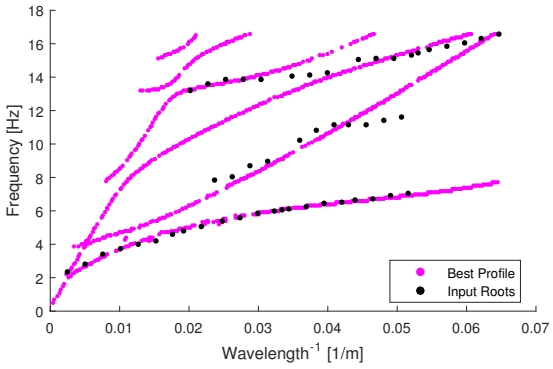

Figure 2.29: Comparison of the objective modes and the theoretical modes of the best candidate, for the IJsselmeer data inversion, position W27.

Figure 2.30: NGI's shear wave vibrator source, deployed at the Gjøa site, offshore Norway [111].

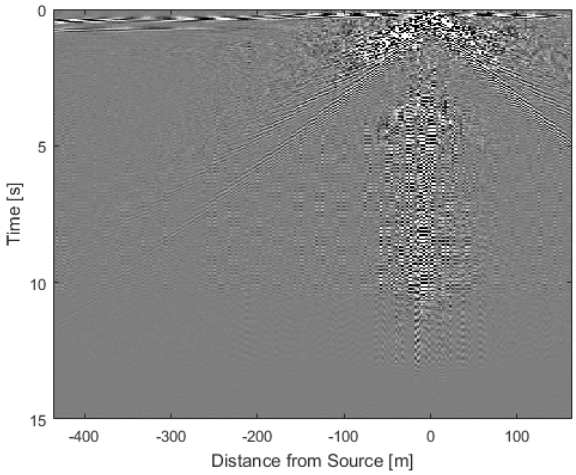

Figure 2.31: Gjøa shot record for vertical velocity of the effective streamer.

Based on the clearly visual modes (Fig. 2.32), this dataset was expected to be of higher quality than the IJsselmeer data, and was therefore selected for attempting the first damping analyses. Therefore, the space-wavenumber transform was performed using

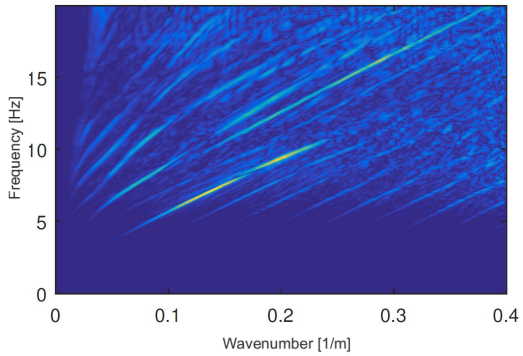

Figure 2.32: Gjøa data f-k spectrum of vertical velocity for the effective streamer.

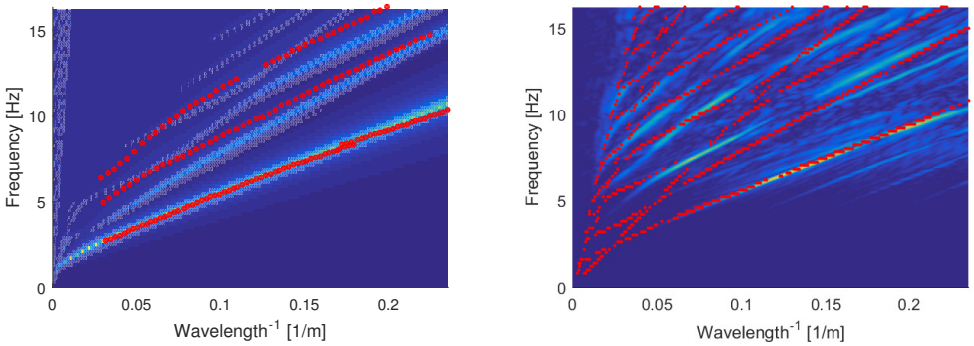

Figure 2.33: Gjøa C_s inversion. Left panel: comparison of the picked objective modes shown on top of the response spectrum of the best candidate. Right panel: comparison of theoretical modes of best candidate shown on top of the measured response spectrum.

the discrete Hankel transform, to account for geometric damping in the resulting f-k spectrum. Where the IJsselmeer data required 4 iterations, only 2 inversion runs were needed to obtain satisfactory results for the Gjøa data, confirming the high quality data. In the second run, excellent convergence was reached, using phased settings (an initial focus on the fundamental mode, including two higher modes after 30 generations), layer stripping and dynamic re-ranging. In the left panel of Fig. 2.33, the picked, objective modes are shown on top of the spectrum of the best candidate soil profile, and in the right panel the modes of the best candidate are compared to the measured spectrum. Finally, Fig. 2.34 compares the picked modes with the best candidate modes. From these figures we can conclude that the fundamental mode is matched very well, however, the 2 higher modes have a less good visual fit. This is most likely related to the used misfit function that does not consider the distance between measured and modelled modes, but just the value of the determinant. Due to the normalisation, the determinant has

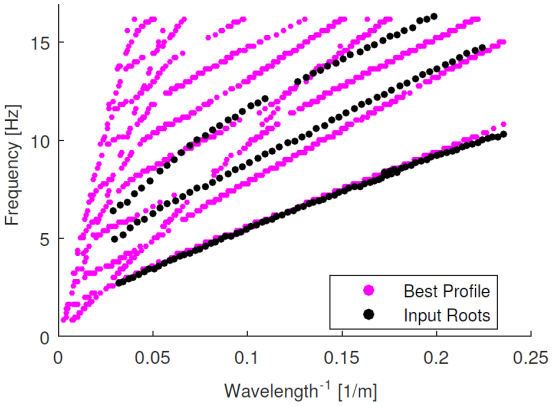

Figure 2.34: Gjøa C_s inversion case 2 comparison of the input modes and the theoretical modes of the best candidate.

quite a constant value in between modes, so no 'punishment' is attributed to placing a mode at a further distance. This could be improved by adjusting the smoothing used in the normalisation. As the 2 higher modes do not match well, only the fundamental mode will be used for the damping inversion. The left panel of Fig. 2.35 shows the top 15% of the last population, including the search ranges; the best to worst (of the top 15%) candidate are indicated using a colour scaling. The profiles compare quite well with previously published results from Socco obtained using the same data [112], shown in the right panel of the same figure. The left panel even suggests that a higher degree of certainty has been found. Socco used a Monte Carlo optimisation in the inversion, and no normalisation of the determinant or layer stripping was applied.

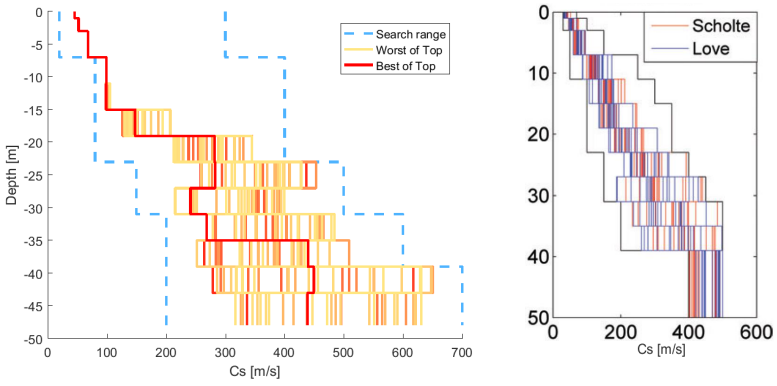

Figure 2.35: Gjøa C_s inversion. Left panel: search range and top 15% of the population with scaled colours based on the suitability. Right panel: Gjøa published stiffness estimate by [112].

Inversion for damping: methodology and testing

With the stiffness profile assumed known, the inversion was extended to also search for the best fit material damping profile that matches the measurements. Where the stiffness profile was updated to match the measured surface-wave phase velocity curves $C_{sch}(\omega)$ of the Scholte wave, the damping inversion aims to match the attenuation coefficients $A_{sch}(\omega)$ of the surface waves. To aid in the following description, it is useful to include the (far field, single-mode) soil response in vertical direction u_z in the space-frequency domain ($r-\omega$, r being the radial distance and ω the angular frequency):

$$u_z(r,\omega) \cong \zeta_g(r,\omega) \mathrm{e}^{-\mathrm{i}\frac{\omega}{C_{sch}(\omega)}r} \mathrm{e}^{-A_{sch}(\omega)r}. \tag{2.12}$$

Here $\zeta_g(r,\omega)$ is the amplitude term that includes geometric damping, which is of the form $\zeta_g(r,\omega) \sim \frac{1}{r^n}$, with $n = 0.5$ for surface waves on a homogeneous half space ($n = 1$ for body waves at depth). As previously mentioned, $C_{sch}(\omega)$ is the phase velocity of the surface (Scholte) wave (or dispersion curve), and $A_{sch}(\omega)$ the attenuation coefficient, which is the product of the modal (material) damping ratio $D_m(\omega)$ and the Scholte wavenumber k_{sch}:

$$A_{sch}(\omega) = D_m(\omega) k_{sch}. \tag{2.13}$$

Several methods are available to determine the attenuation coefficients of measured surface response data and subsequently invert for the material damping profile. Badsar [113] discussed 3 methods, of which the newly developed *modified half-power bandwidth in the f-k domain* method seems most fit for extracting the attenuation coefficients of multiple modes, making it more agile to complex multi-layered soil systems. The other 2 methods (*phase-amplitude regression in the f-x domain* and *amplitude regression in the f-k domain*) focus only on the fundamental mode, and therefore do not account for the fact that the geometric damping term $\zeta_g(r,\omega)$ may contain local increases in amplitude due to interference of the modes. In the half-power bandwidth method (also sometimes known as the Q-factor technique) the damping ratio D of a single degree of freedom (SDoF) system is calculated by extracting from the energy spectrum in the frequency domain, the width $\Delta\omega$ of the resonance peak at half the height of the peak, and dividing by twice the the central frequency ω_c:

$$D_m(\omega) = \frac{\Delta\omega}{2\omega_c} = \frac{1}{2Q}. \tag{2.14}$$

As we focus on the spatial decay, the method will be applied along the wavenumber; the ω in 2.14 is replaced by k. The modification of this classic Q-factor method lies in the added possibility to not consider the width of the peak at only half of the peak energy, but at any desired height of ε times the peak energy. This is convenient for closely spaced modes, where the energy peaks start interfering at some distance from the peak. This is less the case close to the resonance peak, so ε can have a value between 0 and 1, but is chosen to be close to 1 to avoid disturbance of neighbouring resonance peaks. The modified half-power bandwidth is given as

$$D_m(\omega) = \frac{\Delta k}{2k_c\sqrt{\varepsilon^{-2}-1}}. \tag{2.15}$$

To extract the modal damping from modelled response, Misbah [114] proposed to use the *phase damping ratio* as proposed by Carcione [115]. This ratio can be calculated using the complex wavenumber $\mathring{k}$ to calculate the quality factor for surface waves:

$$Q_m(\omega) = \frac{\mathrm{Re}(\mathring{k}^2)}{\mathrm{Im}(\mathring{k}^2)}, \tag{2.16}$$

which gives, using Eq. 2.14:

$$D_m(\omega) = \frac{\mathrm{Im}(\mathring{k}^2)}{2\mathrm{Re}(\mathring{k}^2)}. \tag{2.17}$$

The modified half-power bandwidth and the phase damping ratio methods were tested to yield similar attenuation coefficients for soil profiles published in [113] and [97], respectively. In general, the match was very satisfactory, however in comparing also the higher modes attenuation coefficients published by Foti [97], it was shown that not all complex roots were found by the developed tool (described in the beginning of this subsection), and that some erroneous roots were included. This confirms that finding the complex roots (within reasonable computational time limits) remains one of the most challenging parts of the inversion process. The half-power bandwidth and phase damping methods were additionally checked to produce the same attenuation coefficients.

For the damping inversion, a previously found stiffness profile is used which should result in the measured and modelled modes lining up in the spectrum. The undamped, elastic roots are the starting point for the complex root finder algorithm. As for the stiffness inversion, the genetic algorithm is also used for the damping inversion, and the misfit function is the distance between the measured and modelled modal damping curves $D_m(\omega)$. This is an adaption with respect to Badsar [113], who used the distance between attenuation coefficients. In using the attenuation coefficients, a linear scaling along the wavenumber is applied (see Eq. 2.13), yielding higher weighting to higher wavenumbers (shallower soil layers). It was found that considering the modal damping curves yields a more equal weighting of the different layers over the depth of the damping profile.

In testing the damping inversion on synthetic cases, it was found that the misfit function is very sensitive to the shallow layers (despite using the damping curves instead of the attenuation coefficients). Secondly, the complex root finding was confirmed to be computationally very expensive; when using a normal computer, this limits the amount of layers included in the forward model (the size of the system matrix). As the damping inversion seemed to have a more unique solution, containing less local minima, several local search techniques were tested. Nevertheless, these methods were unsuccessful, and it was found that a layer stripping approach yielded the best results. Fig. 2.36 shows the fit of the best candidate damping curve for a synthetic case. Nevertheless, it was found that a visually good fit of the damping curve, can still lead to large errors in the damping estimation of the deeper layers[2]. This is confirmed by the large errors for the

[2] In this work, the damping related to pressure-wave propagation was assumed equal for that of the shear wave, as the pressure-wave damping was found to have a low influence on the overall response spectrum.

deeper layers of this test case, given in Table 2.2.

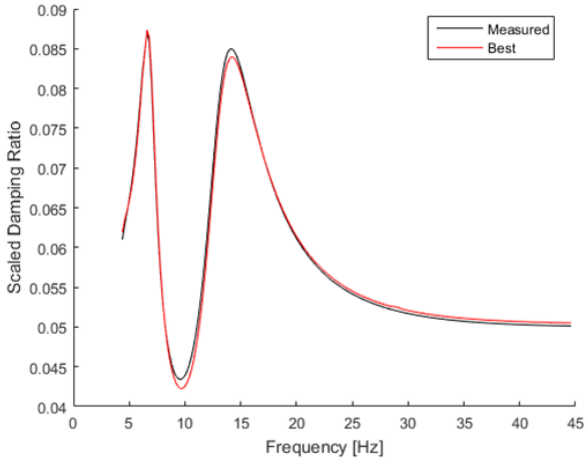

Figure 2.36: The synthetic and estimated damping ratio curves $D_m(\omega)$ have a close visual match, even though there is significant error in the estimated material damping ratio of the (deeper) soil layers, see Table 2.2.

Table 2.2: Damping profile of the best candidate for a synthetic test case. The model included a 5 m water column, soil layers of 3 m thickness and a halfspace.

Layer	ζ_{ref}[%]	$\zeta_{inversion}$[%]	Error [%]
Water	0	0	-
1	5	5.04	0.8
2	3.5	2.90	-17.1
3	2	2.52	26.0
∞	1	1.68	68.0

The small mismatch at the locations of high curvature of the damping curve, needs to be resolved in order to decrease the error in the damping estimation. As all points along the damping curve have equal weight, the many points at more smooth regions of the curve overshadow the crucial points at high curvature. The wavelet compression scheme [116] was used to smartly select the important points on the (modelled) damping curve at locations with high curvature, see Fig. 2.37. This reduced set of points resulted in a much closer match of the best candidate damping profile with the objective profile. Nevertheless, within the best 5 profiles the error again increased, indicating yet a low convergence of the inversion. In a second test case, an incorrectly found low-frequency root caused the deep layer damping estimate to be poor. Nevertheless, a good match

was found for the shallow layers. In summary, multiple improvements on the damping inversion method were implemented and tested on synthetic cases, yielding satisfactory results. Nevertheless, finding all the (correct) complex roots remains computationally challenging.

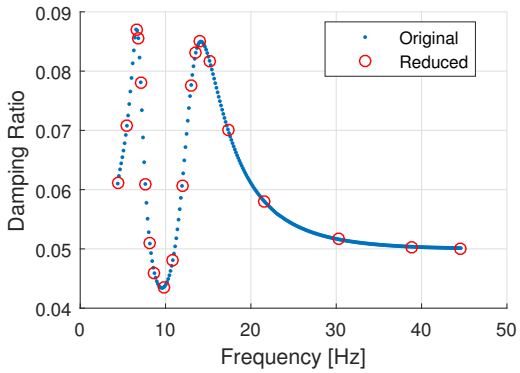

Figure 2.37: Modal damping ratio curve $D_m(\omega)$ before and after wavelet compression.

Inversion for damping: application to Gjøa data

With the gained knowledge, an attempt was made to invert the measured data for the damping profiles of the Gjøa site (for which a higher quality data set is available than for the IJsselmeer site). The time-space Gjøa data (Fig. 2.31) was transformed to the frequency-wavenumber domain (Fig. 2.32) using the FFT and the discrete Hankel transform, respectively. Due to a noisy spectrum, a somewhat scattered damping curve is extracted for the fundamental mode. The scattered points are therefore interpolated to yield a more smooth objective curve for the inversion, as can be seen in Fig. 2.38. Using the previously found best and mean (of the top 15%) stiffness profile, a uniform damping profile was assumed for the initial forward model. The damping curve of this initial model should already roughly match the damping curve extracted from the measurements. Unfortunately however, the inversion was unsuccessful due to failing to find the complex roots. Fig. 2.39 shows the found roots for the best (left panel) and mean (right panel) stiffness profile; the discontinuities should not be there. With the vast share of time spent on preparing the damping inversion (i.e., successful stiffness inversion), insufficient time was left within this project to further investigate and improve the complex root finding - a task which is indeed known to be very challenging [97]. Nevertheless, admirable progress has been made, and a successful inversion for damping in a real data set is deemed to be in relatively close reach for a future research project.

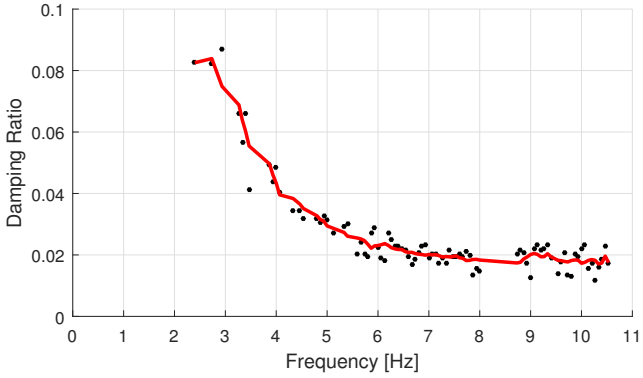

Figure 2.38: Extracted modal damping curve $D_m(\omega)$ for Gjøa fundamental mode.

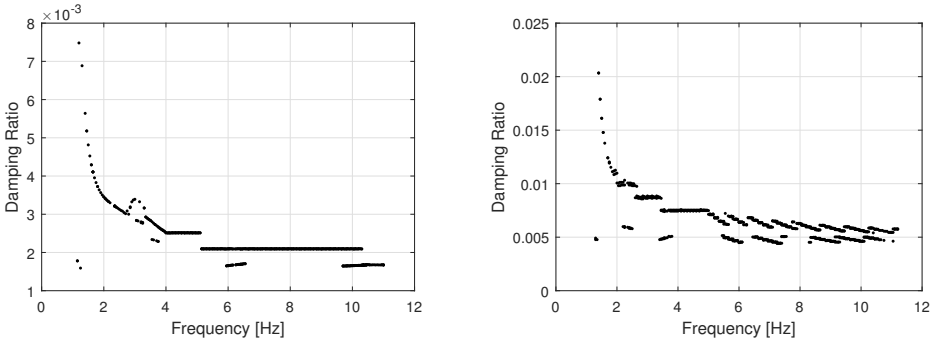

Figure 2.39: Erroneous modal damping curves $D_m(\omega)$ for fundamental Gjøa mode. Left panel: fundamental mode damping ratio curve for best stiffness profile. Right panel: fundamental mode damping ratio curve for mean stiffness profile.

2.4. SUMMARY & CONCLUSIONS

In this chapter we discussed how one can extract the relevant small-strain soil parameters that define the dynamic soil-structure interaction of OWT structures. Due to the high sensitivity of the stiffness to the shear-wave velocity, determining C_s is often the main goal of the discussed measurement techniques. Field measurements have the dual benefit of extracting the soil properties in their in-situ condition (which will be experienced by the structure), and that the soil undergoes little to no disturbance during the measurement - being especially important for small-strain characterisation.

The SCPT is a well established and cost-effective seismic measuring technique, and was therefore performed in the IJsselmeer lake, to yield an a-priory soil stiffness prediction for the MPs of the Westermeerwind wind farm. Two locations were analyzed in Section 2.2: SCPT20 and SCPT45. After installation of the MP of turbine W27 - at the location of MP45/SCPT45 - validation measurements were performed, measuring

the response of the MP during excitation of a shaker (as will be discussed in Chapter 5). Therefore, slightly sharper focus was placed upon deriving a best-estimate stiffness profile for SCPT45, whereas SCPT20 is used for defining 3 stiffness cases to assess the sensitivity of the pile response (discussed in Chapter 3) to the chosen Poisson's ratio and selected interval arrival times of the shear waves at the cone. It was discussed how to best extract these interval times, and a description was given of a developed inversion technique, based on Snell's law for wave refraction. We touched upon the correspondence and differences between the geotechnical, larger-strain CPT output and the geophysical, small-strain shear-wave velocity profiles. We observed that for the SCPT45 profile, the higher stiffness (with regards to SCPT20) from the C_s results, was hardly reflected in a higher internal angle of friction ϕ. This difference also affects the applicability of empirical relations that aim to estimate the shear modulus G with conventional geotechnical strength parameters. Such relations can be very practical, but due to the multiple conditions that influence the shear modulus, caution is warranted for applying them directly, without assurance of the site-specific relation. Finally, it was shown how to derive the remaining elastic constants, the density ρ and Poisson's ratio ν, which are needed for characterising the 3D continuum. The output of Section 2.2 is used as input for a 3D FE model, discussed in the next chapter.

Seismic measurements also allow for the identification of the soil material damping, which is expected to be one of the main damping sources in the SSI of OWT monopiles. Section 2.3 summarizes the work performed within the framework of 4 MSc theses, of which the author was the co-supervisor. An initial attempt in extracting this damping from in-situ measured, vertically spaced accelerometer data (retrieved by means of cone penetration), yielded unphysical results. The assumptions behind the applied Spectral Ratio Slope method seem not to hold for the data at hand. It was decided to move to an approach which involves solving an inverse problem, which implies updating a forward model to match the measurements. Furthermore, it was chosen to focus on the non-invasive surface-wave measurement technique. The propagation of surface waves was confirmed to be very sensitive to the C_s velocity of the soil stratum, and successful attempts of damping identification have been reported for the cost-effective MASW/SASW technique [113]. The response measured with horizontally spaced surface recorders, is transformed to the f-k domain, and the aim of the inversion is to match the modelled and measured f-k spectra. The genetic algorithm is employed to approach the non-linear misfit function in a global way. Multiple improvements were implemented for finding the stiffness profile for a measured data set, based on the position of the picked elastic (undamped) roots. The inversion tool was made very efficient, yielding fast results with relatively high accuracy. Two in-situ measured data sets were successfully inverted to find the stiffness profile. Although the IJsselmeer data set (shot at position W27/SCPT45) was of a lesser quality, a C_s profile was found that matches well with that obtained with the SCPT measurements. For the Gjøa data set supplied by NGI, also satisfactory results were obtained, which are comparable to previously published profiles [112]. We can conclude that the crucial first step in finding the damping profile was achieved; the stiffness profiles can be obtained with quite a high accuracy up to a depth of around 40 m.

In order to additionally match and identify the damping (that effects the spectral energy distribution), the Hankel transform was used. The aim of the inversion is to - with the previously identified elastic roots readily aligned - match the modelled and measured frequency-dependent modal (material) damping curve $D_m(\omega)$. The modelled $D_m(\omega)$ is extracted using the phase damping ratio method, and the measured curve is identified with the modified half-power bandwidth method. The damping inversion was tested and improved using synthetic data. Especially the use of the wavelet compression scheme for a smart selection of damping curve points to be used for inversion, proved to be a valuable improvement. Nevertheless, finding the correct complex roots turned out to be a computationally challenging and time consuming task. This was confirmed when applying the developed techniques to the measured data set of the Gjøa site; erroneous complex roots were found using the previously identified stiffness profile. Improving the efficiency of the complex-root finder will be part of future research. Nevertheless, many valuable milestones have been reached, and the stage is set for finalising this challenging topic of surface wave inversion for the material damping profile.

3

3D MODELS

To capture the complex interaction mechanisms between rigidly behaving piles and soil (discussed in Section 1.2), a pile must be modeled as embedded in a 3D continuum. Only in such a model can we directly characterize the soil reaction with the basic material properties as identified in the previous chapter. This clean and versatile approach, in which the pile and soil are characterised separately, has a clear advantage over the direct use of semi-empirical 1D SSI models which are always bound to the range of pile geometries for which they were tuned.

In this chapter[1] two 3D FE models will be presented. The first model is developed using ANSYS software and is used for retrieving the static responses of MP45 and MP20, which are subsequently employed in the *local* translation method to find their associated static 1D effective Winkler models (as will be discussed in the next chapter, Section 4.2.2). The second model is MATLAB based, and was developed by Barbosa [118]. This model will be used for capturing both the static and dynamic SSI for different pile geometries, which will be used for presenting the *non-local* translation method (Section 4.3) and also for the local method in case of dynamic excitation (Section 4.2.3).

3.1. STATIC RESPONSE

A linear elastic FE model was developed using ANSYS software, meshing the pile with shell elements, and the soil with solid elements. The soil stratum was given a vertical dimension of 50 m, and a radius of 40 times the pile radius. The element size of the pile and that of the soil close to the pile was set to 0.25 m, and a combination of free and mapped meshing was applied. These model dimensions and mesh were verified to have converged for both piles (MP20 and MP45); using smaller element sizes or increasing the size of the soil domain had negligible effect. Taking advantage of the symmetry

[1] Parts of this chapter have been published in Engineering Structures **124**, 221-236 (2016) [78], in Proceedings of the 43rd APM conference (2015) [117] and accepted for publication (Article in Press) in the Journal of Solids & Structures (2017) [79].

of the problem, only half of the circular pile and soil domain was modeled in order to decrease the computational effort. The soil elements within and outside the pile were attached to the pile elements; i.e. no slip, nor gap formation is allowed between the pile and the soil. This simplification is deemed acceptable for the small deformations considered in this research. Fig. 3.1 gives an impression of the 3D model used for the static SSI simulations.

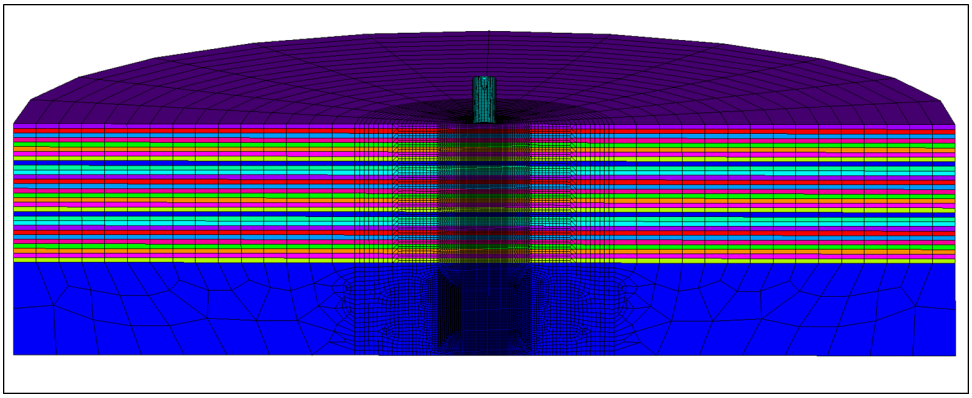

Figure 3.1: An impression of the 3D linear elastic FE model developed in ANSYS. The colours indicate the different soil layers.

MP20 and MP45 both have a pile diameter of 5 m. The embedded length of MP20 is 32 m and that of MP45 is 24 m. Furthermore, a 60 mm wall thickness was assigned to MP20 and 50 mm for MP45. The dimensions of MP45 correspond to 'as-built' in-situ, but the dimensions of MP20 are based on a preliminary design; no such pile was eventually installed at the Westermeerwind wind farm. To simulate a shape of the pile that corresponds to the expected shape of the loaded MP, for MP45 an overturning moment of 9.85 Nm and horizontal force of 1 N were applied at mudline by applying the force at the top of a 9.85 m extension of the pile above mudline. This is the moment-force ratio which was present at mudline during the shaker experiment used in the validation measurements (discussed in Chapter 5). For the response of MP20, a moment-force ratio of 90 m was applied, corresponding to the load eccentricity for this wind farm for most wind speeds (retrieved from the simulated design loads). The wave and wind loading for this wind farm are expected to have the same direction. Obviously, the magnitude of the loading (1 N) is not representative, however, since we use a linear elastic model, the magnitude of the loading does not matter. The soil was assumed to be horizontally stratified in 1 m thick, elastic layers and each layer was assigned the material properties derived for SCPT45 and the different stiffness cases defined for SCPT20, as described in Sections 2.2.3 and 2.2.4. Because of the limited depth reached by SCPT20, the deepest 7 m along MP20 until the lower boundary of the model (from 25 to 50 m depth) was assumed to be one homogeneous layer with the same properties as the layer above (24 to 25 m). For the same reason, the lowest soil layer at 30 to 50 m depth of the MP45 model was given equal properties as the lowest identified layer of SCPT45, see Fig. 2.19.

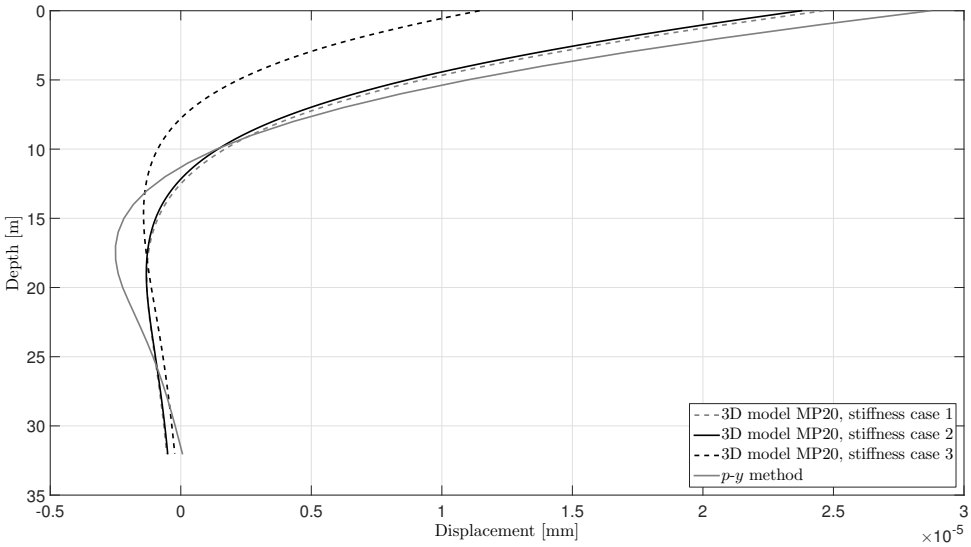

Figure 3.2: Comparison of pile displacements. The grey dashed line is the displacement of stiffness case 1, which is very similar to case 2 (black solid line). The black dashed line is stiffness case 3 (highest stiffness), and the grey solid line is the deflection computed using the p-y method. The piles are loaded by an equivalent static horizontal load of 2 N (1 N for the 3D model, where only half of the symmetric problem was simulated), at a vertical lever arm of 90 m above mudline.

Fig. 3.2 displays the computed 3D pile deflections for the three stiffness cases specified in Table 2.1 for the SCPT20/MP20 profile. These lines represent the horizontal displacement (x-direction in Fig. 4.3) of the nodes of the shell which are, in the undeformed situation, located in the plane (y-z plane, Fig. 4.3) perpendicular to the plane of the applied loading (x-z plane, Fig. 4.3). Fig. 3.2 also includes the deflection shape of a 1D Timoshenko beam on Winkler foundation, of which the stiffness equals the initial stiffness of the p-y curves that were determined according to the design code [106]. It can be observed that the p-y curve approach seems to be conservative (i.e. yielding the largest displacements) in estimating the displacements when compared to all 3 stiffness cases which were calculated with the 3D FE model. In addition, more bending is present in the region between 10 m and 25 m depth in the pile deflection calculated with the p-y curve approach compared to the 3D FE results. The deflection at mudline of case 2 is 17% smaller than that predicted by the p-y curve method. Two factors may be responsible for this. First, the input for the FE model was derived from seismic measurements, which are more appropriate for determining the small-strain shear modulus. Second, the FE model incorporates the 3D global reaction of the soil to the large diameter piles. As discussed, this phenomenon can, for instance, include a large base shear at the pile tip, shearing forces along the pile wall working at a large radius level arm [48] and pressure redistribution in the soil due to the Poisson's effect. Further, as expected (Section 2.2.4), we see that there is little difference in the deflections of cases 1 and 2, defined in Table 2.1. However, it is still interesting to see the influence of

the estimated Poisson's ratio on the deflection, as this is the only parameter that varies between these cases (obviously, due to Eq. 2.1, the associated Young's modulus also changes slightly; see the left panel of Fig. 2.21). The higher Poisson's ratio for case 2 with respect to case 1 (see the right panel of Fig. 2.21) yields a 3.5% smaller deflection at mudline. As both cases have Poisson's ratio profiles that are still well below the incompressibility limit of 0.5, their relative difference does not yield a large difference in stiffness. All the same, we conclude that the shear modulus has the dominant influence on the deflection. More extensive sensitivity studies of the elastic parameters of soil on the response of the MP can also be found in [119] and [120]. As case 2 is deemed most realistic (see Sections 2.2.2 to 2.2.4), we shall only consider this case for MP20 in the remainder of this thesis.

Fig. 3.3 shows the displacement computed by the 3D model for MP45 (black line) and - similar to Fig. 3.2 - also displays the deflections of a 1D beam on Winkler foundation having stiffness equal to the initial stiffness of the corresponding p-y curves (grey line). Although this pile is loaded with a smaller overturning moment (simulating the shaker excitation at interface level, 9.85 m above mudline), it can be observed that MP45 is characterised by a more rigid shape (less bending), reflecting the lower L/D ratio of this pile. Furthermore, the difference in deflection derived with the 2 techniques (3D model and the p-y curve method) is much more apparent. This is to be expected given the lower L/D ratio; the p-y curve method performs better for piles with a higher L/D ratio, as the method was calibrated for piles with $L/D \approx 30$.

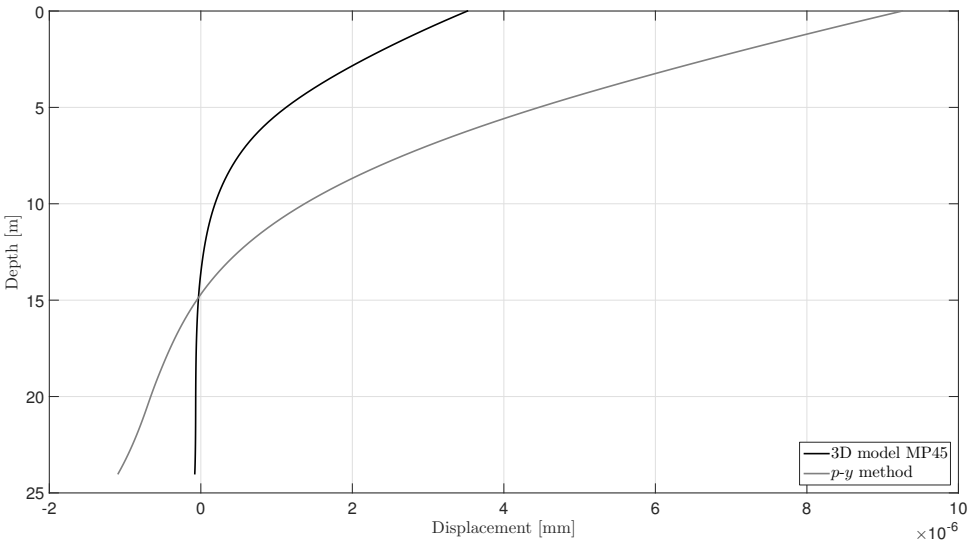

Figure 3.3: Comparison of pile displacements. The black solid line is the displacement of MP45 calculated with the 3D FE model, and the grey solid line is the deflection computed using the p-y method. The piles are loaded by an equivalent static horizontal load of 2 N (1 N for the 3D model where only half of the symmetric problem was simulated), at a vertical lever arm of 9.85 m above mudline.

3.2. DYNAMIC RESPONSE

For simulating the 3D dynamic case in the frequency domain[2], a MATLAB based FE model was developed by Barbosa [118]. It employs axial symmetry to decompose the 3D problem into a set of 2D problems, in which both the soil and the pile are modeled with solid finite elements [121]. To avoid reflections at the edges of the domain, Perfectly Matched Layers (PMLs) (as defined in [118]) are added to the outer boundary of the domain. For very low frequencies, the PMLs are replaced by elastic layers whose dimensions are large enough so that the fictitious boundaries do not influence the results. In order to keep the calculation times small, the size of the elements composing these buffer layers are made successively larger as the distance to the pile increases. The shear modulus of the soil G is made complex, G^*, by including the input soil material damping ratio ζ [122]:

$$G^* = G(1 + \mathrm{i}\eta\,\mathrm{sgn}(\omega)) = \mathrm{G}(1 + 2\mathrm{i}\zeta\,\mathrm{sgn}(\omega)), \tag{3.1}$$

with η the loss factor. The complex continuum stiffness and the geometric damping causes the SSI response to become complex valued.

The applied loading scenario, consisting of a horizontal load F at the free end of the pile and a bending moment M at the same end, is expressed in terms of radial F_R, tangential F_T and vertical F_V forces as

$$F = R\int_0^{2\pi} (F_R(\theta)\cos\theta - F_T(\theta)\sin\theta)\,\mathrm{d}\theta, \tag{3.2}$$

$$M = R^2\int_0^{2\pi} F_V(\theta)\cos\theta\;\mathrm{d}\theta, \tag{3.3}$$

where θ is the angle between the radial and the horizontal direction (in the horizontal plane), and R is the radius of the pile. Assuming that the horizontal force F is uniformly distributed along the perimeter of the pile, the radial and tangential forces are of the form

$$F_R(\theta) = \frac{F}{2\pi R}\cos\theta, \tag{3.4}$$

$$F_T(\theta) = \frac{-F}{2\pi R}\sin\theta. \tag{3.5}$$

Likewise, the force F_V can be described with the cosine as

$$F_V(\theta) = \frac{M}{\pi R^2}\cos\theta. \tag{3.6}$$

The Fourier series of F_R, F_T and F_V leaves us with terms of first order, and therefore only the axisymmetric problem related to the first Fourier term needs to be solved, as explained in reference [121].

[2] In this thesis, we use the Fourier transform $F(\omega) = \int_{-\infty}^{\infty} f(t)\mathrm{e}^{-\mathrm{i}\omega t}dt$ to transform the equations to the frequency domain.

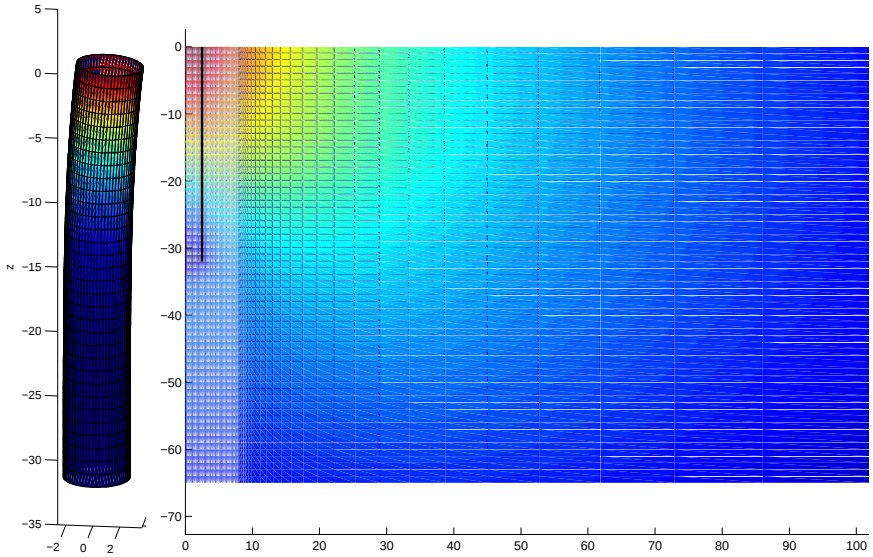

Figure 3.4: Impression of a 3D pile deflection and soil reaction due to a lateral force.

Fig. 3.4 gives an impression of the 3D model used for dynamic SSI simulations, showing the 3D pile deflection in the left panel, and the corresponding soil-stress response in the axisymmetric domain in the right panel. To validate the 3D models, Fig. 3.5 shows a response comparison between the ANSYS and the MATLAB based 3D models for static excitation. It can be observed that the 3D models are in good agreement in both displacement $u(z)$ and rotation $\psi(z)$, and also in their derivatives: the slope $u'(z)$ and curvature $\psi'(z)$, respectively. Finally, Fig. 3.6 shows an example of the complex-valued displacement of MP45 at an excitation frequency of 0.3 Hz, simulated with the MATLAB based model. For this examples, a material damping ratio of 1% was attributed to all soil layers (Equation 3.1).

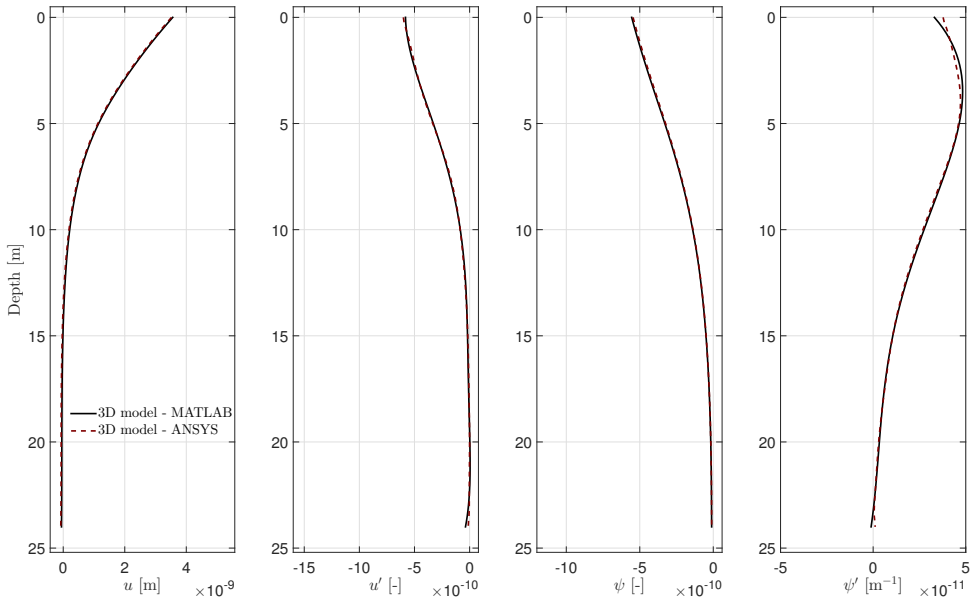

Figure 3.5: Response comparison between the ANSYS based and MATLAB based 3D models for a static excitation of MP45, showing from left to right the displacement $u(z)$, slope $u'(z)$, rotation $\psi(z)$ and curvature $\psi'(z)$. The piles are loaded by an equivalent static horizontal force of 2 N at a vertical lever arm of 9.85 m above mudline.

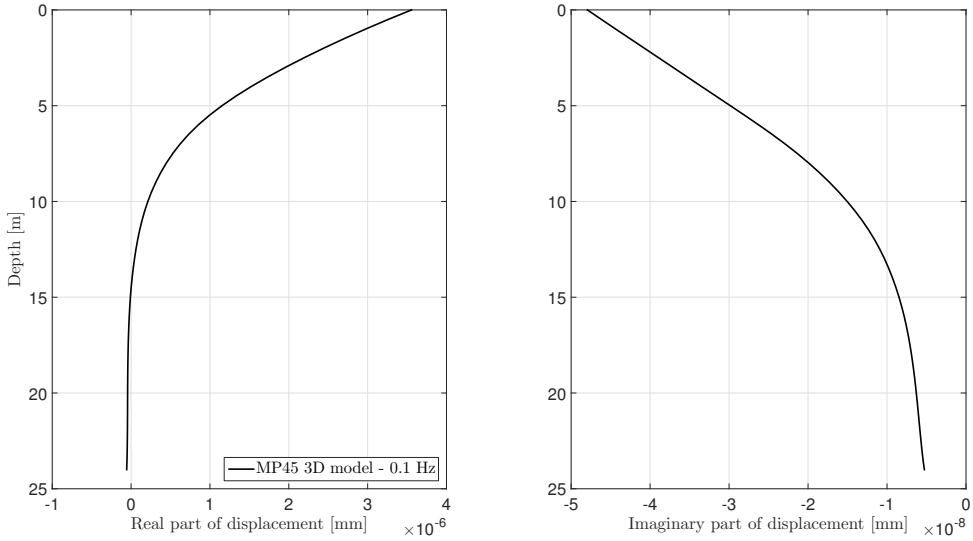

Figure 3.6: Steady-state displacement of MP45 calculated with the MATLAB based FE model.The pile is loaded by a horizontal force of 2 N at a vertical lever arm of 9.85 m above mudline with an excitation frequency of 0.3 Hz. The real part of the displacement is given in the left panel, and the imaginary part is given the right panel.

3.3. SUMMARY

In this chapter, two linear elastic 3D FE models were presented. The first model is developed using ANSYS software and is used for static SSI simulations. The pile is modelled employing shell elements and the soil using solid elements. The second model is MATLAB based and is used for both static and dynamic (frequency domain) simulations; solid elements are employed to model the pile and soil in the axisymmetric problem. The 2 models are used to produce the 3D SSI target response which need to be matched by the effective 1D models that will be presented in the next chapter.

4

1D EFFECTIVE MODELS

Along with the development of rigorous numerical models comes the need to translate the response of those models into simpler, effective models, combining the best of both: accuracy and computational speed [123]. The latter is a requisite for application fields where numerous load cases need to be simulated. Due to the stochastic nature of the loading environment of offshore wind turbines, numerous time-domain simulations (for capturing the nonlinear aeroelastic interaction) of 10 min duration are used to assess the different load cases for the design lifetime of an OWT. Currently about 120,000 of these simulations are performed for an average design case. Significantly decreasing the number of degrees of freedom of the design model whilst not losing much accuracy, is clearly a large gain in such a design community.

If a proper effective model is established for a certain design case, such simple models may facilitate, besides speed, also an improved understanding of the fundamental physics behind the problem at hand; as opposed to advanced models, quick analyses can be run using the effective model, needing to adjust fewer model parameters in between iterations. In this work, we choose the well-known beam-on-Winkler-foundation as the target simple model. The choice of condensing to a full Winkler-type model instead of, for instance, a lumped parameter model, stems from the strong desire of the engineering community to employ such 1D models. Winkler-type models have the advantage of increased physical insight as they directly yield a representation of the soil reaction, and the distribution of stresses within and displacements of the pile. Additionally, the coupling between the lateral and rotational degrees of freedom at the mudline is automatically incorporated. Furthermore, the Winkler based substructure is extendable to include non-linear reaction mechanisms. Therefore, other than only considering the pilehead displacements (as is often done [48, 119]), we will here consider the match in 3D and 1D modelled response of the entire embedded pile in terms of its displacement, slope, rotation and curvature.

In [80] it was shown that, in attempting to translate the 3D modelled response to a 1D model stiffness, simply dividing local forces by the collocated displacements leads to physically meaningless negative stiffness and singularities at certain locations. Surprisingly, this is an issue that was never raised by others who perform the translation in such a manner [32], [124]. In order to avoid dealing with such nonphysicalities, we need to find a way to identify a positive definite 1D stiffness profile that, once applied in a 1D model, yields nearly the same pile response as predicted by the 3D model. A 1D effective stiffness profile $k_{eff}(z)$ ($k_s(z)$ or $k_{s,0}(z)$ in the p-y curve method) is a soil-structure interaction functional parameter, capturing not only the properties of the soil, but also the geometry and material properties of the pile and its interface. That explains why a one-to-one, generalised relation between the basic soil continuum stiffness (Young's and shear modulus) and the stiffness in a 1D Winkler foundation cannot be found; the latter is dependent on the type of structure involved in the SSI. Nonetheless, researchers often attempt to establish such a relation [48, 52, 54, 57], and whilst being practical for preliminary design, the user should bare in mind that such empirical relations are bound to the specific SSI for which they were tuned - thus involving a degree of inaccuracy for structures with a different geometry and/or embedded in another type of soil. Therefore, as mentioned in the objective of this thesis (Section 1.3), in the sequel a *method* is proposed as a general approach for finding a 1D effective model for any specific SSI system, ensuring a higher accuracy than employing a generalised *relation*.

In this chapter[1], two methods are presented to translate the 3D soil-pile model into a 1D equivalent model. The first method is called the *local* method (Section 4.2), as in this approach each Winkler spring acts on a local level, uncoupled from any other spring (similar as assumed in the p-y curve approach). A distribution of lateral springs $k_{eff}(z)$ is sought for that will produce a 1D modelled response that mimics that of the 3D SSI model. In the second, *non-local* method (Section 4.3), we divert from the concept of a distributed springs vector $k_{eff}(z)$, and instead capture the global, fully coupled soil reactions from the 3D model by establishing stiffness kernels that are subsequently implemented in the 1D model. We will discuss the benefits and drawbacks of the two methods for both the static and dynamic SSI. As the significance of the more complex 3D soil reaction mechanisms depends on the type of soil-pile system, this chapter will first address a soil-pile categorisation (Section 4.1).

4.1. SOIL-PILE STIFFNESS CATEGORISATION & CASE SELECTION

The degree of non-local interaction between the structure and the continuum depends on the flexibility of the system. The displacement profile of a flexible pile typically involves multiple crossings of the zero-displacement line when loaded. While a flexible pile evokes a more local reaction of the soil, a rigid pile makes the soil react in a global way; a larger part of the continuum is mobilized to counteract the rigid pile [47]. A local 1D Winkler foundation with uncoupled springs may suffice for flexible piles, but a 1D model for rigid pile behaviour needs additional features to capture the complex SSI.

[1] Parts of this chapter have been published in the journal of Engineering Structures **124**, 221-236 (2016) [78] and accepted for publication (Article in Press) in the Journal of Solids & Structures (2017) [79].

Often the ratio of the embedment length L over the diameter D is used to categorize piles in either slender, (long) flexible piles with a high L/D ratio, or rigidly behaving piles that are short, with a low L/D ratio. However, when only considering the pile geometry in such a categorisation, the interaction with the soil is neglected; a slender pile (high L/D) can still bend in a rigid way when embedded in very soft soil. A useful parameter that incorporates the soil stiffness in the soil-pile categorisation is the relative pile stiffness K_r introduced by Poulos and Hull [125], and used by Abadie [70]:

$$K_r = \frac{EI_p}{E_s L^4} \quad \begin{cases} > 0.208\text{: rigid pile behaviour,} \\ < 0.0025\text{: flexible pile behaviour,} \end{cases} \tag{4.1}$$

in which EI_p is the bending stiffness of the pile and E_s the Young's modulus of the soil. The expression is based on the idea that for a homogeneous, linear elastic soil, there is a certain critical length (L_c) of the pile, beyond which a further increase of the length of the pile has no further influence on the pile head response [125]. The large precision in the boundaries of the behaviour type expressed in Eq. 4.1 seems a bit pretentious, however, together with the L/D ratio, it enables us to graphically classify a few pile-soil systems, as is also done by Abadie [70], see Fig. 4.1. Because the current research originates from the offshore wind industry, we duplicate in this figure some of the typical values of installed monopile foundations and the piles originally used to calibrate the p-y methodology, as shown in [70]. The latter work, however, recommends to use the Young's modulus of the soil at pile-tip level as the value for E_s in Eq. 4.1. Indeed, the pile-tip soil reaction is an important feature in the rigid pile behaviour, but it is believed that the entire soil stratum should be taken into account. It is therefore proposed to take the mean value of the Young's moduli of the different soil layers. Secondly, Abadie uses rather low values of the Young's moduli of different soils: 50 MPa for dense sand, 3 MPa for soft to medium clay, and 30 MPa for stiff clay. Generally somewhat higher values are prescribed [101], and from previous experience [78, 126] (Fig. 2.19), we find that the small-strain Young's modulus for in-situ saturated dense sand can be in the order of 150 - 300 MPa. Because of these differences, the soil Young's modulus used for calculating the flexibility factors of the installed monopile foundations and for the p-y development piles given by [70] are multiplied by a factor of 5 (250MPa/50MPa). The resulting flexibility factors, together with the cases that will be evaluated in this thesis are presented in Fig. 4.1. MP20 and MP45 are the previously discussed SSI systems, see Chapters 2 and 3. MP45 is called "In-situ", as this is the MP on which the shaker validation measurements were conducted, as will be discussed in the next chapter. The other 3 cases involve 2 short piles with a rather low $L/D = 3$ of which one pile is embedded in a relatively softer soil (the "Short-soft" case) and the other in a stiff soil (the "Short-stiff" case), and a "Caisson" type pile with $L/D = 2$, embedded in stiff soil. The geometry of the cylindrical, thin-walled piles, the average Young's modulus of the soil E_s and the flexibility factors of the 5 cases are given in Table 4.1.
Note that for the Short-stiff case, and to a lesser extent also the Caisson case, the piles are embedded in very stiff soil; the Young's modulus is in actual fact comparable to that of (weak) rock like shale and sandstone [127]. Although maybe counter-intuitive, the

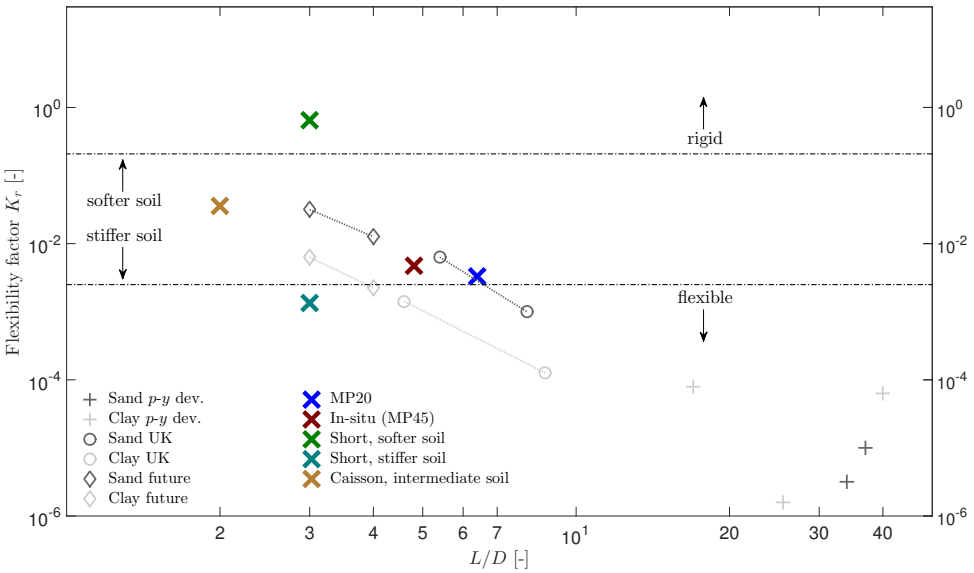

Figure 4.1: Flexibility factors and L/D categorisation. Note that the annotation for softer and stiffer soil applies for the same pile geometry; for 2 equal piles, an embedment in softer soil, yields more rigid behaviour.

	E_s	t	L	D	L/D	K_r
	[MPa]	[mm]	[m]	[m]	[-]	[-]
MP20	172	60	32	5	6.4	0.0033
In-situ (MP45)	319	50	24	5	4.8	0.0047
Short-soft	15	100	30	10	3.0	0.6437
Short-stiff	7368	100	30	10	3.0	0.0013
Caisson	1383	100	20	10	2.0	0.0362

Table 4.1: Pile-soil properties of the 5 considered SSI cases, with t the wall thickness of the pile and E_s the average Young's modulus of the soil profiles.

Short-stiff pile is considered a flexible pile by definition of the relative pile stiffness K_r (Eq. 4.1). SCPT45 and SCPT20 (Fig. 2.19 and repeated in Fig. 4.2) are the profiles of the in-situ MP45 and MP20 case, respectively. For the other 3 cases, scaling factors were applied to the entire Young's modulus profile of SCPT20 in order to obtain the spread in relative pile stiffness: $\frac{1}{12}$, 40 and 10 for the Short-soft, Short-stiff and Caisson case, respectively.

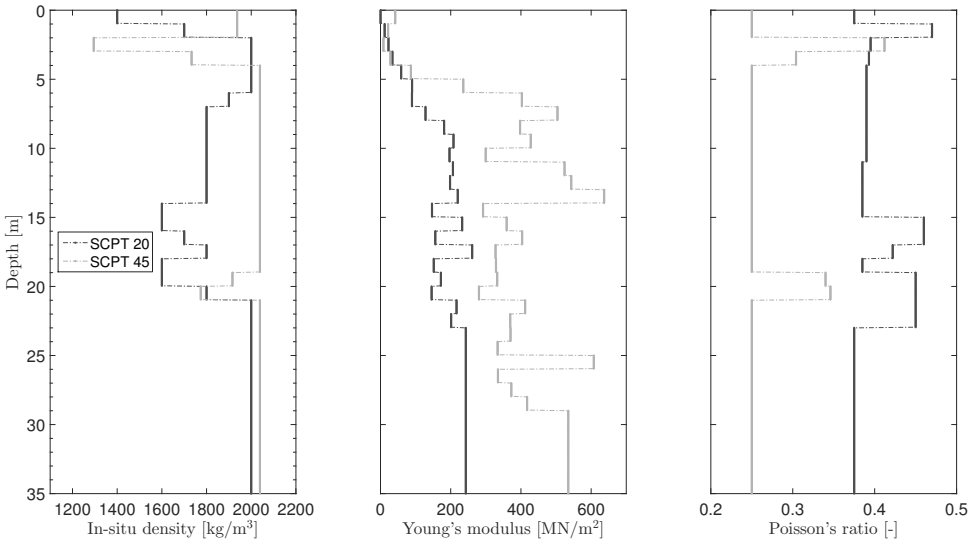

Figure 4.2: In-situ density, Young's modulus and estimated Poisson's ratio for SCPT20 and SCPT45. SCPT45 is used for the 3D model of the in-situ MP45 case, and SCPT20 is the profile of MP20. Scaled versions of the Young's modulus of SCPT20 are used for the Short-soft, Short-stiff and Caisson cases.

4.2. LOCAL METHOD

To find the 1D effective (p-y curve initial) stiffness, $k_{eff}(z)$, we propose to optimize the stiffness profile in the Winkler model so that the 1D model matches both the deflection $u(z)$ and rotation $\psi(z)$ obtained from the more advanced model. Note that we constrain ourselves by only assuming translational springs in the model, as this is often done in the offshore wind design practice. However, as 3D effects can be quite complex, it might, for instance, be reasonable to also introduce rotational springs in the 1D model. In the sequel, the local method is explained, and in Section 4.2.2 results are presented in terms of misfits of the static response of the 3D and 1D model for different SSI cases. In Section 4.2.3, the governing equations are extended to describe the dynamic SSI, applying the local method to additionally find an effective 1D damping profile $c_{eff}(z)$. After presenting the misfits of the complex-valued, steady-state responses of the 3D and 1D effective model, the performance of the local method is discussed in Section 4.2.4.

4.2.1. METHODOLOGY & GOVERNING EQUATIONS

The translation is accomplished by considering integrals of the equilibrium equation of a beam resting on a Winkler foundation, with $u(z)$ and $\psi(z)$ as the "known" 3D response and $k_{eff}(z)$ the unknown stiffness of the distributed springs. First, the 3D nodal solutions need to be translated into a 1D target solution (line). As previously mentioned in Section 3.1, for the horizontal displacement line $u(z)$, the horizontal displacement is taken of the nodes of the shell which are, in the undeformed situation, located on the plane y-z plane (see Fig. 4.3 which shows the sign convention of the 1D model) perpendicular to the plane of the applied loading (x-z plane, Fig. 4.3). For the 1D-target rotation $\psi(z)$, the difference in vertical displacements of the two nodes in the loading plane (x-z plane) are divided by the diameter of the pile. Such numerically computed profiles are not necessarily smooth enough for triple or double differentiation. Especially at the boundaries of the pile this can be an issue. To maintain a smooth shape also for the higher derivatives, the numerical values were approximated by polynomial functions. A piecewise fit was applied, subsequently averaging overlapping parts of the fits of these pieces and refitting a single polynomial through the different piecewise-averaged fits. For the deflections, the shape was split up in 3 parts, with 2 smaller parts focussing on the tip region of the pile. The same split was applied for the rotational shape; however, it was found that an extra split near the mudline (yielding a fourth part focussing on the top of the pile) gave a better overall fit.

We use the Timoshenko beam theory as the basis for the analysis. It was found that the shearing contribution to the rotation included in this theory, was necessary to provide an acceptable match with the 3D response of relatively rigid, large diameter piles.

The equilibrium equations of a Timoshenko beam, representing a monopile without external distributed forcing read

$$GA\kappa\left(\frac{d^2u(z)}{dz^2} - \frac{d\psi(z)}{dz}\right) - k_{eff}(z)\,u(z) = 0, \tag{4.2}$$

$$GA\kappa\left(\frac{du(z)}{dz} - \psi(z)\right) + EI\frac{d^2\psi(z)}{dz^2} = 0, \tag{4.3}$$

where E and G are respectively the Young's and shear modulus of steel, I the second moment of area of the cross section of the pile, A the area of the cross section of the pile and κ the cross-section dependent Timoshenko shearing coefficient. For the shape of the cylindrical cross section of the pile, we use a value of $\kappa = 0.53$. For the current purpose, it is more convenient to rewrite equilibrium equations 4.2 and 4.3 into a single equation. This can be done by differentiating Eq. 4.3 yielding

$$GA\kappa\left(\frac{d^2u(z)}{dz^2} - \frac{d\psi(z)}{dz}\right) + EI\frac{d^3\psi(z)}{dz^3} = 0, \tag{4.4}$$

and differentiating Eq. 4.2 twice to obtain

$$\frac{d^3\psi(z)}{dz^3} = -\frac{1}{GA\kappa}\frac{d^2(k_{eff}(z)u(z))}{dz^2} + \frac{d^4u(z)}{dz^4}. \tag{4.5}$$

Replacing the first term in Eq. 4.4 by $k_{eff}(z)u$ in accordance with Eq. 4.2, and substituting Eq. 4.5 into the second term of Eq. 4.4 yields a single equilibrium equation:

$$EI\frac{d^4u(z)}{dz^4} + k_{eff}(z)u(z) - \frac{EI}{GA\kappa}\frac{d^2(k_{eff}(z)u(z))}{dz^2} = 0, \tag{4.6}$$

which is similar to the Euler-Bernoulli equilibrium equation, but it includes a third term to account for the shearing effect.

The boundary conditions that we consider are

$$GA\kappa\left(\frac{du}{dz}\Big|_{z=0} - \psi(0)\right) = -F, \tag{4.7}$$

$$EI\frac{d\psi}{dz}\Big|_{z=0} = M, \tag{4.8}$$

$$GA\kappa\left(\frac{du}{dz}\Big|_{z=L} - \psi(L)\right) = 0, \tag{4.9}$$

$$EI\frac{d\psi}{dz}\Big|_{z=L} = 0, \tag{4.10}$$

in which F and M are the equivalent lateral force and overturning moment as applied in the 3D model. Note that this, in the case of simulating only half of the symmetric problem in the 3D model (as discussed in Section 3.1), implies that double the force applied in the 3D model has to be applied in the 1D model. It can be checked whether the assumed boundary conditions for a "free-free" 1D beam as stated in Eqs. (4.7) to (4.10) also hold for the 3D solution. When doing so, we find that - due to 3D effects - these force and moment equilibria do not entirely apply for the 3D responses at these locations. Therefore, we could argue that this requires the introduction of discrete lateral and rotational springs at the tip as well as at the top of the pile in the 1D model, in order to reach complete force and moment equilibria at the boundaries. However, here we will not apply any discrete springs at the boundaries, as an effective distributed stiffness can be found that satisfactory captures the 3D response without the application of extra discrete springs.

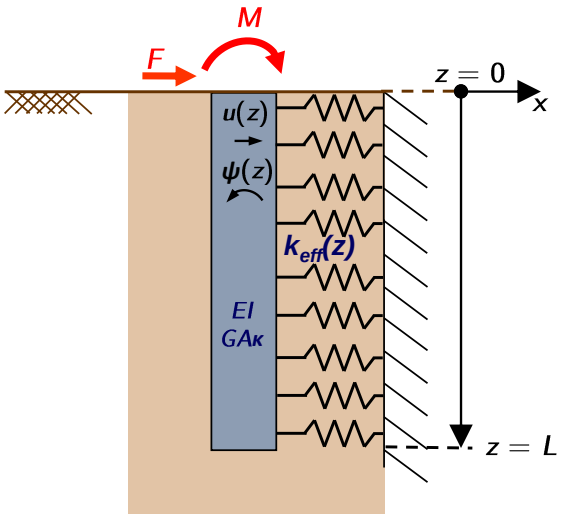

Figure 4.3: Graphical representation of the 1D beam model and the used sign convention.

In order to find the effective 1D stiffness $k_{eff}(z)$, we assume a certain continuous parameterized function. We are only interested in physically realistic solutions, and we therefore do not allow negative stiffness in the resulting stiffness profile. We found that looking for a solution for $k_{eff}(z)$ in the form of a fourth order polynomial suffices to capture the 3D effects. So, we assume

$$k_{eff}(z) = p_0 + p_1 z + p_2 z^2 + p_3 z^3 + p_4 z^4, \tag{4.11}$$

which has 5 unknown constants. To find these 5 constants, we also formulate 5 equations, which are integrals of the force equilibrium Eq. 4.6.

For the first integral, we want the global force balance to hold over the full length of the pile. Taking the integral of the equilibrium equation gives

$$EI\frac{d^3u}{dz^3}\Big|_{z_f^{(1)}}^{z_f^{(2)}} + \int_{z_f^{(1)}}^{z_f^{(2)}} k_{eff}(z)u(z)dz - \frac{EI}{GA\kappa}\Big(\frac{dk_{eff}(z)}{dz}u(z) + k_{eff}(z)\frac{du(z)}{dz}\Big)\Big|_{z_f^{(1)}}^{z_f^{(2)}} = 0, \tag{4.12}$$

in which $z_f^{(1)}$ and $z_f^{(2)}$ are the integration boundaries (subscript "f" indicating a force equilibrium and superscripts "(1)"/"(2)" for a lower or upper integration bound), having values $z_f^{(1)} = 0$ and $z_f^{(2)} = L$ for the global integral 1. We also aim to match the global overturning moment. This can be achieved by multiplying Eq. 4.6 by z and again

integrating over the beam length. Doing so, yields integral 2:

$$zEI\frac{d^3u}{dz^3}\Big|_{z_m^{(1)}}^{z_m^{(2)}} - EI\frac{d^2u}{dz^2}\Big|_{z_m^{(1)}}^{z_m^{(2)}} + \int_{z_m^{(1)}}^{z_m^{(2)}} zk_{eff}(z)u(z)dz - \frac{EI}{GA\kappa}\Big(z\Big(\frac{dk_{eff}(z)}{dz}u(z) + k_{eff}(z)\frac{du(z)}{dz}\Big) - k_{eff}(z)u(z)\Big)\Big|_{z_m^{(1)}}^{z_m^{(2)}} = 0. \quad (4.13)$$

For the global moment equilibrium integral 2, $z_m^{(1)} = 0$ and $z_m^{(2)} = L$ (subscript "m" stands for moment).

We now have 2 equations, so 3 more equations are needed to obtain a square system of equations to solve for the 5 unknowns. To establish these, we take the same integrals, but we now focus on equilibria of parts of the beam: a local force equilibrium and 2 local moment equilibria. As we do not yet know which parts of the beam we should focus on to get the best solution (match), we leave the integration limits unknown. We find the solution by sweeping the upper and lower limits of the integrals in steps ΔL and checking which combination gives the optimal $k_{eff}(z)$. The local "force" integral focuses on the upper part of the pile (by sweeping the integration limits $z_{f,t}^{(1)}$ and $z_{f,t}^{(2)}$ ("f,t": force, top) from 0 to $L-\Delta L$). As for the local "moment" integrals, one focuses on the upper and the other one focuses on the lower part of the pile (from L down to $0+\Delta L$). So, the third integral is given by Eq. 4.12, however, with integration limits that are swept starting from the top:

$$\begin{aligned} z_{f,t}^{(1)} &= 0 \;..\; \Delta L \;..\; (L-2\Delta L), \\ z_{f,t}^{(2)} &= (z_{f,t}^{(1)} + \Delta L) \;..\; \Delta L \;..\; (L-\Delta L). \end{aligned} \quad (4.14)$$

Similarly, the fourth integral, given by Eq. 4.13, focuses on the equilibrium of moments at the top of the pile by sweeping the integration limits in the following way:

$$\begin{aligned} z_{m,t}^{(1)} &= 0 \;..\; \Delta L \;..\; (L-2\Delta L), \\ z_{m,t}^{(2)} &= (z_{m,t}^{(1)} + \Delta L) \;..\; \Delta L \;..\; (L-\Delta L). \end{aligned} \quad (4.15)$$

Finally, the fifth integral, also given by Eq. 4.13, focuses on the equilibrium of moments at the bottom of the pile by sweeping the integration limits as:

$$\begin{aligned} z_{m,b}^{(2)} &= L \;..\; -\Delta L \;..\; 2\Delta L, \\ z_{m,b}^{(1)} &= z_{m,b}^{(2)} - \Delta L \;..\; -\Delta L \;..\; \Delta L. \end{aligned} \quad (4.16)$$

So, in total 6 integration limits (3 local integrals with 2 integration limits each) are swept with steps of ΔL. Note that a linear system of equations is solved for each combination of the integration bounds, giving a unique solution for $k_{eff}(z)$. Of these solutions, only the positive definite stiffness profiles are considered for calculating the corresponding deflection and rotation shapes using the 1D Timoshenko model.

Subsequently, we judge the quality of the solutions and select the optimal one. Depending on the end goal of the analysis, the definition of the optimum might differ. For instance, a full match in bending moment for all depths with respect to the 3D model might be preferred instead of exactly matching the displacement and rotation at mudline. Here, we assess the quality of the solution based on a the fit for the deflection u, the slope $\frac{du}{dz}$ (or u'), the rotation ψ and curvature ψ' of the 1D model with respect to those of the 3D model for all depths. Obviously, such a misfit function can be tailored to the purpose of the user. We define the misfit as

$$\begin{aligned} C_{u,u',\psi,\psi'} \quad &= C_u + C_{u'} + C_\psi + C_{\psi'} = \\ &\frac{\sum_{i=0}^{i=L} |u_{i,1\mathrm{D}} - u_{i,3\mathrm{D}}|}{4\sum_{i=0}^{i=L} |u_{i,3\mathrm{D}}|} + \frac{\sum_{i=0}^{i=L} |u'_{i,1\mathrm{D}} - u'_{i,3\mathrm{D}}|}{4\sum_{i=0}^{i=L} |u'_{i,3\mathrm{D}}|} + \\ &\frac{\sum_{i=0}^{i=L} |\psi_{i,1\mathrm{D}} - \psi_{i,3\mathrm{D}}|}{4\sum_{i=0}^{i=L} |\psi_{i,3\mathrm{D}}|} + \frac{\sum_{i=0}^{i=L} |\psi'_{i,1\mathrm{D}} - \psi'_{i,3\mathrm{D}}|}{4\sum_{i=0}^{i=L} |\psi'_{i,3\mathrm{D}}|}. \end{aligned} \tag{4.17}$$

4.2.2. STATIC RESPONSE

In this section we will evaluate the results retrieved for the static SSI for MP20 and MP45, and also discuss the misfits obtained for the other 3 SSI cases given in Table 4.1.

MP20

For MP20, we obtained satisfactory results by sweeping the 6 integration bounds with steps of $\Delta L = L/15 = 2.13$ m. Fig. 4.4 shows the resulting 1D effective initial stiffness $k_{eff}(z)$, which now incorporates 3D effects and true small-strain reaction properties. For comparison, the initial stiffness as determined with the p-y curve method is shown in the same figure, together with the Young's profile of Fig. 4.2. We can see that the 3D and 1D stiffness profiles share some shape characteristics. However, note that the effective stiffness $k_{eff}(z)$ is a true SSI-parameter; it incorporates both the geometry of the pile, the properties of the soil and the properties of their interface. The shape of $k_{eff}(z)$ can therefore not be one-to-one related to the shape of profiles of (pure) soil-stiffness parameters. As the p-y method should be used for flexible piles that evoke a more local behaviour of the soil, the p-y initial stiffness will more closely follow the pure soil-stiffness profile than our presented $k_{eff}(z)$; the p-y initial stiffness is independent of the geometry of the structure. In Fig. 4.4, we see that a somewhat larger stiffness $k_{eff}(z)$ is mobilized at the upper two-third part of the pile. The weaker soil layer between 13m and 20m depth is - due to a combination of relatively constant shear-wave velocity and 3D effects - not as dominantly present in the effective stiffness as in the p-y stiffness. We also note that at mudline $k_{eff}(z)$ is not zero. The higher stiffness in the shallow region can reflect the phenomenon that was already mentioned in Section 1.2.1: an underestimation of the shallow-depth stiffness. The stiffness of the upper layers of the soil profile has a dominant influence on the displacement of the pile and the natural frequency of the structure.

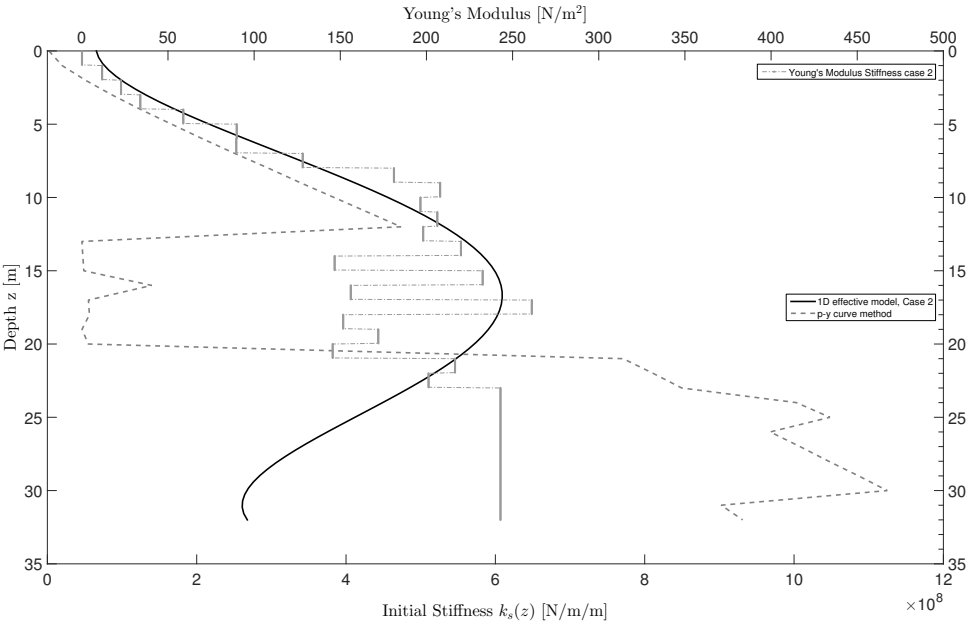

Figure 4.4: The effective $k_{eff}(z)$ of MP20, found for a pile loaded with an overturning moment/horizontal force ratio of 90 m at mudline (black solid line). This initial stiffness $k_{eff}(z)$ incorporates 3D modelling effects, and in-situ seismic small strain characterisation of the soil. As a reference, the p-y curve initial stiffness is given by the grey dashed line. Also the Young's profile which was input for the 3D model, is plotted as a reference (grey dashed-dotted line).

The resulting displacement u, slope u', rotation ψ and curvature ψ' profiles and the fits with the corresponding 3D responses are given in Fig. 4.5. As a reference, the responses of the same beam model on the p-y curve initial stiffness is also displayed. We observe that, similar to what was seen in Fig. 3.2, a stiffer response of the small-strain 3D model (and of the 1D effective models) compared to the p-y curve method. Also, the location of the maximum bending moment (reflected by the curvature ψ' shown in the most right panel of Fig. 4.5) as determined with the p-y curve method is located a couple of meters below that of the 3D model. This disparity is caused by the difference in shallow-layer stiffness between the methods (indicated also in Fig. 4.4). The maximum bending moment of the 3D model is located just below the mudline.

The values of the misfit $C_{u,u',\psi,\psi'}$ and its separate components C_u, $C_{u'}$, C_ψ and $C_{\psi'}$ for the MP20 case are given in Table 4.2. To check the general applicability of this best solution (the effective $k_{eff}(z)$), four other loading cases were simulated in the 3D model. Firstly, a variation of around 10% increase and decrease of the 90 m effective lever arm of the loading for which the effective $k_{eff}(z)$ was inverted, and two more radical differences were evaluated; an effective lever arm of 45 (50% of the original target-shape loading), and a moment-only case. The quality of the fits of the 1D model, using the

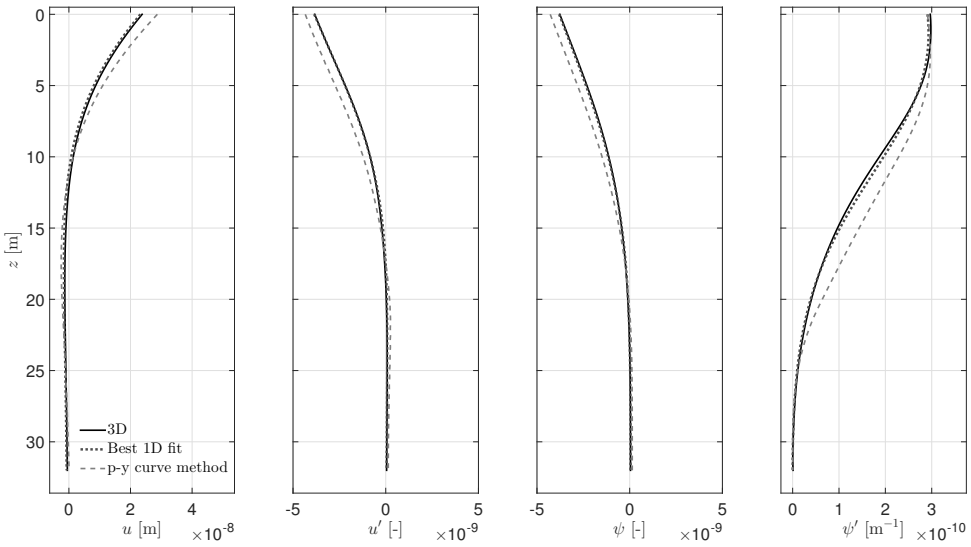

Figure 4.5: MP20: the displacement u, slope u', rotation ψ and curvature ψ' of a 1D Timoshenko beam with the found effective stiffness $k_{eff}(z)$ given in Fig. 4.4 caused by an overturning moment of 180 Nm and 2 N horizontal force at mudline (grey solid lines). The match with the 3D responses (black solid lines) is good. As a reference: the grey dashed lines are the responses of a Timoshenko beam with the initial stiffness derived from the p-y curve method (as also depicted in Fig. 4.4).

1D stiffness profile as presented in Fig. 4.4 with the 3D response of the other load cases was found to be equally satisfactory. As can be seen in Table 4.2, the misfit values for these other load cases are comparable with those obtained for the loading case for which the stiffness was identified.

	$C_{u,u',\psi,\psi'}$	C_u	$C_{u'}$	C_ψ	$C_{\psi'}$
M/F=90m (target)	0.0454	0.0269	0.0057	0.0057	0.0072
M/F=100m	0.0445	0.0260	0.0056	0.0057	0.0071
M/F=80m	0.0466	0.0280	0.0057	0.0056	0.0072
M/F=45m	0.0538	0.0348	0.0061	0.0055	0.0075
M=1 Nm, F=0 N	0.0351	0.0165	0.0058	0.0060	0.0068

Table 4.2: Misfit values (Eq. (4.17) of the best solution (the effective stiffness $k_{eff}(z)$ which yields the lowest value for $C_{u+u'+\psi+\psi'}$) for MP20. The table additionally includes the misfits for 4 other load cases for which the same effective stiffness profile was tested to be compatible.

From Table 4.2, we see that the cost of the fit of the displacement over the full length of the pile is 0.0269. This number should be multiplied by 4 to yield the percentage difference (see Eq. (4.17)): 10.76%. The overall rotations show a 2.28% difference, and the overall curvature (i.e. the correspondence in bending moment) difference is 2.88%. Similar matching efforts (although including rotational springs along the pile and at its base) yielded a difference in static displacement at the top of the pile of 14.0%, and a

difference in rotation at the same location of 8.7% [48]. If we also only consider the top of the pile, the mismatch in static deflection and rotation at this location is 2.40% and 0.88%, respectively.

MP45

The resulting effective stiffness $k_{eff}(z)$ for MP45, found with an integration limit step size of $\Delta L = L/15 = 1.60$ m, is shown in Fig. 4.6. For comparison, the p-y curve initial stiffness is shown in the same figure. The match in displacements, slopes, rotations and curvatures (bending) of a Timoshenko beam supported by the effective stiffness profile of Fig. 4.6 and those of the 3D model is shown in Fig. 4.7. Although the fit in terms of curvature can be improved, the match is satisfactory. As a reference, the responses of a 1D model with the p-y stiffness profile are also included (light grey dashed lines). The (static) effective stiffness profile of Fig. 4.6 will be used as an initial guess in a model-based analysis of the shaker measurements (Section 5.3).

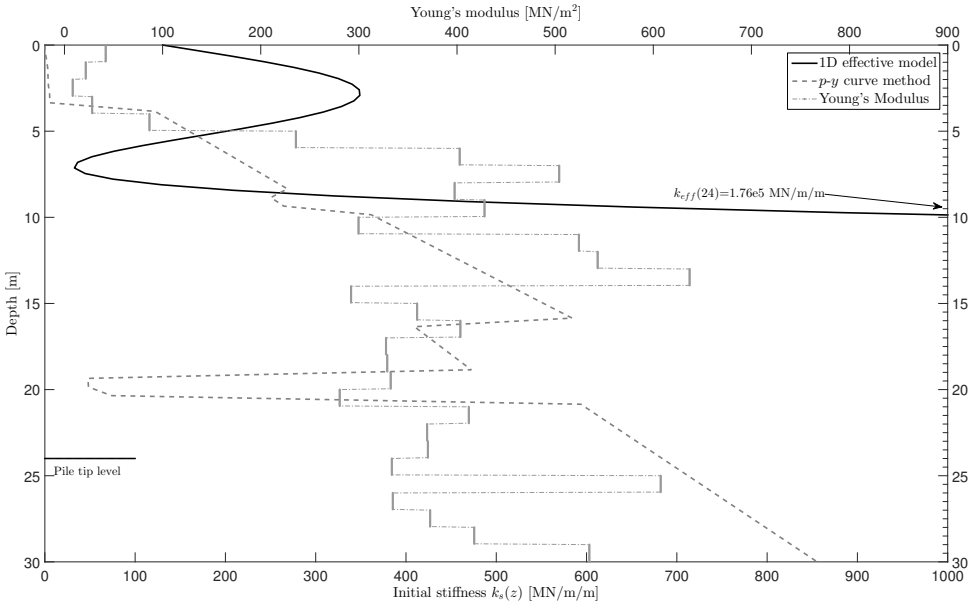

Figure 4.6: The effective $k_{eff}(z)$ (black solid line). This initial stiffness $k_{eff}(z)$ incorporates 3D modelling effects and small-strain elastic properties of the soil obtained using in-situ seismic measurements. As a reference, the p-y curve initial stiffness is given by the grey dashed line. The Young's profile which was input for the 3D model, is included as a reference (grey dashed-dotted line).

The misfit values for MP45 are given in Table 4.3. Although these misfits are considered satisfactory, we conclude that the overall fit is of lower quality than obtained for MP20; $C_{u,u',\psi,\psi'}$ is higher than obtained for the target solution of MP20 (Table 4.2). The poorer result for MP45 is expected to be related to the lower L/D ratio of this pile (L/D=4.8) with respect to that of MP20 (L/D=6.4) and the lower relative pile stiffness

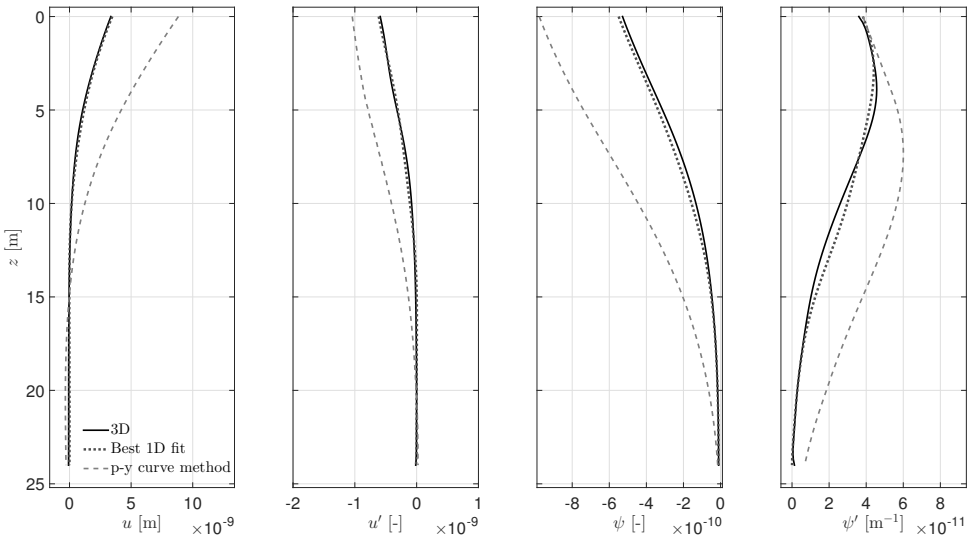

Figure 4.7: MP45: the displacement u, slope u', rotation ψ and curvature ψ' of a 1D Timoshenko beam supported by the effective Winkler profile (Fig. 4.6), compared with the original 3D linear elastic model. As a reference, these 4 quantities for a Timoshenko beam supported by the initial stiffness derived by the p-y curve method are displayed by the grey dashed line. The 3D model was loaded with a horizontal force of 1 N, and overturning moment of 9.85 Nm. The 1D beam models were loaded with double this loading (2 N and 19.70 Nm) since only half of the symmetric problem was simulated in the 3D model.

K_r of MP20 compared to that of MP45 (Table 4.1 or Fig. 4.1) causing MP45 to behave more rigidly than MP20 - invoking more complex 3D reaction mechanisms of the soil. It becomes slightly more challenging to capture those 3D soil reactions with only local, uncoupled lateral springs; despite the fact that their distribution has an optimized shape ($k_{eff}(z)$).

	$C_{u,u',\psi,\psi'}$	C_u	$C_{u'}$	C_ψ	$C_{\psi'}$
MP45	0.0723	0.0184	0.0247	0.0096	0.0197

Table 4.3: Misfit values (Eq. 4.17) of the best solution (the effective stiffness $k_{eff}(z)$ which yields the lowest value for $C_{u+u'+\psi+\psi'}$) for MP45.

OTHER SSI CASES

To further test the performance of the translation method in relation with the relative pile stiffness K_r (Eq. 4.1) and the L/D ratio, the effective stiffness profiles of the 3 other SSI cases (the Short-stiff, Short-soft and Caisson case, see Fig. 4.1 and Table 4.1) were also calculated. The misfits for these 3 cases are listed in Table 4.4, in which for convenience the misfits found for MP20 and MP45 are repeated. The misfits are higher than obtained for the MP20 and MP45 cases, however, no clear relation can be

observed between the performance of the method (misfits) and the flexibility factors. According to the definition of the relative pile stiffness, the Short-stiff case is a flexible pile, and the Short-soft case a rigid one. Although the uncoupled Winkler model is expected to better handle flexible piles, the local translation method yields lower misfit values (a better performance) for the supposedly rigid Short-soft case. Additionally, $C_{u+u'+\psi+\psi'}$ for the Caisson case is the lowest of the lower three extra cases presented in Table 4.4, while it is a less flexible pile than the Short-stiff pile. On the other hand, one could argue that the expected trend of larger misfits with higher relative pile stiffness K_r exists, but that the Short-stiff pile is an outlier. A closer look at the expected relation between the performance (values for $C_{u+u'+\psi+\psi'}$) and the L/D ratio of the 5 presented cases reveals a similar relation; in general, lower performance of the method is observed for lower L/D ratios, however, the Caisson case does not follow that trend. A lower misfit is obtained for the Caisson case than for the Short-soft case. Also these 3 extra cases were evaluated by choosing an integration limit step size ΔL (Eqs. 4.14 - 4.16) of $L/15$, yielding different quantitative values but an equal relative size to the embedment length L.

	K_r	L/D	$C_{u,u',\psi,\psi'}$	C_u	$C_{u'}$	C_ψ	$C_{\psi'}$
MP20	0.0033	6.4	0.0454	0.0269	0.0057	0.0057	0.0072
MP45	0.0047	4.8	0.0723	0.0184	0.0247	0.0096	0.0197
Short-soft	0.6437	3.0	0.2324	0.0591	0.0738	0.0733	0.0262
Short-stiff	0.0013	3.0	0.5239	0.0598	0.0596	0.2988	0.1057
Caisson	0.0362	2.0	0.1880	0.0533	0.0426	0.0738	0.0183

Table 4.4: Misfit values (Eq. 4.17) of the best solutions (the effective stiffness $k_{eff}(z)$ which yields the lowest value for $C_{u+u'+\psi+\psi'}$) for the 5 cases listed in Table 4.1 and shown in Fig. 4.1. The step size ΔL of the integration boundaries for the local force and moment integrals were set to $L/15$, resulting in $\Delta L = 2.13$ m and $\Delta L = 1.60$ m for respectively MP20 and MP45, $\Delta L = 2.00$ m for the Short-soft and Short-stiff piles and $\Delta L = 1.33$ m for the Caisson pile.

Finally, the influence of the shape of the stiffness profile, in terms of a smooth versus an irregular Young's modulus profile, was evaluated by considering a smoother, more averaged version of the SCPT45 profile (Fig. discussed in Chapter 5) for MP45. The slightly improved results for that case ($C_{u,u',\psi,\psi'} = 0.0668$) confirm the expectation that the method can better handle a smoother profile - in line with the continuous shape of the fourth order polynomial that is assumed for $k_{eff}(z)$ (Eq. 4.11).

4.2.3. DYNAMIC RESPONSE

An evident consecutive step after having identified the static effective stiffness, is aiming to match also the dynamic 3D SSI by searching for the effective 1D damping profile $c_{eff}(z)$. In doing so, we first identify the static effective stiffness $k_{eff}(z)$, and subsequently search for $c_{eff}(z)$ so that the 1D model also matches the imaginary part of the complex-valued response of the 3D model for relatively low, quasi-static excitation frequencies between 0 and 0.5 Hz.

Applying the local methodology, we assume the following equations of motion of a Timoshenko beam on Winkler foundation:

$$GA\kappa\left(\frac{d^2u(z)}{dz^2} - \frac{d\psi(z)}{dz}\right) - K(z)u(z) = 0, \tag{4.18}$$

$$GA\kappa\left(\frac{du(z)}{dz} - \psi(z)\right) + EI\frac{d^2\psi(z)}{dz^2} + \omega^2\rho I\psi(z) = 0, \tag{4.19}$$

with

$$K(z) = k_{eff}(z) + \mathrm{i}c_{eff}(z)\mathrm{sgn}(\omega) - \omega^2\rho\mathrm{A}. \tag{4.20}$$

These equations of motion are similar to the static equilibrium equations (4.2 & 4.3), apart from the added lateral and rotary inertia terms ($\omega^2\rho A$ and $\omega^2\rho I$) and the damping term $\mathrm{i}c_{eff}(z)\mathrm{sgn}(\omega)$. The mass term ρA represents the distributed mass of the pile including the contained soil inside the pile. Since we introduced a frequency-independent material damping in the dynamic 3D model (Section 3.2), the 1D effective dashpots $c_{eff}(z)$ are also assumed frequency-independent, as can be seen in Eq. 4.20. Nevertheless, it must be noted that at higher excitation frequencies the presence of geometric damping becomes more pronounced, and such damping - being frequency dependent - is better modelled with viscous dashpots. As we will only consider the quasi-static response regime (low frequencies), it is expected that a frequency-independent $c_{eff}(z)$ will suffice. Additionally, being an effective damping, we should be able to find a certain value and shape for $c_{eff}(z)$ that covers both material and geometric damping.

Rewriting the equations of motions into a single equation (similar as was done for the static equilibrium equations), we obtain

$$EI\frac{d^4u(z)}{dz^4} + K(z)u(z) - \frac{EI}{GA\kappa}\frac{d^2(K(z)u(z))}{dz^2} + \omega^2\rho I\frac{d\psi(z)}{dz} = 0, \tag{4.21}$$

for which we again formulate a force balance by taking the integral and substituting Eq. 4.20 for the dynamic stiffness (omitting the $\mathrm{sgn}(\omega)$ term for convenience; we assume

positive frequencies):

$$\int_{z_f^{(1)}}^{z_f^{(2)}} c_{eff}(z)u(z)dz - \frac{EI}{GA\kappa}\Big(\frac{dc_{eff}(z)}{dz}u(z) + c_{eff}(z)\frac{du(z)}{dz}\Big)\Big|_{z_f^{(1)}}^{z_f^{(2)}} =$$
$$\mathrm{i}^{-1}\Big[-EI\frac{d^3u}{dz^3}\Big|_{z_f^{(1)}}^{z_f^{(2)}} - \omega^2\rho I\psi\Big|_{z_f^{(1)}}^{z_f^{(2)}}$$
$$+\frac{EI}{GA\kappa}\Big(\frac{dk_{eff}(z)}{dz}u(z) + k_{eff}(z)\frac{du(z)}{dz} - \omega^2\rho A\frac{du}{dz}\Big)\Big|_{z_f^{(1)}}^{z_f^{(2)}} - \int_{z_f^{(1)}}^{z_f^{(2)}}(k_{eff}(z) - \omega^2\rho A)u(z)dz\Big], \tag{4.22}$$

and a balance of moments by multiplying Eq. 4.21 by z and taking the integral:

$$\int_{z_m^{(1)}}^{z_m^{(2)}} c_{eff}(z)u(z)zdz - \frac{EI}{GA\kappa}\int_{z_m^{(1)}}^{z_m^{(2)}}\frac{d^2(c_{eff}(z)u(z))}{dz^2}zdz =$$
$$\mathrm{i}^{-1}\Big[-EI\Big(\frac{d^3u}{dz^3}z\Big|_{z_m^{(1)}}^{z_m^{(2)}} - \int_{z_m^{(1)}}^{z_m^{(2)}}\frac{d^3u}{dz^3}dz\Big) - \omega^2\rho I\Big(z\psi(z)\Big|_{z_m^{(1)}}^{z_m^{(2)}} - \int_{z_m^{(1)}}^{z_m^{(2)}}\psi(z)dz\Big)$$
$$+\frac{EI}{GA\kappa}\Big(\frac{d(k_{eff}(z)u(z))}{dz}z\Big|_{z_m^{(1)}}^{z_m^{(2)}} - \int_{z_m^{(1)}}^{z_m^{(2)}}\frac{d(k_{eff}(z)u(z))}{dz}dz\Big)$$
$$-\frac{\omega^2\rho AEI}{GA\kappa}\Big(\frac{du}{dz}z\Big|_{z_m^{(1)}}^{z_m^{(2)}} - u(z)\Big|_{z_m^{(1)}}^{z_m^{(2)}}\Big) - \int_{z_m^{(1)}}^{z_m^{(2)}}(k_{eff}(z) - \omega^2\rho A)u(z)zdz\Big]. \tag{4.23}$$

We assume a real-valued $c_{eff}(z)$, and therefore only consider the real parts of Eqs. 4.22 & 4.23. Taking the real parts of these equations yields better results than considering the imaginary parts, as the imaginary parts relate more to the stiffness terms $k_{eff}(z)$, and the real parts to the damping $c_{eff}(z)$. Moreover, note that in the above equations a frequency dependence of the damping $c_{eff}(z)$ is introduced through the inertial terms. Nevertheless, as the inertial terms for quasi-static excitation frequencies will remain small compared to the stiffness terms, the frequency dependence of $c_{eff}(z)$ will be only minor.

Similar as for $k_{eff}(z)$, we assume a fourth order polynomial for $c_{eff}(z)$, and therefore formulate 5 equations by considering 2 global integrals (over the full length of the pile) and 3 local integrals of which the optimal set of integration limits are sought for by sweeping them with steps ΔL.

Fig. 4.8 shows the fits between the complex-valued response of the 3D and 1D effective models for MP45 at an excitation frequency of 0.1 Hz. The misfits listed in the panels are calculated using Eq. 4.17 for the imaginary ($C_{\mathrm{Im}(..)}$) and the real ($C_{\mathrm{Re}(..)}$) parts of the response separately. In the left panel of Fig. 4.9 the associated $c_{eff}(z)$ and $k_{eff}(z)$ are displayed, which were both found with an integration limit step size of $\Delta L = 1.60$ m. The best $c_{eff}(z)$ is the damping profile that yields the lowest misfit for $C_{u,u',\psi,\psi'}$ according to Eq. 4.17 using the complex-valued responses. As a sidenote it is remarked

that the $k_{eff}(z)$ for MP45 presented in Fig. 4.9 is not equal to the one presented in Fig. 4.6; slightly different assumptions were made regarding the Poisson's ratio and scour depth in defining the input soil parameters to the 3D model. The version presented in the current section serves merely to present the dynamic results of the local method, whereas $k_{eff}(z)$ in Fig. 4.6 is deemed most realistic and is used for the experimental validation discussed in Chapter 5. The presented solution for $c_{eff}(z)$ yields the lowest misfit (Eq. 4.17), when considering the complex-valued response.

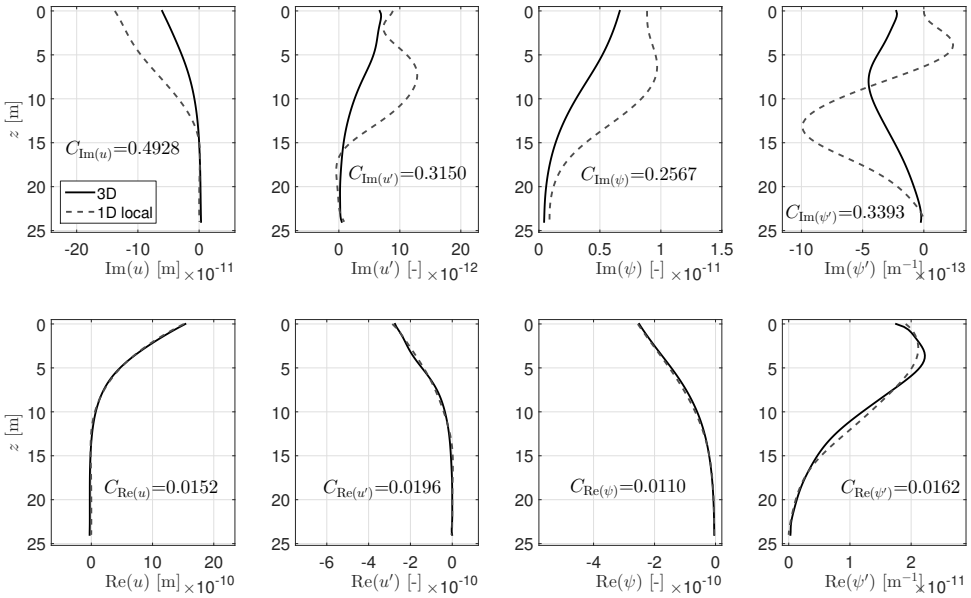

Figure 4.8: Comparison between effective 1D solution retrieved with the local method and the 3D solution for MP45. The applied excitation is a harmonic force of $F = 1$ N and overturning moment $M = 9.85$ Nm at a frequency of $f = 0.1$ Hz.

From Fig. 4.8 we observe that the fit of the imaginary parts of the solution are not satisfactory. It is expected that this is related to the sensitivity of the complex-valued response to the static stiffness $k_{eff}(z)$; the misfit of the static response due to a small error in $k_{eff}(z)$ - or the misfit of the real part of the dynamic response at a low excitation frequency - will lead to a relatively larger misfit in the imaginary part of the complex valued dynamic response.

To test the previous statement on error amplification, a comparison is shown in Fig. 4.10 of two 1D models that have equal $c_{eff}(z)$, but a slightly different $k_{eff}(z)$; the 'estimated' $k_{eff}(z)$ model is given a stiffness profile with an arbitrary error of maximum 20% on a 'true' stiffness profile. We observe that indeed the misfit in the real part of the response is amplified towards more than twice as large a misfit of the imaginary part of the response - despite that fact that the damping profiles are the same.

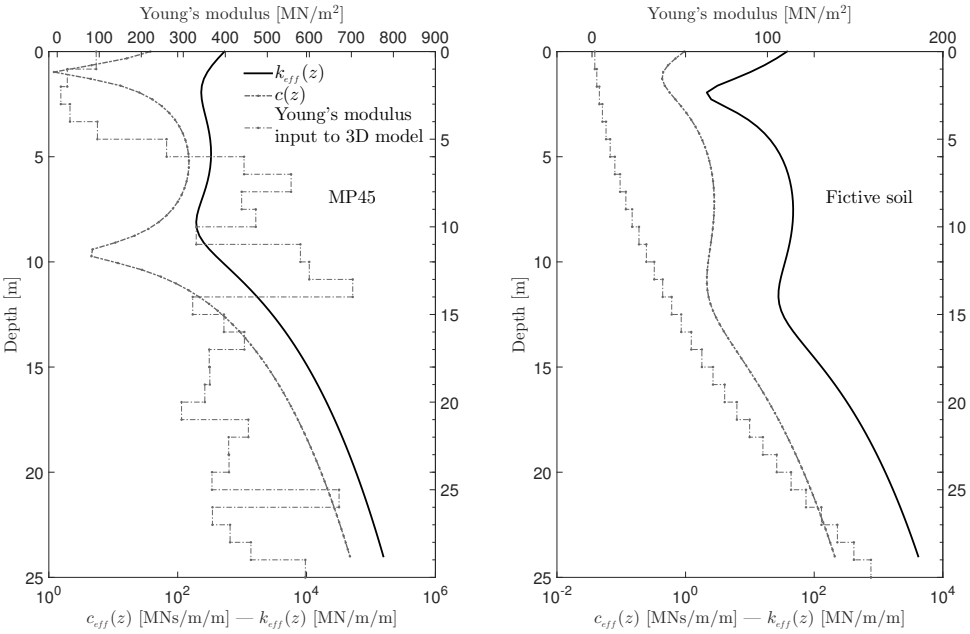

Figure 4.9: Resulting $c_{eff}(z)$ and $k_{eff}(z)$ profiles and the Young's modulus profile that was used in the 3D model for MP45 (left panel) and for the same pile but in a fictive, softer and more smooth profile (right panel).

MP45 could be a too challenging case for finding an effective local dynamic stiffness in the form of distributed $c_{eff}(z)$ and $k_{eff}(z)$, as the error in $k_{eff}(z)$ amplifies the misfits of the imaginary parts of the response. To see if a softer and more smooth soil profile might yield improved results, the same pile (MP45) was simulated as embedded in a fictive soil profile, of which the Young's modulus is shown in the right panel of Fig. 4.9. The obtained $k_{eff}(z)$ and $c_{eff}(z)$ (using a similar integration limit step size of $\Delta L = 1.60$ m and at an excitation frequency of 0.1 Hz) for the fictive soil case are shown in the same panel. The resulting match in response of the 3D and 1D effective model is shown in Fig. 4.11. We observe that the quality of the fit is significantly better than obtained for MP45 embedded in the stiffer, more irregular profile obtained from SCPT45 (left panel of Fig. 4.9). The real parts match better, resulting in also a lower mismatch for the imaginary parts of the response. The derivatives of the response (u' and ψ') nevertheless still yield a somewhat poor match.

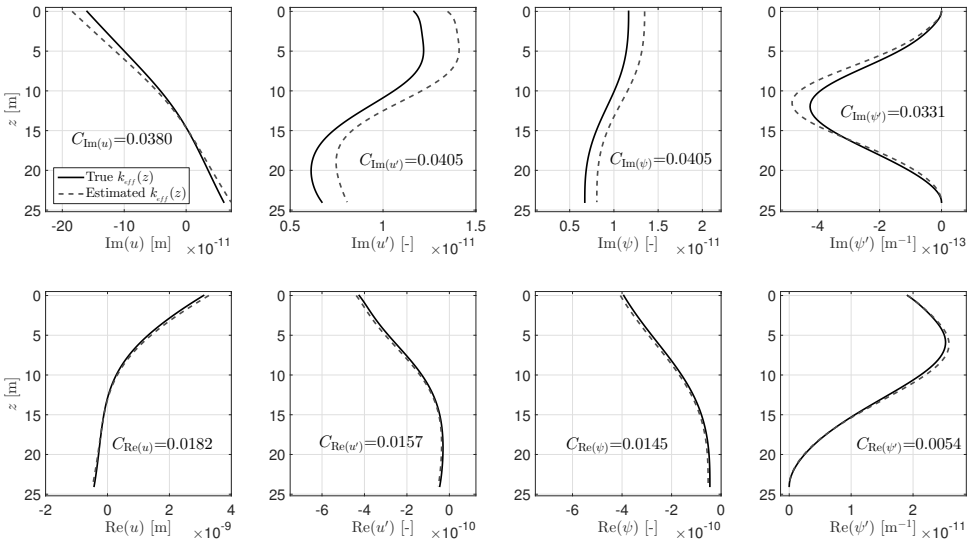

Figure 4.10: An example showing the high sensitivity of the imaginary part of the response to (an error in) the stiffness $k_{eff}(z)$. The two presented models have an equal damping profile $c_{eff}(z)$, however, the 'estimated' $k_{eff}(z)$ model contains a random error of maximum 20% on the 'true' $k_{eff}(z)$. The applied excitation is a harmonic force of $F = 1$ N and overturning moment $M = 9.85$ Nm at a frequency of $f = 0.1$ Hz.

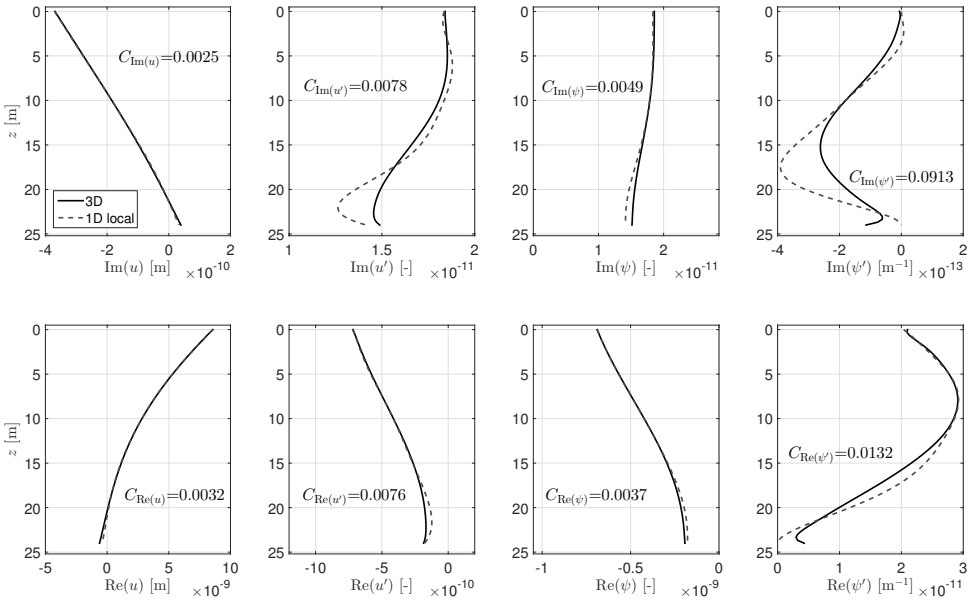

Figure 4.11: Comparison between 1D local and 3D solution for the same pile as MP45, but embedded in a fictive, smoother soil profile with linearly increasing stiffness, shown in the right panel of Fig. 4.9. The excitation force is $F = 1$ N and overturning moment $M = 9.85$ Nm at a frequency of $f = 0.1$ Hz.

4.2.4. DISCUSSION

In this section 4.2, a novel technique was presented to translate 3D soil-pile model into a 1D effective model that adequately matches the original 3D simulated response. Less satisfying results seem to be obtained for lower L/D ratios, or more generally speaking, for SSI cases in which more complex, global soil reaction mechanisms are substantially invoked. To further test the performance of the local translation method in relation to the L/D ratio and the relative pile stiffness K_r (Eq. 4.1), the 1D effective stiffness $k_{eff}(z)$ was additionally calculated for three other SSI cases having a lower L/D ratio and generally higher relative pile stiffness (the Short-stiff, Short-soft and Caisson case, see Fig. 4.1 and Table 4.1). The misfits for these three cases (Table 4.4) are higher than obtained for the MP20 and MP45 cases, however, no clear relation is observed between the performance of the method (misfit) and the relative pile stiffness K_r nor the L/D ratio. The expected trend of lower performance of the method for lower L/D ratio and higher K_r seems to be there, but exceptions exist. Finally, the method was found to yield improved results for a more smooth stiffness profile (as input to the 3D model) than for an irregular profile. This is aligned with the expectation that, due to the continuous and smooth shape of the fourth-order polynomial assumed for $k_{eff}(z)$, a better-fit 1D solution can be found for a smoother stiffness profile in the 3D model.

Altogether, the unpredictability of the outcome of the local translation method can be considered a disadvantage. Furthermore, the involved optimisation step makes the method quite computationally expensive. The sweeping of the integration limits (Eqs. 4.14 - 4.16) is essentially a scan of the entire solution space. Most computational time is related to simulating the 1D beam solution for an obtained positive definite solution for $k_{eff}(z)$. For instance, finding the best $k_{eff}(z)$ for MP45 (Figs. 4.6 and 4.7) takes about 17 hours on an Intel Xeon E5-2690, dual core 260 GHz, 12 GB RAM, obtaining roughly 850.000 positive definite solutions for $k_{eff}(z)$. A smarter optimisation could decrease the computational effort. One could for instance acquire an a priori insight on the probable locations of the local force and moment integrals for the best solution of $k_{eff}(z)$.

A few improvements were considered, these were (amongst others) assuming a fifth-order polynomial for $k_{eff}(z)$, a polynomial with non-integer exponents (similar as is done in [128]), and the incorporation of distributed axial springs in addition to the lateral springs (incorporating the distributed bending moment contribution of the soil that is induced by shear forces on the pile wall acting at a considerable lever arm for large-diameter piles). However, none of these modifications significantly improved the performance of the technique.

Another discussion point involves the discrepancy between on one hand the numerical 3D FE output (in terms of $u(z)$ and $\psi(z)$), and on the other hand the more continuous, analytical assumptions in the 1D beam equations (Eqs. 4.2 and 4.3). As previously mentioned, it was found to be most practical to work with polynomial fits of the 3D numerical results. However, one could question whether it is best to set the target solution of the 1D model as close as possible to the 3D response (employing a high-order polynomial or using the 3D results directly, including the subsequent use of numeric

integration and differentiation in the translation method), or whether to expect that the beam displacements and rotations are rather smooth and hence fit a lower-order polynomial through the 3D target solutions - in line with the assumed polynomial for the stiffness profile $k_{eff}(z)$. The difference between the analytical and numerical results is largest at the boundaries. In fact, as previously mentioned, the 3D response will seldom comply with the boundary conditions as assumed for the free-free Winkler foundation (Eqs. 4.7 - 4.10); the shear force and overturning moment at the tip will not be nil, nor will the total internal forces and moments at the top be exactly equal to the externally imposed horizontal force and overturning moment. Residual forces and moments can be present at the boundaries, which could hence justify the implementation of discrete lateral and rotational springs at these locations in the 1D model. The apparent cause of this discrepancy is the fact that the 3D shell theory is not restricted to the simplifications applied in the 1D Timoshenko relations. The coefficients for such discrete springs at the boundaries are easily obtained by considering the residual forces and moments and the corresponding displacements and rotations in the 3D model. In doing so, it was observed that these coefficients can sometimes (even) have a negative value. It was investigated whether the incorporation of discrete springs would improve the results for the MP20 and MP45 cases, however, their added value was not found to be significant; instead, it proved to be most effective to search for a single, optimized effective $k_{eff}(z)$ that yields a best match between the 1D and 3D modelled response - compensating for any discrepancies between these two models by optimising the shape of $k_{eff}(z)$. Nevertheless, further investigation into diminishing the effect of the discrepancy between the 1D and 3D pile models might improve the performance of the translation method for the more rigid soil-pile cases.

For the low-frequency dynamic case, it was shown that - after having found the static stiffness $k_{eff}(z)$ - we can obtain an effective damping (dashpot) profile $c_{eff}(z)$ that best matches the imaginary part of the complex valued 3D response, using a similar approach as for finding $k_{eff}(z)$. Obtaining a proper 1D effective dynamic stiffness (including both $k_{eff}(z)$ and $c_{eff}(z)$) for the MP45 case turned out to be more challenging due to the fairly high sensitivity of the imaginary part of the response to the stiffness profile $k_{eff}(z)$. The sensitivity of the imaginary part to the damping profile $c_{eff}(z)$ is overshadowed by its sensitivity to $k_{eff}(z)$, making it impossible to find a good $c_{eff}(z)$ without a proper $k_{eff}(z)$. This underlines the necessity of obtaining an adequate $k_{eff}(z)$, yielding a low misfit for the static case, before searching for the damping profile $c_{eff}(z)$. An $c_{eff}(z)$. An improved fit of both the real and imaginary parts of the 3D and 1D responses was obtained for a fictive soil case, having a softer, more smooth stiffness profile as input to the 3D model. In attempting to improve the method, it was investigated whether a larger weighting of the misfit of the imaginary part of the response leads to overall lower misfits. Furthermore, a simultaneous (as opposed to the described subsequential) inversion of both $k_{eff}(z)$ and $c_{eff}(z)$ employing respectively the real and imaginary parts of Eqs. 4.22 and 4.23 was investigated. Nonetheless, none of these attempts yielded improved results.

As a concluding remark we can state that the presented local technique has the advantage of being intuitive in involving basic mechanics through the well-known Winkler foundation with only uncoupled, lateral springs (the engineering community's preferred choice), and yields a better match of 1D and 3D responses than found in literature for linear elastic SSI. The method is relatively straightforward to implement, and the resulting effective 1D stiffness $k_{eff}(z)$ can be directly used in design tools. Nevertheless, an uncertainty exists in the quality of the output (fit with the 3D model); for challenging SSI cases involving substantial 3D, global soil reaction, the uncoupled lateral springs $k_{eff}(z)$ in the 1D target model no longer suffice. As the imaginary part of the complex-valued response for the low-frequency dynamic case is sensitive to an error in the estimated $k_{eff}(z)$, the local translation method yields yet higher misfit values for the dynamic SSI of soil-pile systems with significant non-local soil reaction mechanisms.

A more versatile technique that can capture both the static and dynamic 3D SSI of a wide range of soil-pile systems in a 1D effective model, is discussed in the next section, where a *non-local* translation method is introduced.

4.3. NON-LOCAL METHOD

This section introduces a method to obtain a 1D effective model that accurately incorporates the fully coupled, non-local soil reaction over the entire embedment length of the pile. The method will be shown to be fast in its application (excluding the need of optimisation) and to be applicable to a wide range of SSI systems due to the incorporation of realistic 3D soil reactions in the 1D model. The non-local stiffness method comprises two steps. First, global stiffness kernels need to be extracted from the 3D continuum (Section 4.3.2), and second, these stiffness kernels need to be integrated in the 1D beam model (Section 4.3.3). Any type of solution method can be used to solve the problems associated with the non-local stiffness method; it may be a semi-analytical solution approach, or a numerical one using, for instance, finite elements. In the current work, the continuum is modelled with finite elements, and the governing equations of the 1D integrated beam model (discussed in the next section) are solved using the finite difference (FD) method. The performance of the method is showcased by matching both the static (Section 4.3.4) and the dynamic (Section 4.3.5) responses for MP45, the Short-stiff, the Short-soft and the Caisson case.

4.3.1. GOVERNING EQUATIONS OF THE 1D MODEL

Similar to the local method, we use the Timoshenko beam on a distributed, Winkler-type foundation model as the basis for the 1D effective model. The equilibrium equations for the local, static model read:

$$GA\kappa\left(\frac{d^2u(z)}{dz^2} - \frac{d\psi(z)}{dz}\right) - f(z,u,\psi) = 0, \tag{4.24}$$

$$GA\kappa\left(\frac{du(z)}{dz} - \psi(z)\right) + EI\frac{d^2\psi(z)}{dz^2} - m(z,u,\psi) = 0, \tag{4.25}$$

where Eq. 4.24 describes the balance of lateral forces, and Eq. 4.25 describes the balance of bending moments. In these equations, $f(z,u,\psi)$ and $m(z,u,\psi)$ are respectively the distributed restoring force and moment of the soil. The sign convention of the 1D model is equal to that used for the local method, and is given in Fig. 4.3, in which the conventional case is shown where $f(z,u,\psi)$ reduces to $f(z,u)$ and equals $k_{eff}(z)u$, and $m(z,u,\psi) = 0$. Also, the same boundary conditions are assumed as for the local method:

$$GA\kappa(\frac{du}{dz} - \psi)\Big|_{z=0} = -F, \tag{4.26}$$

$$EI\frac{d\psi}{dz}\Big|_{z=0} = M, \tag{4.27}$$

$$GA\kappa(\frac{du}{dz} - \psi)\Big|_{z=L} = 0, \tag{4.28}$$

$$EI\frac{d\psi}{dz}\Big|_{z=L} = 0. \tag{4.29}$$

Introducing the non-local stiffness operator, the restoring force term $f(z,u,\psi)$ in the force equilibrium, Eq. 4.24, becomes an integral:

$$GA\kappa\left(\frac{d^2u(z)}{dz^2} - \frac{d\psi(z)}{dz}\right) - \int_0^L K^{\mathrm{u,u}}(z,\overline{z})u(\overline{z})d\overline{z} = 0, \tag{4.30}$$

signifying that the lateral restoring force of the soil on the pile at a location z is the product of the displacement of the pile $u(z)$ and stiffness of the soil $K^{u,u}(z,\overline{z}=z)$ at that particular location (similar as in the local approach), *and* of the pile displacements $u(\overline{z})$ and stiffness of the soil $K^{u,u}(z,\overline{z})$ at all other locations along the pile; the latter are the non-local contributions. Note that although the integral in Eq. 4.30 only covers the domain of the pile (from 0 to L), the forces exerted on the pile are the reaction of the continuum as a whole (which extends beyond $z=L$). This is implicit in the stiffness kernel; $K^{u,u}(z,\overline{z})$ is derived based on the 3D reaction of the entire medium (as will be described in Section 4.3.2).

Incorporating also other continuum-related effects like the rotational stiffness $K^{\psi,\psi}$ and the stiffness operators for coupling the lateral stiffness with rotations $K^{u,\psi}$ and vice versa $K^{\psi,u}$, we get

$$GA\kappa\Big(\frac{d^2u(z)}{dz^2}-\frac{d\psi(z)}{dz}\Big)-\int_0^L K^{u,u}(z,\overline{z})u(\overline{z})d\overline{z}-\int_0^L K^{u,\psi}(z,\overline{z})\psi(\overline{z})d\overline{z} \quad =0, \tag{4.31}$$

$$GA\kappa\Big(\frac{du(z)}{dz}-\psi(z)\Big)+EI\frac{d^2\psi(z)}{dz^2}-\int_0^L K^{\psi,\psi}(z,\overline{z})\psi(\overline{z})d\overline{z}-\int_0^L K^{\psi,u}(z,\overline{z})u(\overline{z})d\overline{z} \quad =0 \tag{4.32}$$

The next section explains how to retrieve the global stiffness kernels $K(z,\overline{z})$ from a 3D FE continuum model, and Section 4.3.3 elaborates on implementing these terms in a FD scheme for solving the 1D governing equations (Eqs. 4.31 and 4.32).

4.3.2. EXTRACTING THE 3D CONTINUUM REACTION

For modelling the reaction of the 3D stratified soil continuum, the previously described (Section 3.2) FE model was used. To extract the global stiffness kernels, the soil should be modelled including a cavity for the pile; no stiffness of the steel should be incorporated as the stiffness kernels should only represent the soil reaction. The stiffness of the pile in the 1D model is represented by the first term in Eq. 4.31 and the first two terms in Eq. 4.32. We refer to the space occupied by the pile as the 'cavity' in the 3D model; this is the space the steel of the pile would occupy if it were modelled. Furthermore, if the volume within the pile is to be modelled as only partly filled with soil, such a void needs to be created at this location in the 3D continuum. In the current work we will consider piles that are fully filled with soil. Fig. 4.12 shows the FE mesh of (part of) the soil domain, with a cavity for a pile that is fully filled with soil, with a vertical discretisation $h=0.5$ m and a 1 m soil layer thickness. When using a numerical solution method, the global stiffness kernels $(K^{u,u}(z,\overline{z}),..,K^{\psi,u}(z,\overline{z}))$ will be discretized into stiffness matrices of size $n\times n$, with n the amount of nodes employed to discretize the vertical axis of the 1D model. The terms of the stiffness matrices will depend on the properties of the soil and the diameter D of the pile. In this work, for ease of explanation, the 3D pile and adjacent soil (and consequently also the 1D model) have a regular mesh with fixed vertical discretisation size h. However, it is noted that the presented method can be generalized to any mesh shape.

The extraction of the lateral stiffness matrix $\mathbf{K}^{u,u}$ is straightforward. With reference to

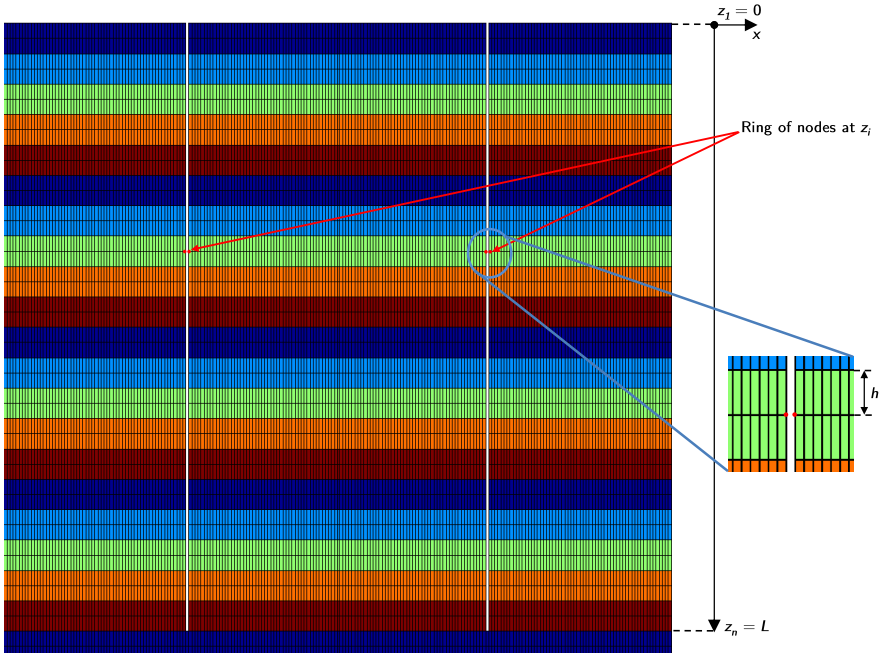

Figure 4.12: Example of the FE mesh, showing the cavity of a pile (with a diameter of 10 m and thickness of 0.1 m) that is fully filled with soil, with a vertical discretisation $h = 0.5$ m and 1 m soil layer thickness. Only part of the soil domain is shown.

Fig. 4.12, for every discrete depth z_i (with $i = 1,..,n$, and discretisation length h, the mudline at $z_1 = 0$ and pile tip at $z_n = L$), we displace the circumferential ring of nodes of the cavity surface with a certain displacement u_i in x-direction (see Fig. 4.3) and collect the sum of the nodal horizontal reaction forces at that ring, but also at all other vertically spaced rings, at depths $z_{j\neq i}$. We thus fill a matrix $\mathbf{F}_{\mathrm{x}}$ with column vectors $f_{x,j}$ being the reaction forces at depths z_j due to the displacements in the continuum at depths z_i. The prescribed displacements are collected in $\mathbf{U}$, which is a diagonal matrix. To be consistent with the integral of Eq. 4.31, we furthermore introduce an auxiliary matrix $\tilde{\mathbf{U}}$ which incorporates the Trapezium rule for integration:

$$\tilde{U}_{i,j} = \begin{cases} \frac{1}{2} h U_{i,j}, & \text{for } i = 1 \text{ and } i = n, \\ h U_{i,j}, & \text{otherwise.} \end{cases} \tag{4.33}$$

With these matrices known, we can readily compute the stiffness matrix $\mathbf{K}^{\mathrm{u,u}}$. To derive the stiffness matrix that can be used in the integral of Eq. 4.31, we write

$$\frac{1}{h} \begin{bmatrix} . & \uparrow & . \\ . & [f_{x,j}] & . \\ . & \downarrow & . \end{bmatrix} = \begin{bmatrix} & \mathbf{K}^{\mathrm{u,u}} & \end{bmatrix} \begin{bmatrix} \tilde{U}_{1,1} & 0 & 0 \\ 0 & \tilde{U}_{i,i} & 0 \\ 0 & 0 & \tilde{U}_{n,n} \end{bmatrix}. \tag{4.34}$$

Note that the unit of the lateral equilibrium forces (Eq. 4.30) is N/m, therefore, in Eq. 4.34, the nodal force matrix $\mathbf{F}_x$ is divided by the discretisation length h. Now we can readily find the stiffness matrix as

$$\mathbf{K}^{u,u} = \frac{\mathbf{F}_x \tilde{\mathbf{U}}^{-1}}{h}. \tag{4.35}$$

In a similar way, the rotational stiffness matrix $\mathbf{K}^{\psi,\psi}$ can be found by imposing a rotation ψ_i on the nodal rings along the circumference of the cavity surface, collecting the nodal reaction forces in vertical direction for all depths $f_{z,j}$, and thus form the matrix $\mathbf{F}_z$. The rotational stiffness relates the rotations to the distributed moment, so we incorporate the lever arm $D/2$ at which the vertical soil reaction forces act with respect to the central axis of the pile:

$$\mathbf{K}^{\psi,\psi} = \frac{D\mathbf{F}_z \tilde{\mathbf{\Psi}}^{-1}}{2h}, \tag{4.36}$$

in which $\tilde{\mathbf{\Psi}}$ is the matrix containing the imposed rotations, adjusted to incorporate the trapezium rule in a similar way as is done for the displacements (Eq. 4.33). Then, the coupling stiffness matrix for the lateral reaction to rotations of the nodal rings is found as

$$\mathbf{K}^{u,\psi} = \frac{\mathbf{F}_x \tilde{\mathbf{\Psi}}^{-1}}{h}, \tag{4.37}$$

and the coupling stiffness matrix for the rotational reaction to lateral displacements of the nodal rings as

$$\mathbf{K}^{\psi,u} = \frac{D\mathbf{F}_z \tilde{\mathbf{U}}^{-1}}{2h}. \tag{4.38}$$

Fig. 4.13 shows examples of the four stiffness matrices (Eqs. 4.35 - 4.38) for a cavity of 5 m diameter, thickness of 0.06 m, 25 m embedment length, modelled with an element length of $h = 0.25$ m, embedded in the stratified SCPT20 soil (Fig. 4.2). Note that the form of the diagonals of these matrices, quite well reflect the shape of the SCPT20 Young's modulus profile. $\mathbf{K}^{\psi,\psi}$ and $\mathbf{K}^{u,u}$ are symmetric matrices, whereas $\mathbf{K}^{\psi,u}$ and $\mathbf{K}^{u,\psi}$ have the following interrelation:

$$K^{\psi,u}_{i,j} = K^{u,\psi}_{j,i}. \tag{4.39}$$

It can be shown that this particular dependence is a direct consequence of the Maxwell-Betti reciprocal work theorem (e.g. [129]), or, for the dynamic case presented in Section 4.3.5, the elastodynamic source-receiver reciprocity relation (e.g. [130]).

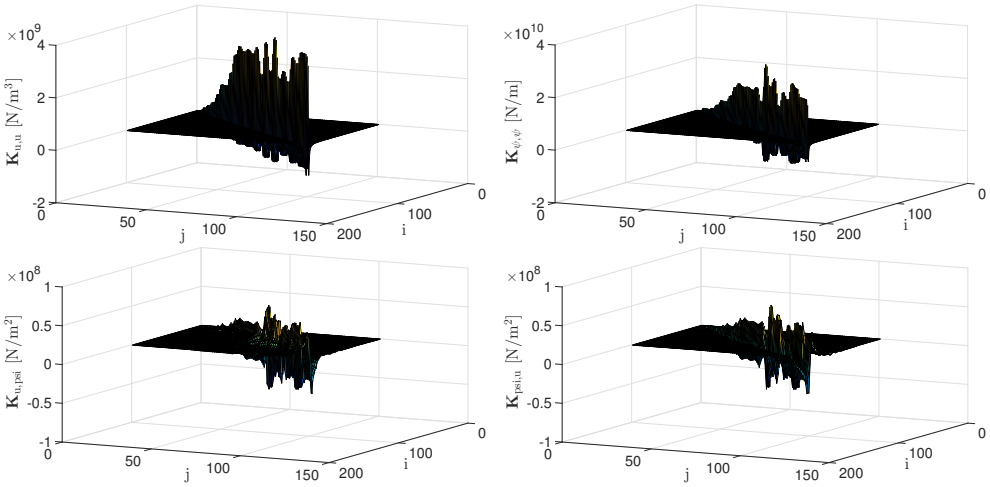

Figure 4.13: Example of $\mathbf{K}_{u,u}$, $\mathbf{K}_{\psi,\psi}$, $\mathbf{K}_{\psi,u}$ and $\mathbf{K}_{u,\psi}$, shown in a clockwise order. The cavity has a length of 25 m, a diameter of 5 m and was discretized with h=0.25 m. The soil profile is that of SCPT20, given in Fig. 4.2.

The next section covers the implementation of the global stiffness matrices in a FD scheme to solve the 1D beam equations.

4.3.3. IMPLEMENTATION IN A 1D MODEL

Euler's central finite difference scheme [131] is used to approximate the solution of a Timoshenko beam on a non-local Winkler foundation. Let u and ψ be sufficiently smooth functions of z, which we wish to evaluate in a domain of length L at n equally spaced points, creating a discretisation length $h = L/(n-1)$. In this schematisation, we approximate (with error $O(h^2)$) the first and second derivative terms of Eqs. 4.31 and 4.32, and write - invoking summation over repeated indices:

$$\frac{GA\kappa}{h^2}(u_{i-1} - 2u_i + u_{i+1}) - \tilde{K}^{u,u}_{i,j} u_j - \frac{GA\kappa}{2h}(-\psi_{i-1} + \psi_{i+1}) - \tilde{K}^{u,\psi}_{i,j} \psi_j = 0, \tag{4.40}$$

$$\frac{GA\kappa}{2h}(-u_{i-1} + u_{i+1}) - \tilde{K}^{\psi,u}_{i,j} u_j - GA\kappa\psi_i + \frac{EI}{h^2}(\psi_{i-1} - 2\psi_i + \psi_{i+1}) - \tilde{K}^{\psi,\psi}_{i,j} \psi_j = 0, \tag{4.41}$$

with $i = 1,..,n$ and $j = 0,..,n+1$, $z_1 = 0$ representing the location of the pile head and $z_n = L$ that of the pile tip. This implies we use 2 ghost nodes ($j = 0$ and $j = n+1$) to solve the equations at the boundaries of the domain. Similar to Eq. 4.33, the tilde over the global stiffness matrices ($\tilde{K}^{u,u}_{i,j}$, .. ,$\tilde{K}^{\psi,u}_{i,j}$) in Eqs. 4.40 and 4.41 indicates that these matrices are auxiliary matrices, incorporating the Trapezium rule modifications, where in this case the first and last columns of the original stiffness matrices are multiplied by $\frac{1}{2}$:

$$\tilde{K}^{u,u}_{i,j} = \begin{cases} \frac{1}{2} h K^{u,u}_{i,j}, & \text{for } j = 1 \text{ and } j = n, \\ h K^{u,u}_{i,j}, & \text{otherwise,} \end{cases} \tag{4.42}$$

with $K_{i,j}^{u,u}$ the stiffness matrix calculated in Eq. 4.35. Furthermore, a column of zeros is added to the left and right side of the matrix to incorporate the ghost nodes:

$$\tilde{K}_{i,j}^{u,u} = 0, \text{ for } j = 0 \text{ and } j = n+1. \tag{4.43}$$

$\tilde{K}_{i,j}^{u,\psi}$, $\tilde{K}_{i,j}^{\psi,u}$ and $\tilde{K}_{i,j}^{\psi,\psi}$ incorporate similar modifications.

Next we rewrite the boundary conditions (Eqs. 4.26 - 4.29), isolating the ghost nodes:

$$\begin{aligned} GA\kappa(\tfrac{-u_0+u_2}{2h} - \psi_1) &= -F, \\ u_0 &= \tfrac{2h}{GA\kappa}F - 2h\psi_1 + u_2, \end{aligned} \tag{4.44}$$

$$\begin{aligned} EI(\tfrac{-\psi_0+\psi_2}{2h}) &= M, \\ \psi_0 &= \tfrac{-2h}{EI}M + \psi_2, \end{aligned} \tag{4.45}$$

$$\begin{aligned} GA\kappa(\tfrac{-u_{n-1}+u_{n+1}}{2h} - \psi_n) &= 0, \\ u_{n+1} &= 2h\psi_n + u_{n-1}, \end{aligned} \tag{4.46}$$

$$\begin{aligned} EI(\tfrac{-\psi_{n-1}+\psi_{n+1}}{2h}) &= 0, \\ \psi_{n+1} &= \psi_{n-1}. \end{aligned} \tag{4.47}$$

These expressions need to be substituted into the system of equations given by 4.40 and 4.41 for $i = 1$ and $i = n$ in order to eliminate the ghost nodes. Doing so for the first equilibrium equation (4.40), for the upper boundary at z_1 (pile head), we obtain:

$$\frac{GA\kappa}{h^2}(-2u_1 + 2u_2) - \tilde{K}_{1,j}^{u,u}u_j - \frac{2GA\kappa}{h}\psi_1 - \tilde{K}_{1,j}^{u,\psi}\psi_j = -\frac{2F}{h} + \frac{GA\kappa M}{EI}, \tag{4.48}$$

and at the lower boundary z_n:

$$\frac{GA\kappa}{h^2}(2u_{n-1} - 2u_n) - \tilde{K}_{n,j}^{u,u}u_j + \frac{2GA\kappa}{h}\psi_n - \tilde{K}_{n,j}^{u,\psi}\psi_j = 0. \tag{4.49}$$

Similar for the second equilibrium equation 4.41, around the first point $i = 1$:

$$-\tilde{K}_{1,j}^{\psi,u}u_j + \frac{EI}{h^2}(-2\psi_1 + 2\psi_2) - \tilde{K}_{1,j}^{\psi,\psi}\psi_j = F + \frac{2M}{h}, \tag{4.50}$$

and the last equation, at the last point $i = n$:

$$-\tilde{K}_{n,j}^{\psi,u}u_j + \frac{EI}{h^2}(2\psi_{n-1} - 2\psi_n) - \tilde{K}_{n,j}^{\psi,\psi}\psi_j = 0. \tag{4.51}$$

For the inner domain, Eqs. 4.40 and 4.41 remain unchanged. The outer ghost nodes ($j = 0$ and $j = n+1$) have now been eliminated, resulting in a square matrix that can be inverted; by collecting the terms in Eqs. 4.48 - 4.51 in a coefficient matrix $\mathbf{A}$ and a right hand side vector $\mathbf{b}$, we can find the solution vector $\mathbf{x}$ (containing u and ψ) by solving the linear equation $\mathbf{Ax} = \mathbf{b}$.

4.3.4. STATIC RESPONSE

The MATLAB based 3D FE model described in Section 3.2 is used for the 3D SSI target solutions and for extracting the global stiffness matrices (modelling the soil domain excluding the pile). As previously mentioned, the considered piles are assumed to be fully filled with soil.

The comparison of responses for a static horizontal force of $F = 1$ N and an overturning moment $M = 45$ Nm for the In-situ case, the 2 short piles and the Caisson case is given in Figs. 4.14 - 4.17, where for each case the same coloring is used as in the categorisation of Fig. 4.1. The misfits (as calculated with Eq. 4.17) are displayed in the figures, and summarized in Table 4.5.

The quality of the fit of the presented cases is very good. As listed in Table 4.3, the local method for finding a $k_{eff}(z)$ for MP45 yielded a misfit of $C_u = 0.0184$, $C_{u'} = 0.0247$, $C_\psi = 0.0096$ and $C_{\psi'} = 0.0197$ ($C_{u,u',\psi,\psi'} = 0.0723$). The misfits associated with the fits using the non-local method are summarized in Table 4.5. Besides the fact that the misfit using the non-local technique are more than twice as low, Figs. 4.14 - 4.17 show that the method is quite insensitive for the type of SSI, demonstrated by the wide range in flexibility factors K_r and L/D ratios that were chosen for the 4 cases (Fig. 4.1). We do see a somewhat poorer result for the Short-stiff case. Nevertheless, these misfits are still considered satisfactory. Using the local technique for the Short-stiff case yielded unusable results (see Table 4.4). Furthermore, the non-local stiffness technique has the advantage of being a direct approach, whereas the local technique requires optimisation, involving much more uncertainty (and computational cost) than the non-local stiffness method.

	$C_{u,u',\psi,\psi'}$	C_u	$C_{u'}$	C_ψ	$C_{\psi'}$
In-situ	0.0179	0.0074	0.0050	0.0018	0.0038
Short-soft	0.0360	0.0092	0.0111	0.0081	0.0076
Short-stiff	0.1342	0.0648	0.0296	0.0209	0.0189
Caisson	0.0727	0.0336	0.0165	0.0097	0.0129

Table 4.5: Misfit values (Eq. 4.17) for the 4 SSI cases, static solution (Figs. 4.14 - 4.17).

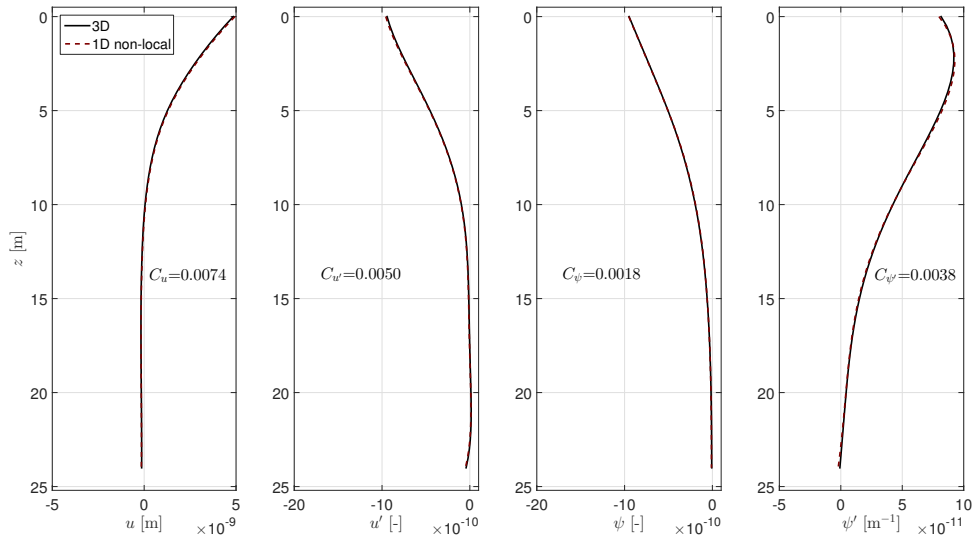

Figure 4.14: In-situ case (MP45), comparison between 1D non-local and 3D solution for a static force of $F = 1$ N and an overturning moment $M = 45$ Nm.

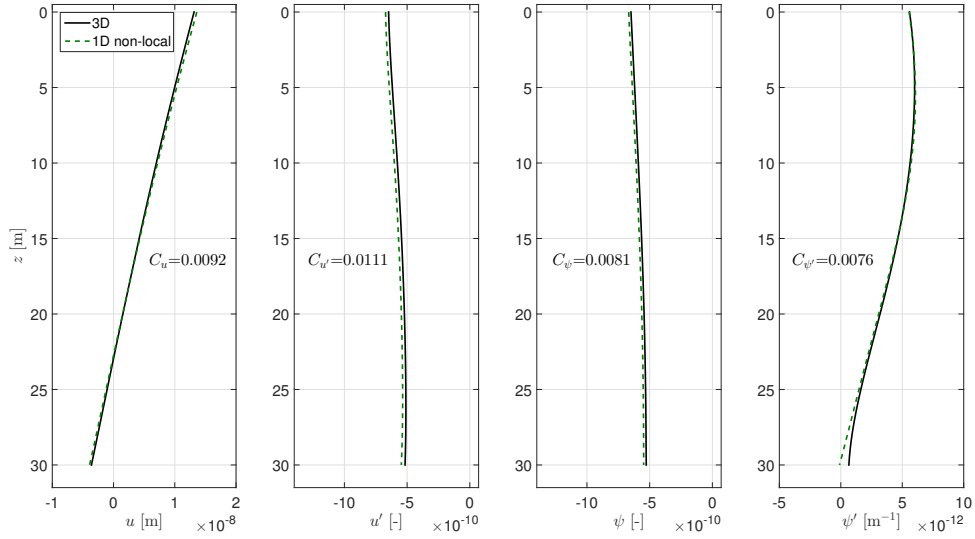

Figure 4.15: Short-soft case, comparison between 1D non-local and 3D solution for a static force of $F = 1$ N and an overturning moment $M = 45$ Nm.

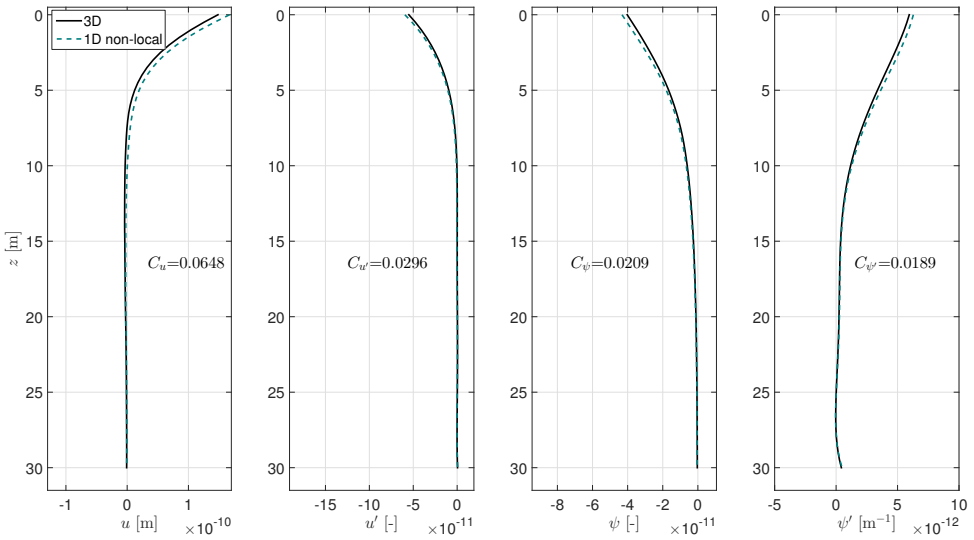

Figure 4.16: Short-stiff case, comparison between 1D non-local and 3D solution for a static force of $F = 1$ N and an overturning moment $M = 45$ Nm.

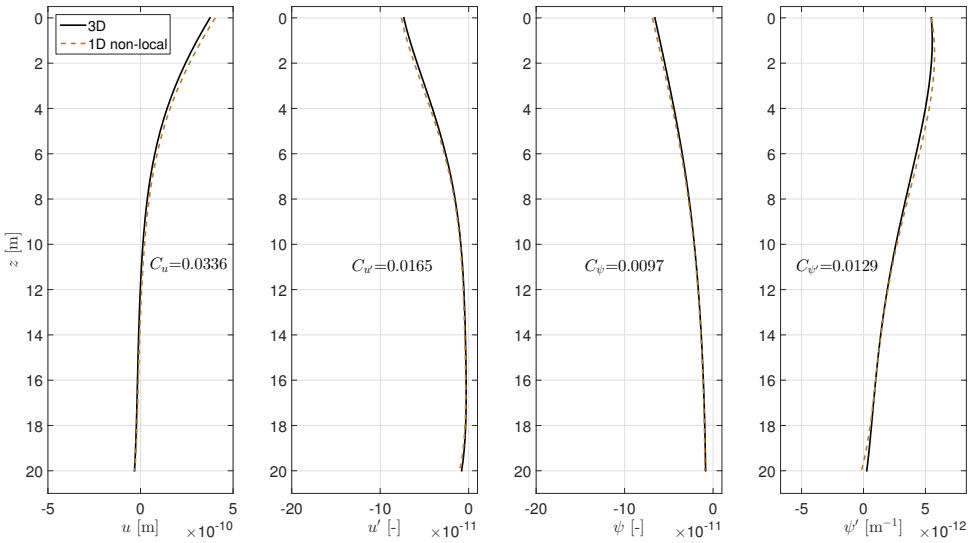

Figure 4.17: Caisson case, comparison between 1D non-local and 3D solution for a static force of $F = 1$ N and an overturning moment $M = 45$ Nm.

4.3.5. DYNAMIC RESPONSE

As mentioned in Section 3.2, for the dynamic case, the shear modulus of the soil in the 3D FE model becomes complex valued due to a non-zero material damping and the occurring geometric damping. The soil response and thus the global stiffness matrices (Eqs. 4.35 - 4.38) also become complex-valued. A 1% ($\zeta = 0.01$, see Eqs. 3.1) material damping was assigned to all layers in the 3D models. The 1D equilibrium equations (Eqs. 4.31 and 4.32) for the dynamic case, written in the frequency domain, become

$$GA\kappa\Big(\frac{d^2u(z)}{dz^2} - \frac{d\psi(z)}{dz}\Big) - \int_0^L \mathring{K}^{\mathrm{u,u}}(z,\overline{z})u(\overline{z})d\overline{z} - \int_0^L \mathring{K}^{\mathrm{u},\psi}(z,\overline{z})\psi(\overline{z})d\overline{z} + \omega^2\rho A u(z) = 0, \tag{4.52}$$

$$GA\kappa\Big(\frac{du(z)}{dz} - \psi(z)\Big) + EI\frac{d^2\psi(z)}{dz^2} - \int_0^L \mathring{K}^{\psi,\psi}(z,\overline{z})\psi(\overline{z})d\overline{z} - \int_0^L \mathring{K}^{\psi,\mathrm{u}}(z,\overline{z})u(\overline{z})d\overline{z} + \omega^2\rho I\psi(z) = 0, \tag{4.53}$$

containing complex-valued stiffness kernels $\mathring{K}^{\mathrm{u,u}}(z,\overline{z})$, .. ,$\mathring{K}^{\psi,\mathrm{u}}(z,\overline{z})$, lateral inertia ρA and rotary inertia ρI, with ρ the mass density of the pile. Apart from the steel mass, the pile is assumed to be fully filled with the same soil as outside of the pile. The frequency-dependent inertia forces of the soil are automatically incorporated in the complex-valued stiffness matrices, which are calculated with the obtained frequency response, see Eqs. 4.35 - 4.38.

The resulting comparison of the dynamic response of the 3D and 1D models for the 4 cases, excited by a harmonic horizontal force of $F(\omega) = 1$ N, an overturning moment $M(\omega) = 45$ Nm and excitation frequency $f = 0.3$ Hz ($\omega = 2\pi f = 1.88$ rad/sec) is given in Figs. 4.18 - 4.21. This excitation frequency is rather arbitrary, however, a frequency of $f = 0.3$ Hz is surely below the first resonance frequency of the considered soil-pile systems, ensuring a stiffness-dominated response (rather than inertia-dominated), which is the focus of this research. Furthermore, $f = 0.3$ Hz is close to the typical first natural frequency of offshore wind turbine structures.

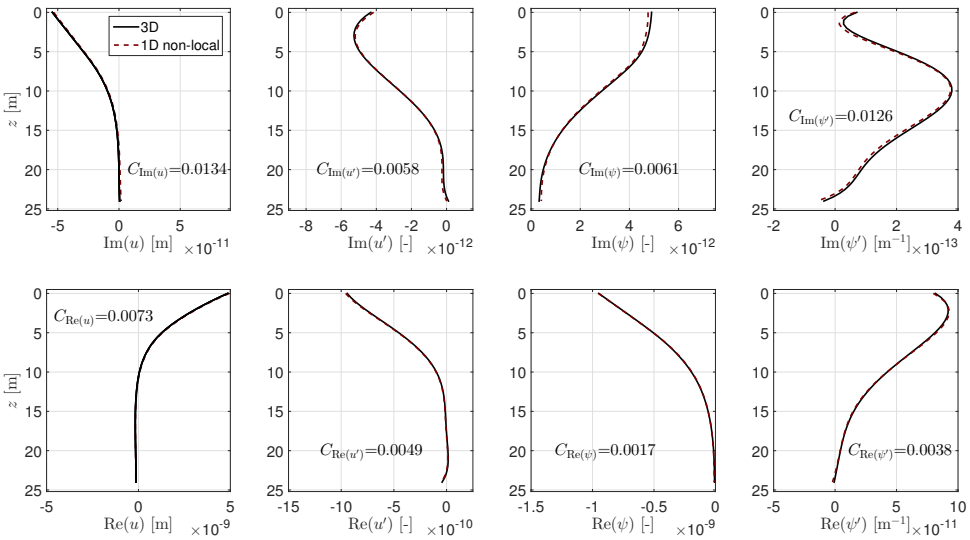

Figure 4.18: In-situ case (MP45), comparison between 1D non-local and 3D solution for a harmonic force of $F = 1$ N and overturning moment $M = 45$ Nm at a frequency of $f = 0.3$ Hz.

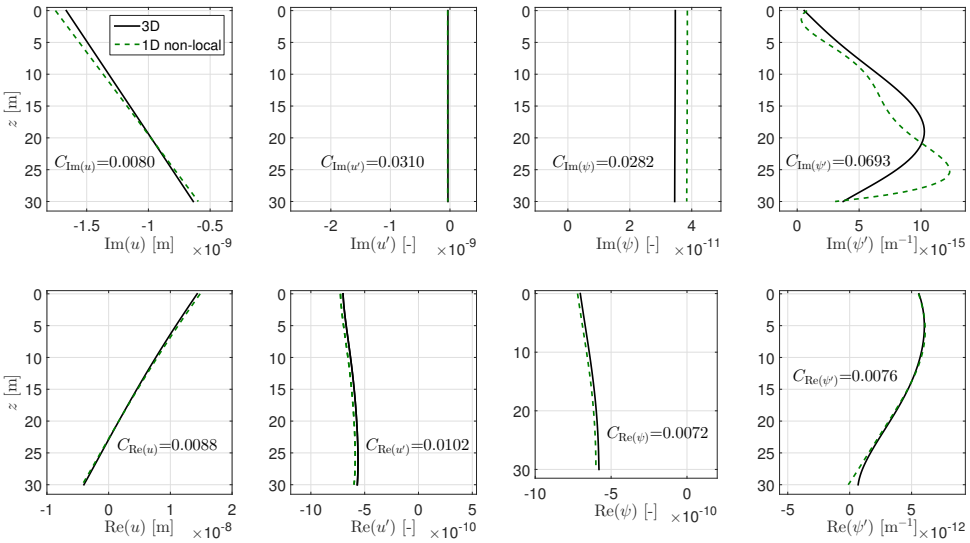

Figure 4.19: Short-soft case, comparison between 1D non-local and 3D solution for a harmonic force of $F = 1$ N and overturning moment $M = 45$ Nm at a frequency of $f = 0.3$ Hz.

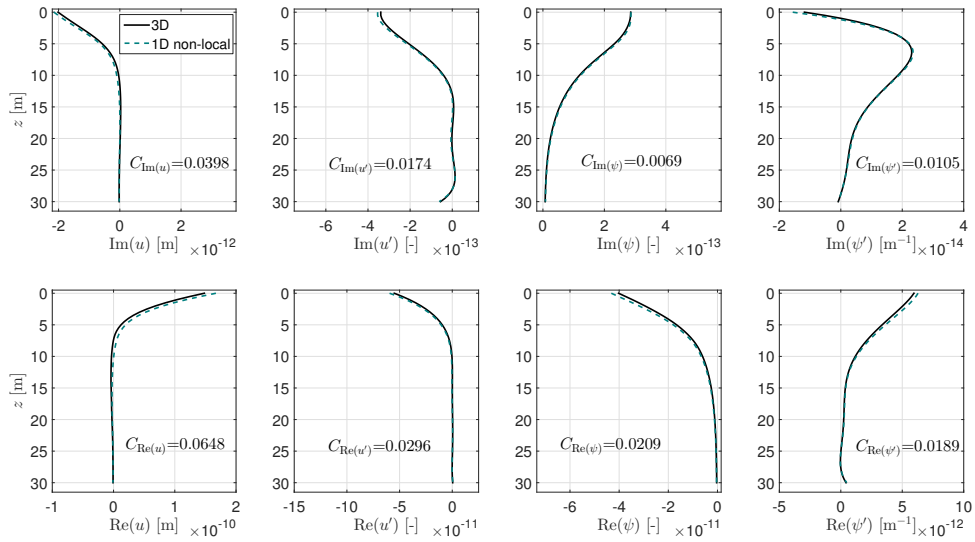

Figure 4.20: Short-stiff case, comparison between 1D non-local and 3D solution for a harmonic force of $F = 1$ N and overturning moment $M = 45$ Nm at a frequency of $f = 0.3$ Hz.

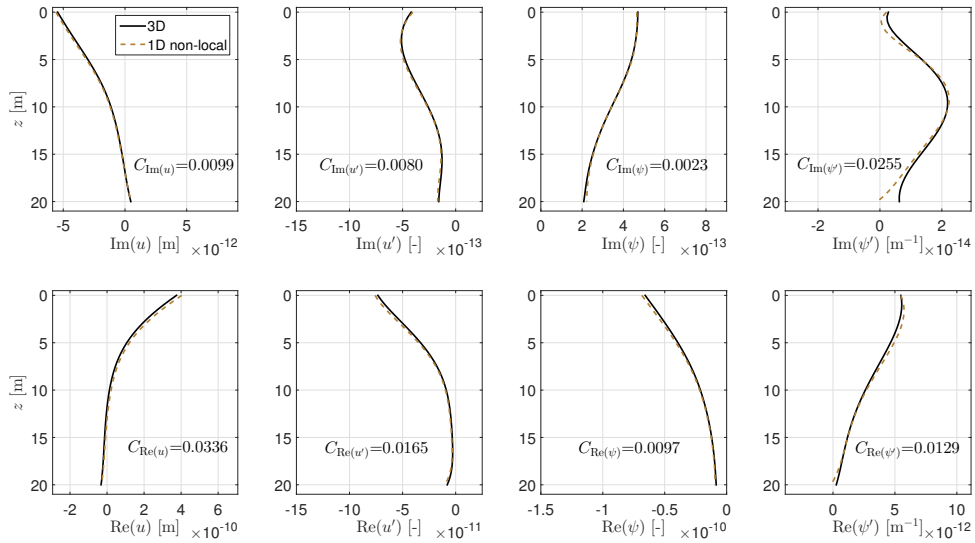

Figure 4.21: Caisson case, comparison between 1D non-local and 3D solution for a harmonic force of $F = 1$ N and overturning moment $M = 45$ Nm at a frequency of $f = 0.3$ Hz.

The fits for the imaginary and real parts of the response in case of a dynamic excitation, as presented in above Figs. 4.18 - 4.21, are very satisfactory. The misfit of the imaginary parts ($C_{\mathrm{Im}(..)}$) are comparable to those of the real parts ($C_{\mathrm{Re}(..)}$); in some cases they are larger than the misfit of the real part (for instance, $C_{\mathrm{Im(u)}} > C_{\mathrm{Re(u)}}$) for the In-situ and Short-soft cases (Figs. 4.18 and 4.19, respectively). However, the opposite also occurs: $C_{\mathrm{Im(u)}} < C_{\mathrm{Re(u)}}$ for the Short-stiff and Caisson cases (Figs. 4.20 and 4.21, respectively). Although the imaginary part of the rotations of the Short-soft case are matched quite well, the misfit for its derivative $C_{\mathrm{Im}(\psi')}$ is quite high. The misfit values of the above presented results are summarized in Table 4.6.

	$C_{u,u',\psi,\psi'}$		C_u		$C_{u'}$		C_ψ		$C_{\psi'}$	
	Re	**Im**	**Re**	**Im**	**Re**	**Im**	**Re**	**Im**	**Re**	**Im**
In-situ	0.0178	0.0379	0.0073	0.0134	0.0049	0.0058	0.0017	0.0061	0.0038	0.0126
Short-soft	0.0338	0.1365	0.0088	0.0080	0.0102	0.0310	0.0072	0.0282	0.0076	0.0693
Short-stiff	0.1342	0.0747	0.0648	0.0398	0.0296	0.0174	0.0209	0.0069	0.0189	0.0105
Caisson	0.0727	0.0456	0.0336	0.0099	0.0165	0.0080	0.0097	0.0023	0.0129	0.0255

Table 4.6: Misfit values (Eq. 4.17) for the 4 SSI cases, dynamic solution (Figs. 4.18 - 4.21). The misfits are defined for the real (Re) and imaginary (Im) parts of the solutions.

As previously mentioned, similar efforts in matching 3D and 1D responses have been performed in [48]. As opposed to these authors, we do not aim to develop general relations between 3D and 1D SSI stiffness parameters. Instead, a technique was developed to accurately translate the 3D SSI into 1D effective parameters for each case. In [48], a 20% accuracy of the pile head displacement and a 13% accuracy for the pile head rotations is reached (the responses over the soil depths are not addressed), for a pile of 2 m diameter, length of 8 m, embedded in a 3-layer soil profile with an average $E_s = 25$ MPa, and an excitation frequency of 5 Hz. For the presented cases, we reach an *overall* (for all z) accuracy range of 3.43% (Short-soft case) - 24.16% (Short-stiff) for the magnitude (absolute values) of the displacements $u(z)$ and 4.45% (Caisson) - 5.57% (Short-stiff) for the magnitude of the rotations $\psi(z)$. Note that Table 4.6 gives the misfits of the imaginary and real parts of the response separately, not of the absolute values (which are considered in [48]). In case of only considering the mudline correspondence - as is often done - we reach a 1.92% (In-situ) - 11.15% (Short-stiff) accuracy for the displacement $u(0)$, and 1.61% (In-situ) - 6.89% (Short-soft) for the rotation $\psi(0)$.

4.3.6. DISCUSSION

The presented fits of both the static and dynamic responses of the 1D models with those of the 3D models are very satisfactory, and within accuracy limits that are acceptable for structural designers. Nevertheless, although this 1D non-local approach could be considered an exact equivalent modelling method for the 3D models, there are still differences between the responses of these 2 models.

One cause could be the difference between the modelling methods of the pile: the 1D Timoshenko beam versus the solid elements used in the 3D model. To further investigate this difference, 3 other cases were considered. First a static cantilever pile (to

exclude the soil reaction) with $L = 25$ m, $D = 5$ m and $t = 60$ mm was analyzed using the 3D FE solid elements, and the 1D FD solution. The overall mismatch in deflections between these two models was $C_u = 0.0068$, which is small, but is of the same order as the values presented for the static SSI cases in Table 4.5. For completeness it is noted that the misfit of the FD solution and the analytical solution for a 25 m cantilever beam gave an error for the deflection of $C_u = 5.997 \cdot 10^{-5}$ for $h = 0.5$ m. In the second comparison, a Timoshenko beam FE model embedded in a 3D solid continuum (with the same pile properties as the cantilever, and a similar soil profile as SCPT20, Fig. 4.2) was compared to the 3D model as used in the previous sections (solid elements to model the pile). The third case is similar to the second, but employs shell elements for the 3D pile. The misfit of deflections for these two cases was $C_u = 0.0020$ for the pile meshed with solid elements and $C_u = 0.0068$ for the pile meshed with shell elements. Again, these values are small, but not negligible and they are of the same order as the values presented in Table 4.5. Obviously, these misfit values will vary for different pile geometries and soil combinations. The difference in 3D and 1D pile modelling is expected to be the main cause for the higher misfit obtained for the Short-stiff case; the ovelisation of the 3D pile in this high soil-stiffness case was verified to be higher than that in the Short-soft case (having the same pile geometry, but softer soil). We can conclude that the modelling difference between a 3D pile and the used beam theory can be a cause of the remaining mismatch between the observed 3D and 1D responses.

The modelling difference between a 3D pile and the beam theory could furthermore cause an inaccuracy in the modelled interaction of the pile with the soil; to extract the global stiffness matrices, beam-shaped (rigid ring) deformations are prescribed to the soil, whereas the 3D soil-pile model allows for circumferential dependence of the displacements.

Additionally we note that, in case an even higher accuracy is required, the small remaining difference in stiffness can be easily further diminished by optimising the global stiffness matrices, leading to lower misfits. Multiplying the global stiffness matrices by a factor α - to be optimized - can compensate for the above discussed difference in 3D pile and beam theory.

4.4. SUMMARY

Two methods were presented to obtain an effective 1D model that can mimic the modelled 3D response of rigidly behaving soil-pile systems. For such systems, incorporating the 3D effects in the interaction between the pile and soil are crucial for simulating the correct pile behaviour. Rigid piles invoke a more global reaction of the soil; where flexible piles can have multiple crossings of the zero-displacement line, involving more localized soil reaction mechanisms, for rigid piles the soil stratum tends to react as a whole. Furthermore, the extra reactional shear forces and moment at the (displacing and rotating) pile tip and the distributed moment along the pile shaft created by the vertical shear forces acting at a considerable lever arm (the radius of the pile), mobilize more restoring mechanisms for rigid piles than for flexible systems - for which modelling only the lateral, uncoupled soil resistance suffices.

Therefore, it is warranted to employ a 3D SSI model for predicting the behaviour of piles with $L/D < 7$. As engineering design often involves the simulation of many load cases, the use of a 3D model is uneconomical. The here presented methods were developed to provide the designer with a tool such that the 3D model can be used only once: to extract the effective 1D model that is subsequently used for load simulations. The effective 1D model hence has the dual benefit of being accurate (calibrated by the 3D model) and - being a 1D model - computationally fast.

The first discussed *local* translation method (Section 4.2) involves using the 3D modelled displacement $u(z)$ and rotation $\psi(z)$ profiles to find an effective 1D stiffness profile $k_{eff}(z)$ that renders the response of the 1D Winkler model the same as that of the 3D model. The technique is local, as the target 1D Winkler model consists of uncoupled lateral springs. It is assumed that the effective stiffness profile $k_{eff}(z)$ can be described with a 4^{th} order polynomial, of which the coefficients are found by solving global and local force and moment balances along the pile. An optimisation is involved in finding the best-fit domains of the local integrals, yielding the lowest misfit between the 3D and the 1D model. A good match is obtained between the 3D and 1D displacement $u(z)$, slope $u'(z)$, rotation $\psi(z)$ and curvature $\psi'(z)$ for the MP20 and MP45 piles, having a L/D ratio of respectively 6.4 and 4.8. Similar matching efforts between 3D and 1D effective modelling have been published, but for more simple 3-layered profiles [48], or 2-layered profiles including a non-linear soil reaction [124]. However, often only the pile head responses are compared; comparisons over the full embedment length are hardly encountered in the literature.

Compared to MP20, slightly poorer results are obtained for the more rigidly behaving MP45 pile. Tests (of the method) on other SSI cases having lower L/D ratio and other relative pile stiffness K_r (Eq. 4.1) suggest that indeed the optimized stiffness profile $k_{eff}(z)$ is less capable of fully capturing the 3D effects. Although the shape of $k_{eff}(z)$ is optimized, using only uncoupled, lateral springs for the target 1D solution no longer suffices.

The local method was shown to additionally be useable for obtaining an effective 1D damping profile $c_{eff}(z)$ for the low-frequency dynamic case. The dashpot distribution $c_{eff}(z)$ is obtained in a similar way as explained for $k_{eff}(z)$, by establishing its shape based on the complex-valued 3D response. The identification of a proper $k_{eff}(z)$ for the static excitation is a strict requisite, as it was found that the error made in modelling the real part of the dynamic response, is amplified to a larger error in the imaginary part of the response - overshadowing the sensitivity of the imaginary part of the response to the damping profile $c_{eff}(z)$. Finding the local, 1D effective damping profile is therefore, in line with the above explained restrictions for obtaining an adequate $k_{eff}(z)$, bound to application for only flexible to semi-rigidly behaving piles.

To obtain a more versatile translation method that can handle a wider range of SSI-flexibility at a higher accuracy, the *non-local* method was developed (Section 4.3). The fully coupled 3D soil response is integrated in a 1D model by employing global stiffness kernels which are directly obtained from the 3D model. For the dynamic case, the stiffness kernels become complex valued, incorporating, besides inertial effects, the material and geometric damping simulated in the 3D model. High quality fits between the 3D and 1D modelled response were obtained for 4 different soil-pile systems for both the static and the dynamic SSI. Another advantage of the non-local technique is the fact that it, as opposed to the local method, does not involve any optimisation and the resulting output is therefore less uncertain.

5

EXPERIMENTAL VALIDATION

This chapter[1] presents the in-situ, controlled dynamic excitation tests that were performed on a full-scale, stand-alone monopile foundation of an offshore wind turbine in the near-shore Westermeerwind wind farm. A large part of this chapter has been published in [126], and it was chosen to maintain this content 'as published' (besides minor textual changes), presented in Sections 5.1 - 5.3. An addendum is included (Section 5.5) which incorporates additional analyses employing the non-local method and an updated soil profile.

As explained in Chapters 1 and 2, the response of the structure to the often design-driving fatigue loads is dictated by the small-strain, dynamic soil properties, and these properties are the focus of the current research. A test pile for this response regime should therefore be dynamically (harmonically) excited. Furthermore, to increase the chance of successful system identification, the pile should be excited by a known, controlled force input. In addition, testing a real MP allows to - besides including realistic geometric, soil saturation and pile installation effects - link the identified SSI characteristics to subsequent response of a complete operational OWT. As will be shown in this chapter, due to the high sensitivity of a stand-alone MP to the soil reaction, this setup offers the highest degree of certainty for validating a SSI model - as opposed to using the structural response of the full OWT.

The above described wishes led to the design of a test setup (described in Section 5.2), placed at the MP45 pile (previously described in Sections 2.2.3, 3.1 and 4.2.2), of which the output of the extensive soil-characterisation is briefly repeated in Section 5.1. Of the two tested MPs, only MP45 was fully equipped with strain gauges and sensors in the soil, and is therefore the pile discussed in this thesis. In the model-based identification (Section 5.3) of the SSI properties in terms of stiffness, damping and possible inertia effects, we aim to match measured transfer and transmissibility functions with

[1] Most of this chapter has been published in Soil Dynamics & Earthquake Engineering **102**, 241-262 (2017) [126]. Minor textual changes have been applied to ensure coherence with the rest of the thesis.

modelled counterparts using a 1D model and 2 modifications of that model. The local effective stiffness method is used to calculate the in-situ 1D stiffness $k_{eff}(z)$, which is subsequently employed as a starting point for the identification. It is investigated (validated) how well $k_{eff}(z)$ performs in comparison with the often used p-y stiffness method; the mismatch between the modelled and measured pile responses is quantified for both methods. In Section 5.4 we discuss the three observed frequency regimes, the damping and natural frequency of the full OWT structure, and we reflect on the linear-soil assumption. In [126] (and Section 5.3), the in-situ stiffness is identified based on a prediction of $k_{eff}(z)$ using the local method. However, now that the non-local method is available (see Section 4.3 and [79]), an addendum is included in Section 5.5 in which the response predicted by the effective non-local 1D model is also compared to the measured response of the in-situ pile. Furthermore, an alternative shear-wave velocity profile for the test location (SCPT45) is introduced, which is a smoother, more averaged reflection of the version presented in Chapter 2, Fig. 2.18. The latter is a direct representation of the inverted C_s velocities, whereas the smoother profile contains engineering judgement by removing some of the outliers. The chapter is concluded by Section 5.6, in which the main findings are collected.

5.1. SITE CHARACTERISATION

As previously mentioned, the shaker tests were performed on monopiles of the Westermeerwind wind farm - a near-shore farm in the Netherlands, situated at the East side of the IJsselmeer lake, see Fig. 5.1. The saturated soil conditions being quite similar to sandy North Sea sites in combination with the limited water depth of 4-5 m and good accessibility, make it an appropriate location for the experimental investigation of soil-structure interaction. For reading convenience, some of the soil profiles of the testing location shown and discussed in Chapter 2 are repeated here. The in-situ density ρ and the effective angle of internal friction φ' for location MP/SCPT45 are shown in the left and right panel of Fig. 5.2, respectively. The internal friction angle is merely given as a reference, as it is an important input parameter for the p-y curve method. As supplementary information, Fig. A.2 in Appendix A shows the CPT profile captured by SCPT45. The estimated Poisson's profile and computed Young's modulus for location W27 are given in Fig. 5.3. As explained in Chapter 3, the elastic continuum parameters (Young's modulus, density and Poisson's ratio) were input for the ANSYS-based 3D soil-pile model, of which the response was used in the local method (Section 4.2.2) to obtain the 1D effective stiffness $k_{eff}(z)$ for the tested monopile. This (static) effective stiffness profile (Fig. 4.6) will be used as an initial-guess in the model-based analysis of the shaker measurements, discussed in Section 5.3.

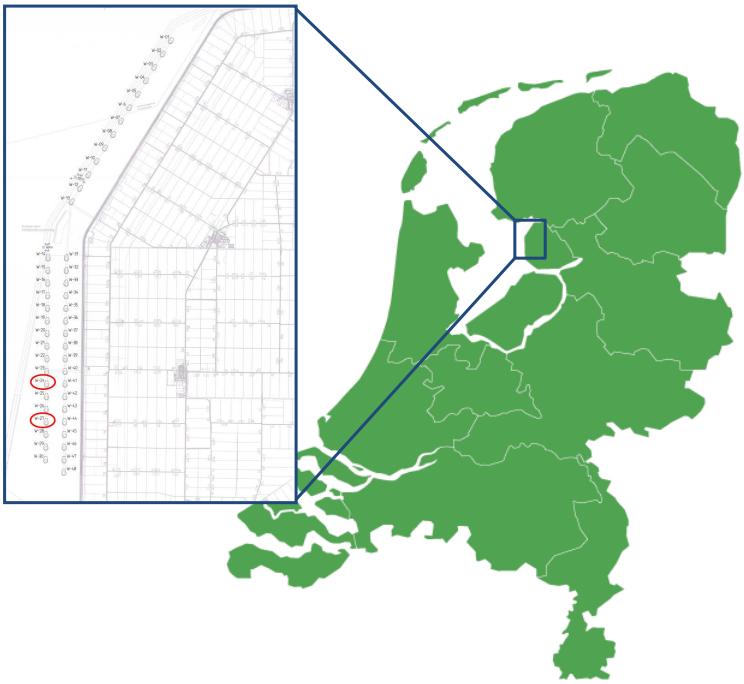

Figure 5.1: Location of Westermeerwind wind farm. The red circles indicate the shaker testing locations, named 'W24' and 'W27' (southernmost position of the two).

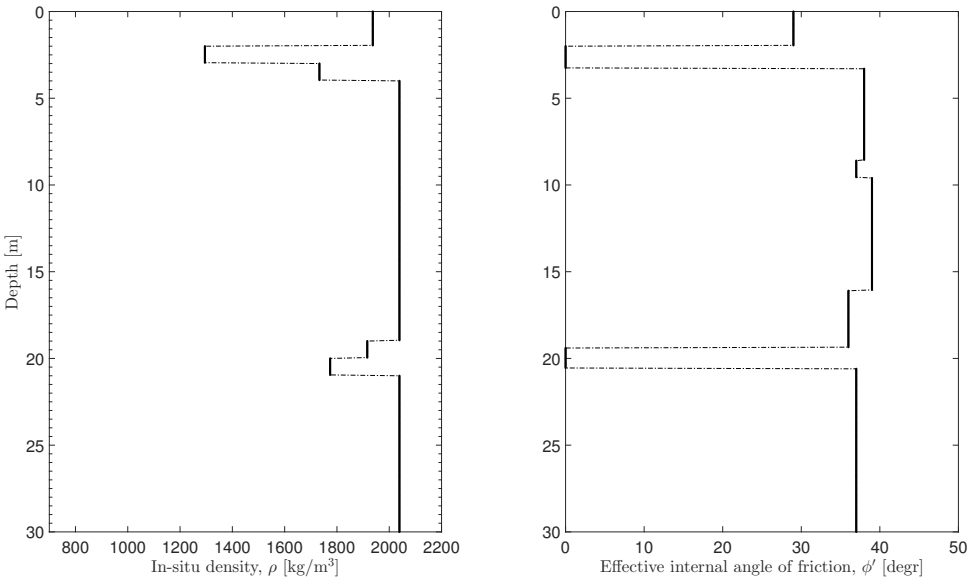

Figure 5.2: In-situ density ρ (left panel) and effective angle of internal friction φ' (right panel) of turbine location W27 (MP/SCPT45). The mean values of the in-situ density of the different soil types and layers encountered in the farm were determined based on unit weight, water content, oedometer and triaxial tests. The angle of internal friction was estimated using the correlation with the relative density according to Jamiolkowski [132], as prescribed by the standards [133], and validated with the output of triaxial tests. For the layers classified as cohesive material, φ' is set to zero.

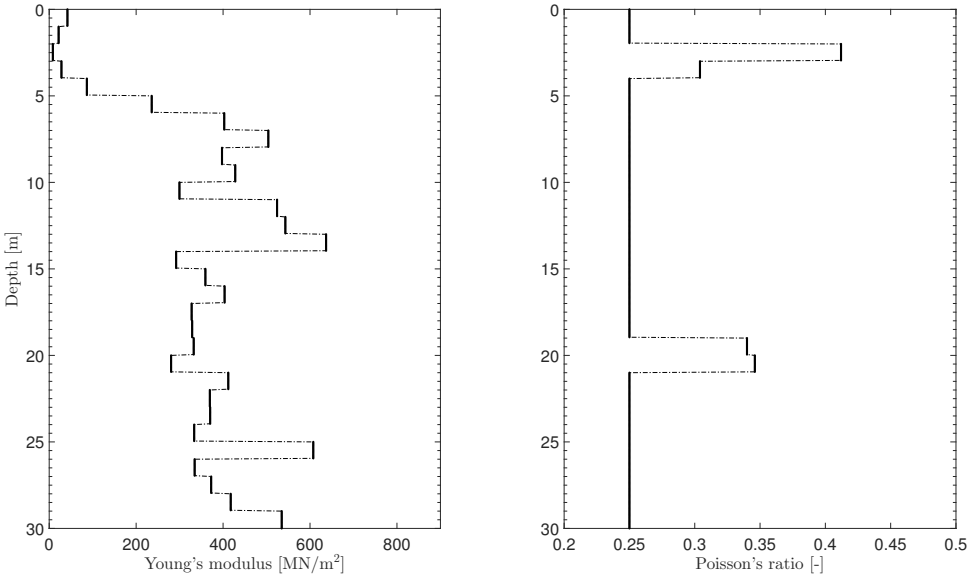

Figure 5.3: The Young's modulus profile (left panel) and Poisson's ratio profile (right panel) are input for the 3D linear elastic model for MP45.

5.2. MEASUREMENT SETUP & DATA PRE-PROCESSING

Fig. 5.4 shows the measurement setup for pile MP45 (of turbine W27): 7 rings of strain gauges are attached to the inner pile wall, with 6 rings below, and 1 ring just above mud-line. Each ring contains 4 strain gauges: one for each quadrant. The rings are vertically distributed, with a concentration around the location where most bending was expected to occur. Besides standard protection covers for the strain gauges, fibreglass reinforced composite cable trays were glued on the pile-wall to guide and protect the cables. Steel wedges were welded on the pile near the pile tip to protect the lower edges of the cable trays during installation of the pile. During hammering of the pile, 7 strain gauges were damaged: the lowest ring of strain gauges and three strain gauges of rings no. 3, 4 and 6 (see Fig. 5.4) on the axis perpendicular to the shaker-loading direction. Furthermore, 2 Althen AAA320 accelerometers were attached to the inner pile wall at the top of the pile for measuring the pile accelerations in North-South and East-West direction. The company HBM installed all pile-related sensors and provided the data acquisition system.

To monitor the soil-structure interaction during dynamic excitation of the MP, the reaction of the soil and of the pile were synchronically measured. To this end, 16 cones with accelerometers and piezometers were placed at various depths and radial distances from the pile. The data retrieved from these soil sensors will, however, not be discussed in the current work.

As can be observed in the right panel of Fig. 5.5, the shaker consists of 2 large cogwheels (ensuring synchronisation) that are hydraulically powered. On top of these cogwheels, multiple steel plates with various weights can be attached at different radii from the center of the cogwheel. An artist impression of the shaker is given in the left panel of Fig. 5.5. The shaker can deliver a maximum hydraulic power of 50 kW, rotate at a maximum frequency of 8.6 Hz and was designed to not supersede an excitation force of 160 kN. The total weight of the shaker (excluding ballast plates, including frame) is 4500 kg. An accelerometer was attached to the shaker frame, and a tachometer measured the rotational velocity of the cogwheels. All sensors were sampled with a frequency of 600 Hz.

Fig. 5.6 shows an aerial photo of the mobilized barges and crane that were used for performing the measurements.

Three weight setups were used for exciting the monopile:

- Heavy weight: 10 plates of 20.5 kg on each cogwheel = 410 kg
- Middle weight: 3 plates of 20.5 kg on each cogwheel = 123 kg
- Light weight: 1 plate of 20.5 kg on each cogwheel = 41 kg

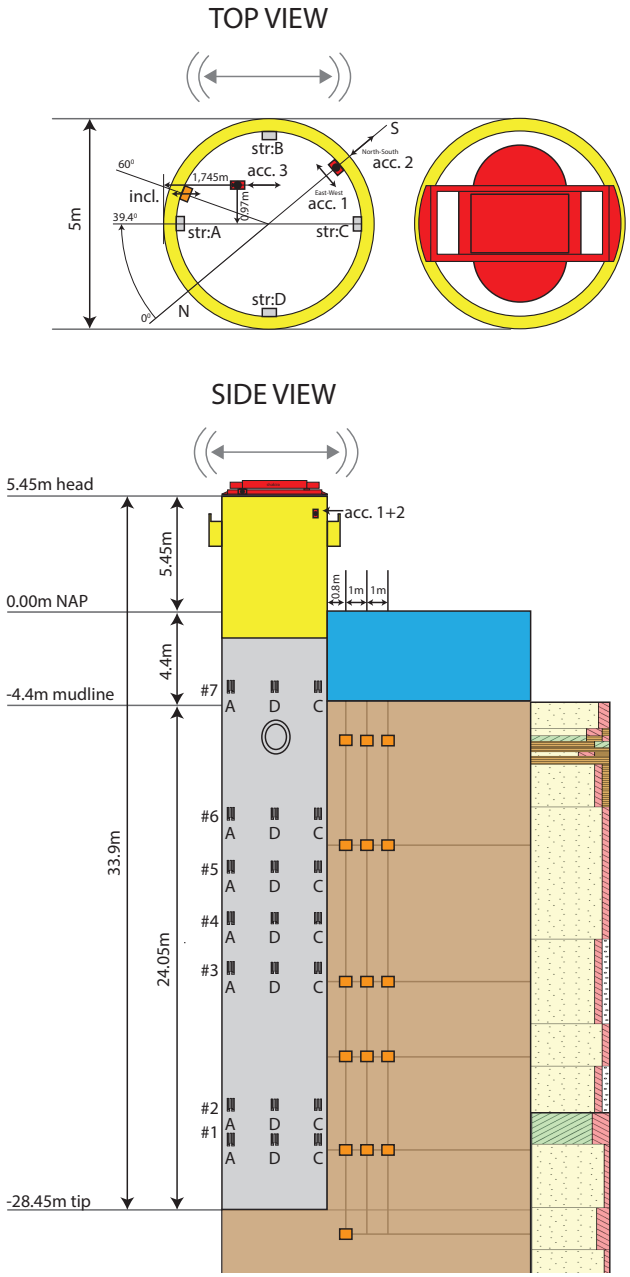

Figure 5.4: Measurement setup for MP45. Side view: the vertical levels are in relation to NAP (Dutch equivalent of Mean Sea Level). The orange boxes indicate the positions of the cones equipped with accelerometers and pore water pressure meters. The hatched spots on the pile (named A-D-C) indicate the position of the strain gauges, with their ring number indicated at the left side of the pile. The cable entry hole is indicated below strain gauge D7. A borehole classification of the soil is given in the right part of the figure, with yellow indicating sand, green for clay and brown for peat, see Fig. 2.18.

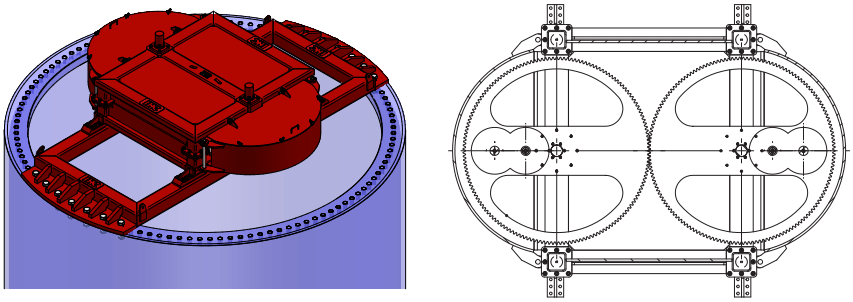

Figure 5.5: Artist impression of the shaker on the monopile (left panel) and top-view drawing of the shaker, showing the cogwheels that ensure synchronized revolution of the masses (right panel).

Figure 5.6: Aerial photo showing the shaker on MP45 (the foundation pile of turbine W27), the mobilized barges and crane.

The shaker was calibrated in a test centre by connecting it to a rigid frame which was placed on a large-mass concrete foundation slab. An extensive study was performed on the recorded data from the different force transducers that were placed between the shaker and the rigid frame [134]. This study determined an effective arm R for the different setups, which can be used to compute the centrifugal force amplitude:

$$F = m\omega^2 R. \tag{5.1}$$

Here ω is the angular frequency at which the mass m of the shaker is rotating. The products of the effective arm and mass for the 3 setups (including for instance the mass of spacer rings used to install the plates and manufacturing imperfections) can be found in Table 5.1. The table additionally lists the considered frequency ranges of excitation and the associated maximum and minimum forces as applied on the MP. Finally, for later use (Section 5.3.1), also the force ratio between the setups for excitation at equal frequency is given.

	Arm x mass [mkg]	Force ratio [-]	Performed freq. range [Hz]	Min. force [kN]	Max. force [kN]
Heavy weight	239.32	1	1.04 - 4.03	10.31	153.42
Middle weight	88.76	0.37	1.06 - 6.70	3.95	157.31
Light weight	32.08	0.13	5.04 - 8.68	32.15	95.40

Table 5.1: Conducted tests analyzed in the current work

Three types of tests were conducted with the shaker: a constant frequency sweep (constant increase of ω), a step-wise increase of the frequency aimed at creating steady-state conditions during the constant-frequency plateaus, and an emergency stop aimed at decay tests. Unfortunately, the decay data seems to indicate that the motions of the MP were damped out faster than the time it took for the shaker to come to a standstill, making it challenging to analyze this data. The current work only considers the step-wise tests, in which it is assumed that steady-state conditions of the system have been reached. Fig. 5.7 gives an example time trace of the revolutions per second (RPS) of the tachometer recording during the step-wise test with the Middle weight setup.

Time windows were manually selected for a series of frequency plateaus for each weight setup. The start and end points of these windows were selected such that, based on visual inspection of the signals, no transients were included (resulting from a shift in excitation frequency). Each signal within these time windows (each frequency plateau) was low-pass filtered using a cut-off frequency of 1.5 times the considered excitation frequency. The location of this cut-off frequency was verified to have negligible influence on the amplitudes at the frequency of interest. After removing the zero-frequency component, all the maxima (peaks) within the window were selected for each of the considered sensors: strain gauges 2A,2C - 7A,7C and the 3 accelerometers, see Fig. 5.4. The mean of the selected maxima was taken as the steady-state amplitude of the signal. We used the mean of the amplitudes of strain gauges A and C as the strain amplitude

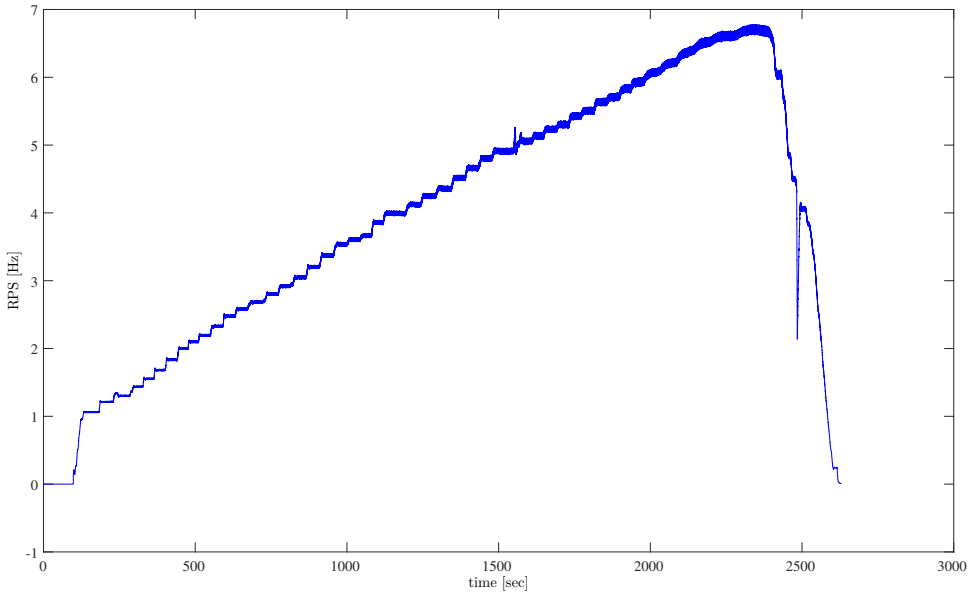

Figure 5.7: Tachometer signal for the step sweep of the Middle weight setup, showing the constant-frequency plateaus.

for the associated height on the pile. Henceforth, these measured strain amplitudes will be indicated with ϵ_i with $i = 2,..,7$. Fig. 5.8 shows an example of the filtered strain gauge responses of the 2.68 Hz frequency plateau (Middle weight setup). The selected maxima are encircled and the steady-state (mean) amplitudes are indicated with the horizontal red lines. The lowest panel of Fig. 5.8, containing the lowest strain gauge (no. 2) response, shows a less steady signal. The low strain amplitudes occurring at this level in the pile, being excited with a small force amplitude (25.19 kN), are close to the resolution of the strain gauges ($0.1\mu\epsilon$) and the noise contamination is relatively large. We thus have to be aware of less reliable recordings for low forcing levels and locations along the pile where limited bending moments occur.

The corresponding responses of the accelerometers are shown in Fig. A.1 in Appendix A. The signals of the accelerometers on the pile (accelerometer 1 and 2, located 1.07 m below the accelerometer on the shaker) were projected onto the direction of the shaker excitation. The amplitudes of this single signal will henceforth be called A_p and those recorded by accelerometer 3 installed on the shaker A_{sh}.

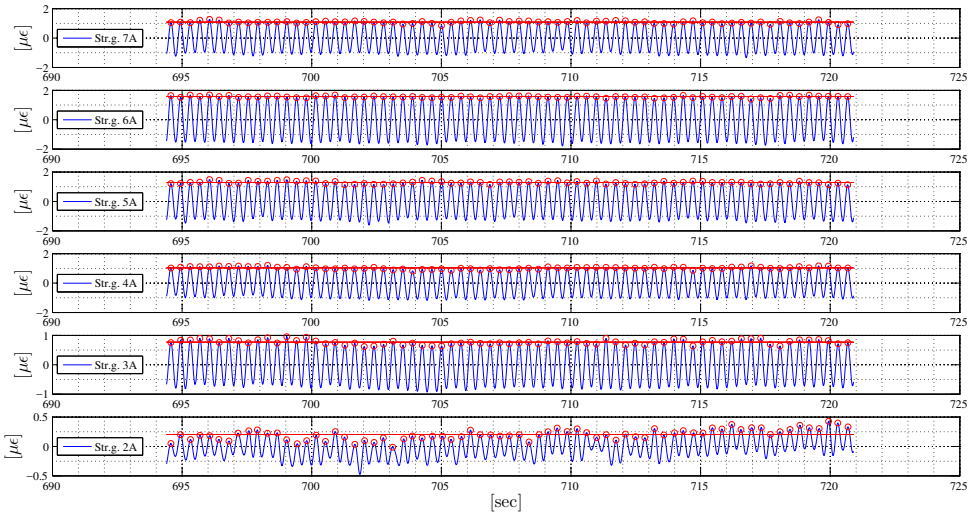

Figure 5.8: Strain gauge responses after low-pass filtering for frequency plateau 2.68 Hz, Middle weight setup. The red circles indicate the picked peaks, of which the mean was taken over the selected window (red line).

5.3. MODEL-BASED IDENTIFICATION & EFFECTIVE STIFFNESS VALIDATION

In the sequel, an assessment of the stiffness, damping and possible inertia properties of the observed SSI is given, in which we focus on the performance of $k_{eff}(z)$ which was derived in Section 4.2.2 with the effective stiffness method. For the selected (excitation) frequency plateaus of the three weight setups, the measured strain and acceleration amplitudes are compared to those modeled using $k_{eff}(z)$, Fig. 4.6, for a beam on Winkler foundation model. The local effective stiffness method yielding $k_{eff}(z)$, will be evaluated/validated by assessing the mismatch between modelled and measured pile response by calculating a single correction factor γ to $k_{eff}(z)$ that minimizes this mismatch. The results of the analyses lead us to consider three 1D models to be used for this minimisation, which will be presented in the next subsections: first, a Timoshenko beam on Winkler foundation, which we will call the basic model. Second, this basic model is extended to include a soil-mass resonance effect in which the soil has its own degree of freedom. In the last subsection 5.3.3, instead of the soil acting as a separate resonator, the inertia of the soil is accounted for by means of an added pile mass. In Section 5.4 the identification results and possible implications are further discussed, and we additionally check the performance of the p-y stiffness profile.

5.3.1. BASIC 1D MODEL

A graphical representation of the basic Timoshenko beam on Winkler model used for the stiffness optimisation is given in Fig. 5.9, in which $u(z)$ and $\psi(z)$ are the frequency domain displacements and rotations of the pile respectively. m_2 represents the mass of the internal air-tight platform (5000 kg). Due to the presence of this concentrated mass at 3.5 m below the top of the pile, the model domain is split into 2 regions at which the displacements and rotations (and their derivatives) are solved for. The subscripts "1" and "2" for the displacements and rotations indicate these regions. The concentrated mass m_1 in the model represents the local masses of the MP top flange (4508 kg) and that of the shaker (4500 kg). The trunnions (1800 kg) lie in between these 2 locations; therefore, their mass is partly assigned to m_1 and partly to m_2. Furthermore, F is the horizontal excitation force amplitude induced by the shaker, M is the overturning moment amplitude caused by the presence of a small vertical lever arm (of on average 0.48 m) between the mid-point of the eccentric masses of the shaker and the MP flange. $k_{eff}(z)$ is the 1D effective Winkler stiffness and $c(z)$ an effective viscous soil damping that covers the sum of the occurring soil damping mechanisms. In this assessment it is assumed that the shape of the damping dashpots $c(z)$ is related to the shape of the SSI stiffness profile $k_{eff}(z)$ and will be tuned as

$$c(z) = \alpha k_{eff}(z), \tag{5.2}$$

with α having unit [s] in case of viscous damping (as assumed here). Note that we assume that all damping in the system originates from the interaction with the soil. This is expected to be an acceptable assumption given the expected relatively small damping contributions from the hydrodynamic interaction and the steel hysteresis.

$EI(z)$ is the product of the Young's modulus of the structural steel E and the second moment of area of the cross section of the pile $I(z)$. Due to the fact that the properties of the pile are not constant over the length of the pile, the modelled pile parameters are also made z-dependent. $GA\kappa(z)$ is the product of the shear modulus of the structural steel G, the area of the cross section $A(z)$ and κ, as previously explained, is the cross section-dependent Timoshenko shearing coefficient for which $\kappa = 0.53$ was assumed. $\rho A(z)$ is the product of the mass density $\rho(z)$ and $A(z)$. Apart from the steel mass, a soil plug with a density of 1500 kg/m^3 (as was assumed in design) was added to the mass density of the embedded part of the pile. The top 2.75 m of the soil plug was removed and replaced by water, as in reality this soil was excavated from the inner part of the MP to access the embedded electricity cables (see the cable hole in Fig. 5.4). Additionally, in another study [135] it was pointed out that for a stand-alone MP, the quantification of the added mass of the water can have a noticeable effect on the first natural frequency. Therefore, the proposed frequency- and deflection-shape dependent added mass was taken into account. Besides the properties named here, additional model properties are included in Table A.1 in Appendix A.

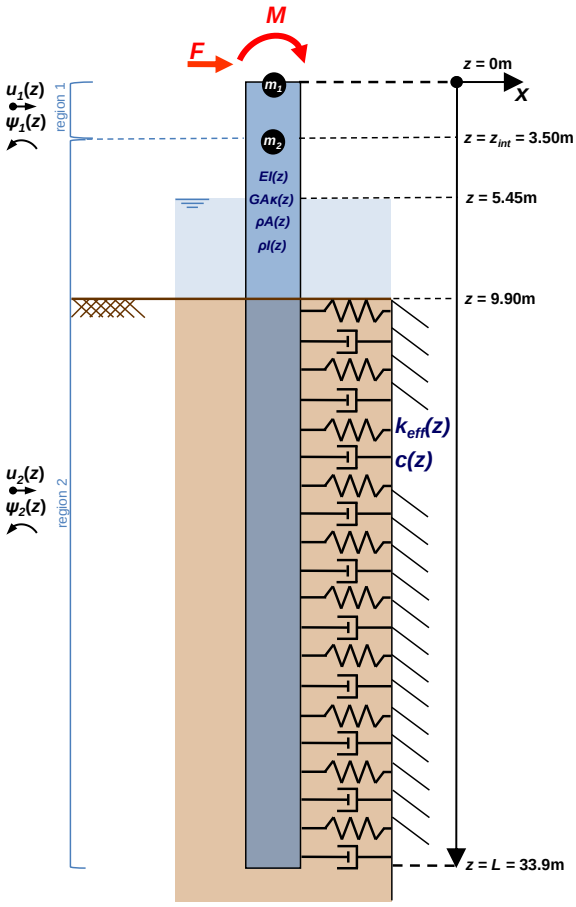

Figure 5.9: Graphical representation of the basic 1D model, the used reference frame and sign conventions. The symbols are defined in the main text.

If we assume that steady-state conditions apply for the selected amplitudes (Section 5.2), and that the horizontal harmonic excitation force $\bar{F}$ (time domain) can be approximated by $\bar{F} = Fe^{i\omega t}$, the equations of motion of the Timoshenko beam model can be expressed in the frequency domain as [129]:

$$GA\kappa\left(\frac{d^2u}{dz^2} - \frac{d\psi}{dz}\right) - K(z)u = 0, \tag{5.3}$$

$$GA\kappa\left(\frac{du}{dz} - \psi\right) + EI\frac{d^2\psi}{dz^2} + \omega^2\rho I\psi = 0, \tag{5.4}$$

with the dynamic stiffness $K(z)$ equal to

$$K(z) = k_{eff}(z) + i\omega c(z) - \omega^2\rho A. \tag{5.5}$$

Note that for brevity we omit the z-dependence of the structural properties. Additionally, due to the minor and localized z-dependence of the wall thickness and for the

considered range of frequencies, we verified that constant pile properties in the second order terms given above can be assumed.

The considered boundary conditions are:

$$GA\kappa\left(\frac{du_1}{dz}-\psi_1\right)\Big|_{z=0} = -F-\omega^2 m_1 u(0), \tag{5.6}$$

$$EI\frac{d\psi_1}{dz}\Big|_{z=0} = M, \tag{5.7}$$

$$GA\kappa\left(\frac{du_2}{dz}-\psi_2\right)\Big|_{z=L} = 0, \tag{5.8}$$

$$EI\frac{d\psi_2}{dz}\Big|_{z=L} = 0. \tag{5.9}$$

The presence of m_2 at $z = z_{int} = 3.5$ m (Fig. 5.9) can be taken into account by formulating the interface conditions:

$$u_1(z_{int}) - u_2(z_{int}) = 0, \tag{5.10}$$

$$\frac{du_1}{dz}\Big|_{z_{int}} - \frac{du_2}{dz}\Big|_{z_{int}} = 0, \tag{5.11}$$

$$GA\kappa\left((\frac{du_1}{dz}-\psi_1)-(\frac{du_2}{dz}-\psi_2)\right)\Big|_{z_{int}} = \omega^2 m_2 u_1(z_{int}), \tag{5.12}$$

$$\frac{d\psi_1}{dz}\Big|_{z_{int}} - \frac{d\psi_2}{dz}\Big|_{z_{int}} = 0. \tag{5.13}$$

The above relations ensure (from top to bottom) the continuity of displacement and slope, a dynamic shear force balance, and continuity of bending moment at the interface location.

For the excitation of the model we can apply the force of the shaker (equation 5.6). Alternatively, we can use the acceleration amplitude that was measured by the accelerometer attached to the shaker. In that case, the boundary condition given by equation 5.6 is replaced by

$$u_1(0) = \frac{A_{sh}}{\omega^2}, \tag{5.14}$$

in which A_{sh} is the steady-state acceleration amplitude measured on the shaker. In calculating the modeled response by either using equation 5.6 (force-controlled) or 5.14 (acceleration-controlled) as a boundary condition, a mismatch was observed between these two modeled responses. If we presume that measurement errors can be neglected, this mismatch could be caused by the fact that the model does not fully reflect the correct physics of the system. In the following analyses, both cases (force- and acceleration-controlled) were considered to determine what stiffness correction factor is needed for the modeled response to match the measurements.

STIFFNESS OPTIMISATION

To reduce the mismatch with the measurements, the stiffness profile of the 1D model was optimized by applying a single factor, γ, to the 1D effective stiffness profile $k_{eff}(z)$. In this, we thus assume the shape of the previously derived effective 1D stiffness to be correct, but we search for a (single) correction factor γ so that the predicted response globally matches the measured one for each of the selected frequencies; we assign equal weight to the fit of all 6 strain gauge positions and the 2 accelerometers. The stiffness correction factor γ is defined as the factor applied to the effective stiffness $k_{eff}(z)$ (Fig. 4.6) that minimizes the global root mean square error (L_2 norm):

$$\min_{\gamma} \left| \left(\frac{\sum_{i=2}^{i=7} |\epsilon_i - \overline{\epsilon}_{i(\gamma)}|^2}{\sum_{i=2}^{i=7} |\epsilon_i|^2} + \frac{|A_{sh} - \overline{A}_{sh(\gamma)}|^2}{|A_{sh}|^2} + \frac{|A_p - \overline{A}_{p(\gamma)}|^2}{|A_p|^2} \right)^{\frac{1}{2}} \right|. \tag{5.15}$$

The overlined symbols in Eq. 5.15 indicate that these are the corresponding modeled quantities. The modeled strain is computed as

$$\overline{\epsilon}_i = \frac{D}{2} \left| \frac{d\psi}{dz}|_{z_i} \right|, \tag{5.16}$$

with D the diameter of the pile.

RESULTING FREQUENCY-DEPENDENT STIFFNESS

The resulting stiffness correction factors γ for the three setups are given in Fig. 5.10, in which the dotted lines are the factors obtained with a force-controlled model (Eq. 5.6) and the continuous lines are those obtained when using an acceleration-controlled model (Eq. 5.14). The green line reflects the aim; a factor γ of 1 indicates a spot on match.

In Fig. 5.10 the following trends can be observed. First, the stiffness slightly decreases with frequency and reaches a minimum situated between 4.5 and 5.5 Hz, after which it increases again. The stiffness thus seems frequency dependent; $\gamma = \gamma(f)$. Second, a force or displacement dependency of the stiffness can be observed: from the more or less parallel lines of the Heavy and Middle weight setup (higher stiffness for a lighter weight/smaller force), but also from the parallel lines of the Middle and Light weight setup. As a reference, the force ratios of the setups for an equal excitation frequency are listed in Table 5.1. Finally, the first point for the Middle weight setup is an outlier, and should therefore not be considered in defining a trend.

It could be reasoned that the actual stiffness is somewhere in between the two factors given in Fig. 5.10 (force- and acceleration-controlled models). Fig. 5.11 gives an example fit of the force-controlled and acceleration-controlled modelled strains with respect to the measured strains of the Heavy weight setup, with excitation at 1.045 Hz, for a mean γ of 0.64 applied to the original effective 1D stiffness profile. For extra insight, also the modelled shear forces and displacements are shown.

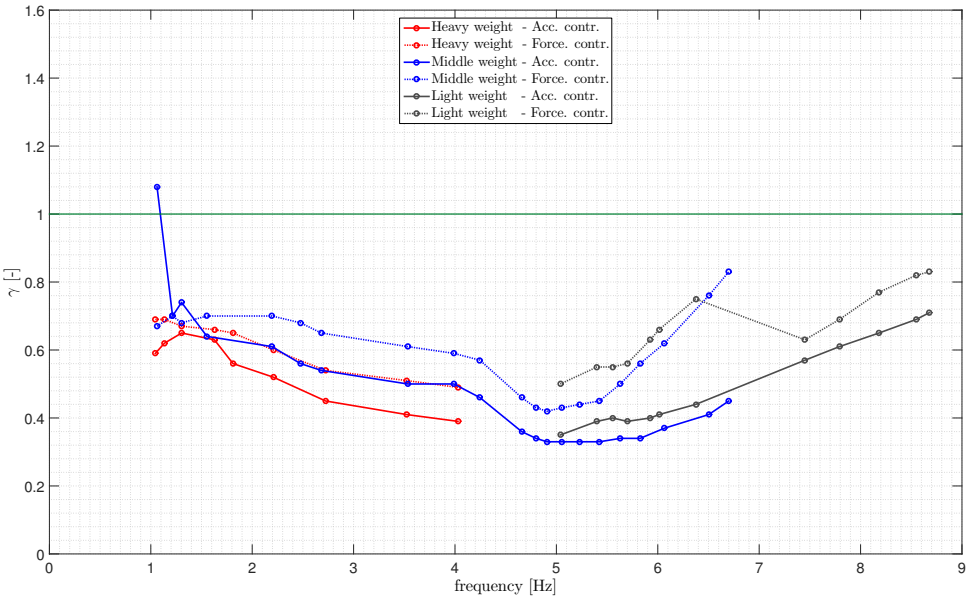

Figure 5.10: Correction factors γ applied to the effective 1D stiffness profile (as presented in Fig. 4.6) to minimize the mismatch between modeled and measured response amplitudes of the 3 weight setups. The continuous lines represent the factors found with an acceleration-controlled model, and the dotted lines are the factors found with a force-controlled model. The green line reflects the aim; a factor γ of 1 indicates a spot on match of the measured and the (unadjusted) modelled response.

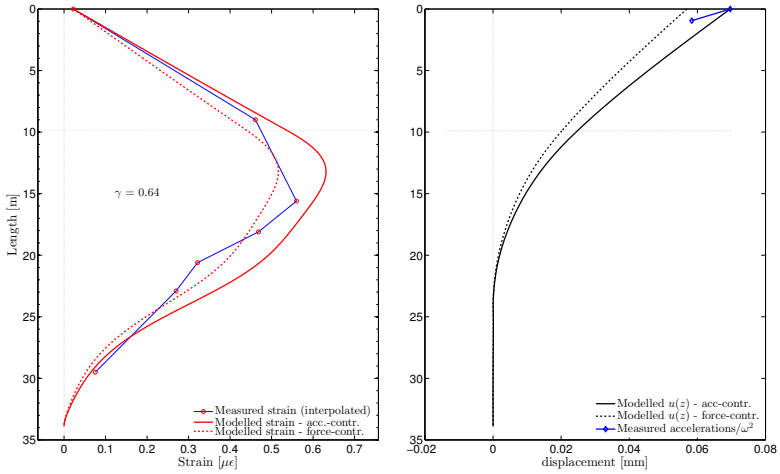

Figure 5.11: Match in strains with a stiffness correction factor γ equal to the mean of the force- and acceleration-controlled factors from Fig. 5.10, for the Heavy weight setup, excitation frequency of 1.045 Hz. The absolute values of both the acceleration- and force-controlled modelled responses are shown in terms of shear force and strain (left panel) and displacements (right panel). The vertical axis is the length of the pile, where the mudline is indicated at 9.9 m.

To overcome the discrepancy between the force- and acceleration-controlled responses, we consider internal transfers of the system, sometimes also referred to as (internal) transmissibility: the ratio between the strain amplitudes at several locations and the displacement amplitudes, u_p, retrieved from the accelerometer attached to the top of the pile ($u_p = A_p/\omega^2$, assuming no drift in the displacements or velocities (integration constants equal to zero)). The advantage of considering this quantity is that it is (excitation) source independent. In optimising the stiffness of the 1D model to match the transmissibilities of the measurements, the following minimisation function is used:

$$\min_{\gamma} \left| \left(\frac{\sum_{i=2}^{i=7} |T_i - \overline{T}_{(\gamma)i}|^2}{\sum_{i=2}^{i=7} |T_i|^2} \right)^{\frac{1}{2}} \right|, \tag{5.17}$$

with the (amplitude of the) internal transmissibility function given as

$$T_i(f) = \frac{\epsilon_i(f)}{u_p(f)} = \frac{\epsilon_i(f)\omega^2}{A_p(f)}. \tag{5.18}$$

The resulting stiffness correction factors γ are given by the thick lines in Fig. 5.12. As a reference, the γ factors of Fig. 5.10 are also included with thin lines. The acceleration-controlled model was used to calculate the transmissibilities, but the force-controlled model led to nearly the same correction factor γ - indicating the desired source independency. Therefore, henceforth only the transmissibilities will be considered for further stiffness optimisation.

Fig. 5.13 shows the internal transfers (Eq. 5.18) corresponding to the frequency-dependent stiffness γ of the Middle weight setup (thick blue continuous line in Fig. 5.12). In the sequel, we will only considering transfer functions and transmissibilities retrieved for the Middle weight setup only, as the tested frequency range for this setup is broadest. As we do not vary the shape of the stiffness profile retrieved from the 3D model, there is no good match for all individual sensor locations and for all frequencies in Fig. 5.13. Still, the internal transfers of the two strain gauges located closest to the top (where the largest strains occur; red and green lines in Fig. 5.13) match reasonably well for the entire frequency range.

To assess the resonance of the system and estimate the effective damping, we can compute (the amplitude of) the transfer functions by dividing the responses by the input force (Eq. 5.1):

$$H_i(f) = \frac{\epsilon_i(f)}{F(f)}. \tag{5.19}$$

When using the stiffness reduction factors as given by the thick blue continuous line in Fig. 5.12 (optimisation for transmissibility for the Middle weight setup), we get (force-controlled) modelled transfer functions given in Fig. 5.14; the corresponding measured transfer functions are included for comparison. In Fig. 5.14 we observe a resonance

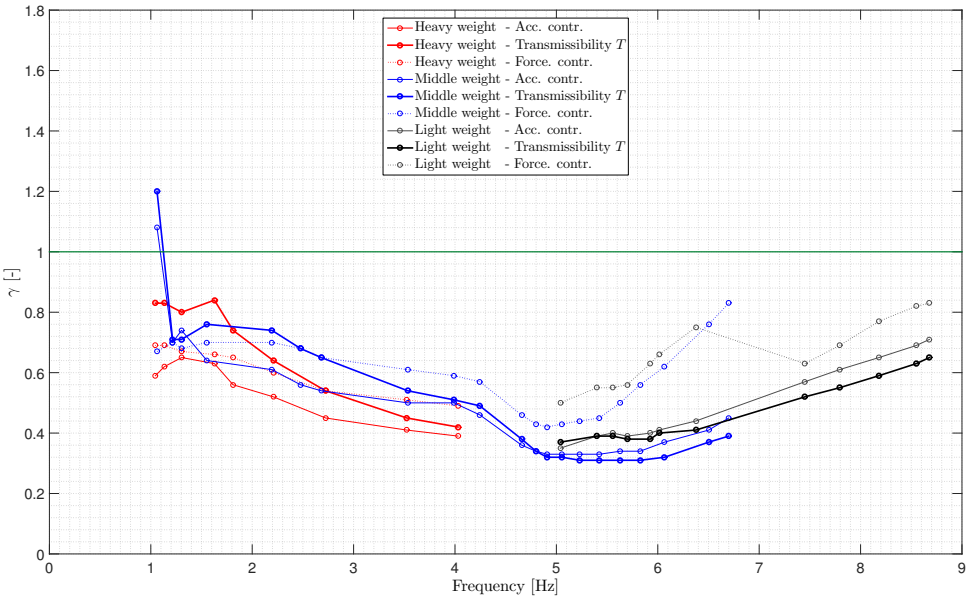

Figure 5.12: Factors γ applied to the effective 1D stiffness profile (as presented in Section 4.2.2) to minimize the mismatch between modeled and measured transmissibilities T (Eq. 5.17) of the 3 weight setups (thick continuous lines). As a reference, the factors retrieved for direct minimisation of strain and acceleration error (Eq. 5.15) with the acceleration-controlled (thin continuous lines) and force-controlled models (thin dotted lines) are shown.

frequency around 5.4 Hz. In addition, the figure shows that the dotted lines of the modelled response do not completely match the measured (continuous lines) for all strain gauges, but rather correspond in a global way (as discussed previously). Furthermore, we see that the modeled strain transfer functions for numbers 3-6 draw closer towards each other at resonance and post-resonance than those that were measured. This is related to a localized smaller dynamic stiffness (Eq. 5.5) in the modelled response at these frequencies; either the modelled inertia contribution or the modelled frequency-dependent stiffness is not fully correct. This can also be clearly seen in fits for higher frequencies shown in Figs. A.4 and A.5 in Appendix A; the modelled response shows larger inertia effect (or smaller stiffness) than measured for depths larger than 17 m. Finally, the modeled dynamic stiffness (Eq. 5.5) for the post-resonance regime seems to be a bit larger than measured, indicating either too small mass $\rho A(z)$ or too large stiffness.

DAMPING ESTIMATION

The resonance peak allows us to tune the dashpot coefficients $c(z)$ for the modeled response. In actual fact, finding the matching stiffness and damping is done in 1 or 2 iterations: with the updated dashpot coefficients, the stiffness correction factors are re-assessed, etc. For the modeled transfer functions in Fig. 5.14, $\alpha = 2.08 \cdot 10^{-2}$s (Eq. 5.2). Using the obtained damping coefficients and a mean stiffness correction factor γ

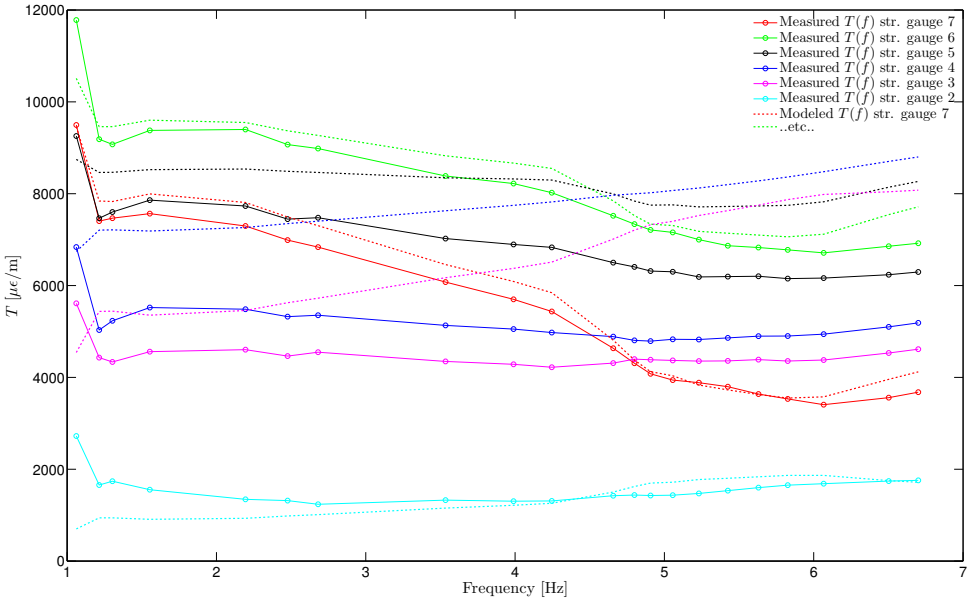

Figure 5.13: Measured (continuous lines) and modeled (dotted lines) transmissibility functions (Eq. 5.18) of the strain gauges for the Middle weight setup, using factors on stiffness γ given by the thick blue line given in Fig. 5.12: optimisation for transmissibility.

of the frequencies around resonance to simulate a response, we extracted the damping contribution of the soil with the half-power bandwidth method [136], yielding a critical damping ratio of $\zeta = 20\%$ for this stand-alone MP. Note that the dashpots coefficients are tuned based on a visual fit of the transfer functions. The stated damping ratio should therefore be considered an estimate. An analysis of the variance of this number is beyond the scope of this research. In Section 5.4.4 we discuss how this damping contribution could relate to the damping of the full OWT structure.

Concluding this subsection, we may state that a frequency-dependent stiffness is needed to match the measurements with the response predicted by a beam on Winkler foundation model as shown in Fig. 5.9. Three frequency regimes can be distinguished: a pre-resonance regime (up to 4.2 Hz) in which the stiffness slightly decreases with frequency, a resonance regime (4.2 - 6 Hz) in which the stiffness decreases further, and a post-resonance regime where the stiffness sharply increases (Fig. 5.12). Although we lack measurements below 1 Hz, it is expected that the effective 1D stiffness as presented in Fig. 4.6 overestimates the true stiffness at low frequencies with about 22% ($\gamma = 0.78$), see low frequency $\gamma(f)$ in Fig. 5.12. Optimising the stiffness to match the measured internal transmissibilities seems a good approach to overcome the ambiguity in choosing the correct excitation boundary condition in the model. From the transfer functions, the effective damping ratio of the system was estimated to be 20% of critical - assumed to be mainly caused by the interaction with the soil. In the next sections we investigate whether the observed frequency dependency of the stiffness of the system

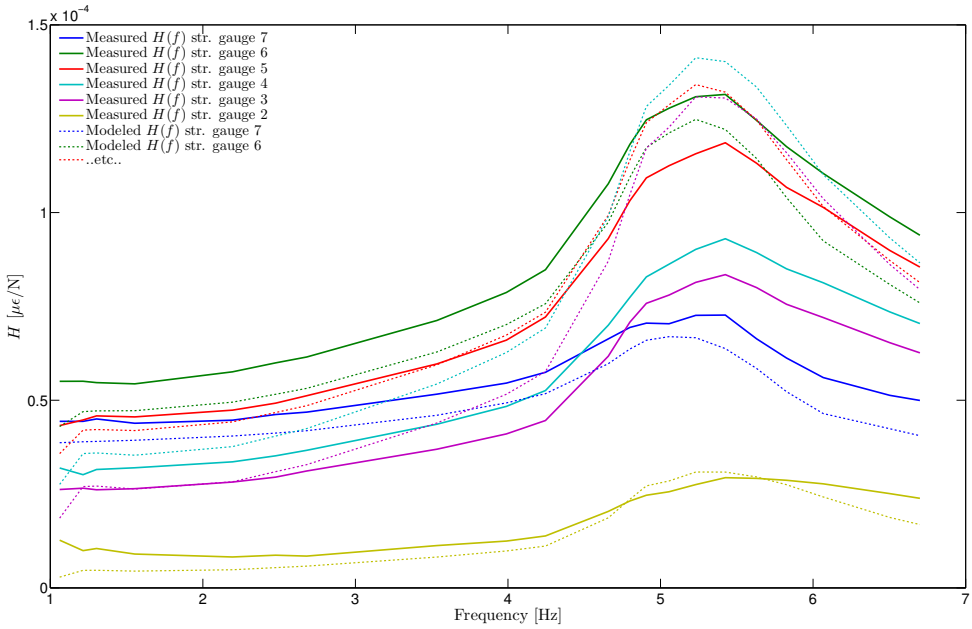

Figure 5.14: Measured (continuous lines) and modeled (dotted lines) transfer functions for the strain gauges along the pile (Middle weight setup). For the modeled response, the factors on stiffness as given by the thick blue line given in Fig. 5.12 (optimisation for transmissibilities: Eq. 5.17) were applied to the effective 1D soil stiffness profile given in Fig. 4.6. The dashpot coefficients were tuned to a value of $c(z) = 2.08 \cdot 10^{-2} k_{eff}(z)$, yielding a critical damping ratio of 20%.

can be attributed purely to the effective soil stiffness (as was assumed in this section), or whether other mechanisms might be responsible for the measured response.

5.3.2. SOIL RESONATOR MODEL

The resonance peak observed in Fig. 5.14 and the associated decrease in stiffness around these frequencies (Fig. 5.12) can be related to the first resonance frequency of the monopile-soil system. However, it might also be related to a resonance of the soil itself; i.e., a resonance of the layered system or a resonance as commonly observed in cavity expansion problems [137]. If this is the case, the soil acts as a resonator, highly influencing the total system response at the resonance and post-resonance frequencies. To assess this possibility, a distributed resonator mass $M_s(z)$ is added to the 1D model, as shown in Fig. 5.15.

The addition of this mass to the 1D model only modifies the soil-resistance term in Eq. 5.3 and the expression for the dynamic stiffness (Eq. 5.5), while the rest of the governing equations (5.4, 5.6 - 5.13) remain unchanged. Eq. 5.3 becomes:

$$GA\kappa\left(\frac{d^2u}{dz^2}-\frac{d\psi}{dz}\right)-\left(2\widetilde{K}(z)\frac{(2\widetilde{K}(z)-M_s(z)\omega^2)}{(4\widetilde{K}(z)-M_s(z)\omega^2)}-\omega^2\rho A\right)u=0, \tag{5.20}$$

with

$$\widetilde{K}(z)=k_{eff}(z)+\mathrm{i}\omega c(z), \tag{5.21}$$

and

$$M_s(z)=\frac{2k_{eff}(z)}{(2\pi f_s)^2}, \tag{5.22}$$

with f_s the resonance frequency of the soil. In the case the soil acts as a resonator, the effective soil stiffness $k_{eff}(z)$ can be assumed to be frequency-independent; the decrease in resistance with frequency observed in Fig. 5.12 is then attributed to the dynamic interaction with the soil mass $M_s(z)$. This frequency-independent stiffness can be identified using the optimisation results for the lower frequencies (note that, for low frequencies, the soil resistance term in Eq. 5.20 equals that of the basic model (Eq. 5.3)). Neglecting the outlier of the lowest frequency of the Middle weight setup in Fig. 5.12 (blue line), taking an average constant γ of 0.78 for the lower frequencies seems reasonable. In matching the transfer functions by tuning the resonator frequency f_s (therefore the magnitude of the soil mass M_s, Eq. 5.22) and the damping $c(z)$, it was however noticed that the shape of the resonance peak was not well captured when assuming frequency independent stiffness. Therefore a stiffness optimisation was performed of which the resulting $\gamma(f)$ are presented in Fig. 5.16. This $\gamma(f)$ was determined with $f_s=6.7$ Hz and a damping tuning coefficient $\alpha=7.9\cdot10^{-3}$ - based on the initial fit of the transfer functions.

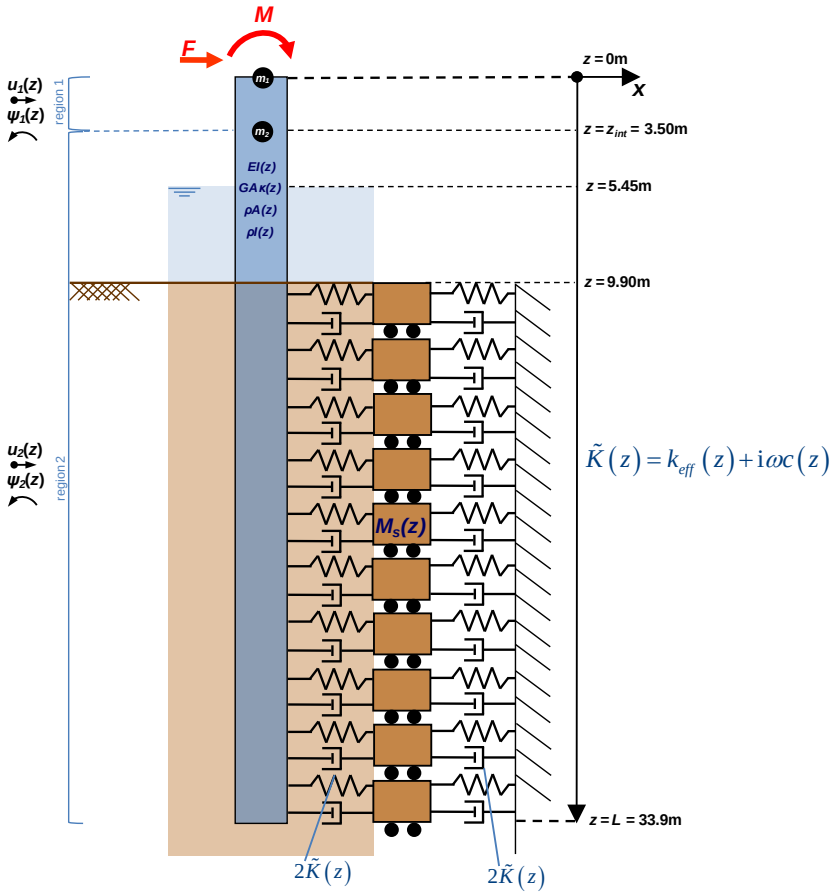

Figure 5.15: The 1D model including a distributed resonator.

In Fig. 5.16 we indeed observe - due to the presence of the resonator - a more constant stiffness ($\gamma(f)$) for the pre-resonance and resonance regime, a drop in stiffness in the post-resonance regime, and eventually a similar stiffening as observed in Fig. 5.12 for the highest frequencies. Using this $\gamma(f)$, the soil resonator frequency was further tuned to $f_s = 6.95$ Hz and damping tuning coefficient $\alpha = 9.6 \cdot 10^{-3}$ to yield the transmissibility and transfer functions as presented in Figs. 5.17 and 5.18. Applying the same damping determination method as described in previous Section 5.3.1, these dashpot coefficients yield a critical damping ratio of $\zeta = 12.6\%$. Note however, that the presence of the resonator causes the main resonance peak to have a less symmetric shape, making the half-power bandwidth method only an approximate method to determine the damping of this system.

The resulting matches of this soil-mass resonator model with the measurements in terms of transmissibilities and transfer functions are acceptable, however, those of the basic model seem better (Figs. 5.13 and 5.14). Especially the match of the transfer functions for the post-resonance regime is better using the basic model; in case of the resonator model, the dynamic stiffness seems too large for these frequencies. Additionally, the transmissibility functions seem to match better using the basic model.

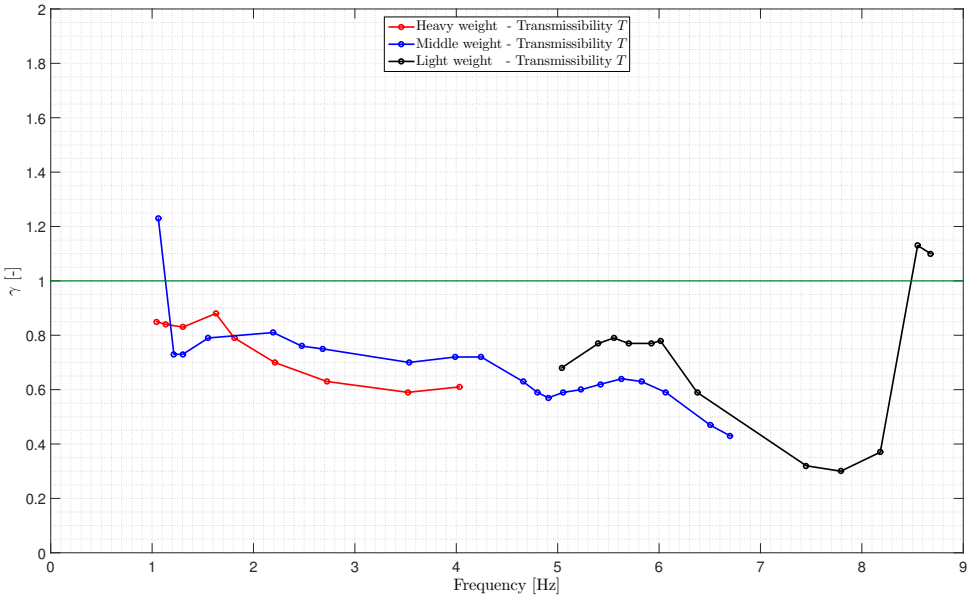

Figure 5.16: Stiffness correction factors γ found for optimising a mass-resonator model with $f_s = 6.7$ Hz (Eq. 5.22) and $\alpha = 7.9 \cdot 10^{-3}$, to match the measured internal transmissibility function $T_i(f)$ (Eq. 5.18).

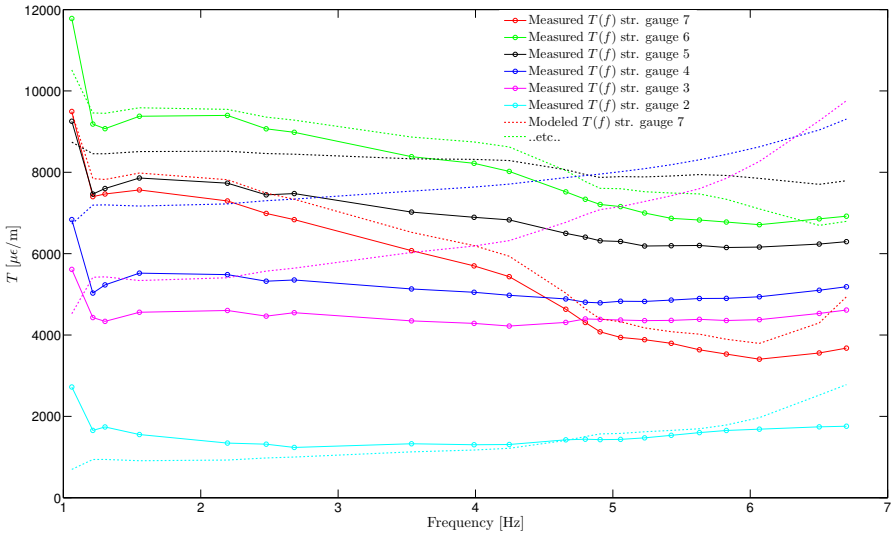

Figure 5.17: Measured (continuous lines) and modeled (dotted lines) transmissibility functions (Eq. 5.18) of the strain gauges for the Middle weight setup. The modeled response is calculated with the mass-resonator model of Fig. 5.15 with a frequency-dependent stiffness correction factors $\gamma(f)$ (blue line, Fig. 5.16) applied to the effective 1D soil stiffness profile. Furthermore, $\alpha = 9.6 \cdot 10^{-3}$, and $f_s = 6.95$ Hz.

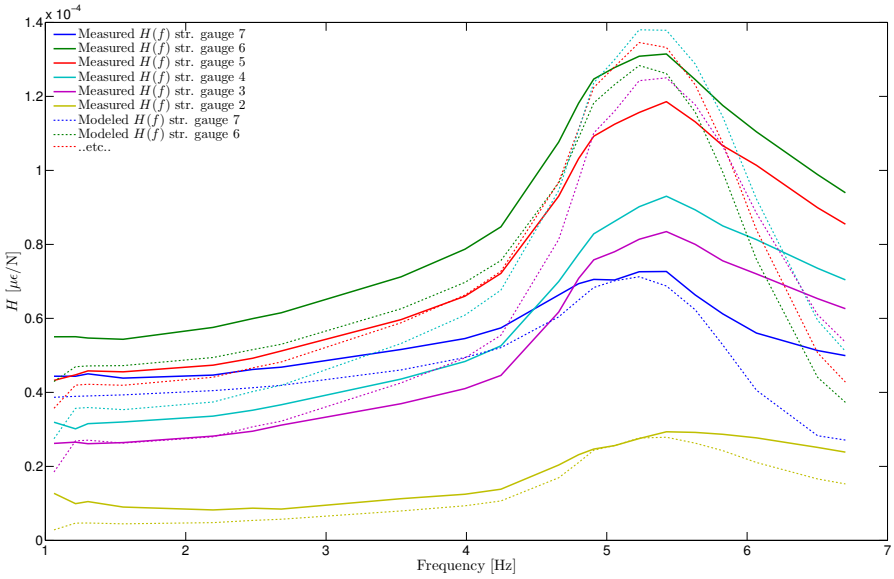

Figure 5.18: Measured (continuous lines) and modeled (dotted lines) transfer functions for the strain gauges along the pile (Middle weight setup). The modeled response is calculated with the mass-resonator model of Fig. 5.15 with frequency-dependent stiffness correction factors $\gamma(f)$ (blue line, Fig. 5.16) applied to the effective 1D stiffness profile. The dashpot coefficients were tuned to $\alpha = 9.6 \cdot 10^{-3}$, yielding a critical damping ratio of 12.6%. The resonance frequency of the soil was tuned to $f_s = 6.95$ Hz.

5.3.3. ADDED MASS MODEL

In the case the observed decrease in dynamic stiffness (Eq. 5.5) with frequency is indeed caused by extra mobilized inertia, this can also be due to a more direct added mass of the soil in the vicinity of the pile (as opposed to the previous analyzed soil resonator system). This is incorporated in the basic model (Fig. 5.9) by multiplying the embedded part of the distributed mass $\rho A(z)$ by a factor η. Also in this case it was observed that a constant stiffness with frequency (again a γ of 0.78) does not adequately capture the post-resonance regime. Performing an iteration for $\gamma(f)$, η and $c(z)$ (based on transfer functions and stiffness optimisation, Eq. 5.17), yields the final $\gamma(f)$, transmissibility and transfer functions as shown in Figs. 5.19, 5.20 and 5.21, respectively. The soil added mass factor is in this case $\eta = 3.4$ (of the original embedded pile mass) and dashpot tuning coefficient $\alpha = 8.4 \cdot 10^{-3}$, yielding a damping ratio $\zeta = 11\%$ critical for the MP-only system.

In Fig. 5.19 we see - as expected - a more constant, frequency-independent stiffness (as opposed to those found with the basic model) up until the post-resonance regime, after which again a sharp increase in stiffness factors is observed. The transmissibility functions and transfer functions are reasonably matched. However, also this model does not seem to perform better in matching the modelled and measured functions than the basic model (Figs. 5.13 and 5.14). Nevertheless, the match in transfer functions for the post-resonance frequencies is better than that of the soil-mass resonator model (Fig. 5.17).

Concluding, the two models incorporating more mobilized soil mass seem to allow for a frequency-independent stiffness for the pre-resonance regime (up to 4 Hz), however, they do not permit to exclude a frequency dependency of the stiffness for the resonance and post-resonance regimes.

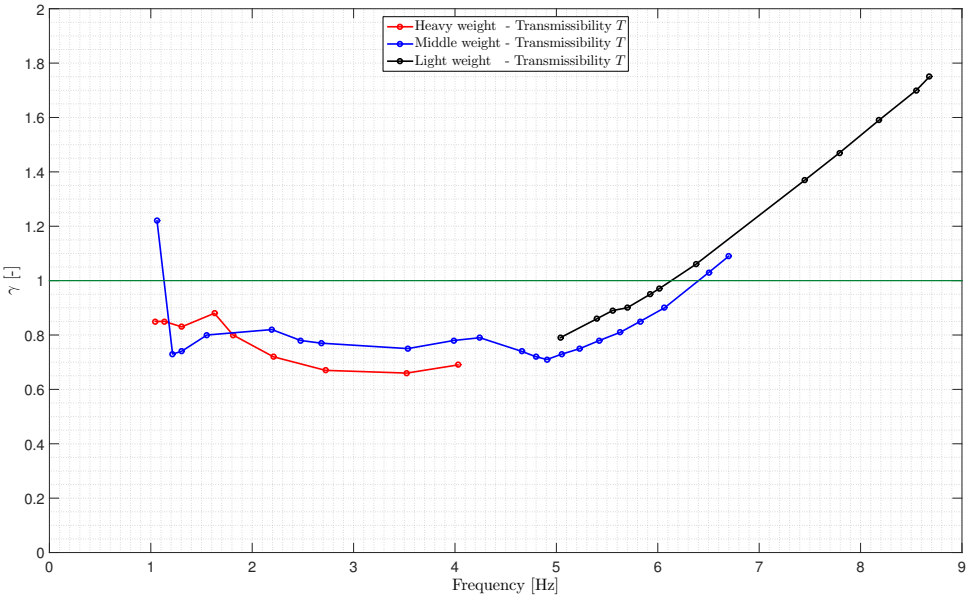

Figure 5.19: Stiffness correction factors γ found for optimising the basic model with an added mass factor $\eta = 3.4$ times the embedded pile mass, and $\alpha = 8.4 \cdot 10^{-3}$, to match the measured internal transmissibility function T.

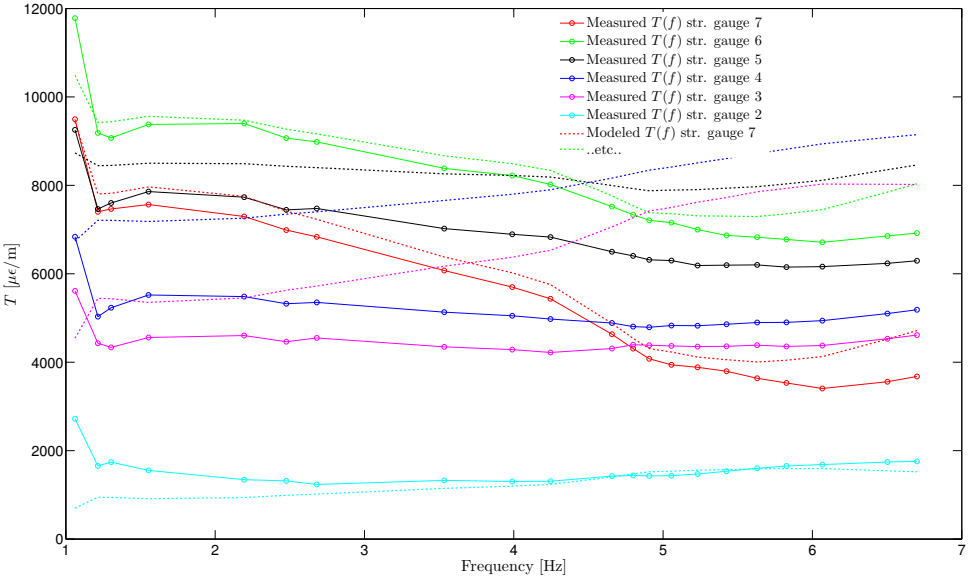

Figure 5.20: Measured (continuous lines) and modeled (dotted lines) transmissibility functions (Eq. 5.18) of the strain gauges for the Middle weight setup. The modeled response is calculated with the basic model including added mass of the soil, with a frequency dependent stiffness correction factor γ (blue line, Fig. 5.19) applied to the effective 1D soil stiffness profile. Furthermore, $c(z) = 8.4 \cdot 10^{-3} k_{eff}(z)$, and an added mass factor $\eta = 3.4$ times the original embedded pile mass.

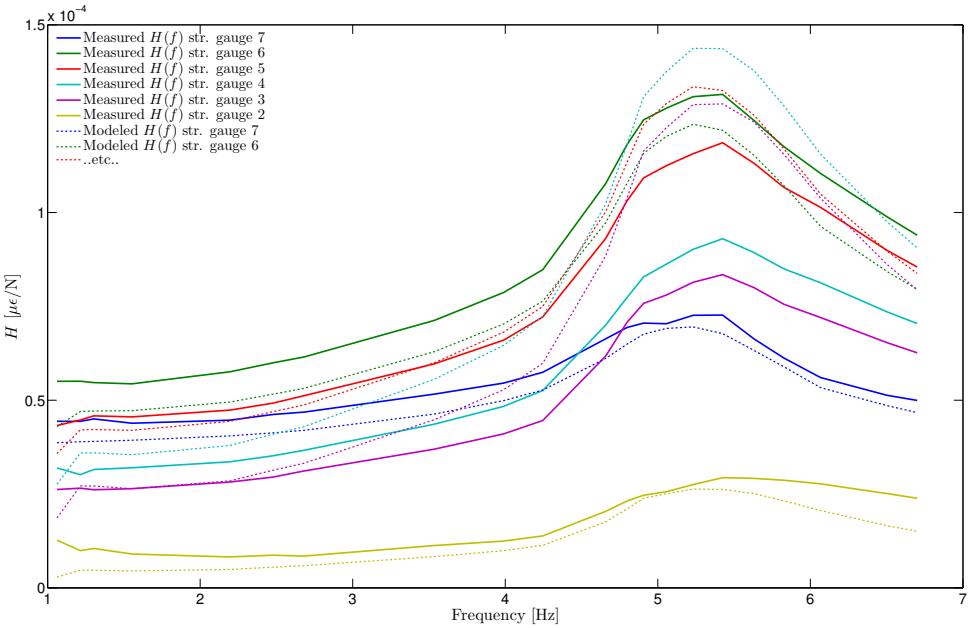

Figure 5.21: Measured (continuous lines) and modeled (dotted lines) transfer functions for the strain gauges along the pile (Middle weight setup). The modeled response is calculated with the basic model of Fig. 5.9 including added (soil) mass for the embedded part of the pile ($\eta = 3.4$), and the frequency-dependent factors on stiffness γ (applied to the effective 1D stiffness) given by the blue line in Fig. 5.19. The dashpot coefficients were tuned to $\alpha = 8.4 \cdot 10^{-3}$, yielding a critical damping ratio of 11%.

5.4. DISCUSSION

In this section we discuss the 3 observed frequency regimes: the low, pre-resonance regime relevant for OWTs, the resonance, and the post-resonance regime. We compare how the design p-y curve stiffness performs in predicting the measurement data, and how the presented findings relate to the preliminary identified full OWT structure fundamental natural frequency. Additionally, the full structure damping and possible soil non-linearity are discussed.

5.4.1. LOW FREQUENCY STIFFNESS VALIDATION - RELEVANT FOR OWT DESIGN: EFFECTIVE 1D METHOD VS p-y METHOD

Irrespective of the assumptions regarding the soil (added) mass, all 3 stiffness optimisation results indicate that the effective 1D stiffness overestimates the occurring stiffness at low frequencies with roughly 20% (γ = 0.78 - 0.8). Although we do not have measurements for frequencies lower than 1 Hz, it is reasonable to assume the stiffness between 0 and 1 Hz to be either higher or equal to that observed at 1-2 Hz. A correction factor of 0.8 is not insignificant, however, given the uncertainty in the characterisation of dynamic soil properties and SSI modelling, the 1D effective stiffness method [78] is deemed promising. Furthermore, it is expected that the method can be improved; a fully linear elastic model was used in which the soil elements were attached to the shell elements of the pile. Nonlinearities such as sliding and release between soil and pile can be incorporated in the future. Finally, another aspect that can bring the measured and predicted stiffness closer together is the pile set-up effect; although there is still much uncertainty in this research field [138], the capacity (and SSI stiffness) of piles in both clay and sand is known to increase with time [139]. The here presented tests were performed 50 days after the installation of the pile, and the "aging" process is known to have time frames larger than 400 days [140].

In judging the performance of the proposed stiffness method [78] it is also relevant to see what strain levels the design standard predicts. As expected, the p-y curve method proved to significantly underestimate the stiffness experienced by the pile. We therefore also computed the stiffness correction factors γ needed to be applied to the p-y initial stiffness to match the measured pile responses. For this exercise, we took a best estimate set of p-y curves; minimum conservatism with respect to the input parameters and half a meter of scour was assumed. For the low frequencies, a γ of roughly 2.4 was needed to best match the internal transmissibilities. The more conservative design p-y curves yielded a γ of around 5. The $\gamma(f)$ for the best estimate p-y initial stiffness is shown in Fig. 5.22. For the p-y stiffness, the low-frequency limit of γ is less clear due to the large spread in stiffness factors for the low-frequency regime. It is expected that this is caused by the fact that this p-y profile is less stiff than the effective 1D stiffness, and also the profile shape might be erroneous.

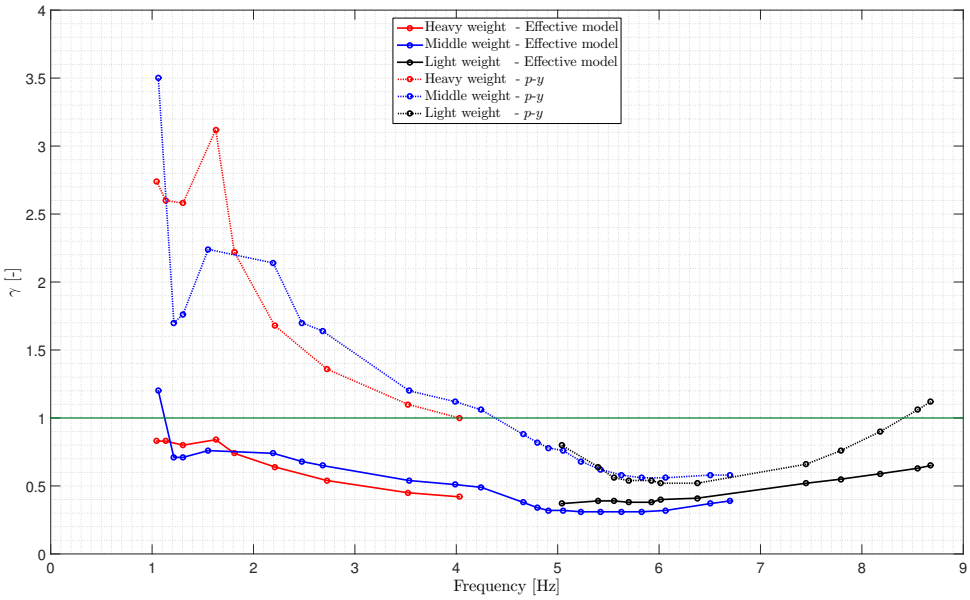

Figure 5.22: Stiffness correction factors γ found for optimising the basic model (Fig. 5.9) with the p-y initial stiffness profile (Fig. 4.6), to match the measured internal transmissibility function T. As a reference, the $\gamma(f)$ for the effective stiffness of Fig. 5.12 are also shown.

5.4.2. RESONANCE FREQUENCY

In Sections 5.3.2 and 5.3.3 we examined whether the observed decrease in dynamic stiffness (Eq. 5.5) in the pre-resonance regime could be attributed to the mobilisation of (extra) soil mass. In the case of soil resonance, the observed resonance in the transfer functions can be related to a natural frequency of the soil layer f_s, which can be approximated as

$$f_{s,n} = \frac{(2n-1)C_s}{4H}, \tag{5.23}$$

where n is the mode number, H the soil layer thickness and C_s the shear-wave velocity. The effective thickness of the layer in this respect is debatable, but often the depth until the location of bedrock is taken. For a first resonance frequency of 5.42 Hz as observed in the transfer functions of the Middle weight setup, and an approximate shear-wave velocity of $C_s \approx 300$ m/s (see Fig. 2.18), the bedrock would be located at about 14 m depth, which we know is not the case. At this part of the Netherlands, bedrock known as the Appelscha formation is present at 60-100 m depth. Assuming the same C_s, the first mode resonance frequency of the soil would be located at 1.25 Hz ($H = 60$ m) or 0.75 Hz ($H = 100$ m). If the observed resonance frequency is indeed associated with the soil, it is more likely to belong to the second soil mode, and in that case the presence of the first mode is, apparently, not observable in our data. Altogether, it is hard to draw solid conclusions about the dynamics (in terms of (added) mass, stiffness and resonance frequencies) of this layered soil system without knowledge about the position of the bedrock and the use of a dynamic continuum model of the soil. Despite the

simplifications of the 1D model, the low-frequency range stiffness can be extracted (as it is more or less equal for the 3 tested models).

We believe however, that the basic model (possibly including some added mass of the soil) is most applicable, as the transfer functions and transmissibilities are best matched with this model. Also, as will be discussed in Section 5.4.4, the estimated soil damping contribution from this model agrees best with the identified total damping of the idling OWT. Finally, at a later stage, additional boat and hammer impact tests were performed on the pile, which confirmed that the observed resonance peak of around 5 Hz is most likely associated with the fundamental frequency of the soil-pile system. Although the hammer test data would not have produced any decisive results without a priori knowledge of the first resonance frequency of the pile (due to a large scatter in the obtained transfer functions), a resonance peak around 5 Hz was observed in some of the records. The boat impacts however, revealed clearly that indeed the post-impact decaying oscillations had a frequency content of around 4.5 Hz (see Fig. A.6 in Appendix A) - slightly lower than during shaker excitation: possibly due to the concrete main platform and a generator that were present during the boat impact, and/or the soil excavation and backfilling that was performed to insert the electric cable (as will be explained in the paragraph here below).

To further assess the performance of the different soil stiffness profiles, the predicted (modelled) fundamental natural frequency f_1 was compared to that identified from preliminary measurements on the operational OWT (full structure). A natural frequency of $f_1 = 0.296$ Hz was identified for the fore-aft bending mode with the turbine in idling state. Four different stiffness profiles were used in an excitation decay simulation (including aerodynamics) using BHawC (the aeroelastic code used by Siemens Wind Power): the effective stiffness profiles $k_{eff}(z)$, the optimized low-frequency profile ($\gamma = 0.78$), the best-estimate p-y stiffness profile and the optimized best-estimate p-y stiffness profile ($\gamma = 2.4$ is estimated to be applicable for the low-frequency limit). The resulting natural frequencies are listed in Table 5.2.

	f_1 **- idling - [Hz]**	Δ **w.r.t. identified**
Identified	0.296	-
p-y **curve**	0.295	-0.34%
p-y **curve** $\gamma = 2.4$	0.300	+1.35%
Eff. stiffness	0.306	+3.38 %
Eff. stiff. $\gamma = 0.78$	0.305	+3.04 %

Table 5.2: Overview of the identified and predicted (BHawC-simulated) natural frequencies using various soil stiffness profiles. The frequency belongs to the fore-aft vibrational mode (first bending mode) of the full OWT structure in idling state.

From the frequencies listed in this table, we observe that soil models whose responses match the shaker measurements best, seem to slightly over-predict the fundamental natural frequency of the full OWT. Although we can at this stage only speculate on

the reason for this deviation, it could be caused by an identification or structural model error[2], but could also be related to the soil excavation that took place after the shaker measurements; 2 soil wedges of 2.5 m depth, base-width of 3 m and slopes of 1:2.5 were excavated at the North and South-East sides of the MP to insert the electric cables. These wedges were subsequently refilled, resulting in weaker soil than during the shaker experiment. As the stiffness of the shallow soil layers highly influences the overall SSI stiffness, the softening of this region leads to a lower natural frequency.

From Table 5.2 we also observe that the differences in predicting the natural frequencies (the errors) are much smaller than would be expected from the analyses of the pile-only response. This is caused by the smaller influence the soil stiffness has on the full structure (extending 95 m above water level) as opposed to the monopile only (extending 5.45 m above water level). Beneficially for the design community, the error made in modelling the soil reaction, converges to much smaller values for tall OWT stuctures than foundation-only structures. In line with this reasoning, we can state that, due to the high sensitivity of a MP-only structure to the soil-reaction, such a system is much more fit for identifying (validating) a soil model than a full OWT system. Aiming to visualize this sensitivity, Fig. 5.23 shows the relation between the natural frequencies versus variation in the stiffness (for both the p-y and the effective stiffness profiles) for the MP-only case and the full structure case. Similar as in Table 5.2, the full structure natural frequencies were extracted from excitation decay simulation using BHawC. For equal comparison between the MP-only cases (upper two panels), the bounds of the vertical axes of these figures (the variation of natural frequencies) are set to 33% variation around the central frequency. All four panels show equal stiffness scaling factors in the range of 0.1 to 4 (horizontal axes).

Fig. 5.23 also reflects the asymptotic relation between the stiffness and the natural frequency of the full OWT structure; the stiffer the profile, the closer we get to the situation where the pile can be considered as clamped at mudline (a cantilever), the smaller the variation in natural frequency. This trend can be observed by comparing the lower p-y stiffness for the full structure (lower right panel), and the larger effective stiffness which converges even faster (lower left panel). Therefore, the added value of monopile-only testing is larger for stiff site conditions; a softer soil profile is more fit for soil-model validation based on the full OWT response due to a larger sensitivity. This short study has been included to reflect on the fact that soil models are often judged solely on the natural frequencies of the full OWT; due to (other) structural uncertainties and a lower sensitivity to the soil stiffness for stiff profiles, it is not surprising that the measured frequencies of installed OWTs can deviate a few percentages (often

[2] An in-house study [141] showed that for instance a 2% mass deviation of the nacelle (which is a realistic deviance) can lead to $\pm 0.5\%$ variation of the natural frequency. Of course such a relation is structure and site dependent. Similar sensitivity relations can be found in [33].

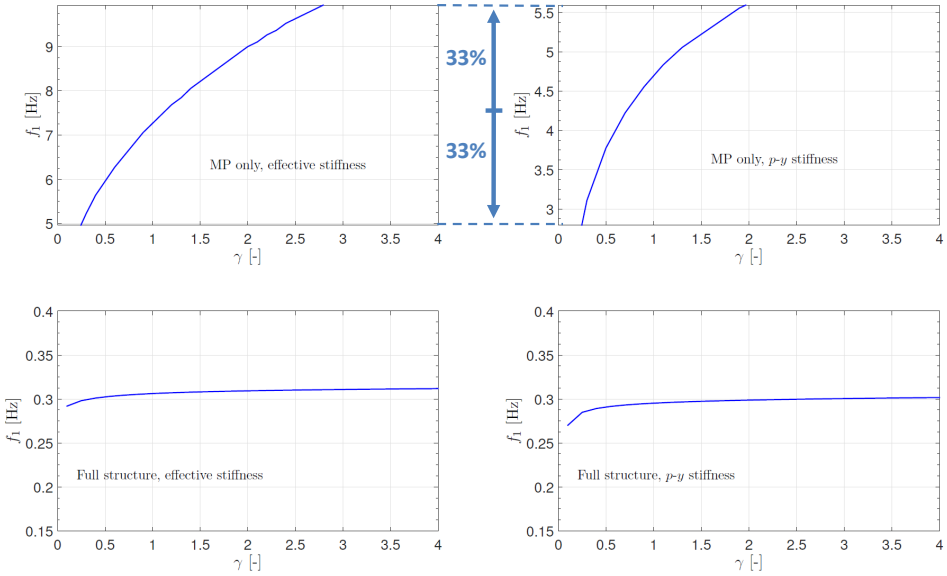

Figure 5.23: Sensitivity of the natural frequency to the effective and p-y stiffness profiles for the monopile-only case (calculated with the basic model, Fig. 5.9) and the full OWT structure (extracted from excitation decay simulation using BHawC). For equal comparison between the MP-only cases, the bounds of the vertical axes of the upper panels are set to a 33% variation around the central frequency.

$<5\%$ [33]) from the design target[3] - even for 'almost correct' soil models. For similar reasons pile-only measurements can be considered more fit for identifying soil damping than full OWT records. Additionally, pile-only systems lack the aerodynamic damping contributions, making the identification of the soil contribution less ambiguous.

5.4.3. POST-RESONANCE FREQUENCY

A stiffness increase occurs at post-resonance frequencies. We observe this in the stiffness optimisation of the 3 models, however, most pronounced for the basic model (Fig. 5.12), and the basic model with added mass (Fig. 5.19). Although a preliminary investigation [142] indicated no pore pressure build-up recorded in the piezometers in the soil until 4 Hz (only the Heavy weight setup was analyzed), the undrained behavior of the soil is a physical mechanism that might cause this stiffness increase at the higher frequencies.

[3] A deviation within $\pm 5\%$ is often accepted by the certifying bodies, but a 5% lower observed natural frequency than designed for, can significantly increase the endured fatigue loads due to dynamic amplification at the low-frequency wave spectrum. On the other hand, a higher measured natural frequency than designed for indicates an over-dimensioned, thus overpriced foundation design - or can facilitate design lifetime extension of the structure.

5.4.4. DAMPING OF OWT

In Section 5.3.1 we estimated the damping contribution of the soil for the stand-alone MP to yield a damping ratio of $\zeta = 20\%$ (for the basic model, Fig. 5.9). To get a rough idea of this contribution to the damping of the full structure (including tower and RnA), we extended the top of the MP to the hub height and included a point mass at the top representing the RnA. This mass was tuned to match the natural frequency that was identified for the full structure. Furthermore, a γ of 0.78 was applied to the effective stiffness as this seems to be applicable for the low-frequency regime (see Fig. 5.12). Applying the half-power bandwidth method on the response of this simplified full-structure model yielded $\zeta = 0.14\%$. Note that we thus assumed the dashpots to be frequency independent; although they were tuned based on the resonance peak at 5.4 Hz, we also used them for the lower frequency regime. For the soil resonator and the added soil mass models, the damping of the full structure would be $\zeta = 0.062\%$ and $\zeta = 0.054\%$, respectively. Damping identification (using Operational Modal Analyses, Stochastic Subspace Identification [40]) performed on the preliminary data retrieved from the full OWT structure in idling state, indicates 2 to 3% total logarithmic decrement support structure damping (often indicated with δ[4]), which gives $\zeta \approx 0.48\%$ damping ratio (of critical). The sum of the soil damping contribution based on the basic model ($\delta \approx \zeta(= 0.14\%) \times 2\pi = 0.88\%$ logarithmic decrement) and the assumed contributions (approximated for the current site conditions [35]) of the structural steel ($\delta \approx 1.2\%$), the water ($\delta \approx 0.5\%$, only 5 m water depth) and air ($\delta \approx 0.5\%$ for idling, low wind velocity) lies in the expected range of 2 to 3% logarithmic decrement. The soil damping values retrieved with the soil resonator and soil added mass model seem too low. In general we can state that the soil damping contribution is quite low (even compared to values generally assumed in design), which is probably due to the stiff soil conditions at this location, limiting displacements and therefore energy dissipation. For this particular wind farm, this stiff-soil effect was taken into account in design; a similar low damping value was used in the simulations.

5.4.5. SOIL NONLINEARITY

In the effective stiffness model we have assumed the soil to react in its linear-elastic regime - expecting that this is applicable for most of the occurring soil strains during operation of the OWT [66]. Clearly, in validating this model we have to assess whether indeed the soil reacted linearly for the actual displacements during the shaker experiment. Fig. 5.12 shows for example that the soil appears to have been excited (displaced) in its nonlinear regime for a part of the excitation frequencies. This can be concluded from the more or less parallel lines for the different weight setups in the optimized stiffness plot; the thick continuous blue and red lines of respectively the Middle weight and Heavy weight setups for frequencies between ~2 Hz and 4 Hz, and the same blue line parallel to the thick continuous black line (Light weight) between 5 and 6.8 Hz, indicate a lower stiffness for a larger excitation force (displacement). Another indication of non-linearity

[4] In the OWT industry, damping is often quantified in terms of the logarithmic decrement δ, which relates to the exponential decay between the maxima x_0 and x_n over n periods as $\delta = \frac{1}{n}\ln(x_0/x_n)$. The relation between the damping ratio ζ and the logarithmic decrement is $\zeta = 1/\sqrt{1+(\frac{2\pi}{\delta})^2}$. In practice, for small damping $\delta \ll 4\pi^2$, $\delta \approx 2\pi\zeta$.

is the slightly higher resonance frequency of 5.7 Hz observed in the transfer functions of the Light weight setup (Fig. A.7 in Appendix A) as opposed to the 5.4 Hz for the Middle weight setup. This could indicate a softening of the soil stiffness for larger applied forces.

The force - pile head displacement relation is often used to reflect the nonlinearity of the SSI system. Fig. 5.24 shows this relation for the calibrated shaker force (Eq. 5.1, Table 5.1) and the measured displacements (retrieved from the accelerations in a similar way as in Eq. 5.14), yielding a (model-independent) force-displacement relation for the pile-head. However, note that this is a *dynamic* force displacement relation; the inertial effects are included in these displacements. The excitation frequencies are noted next to the measurement points.

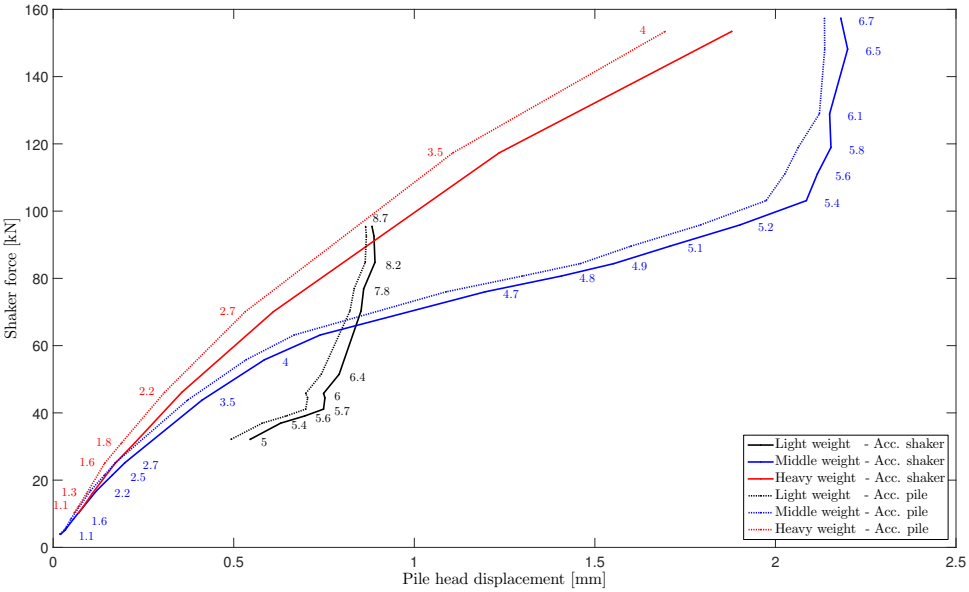

Figure 5.24: Shaker force - pile head displacement relations (at various frequencies) for the three different weight setups. The displacements were retrieved from the accelerometers attached to the pile and shaker. This can be considered a dynamic stiffness relation, as it includes inertial forces. The increase of dynamic stiffness for frequencies higher than 5.4 Hz is also clearly visible (blue and black lines).

To derive the more classical pile head stiffness, these inertial effects were corrected for by considering the displacements with respect to the sum of the external (shaker) and internal (inertial) forces. To derive the total inertial force, first the single-degree-of-freedom (SDOF) equivalent stiffness term was determined for the top of the pile in the (calibrated) basic model for a low frequency; for $\omega \to 0$ and a unit forcing, this is equal to the real part of the inverse of the displacement. Subsequently, the SDOF equivalent mass for the other frequencies ($\omega > 0$) was determined by taking into account the previously found stiffness contribution in the obtained modelled displacements. Fig.

5.25 shows the stiffness of the pile head: the sum of shaker and inertial forces in relation to the displacements. From this we conclude that a rather linear effective soil stiffness applies for most of the displacements.

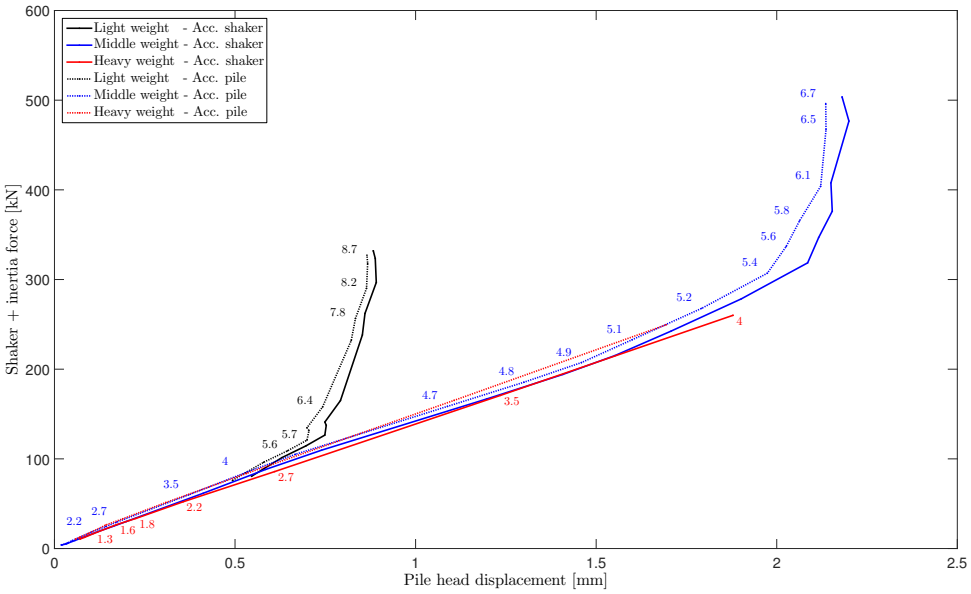

Figure 5.25: Sum of shaker and inertial force - pile head displacement relations for the three different weight setups. Initially, the relation is linear. The increase of stiffness for frequencies higher than 5.4 Hz is clearly visible (blue and black lines).

Both in Figs. 5.24 and 5.25 the post-resonance (>5.4 Hz) stiffness increase can be clearly observed (indicated by the black and blue lines of respectively the Light and Middle weight setups). This stiffening is not necessarily related to a soil nonlinearity; although not verified at this stage, and while no pore-pressure build-up was observed [142] up to 4 Hz excitation and the permeability of the sand seems to be high (as discussed in 2.2.3), the stiffening beyond 5.4 Hz could be related to undrained behaviour of the soil.

Furthermore, the soil strains in lateral direction (the direction of loading) in the static linear-elastic 3D model (Section 3.1) were verified to be approximately $1 \cdot 10^{-6}$ for the shallowest 6 m of soil at a forcing of around 10 kN, corresponding to the Heavy weight setup exciting at 1 Hz. For a linear-elastic model, these numbers can be linearly scaled; a (static) force of 100 kN would induce strains in lateral direction in the order of $10 \cdot 10^{-6}$. Note however, that the strains predicted by the linear model can be underestimated. The often referred stiffness-strain degradation curve for sand of Atkinson & Sallfors [91] shown in Fig. 5.26, indeed shows that for strains up to roughly $50 \cdot 10^{-6}$ the soil shear modulus only degrades with a small percentage.

Lastly, we check the embedded pile displacements of the (calibrated) basic model, for the forcing of the Middle weight setup at a frequency of 5.4 Hz. According to Figs. 5.24 and 5.25 - these are the largest pile head deflections before the stiffening at higher frequencies are observed. The deflection at mudline is around 1 mm. This can be considered small; it is situated in the beginning of the initial linear branch of the associated p-y curve.

Concluding this discussion, we believe that - although not all observations are completely aligned - it is reasonable to assume linearly behaving soil in modelling the pile deflections during the shaker experiment.

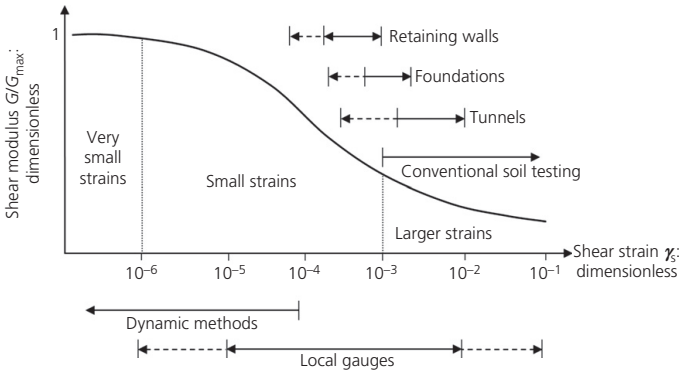

Figure 5.26: Typical stiffness - strain relation for sand [91].

5.5. ADDENDUM: INCORPORATING NON-LOCAL MODEL & DESIGN STIFFNESS PROFILE

As explained in the introduction of this chapter, the previous sections contain the content of [126]. However, that paper does not consider the use of the non-local technique to establish the first-guess effective stiffness for MP45; therefore, that will be addressed in this addendum. The effective stiffness methods received a 'Technology Qualification' from DNV GL [88], and during this qualification procedure, it was advised to incorporate more engineering judgement in establishing the C_s profile of the test location shown in Fig. 2.18, as in actual fact, when directly employing the inverted C_s values (as was done in Section 5.3 and [126]), one assigns a 100% certainty to the measured/inverted data. It is better practice to incorporate some user-assessment in determining the profile that is to be used for modelling the SSI, removing (for instance) outliers and other unexpected values. This process can be aided by relating the identified values to the soil layers (with a reference to the CPT-output profiles) or by applying a certain averaging over the layers. First we shall assess the difference in using either the previously applied local technique or the non-local technique in combination with the original 3D model (C_s profile) in Section 5.5.1. Section 5.5.2 presents the obtained stiffness correction factors for the low-frequencies when employing a smooth profile in combination with the non-local technique for finding the 1D effective stiffness. Finally, in Section 5.5.3, we discuss the remaining difference in predicted and identified in-situ stiffness. In this addendum, only the lowest 4 frequencies of the Heavy weight setup are assessed, as the loading of these measurements is most comparable to the loading for OWTs.

5.5.1. THE NON-LOCAL MODEL & ORIGINAL C_s PROFILE

To evaluate the effect of employing the non-local method to establish a first-guess stiffness for MP45, we first recapitulate the performance of the local method. Fig. 5.27 shows the match in strains of the optimized local 1D model which was based on the original C_s profile (the basic model of Section 5.3.1). The figure displays both the unfactored (γ=1) and the optimized modelled response; a γ=0.82 is obtained - in line with the previous conclusions on the low-frequency stiffness in Section 5.4.1. And similarly as previously found, γ has a comparable value for the first 4 frequencies (1.04 - 1.63 Hz) of the Heavy weight setup. As additional information the mismatch between the modelled and measured transfer functions is given in the left panel; this is the value computed with Eq. 5.17. Furthermore, the right panel of the figure shows the modelled displacement profiles in relation to the identified displacements retrieved from the measured accelerations on the pile and shaker.

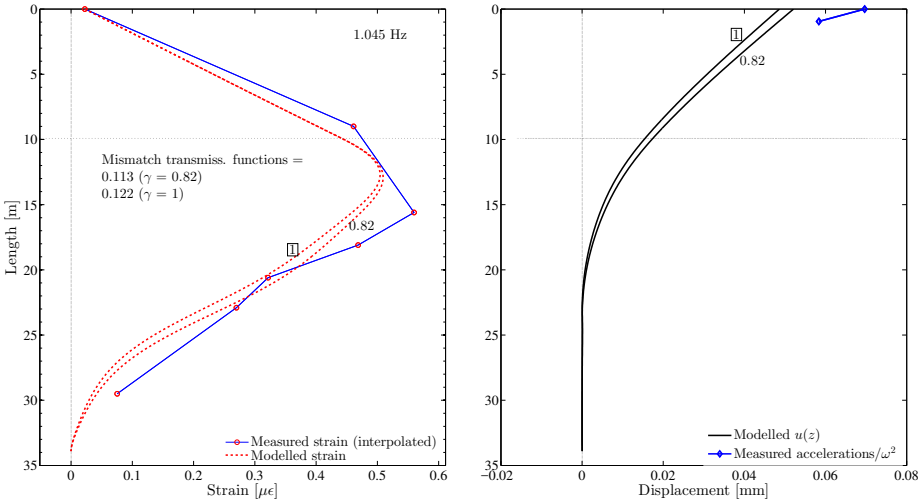

Figure 5.27: Match in bending strains (left panel) obtained with the local 1D model which was used to translate the original 3D model (of which the C_s profile is shown in Fig. 2.18). The optimized γ is 0.82, and a mismatch (Eq. 5.18) of 0.113 is obtained. As a reference, also the unfactored (γ=1) model is shown. The right panel shows the displacements of the unfactored and the optimized model. The blue dots indicate the identified displacements (obtained from the measured accelerations).

5

As was already shown in Section 4.3.4, in modelling the 1D effective counterpart of the original 3D modelled response, the non-local method of MP45 yields a better match than the local technique. A response comparison is given in Fig. 5.28, showing the original 3D model (black solid line), the (fits of the) 1D local model (grey dotted line) and those of the 1D non-local model. In observing the mudline displacement and rotations, we can see that the original 3D model behaves stiffer than the 1D effective models. As the non-local model matches the 3D model more closely, we expect a lower value for the optimized γ of the non-local 1D model (to match the measured response) than obtained with the local method. This is indeed confirmed by Fig. 5.29; γ=0.56 is found to yield the lowest misfit in transmissibilities. As expected, the mismatch in transmissibilities of the unfactored model (γ=1) are higher than obtained with the local model. However, the optimized non-local 1D model (γ=0.56) shows a lower mismatch with the measured transmissibilities than obtained with the optimized local model. This is also confirmed by the visually closer fit of the modelled strains and displacements with those obtained from the in-situ measurements (compared to the fit shown in Fig. 5.27). This could reflect that the *shape* of the non-local stiffness (and hence the 3D stiffness reaction) reflects reality in a better way than the previously applied 1D local $k_{eff}(z)$.

The damping for the stiffness optimization using the non-local model was tuned in a similar way as previously discussed for the local 1D model (Eq. 5.2); non-local, viscous damping matrices $\mathbf{C}^{\psi,\psi},..,\mathbf{C}^{u,\psi}$ were adopted proportional to the stiffness matrices ($\mathbf{K}^{\psi,\psi},..,\mathbf{K}^{u,\psi}$) with a (single) tuning factor α: $\mathbf{C}^{x,x} = \alpha\mathbf{K}^{x,x}$, where $x = u, \psi$. Based on the transfer functions, $\alpha = 5.00 \cdot 10^{-3}$s seemed appropriate for this non-local model

based on the original C_s profile, and also for the 2 soil profiles discussed in the next two subsections.

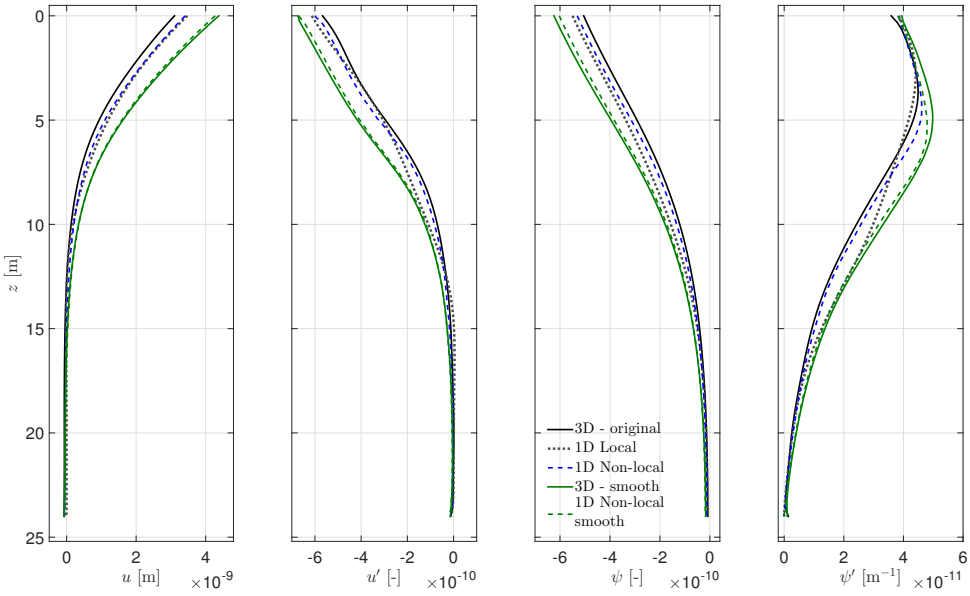

Figure 5.28: Response comparison between 3D and 1D models based on the original C_s profile (Fig. 2.18) and the smoother C_s profile shown in Fig. 5.30.

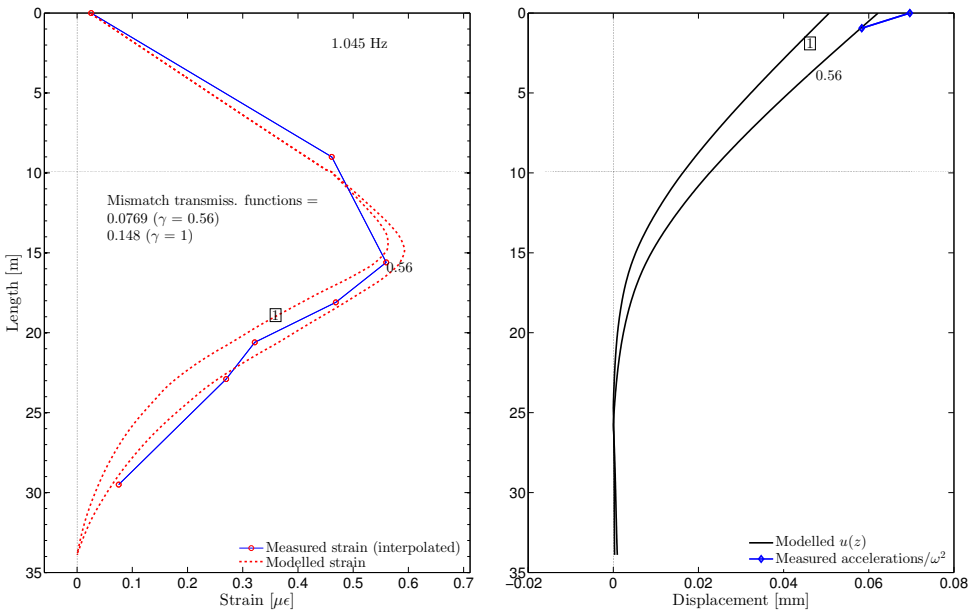

Figure 5.29: Match in bending strains (left panel) obtained with the non-local 1D model which was used to translate the original 3D model (of which the C_s profile is shown in Fig. 2.18). The optimized γ is 0.56, and a mismatch (Eq. 5.18) of 0.077 is obtained. As a reference, also the unfactored (γ=1) model is shown. The right panel shows the displacements of the unfactored and the optimized model. The blue dots indicate the identified displacements (obtained from the measured accelerations).

5.5.2. THE NON-LOCAL MODEL & SMOOTH C_s PROFILE

As pointed out in the beginning of this section, an improvement was applied in establishing the C_s profile for MP45. Fig. 5.30 shows an updated version of the profile (thick green line), which is shaped by double averaging the original (identified, blue dots) C_s values and a manual adjustment of the top 2 layers, resulting in a smoother, C_s profile.

The resulting match in strains and displacements of the non-local model that is associated with the updated, smoother C_s profile in comparison with the 1.04 Hz measurement of the Heavy weight setup is shown in Fig 5.31. The γ factors obtained for the other 3 measurements are 0.76, 0.75 and 0.82 for excitation frequencies of 1.13, 1.30 and 1.63, respectively; removing the high stiffness peaks in smoothing the profile makes the profile less stiff. A γ of around 0.8 is comparable to the overestimation of the stiffness that was initially obtained using the original C_s profile and the local translation technique, discussed in Section 5.3.1. However, note that the currently obtained mismatch in transmissibilities is lower (comparing Figs. 5.27 and 5.31), and also the visual match in strains and displacement is clearly much better than the previous method and profile. Nevertheless, the 'smooth' 3D model and hence the non-local 1D effective counterpart still behave too stiff in comparison with the field observations.

5.5.3. THE NON-LOCAL MODEL & DEGRADED, SMOOTH C_s PROFILE

With the proposed improvements in this addendum section we obtain a better fit of the measured strains and displacements than previously found using the local method and original C_s profile, but the effective stiffness method still seems to overestimate the in-situ stiffness with about 20%. This could be related to various sources of error, but the most evident sources are within the soil characterisation step, and within the 3D modelling; the last step of determining the 1D effective stiffness is easily verified by evaluating (for instance) the obtained misfit values of the 3D and 1D effective model. The 3D model being fully linear, in both soil modulus versus strain and the pile-soil interface, is a clear simplification. Although from the discussion in Section 5.4.5 we might conclude that no substantial nonlinear behaviour was observed, including stick-slip behaviour of the pile-soil interface should improve the 3D response prediction. Employing a conservative best-estimate of the 3D-input stiffness profile, by applying a 20% degradation of the Young's modulus profile which is related to the smooth C_s profile, we obtain the match in response shown in Fig. 5.32. As expected (in using linear models), a 20% degradation of the input-stiffness profile, results in an (almost) spot-on match of the measured strains and displacements. The γ factors obtained for the other 3 measurements are 0.96, 0.94 and 1.03 (for f=1.13, 1.30 and 1.63 Hz, respectively) which can be considered to be $\gamma \approx 1$.

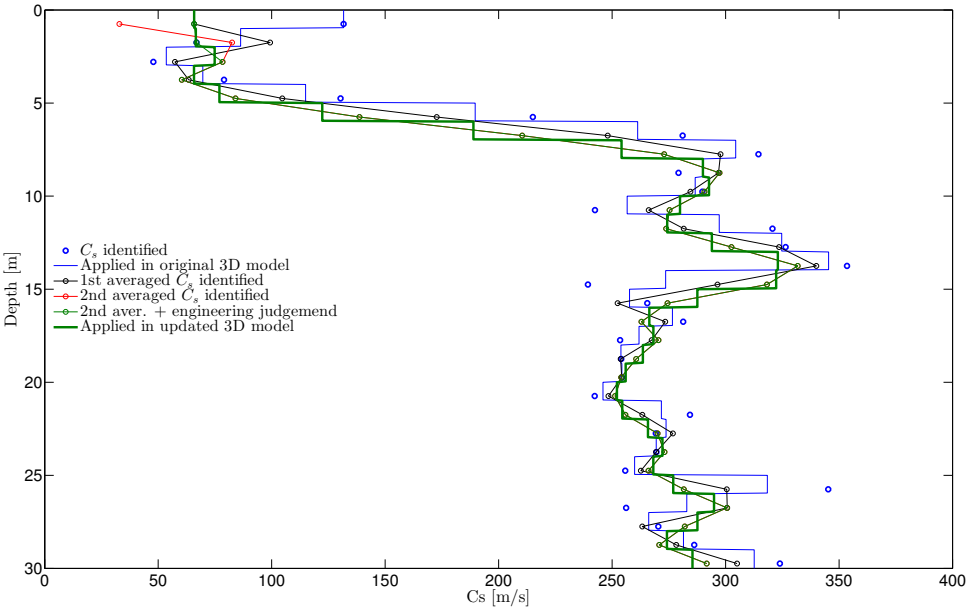

Figure 5.30: Updated shear-wave velocity profile, input for the 3D model (thick green line). Where previously the identified C_s values were directly applied in the 3D model (thin blue line), the updated profile contains more averaging and some engineering judgement in shaping the profile. For this particular profile a double averaging procedure plus a manual adjustment to the top layer was applied.

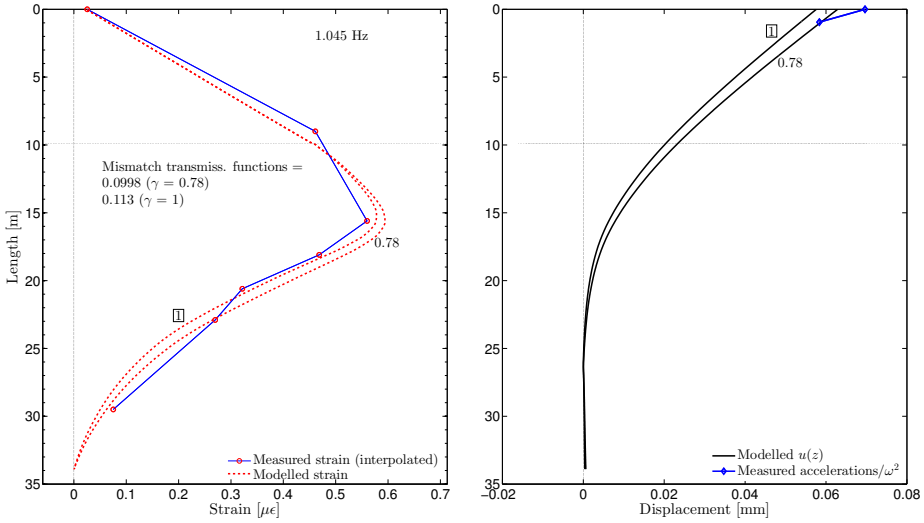

Figure 5.31: Match in bending strains (left panel) obtained with the non-local 1D model which was used to translate an updated 3D model of which the C_s profile is the smoother, engineering judgement profile shown in Fig. 5.30). The optimized γ is 0.78, and a mismatch (Eq. 5.18) of 0.100 is obtained. As a reference, also the unfactored (γ=1) model is shown. The right panel shows the displacements of the unfactored and the optimized model. The blue dots indicate the identified displacements (obtained from the measured accelerations).

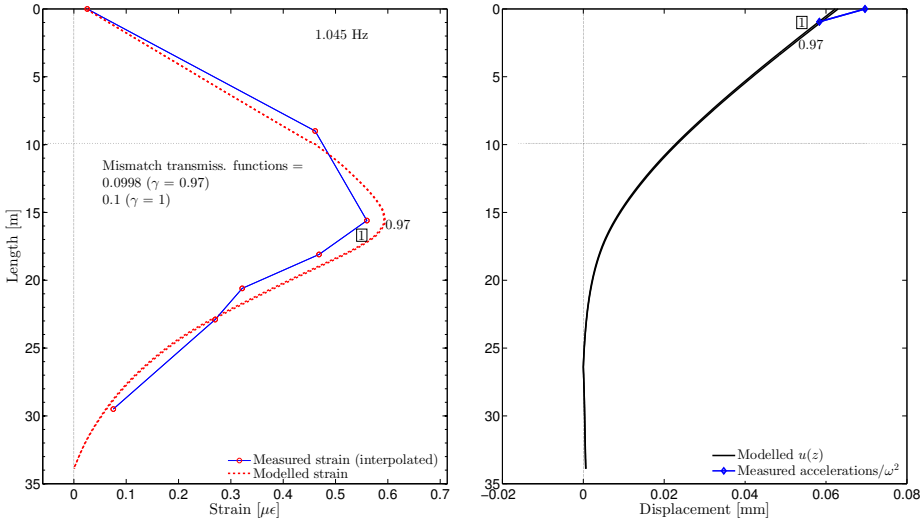

Figure 5.32: Match in bending strains (left panel) obtained with the non-local 1D model which was used to translate an updated 3D model of which the Young's modulus profile is 80% of the value obtained when considering the smoother, engineering judgement C_s profile shown in Fig. 5.30). The optimized γ is 0.97, and a mismatch (Eq. 5.18) of 0.100 is obtained. As a reference, also the unfactored (γ=1) model is shown. The right panel shows the displacements of the unfactored and the optimized model. The blue dots indicate the identified displacements (obtained from the measured accelerations).

5.6. CONCLUSIONS

In this chapter we analyzed data obtained from a unique measurement setup; a monopile foundation in a near-shore wind farm was - prior to installation of tower and turbine - excited by an eccentric-mass shaker to assess the lateral dynamic (small-strain) response of the pile. This data yielded a 'first-off' opportunity to validate a soil-structure interaction model for an in-situ rigidly behaving pile.

Sections 5.1 - 5.3 contains the published content of [126], with Section 5.3 presenting the identification analyses. With the controlled, known-input excitation - excluding aerodynamic and super-structure disturbances - the transfer and internal transmissibility functions between the strain gauges along the entire shaft of the pile and accelerometers attached to the top of the pile were determined. A model-based identification was performed with a Timoshenko beam on Winkler foundation, of which the initial-guess stiffness profile $k_{eff}(z)$ was determined according to the local effective stiffness method for capturing the modulus of horizontal subgrade reaction for large-diameter piles, presented in Section 4.2.

Three tests with different eccentric weight setups were performed, at excitation frequencies ranging from 1.0 to 8.7 Hz. A frequency dependence of the stiffness is observed. The first resonance frequency of the soil-pile system appears to be situated around 5.4 Hz. The post-resonance response is characterised by an increase of the dynamic stiffness of the system. The (the initial-guess) effective stiffness profile $k_{eff}(z)$ was optimized to better match the measured response. Furthermore, two modifications of the conventional 1D model were applied to assess whether the frequency dependency of the dynamic stiffness can be attributed to simple inertia effects. In the first modification, the observed resonance was assumed to be caused by the soil acting as a resonator, and in the second modification, the mass of the soil in the vicinity of the pile was added to the pile. Both these modifications lead to a rather constant soil-stiffness at frequencies up to the resonance regime. Based on the better match of the transfer and transmissibility functions, the basic model - including a frequency-dependent soil stiffness and possibly some added mass of the soil - is deemed most appropriate. Additionally, the damping contribution from the soil predicted by the basic model with the full OWT included, yielded the best agreement with the identified value.

Irrespective of the assumed 1D model, the low frequency-regime soil stiffness (relevant for OWTs) seems to be overestimated by the local effective stiffness with roughly 20%; including some added mass, a stiffness correction factor of 0.8 had to be applied to the effective stiffness profile $k_{eff}(z)$ to best match the internal transmissibilities. This error, although not insignificant, is still small compared to the obtained mismatch when using the method prescribed by the design standards; a best estimate p-y stiffness profile underestimates the observed stiffness for the low frequencies with a factor of 2.4 (140% underestimation).

Soil stiffness profiles that yield agreement with the (low-frequency) shaker measurements were used to predict the full OWT structure natural frequency using Siemens

Wind Power in-house simulation software BHawC. Although these predictions come close to the identified (monitored) fundamental frequency, a slight over-prediction is observed. This remaining difference could be related to identification or structural modelling errors, and could additionally be caused by the soil excavation and backfilling works (which degrade the soil stiffness of the shallowest layers) that took place after the shaker measurements to pull in the electric cable. Furthermore, the sensitivity of the natural frequency of a stand-alone MP and a full OWT to the soil stiffness were discussed, arguing that the former is much more suitable for validating a soil model - especially for the stiff ground conditions encountered at the site of investigation.

With the use of the basic model, the effective soil damping contribution for the pile-only situation is estimated to be around 20% damping ratio (of critical). Assuming frequency-independent damping coefficients, this damping contribution is estimated to result in a 0.14% damping ratio for the full structure including tower and RnA. Summed with commonly accepted values of the other damping contributions, this soil-pile damping is in agreement with the identified total damping ratio of 0.48%. This rather low soil damping could be related to the stiff character of the soil profile, leading to small displacements. Furthermore, it was found that the assumption of linear elastic soil reactions for frequencies lower than the resonance frequency is acceptable.

In the final section, additional analyses were presented as an addendum to the published content of [126], discussing the performance of the non-local effective stiffness method and the effect of incorporating an improved estimate of the shear-wave velocity profile. Similar as observed in Section 4.3.4, the non-local model was shown to mimic the 3D model more closely. As the 3D model of MP45 (based on the original C_s profile, used in Section 5.3) behaves stiffer than the local 1D model, it was shown (as expected) that the non-local effective model of that 3D response is also stiffer than the local version; a lower γ of around 0.6 is obtained. The mismatch in transmissibilities and visual fit of the strains and displacements obtained with the optimized non-local model is however much better than found with the local model, indicating an improvement of the shape of the stiffness profile.

In directly incorporating the C_s values as found after inversion (Fig. 2.18), one attributes a 100% confidence in the measured (inverted) values. It is better practice to incorporate some engineering judgement in establishing the profile; a smoother C_s profile is obtained by double averaging the inverted values and slight manual adjustments, thereby removing outliers. The non-local effective model that is based on the updated, smoother C_s profile (updated 3D model) was shown to overestimate the low-frequency stiffness with 20%; a stiffness correction factor γ of 0.8 was needed to best fit the transmissibility functions. Again, the obtained misfit in transmissibilities and the visual fit of the measured strains and displacements with those predicted by the latter model are better than obtained with the original 3D model and its local 1D effective model.

Despite the improved match with the field measurements, the in-situ stiffness is still overestimated using the presented effective stiffness method. The remaining errors are

expected to be related to either the, inherently uncertain, soil-characterisation step or the 3D modelling step. The 3D model can be improved by incorporating nonlinearities related to the soil modulus and to the interface between the pile and soil. A 20% degradation of the Young's modulus profile that is based on the smooth C_s profile, results in a spot-on match with the measured pile response.

In this chapter, a novel test setup for rigidly behaving, real-sized piles was presented in combination with an interpretation method that is suitable for analysing forced vibrations of a highly damped system. The damping for the extended structure was shown to be in line with the value assumed in design, however the stiffness was shown to be underestimated by the design standards. In the model-based identification, we showed that the developed effective stiffness methods yield a significantly higher accuracy in predicting the pile response than the p-y stiffness approach.

6

Conclusions & Recommendations

In the endeavour of minimising the detrimental effect of the human-induced acceleration of climate change, offshore wind generated electricity can play a significant role in creating a global sustainable energy supply that does not limit the possibilities of future generations. An improved characterisation of the soil-structure interaction in the design of the monopile (MP) foundation, aids this energy source to become even more financially competitive. The current thesis is aimed at providing the design community with a more accurate - but equally efficient - small-strain soil-structure interaction (SSI) design approach, as an alternative for the currently adopted p-y curve stiffness method, which is expected to yield too conservative, over-dimensioned support structures. As the cost for such support structures typically constitute more than 20% of the total capital cost of an offshore wind farm, the presented and validated work is foreseen to have a significant beneficial impact on the feasibility of future offshore wind projects.

The main contribution of the work can be summarized as follows:

in the presented doctoral thesis work, a full 'research-cycle' was conducted, of which the first 3 steps comprise those of the developed 'effective stiffness method', involving

1. an a priori characterisation of the small-strain in-situ soil conditions, based on performed seismic field measurements (Chapter 2),

2. a simulation of the 3D interaction between pile and soil, yielding a more realistic and less conservative pile-response estimation for rigidly behaving piles than obtained with the current 1D p-y curve approach (Chapter 3),

3. the establishment of 2 novel techniques for creating effective 1D models that mimic the 3D model for both static and dynamic soil-structure interaction (Chapter 4),

4. the a posteriori validation of the first three steps by comparing the modelled response using the predicted effective stiffness to the response observed for an in-situ installed monopile that was equipped with an extensive sensor setup and harmonically excited using a shaker (Chapter 5).

The validation campaign revealed that, based on the internal transmissibility functions, the proposed design procedure yields a 7 times higher accuracy in predicting the in-situ initial stiffness than the best-estimate p-y curve model. An initial estimation of the possible benefit of the developed stiffness method, showed a 8% saving potential for the primary steel (shell) mass of the complete support structure (MP, transition piece and tower). This exercise was performed for a contemporary soil-pile case, for which (only) the FLS-driven wall thickness was optimized with respect to the thickness needed for the conventional (softer) p-y curve profile.

The above being an executive summary of the thesis' contributions, a more detailed account of the main conclusions is given in the following section, after which recommendations for future work are given in Section 6.2.

6.1. RECAPITULATION OF THE MAIN FINDINGS

The next 3 subsections describe the motivation and main findings of the 3 main contributions of this work, being the promotion and execution of in-situ seismic soil testing for OWT foundation design (Chapter 2), the translation of 3D models into 1D effective models (Chapter 4) and the validation of the methods by controlled in-situ monopile testing (Chapter 5).

6.1.1. SMALL-STRAIN SOIL CHARACTERISATION

In Chapter 1 we discussed that the small-strain soil characteristics define the dynamic properties of the monopile-based OWT support structures, and therefore strongly influence the extent of the (often design-driving) fatigue damage accumulation. Nevertheless, the industry applies large-strain testing techniques like the Cone Penetration Test (CPT) to extract the *strength* characteristics of the soil, which are then tied to the (small-strain) 1D SSI *stiffness* properties using the empirical p-y curve method. As the p-y curve method was calibrated on long flexible piles that invoke a different type of SSI than the currently applied short, rigidly behaving monopiles, it is not surprising that the observed dynamic properties of the installed structures do not match those anticipated in design.

In this work it was advocated to add in-situ seismic measurements to the standard soil-characterisation scope for offshore wind farms. Although maybe more challenging to analyse, such geophysical testing can (more directly) identify the true dynamic, small-strain soil properties, by characterising the propagation of waves within the soil and along the soil surface. These testing methods hold the additional advantage that they yield a more global rendition of the (undisturbed) properties of the soil through which the waves propagate - as opposed to the CPT, which reflects very local properties of the soil through which it penetrates. In this research, the Seismic CPT (SCPT) was

applied in estimating the in-situ shear-modulus G profile at two turbine positions in the Westermeerwind wind farm in the IJsselmeer lake. Chapter 2 presented an inversion method for the collected SCPT data, in which particular attention was given to the timing of the arrival of the shear waves, to cone misalignment issues and how to correctly account for a horizontal offset between source and receivers (the cone). Smooth C_s profiles were identified, which showed similarities but also differences with the measured CPT parameters - the latter of which are to be expected for the outputs of these fundamentally different measurement types. That difference was also reflected in employing one of the many available empirical relations that establish the stiffness property G of the soil based on the strength properties identified with the CPT. Together with the identified in-situ density and an estimate of the Poisson's ratio profile, all the required parameters were available to characterise the linear elastic soil domain of a 3D soil-pile model that can accurately capture the complex SSI of monopiles. In this work, the soil is assumed to behave as a linear elastic material for the small-strain regime related to fatigue loading.

Besides the stiffness (shear modulus) profile, a research track was set up to capture the material damping profile by means of seismic measurements. As an initial attempt of identifying the damping with a vertically spaced sensor setup (similar to the SCPT setup) yielded unphysical results, the focus was shifted towards the inversion of surface waves, recorded with the Multichannel Analysis of Surface Waves (MASW) technique; a horizontal sensor array placed at the mudline records the propagation of surface waves (induced by a seismic source close to, or placed at the seabed, like, for instance, an airgun). The time-space data is transformed to the frequency-wavenumber domain, as the highly stratification-sensitive (geometric) dispersion characteristics of the wavefield are more accessible in this domain. Furthermore, the forward model used in the inversion is solved in this domain. The surface-wave propagation was shown to be sensitive to the C_s profile, and using a genetic algorithm to find the global minimum of the highly nonlinear inversion problem, the MASW performed at the 'W27' position was shown to yield a similar C_s profile as the performed SCPT. Intuitively, the SCPT is deemed to provide a higher certainty in identifying the C_s profile, being related to the more direct vertical measurement of the SCPT, and the successive 'layer-stripping' measurement and inversion procedure. The developed MASW inversion tools additionally showed to yield similar C_s profiles as published for the Gjøa site, of which high-quality data was supplied to us by NGI. The proper inversion of the stiffness profile is a requisite for the damping estimation. Valuable first steps in identifying the material damping profile were carried out, however, in inverting the in-situ measured data, issues in finding the complex roots of the highly fluctuating determinant function of the forward model prohibited conclusive results.

6.1.2. IDENTIFYING AN EFFECTIVE 1D MODEL

The accuracy of a 3D SSI model is a great benefit in serving as a more realistic benchmark for the conservative design method used today. Nevertheless, significantly higher gain lies in using the accurate 3D model directly for design. In the wind industry, but equally so in many other engineering applications, the simulation burden in the design process is too high for employing the computationally expensive 3D model. For that reason - being one of the major contributions of this doctoral work - 2 methods were developed to establish the effective 1D, Winkler-type model that mimics the response of the 3D model. Both the effective 'local' and 'non-local' 1D models closely match the 3D response in terms of displacement, slope, rotation and curvature along the full length of the pile - for both static, and for low-frequency, steady-state dynamic loading.

The local technique holds the advantage that it produces a 1D stiffness profile $k_{eff}(z)$ that is conceptually similar to that currently employed in design: a depth-dependent lateral stiffness profile of local, uncoupled springs. Although not reported in the related literature, it was found that, due to 3D effects, simply dividing local soil reaction forces by pile displacements - the local 1D stiffness - may yield unphysical (negative or singular) stiffness near the pivot point of the pile. The local effective stiffness method employs weak formulations of the balance of forces and moments at different parts of the pile, optimizing the shape of $k_{eff}(z)$ to best match the static stiffness response of the 3D model. Although the method proved to be quite versatile to different soil-pile combinations, poorer results are obtained for piles with L/D ratios smaller than about 4.5 and/or soft, very irregular soil profiles. For identifying the 1D effective damping dashpots $c_{eff}(z)$ that yield the best 1D fit of also the imaginary part of the 3D complex-valued dynamic response, the same methodology proved to yield reasonable results - provided that, in a previous step, a proper stiffness $k_{eff}(z)$ was found for the static SSI. The success in matching the imaginary part of the response proved sensitive to the misfit of the static response.

In the non-local method, the complex, global soil reactions are extracted from the 3D model and inserted in a 1D Winkler-type model. Hence, this method yields an *exact* representation of the 3D soil reaction. The minor difference in response of the 1D and 3D models obtained for some SSI cases is related to the different models used for the pile: the 1D beam versus the shell or solid elements of the 3D model. With the use of the global stiffness kernels for the lateral and rotational DOFs, the need of searching for various separate 1D stiffness elements, like distributed lateral and rotational springs along the pile or similar discrete springs at the pile tip, has become obsolete; the mechanisms associated with such springs are all automatically incorporated in the global stiffness kernels. The method was shown to yield accurate fits of both the static and dynamic response for a very large range of SSI systems in terms of relative pile stiffness (relating to both pile geometry and soil stiffness). The 1D model for a certain soil-pile case has to be established only once (as is the case for the local method), and does, other than the local method, not involve optimization. The procedure is therefore faster and its outcome less uncertain than the local method.

All in all, the methods circumvent the, in geotechnical engineering, often employed empirical relations; in the p-y curve methodology, the empiricism lies in connecting large-strain soil properties directly to the stiffness properties of a SSI system. Such a connection requires calibration - in the case of the p-y curve method, Matlock [43] and Reese [44] employed field tests on long, flexible piles. Furthermore, although originally not intended by the researchers, this large-strain method, is empirically connected to describe also the small-strain regime. Rather than re-establishing generalized empiric *relations* between pure soil stiffness properties like G and SSI stiffness parameters like $k_s(z)$, the aim of this work was to present a *method* to establish this link each time for a specific soil and specific pile. Although such empiric relations are popular in the geotechnical community, they inherently generalize the problem. Providing a method - although being maybe a slightly higher threshold for implementation - yields more accuracy for the specific SSI of interest.

6.1.3. IN-SITU VALIDATION OF THE METHODS

The 3 steps involved for producing the effective stiffness - namely 1) in-situ seismic testing to capture the true dynamic soil properties, 2) using those properties to describe the layered soil in a 3D SSI model, and 3) establishing the 1D effective model that mimics the response of the 3D model - on itself can be trusted to be an improvement compared to the p-y curve methodology applied in design. As explained in the last two sections, the increased accuracy lies in the first two steps.

Nevertheless, validation testing on real piles increases the confidence in the method, and aids in quantifying possible errors. To that end, a unique measurement campaign was set up comprising the in-situ testing of 2 monopile foundations in the Westermeerwind wind farm, prior to the installation of their super structures (tower and RnA). As described in Chapter 5, the piles were excited at frequencies between 1.0 and 8.7 Hz, employing 3 weight setups on a custom-made shaker. The main test pile, MP45 (of turbine W27), was equipped with an extensive sensor set, measuring the response of both the pile and the soil.

The stiffness was observed to be frequency dependent, and the first resonance frequency of the soil-pile system was identified around 5.4 Hz. The stiffness of the system decreases with frequency, with a minimum stiffness observed at resonance and an increase of the stiffness at post-resonance frequencies. It was investigated whether the observed frequency dependency of the dynamic stiffness can be attributed to simple inertia effects. Based on the models used for these investigations, no strict conclusions could be drawn, but the combination of a frequency dependent stiffness and some added mass of the soil is deemed the most appropriate description of the observed dynamic stiffness.

By comparing the modelled and measured internal transmissibility between the accelerometer at the pile head and strain gauges along its shaft, it was concluded that the effective stiffness $k_{eff}(z)$ computed by the local method overestimates the low-frequency, in-situ stiffness with 20% percent; a single correction factor γ of 0.8 was

applied to $k_{eff}(z)$ to best match the observed low-frequency response. Compared to the best-estimate p-y curves, the effective stiffness predicts the in-situ stiffness with 7 times higher accuracy; a γ of 2.4 needed to be applied to the best-estimate (unconservative curves to fit the response, meaning a 140% underestimation of the observed stiffness. A γ of 5 was found for the more conservative design p-y curves.

The optimised stiffness profile that yields a match of the pile-only response was used to predict the full OWT natural frequency. Although these predictions come close to the identified (monitored) fundamental frequency, a slight overprediction of 3% is observed. This difference could be related to identification or modelling errors, (and/) or could additionally be caused by the soil excavation and backfilling works that took place after the shaker measurements to pull in the electric cable. In light of the remaining slight difference between predicted (using a stiffness profile that was validated with high fidelity pile-only measurements) and observed full OWT natural frequency, the sensitivity of the natural frequency of the stand-alone MP and the full OWT to the soil stiffness was computed, showing that the former is much more suitable for validating a soil model - especially for the stiff ground conditions encountered at the site of investigation. Related to such insensitivity of the full OWT to the soil properties in combination with other structural mass and stiffness related modelling uncertainties, an accuracy in predicting an OWT's natural frequency smaller than about 5% seems generally infeasible.

The effective soil damping contribution for the pile-only situation was estimated to be around 20% damping ratio (of critical). Assuming frequency-independent damping coefficients, this damping contribution is estimated to result in a 0.14% damping ratio for the full structure including tower and RnA. Summed with commonly accepted values of the other damping contributions, this soil-pile damping is in agreement with the identified total damping ratio of 0.48%. This rather low damping could be related to the stiff character of the soil profile, leading to small displacements.

Finally, it was concluded that the simplification of the soil reacting in a linear elastic way to the pile at frequencies lower than the resonance frequency is acceptable.

The above conclusions relate to the effective stiffness as produced by the local method; this content was published in [126] and was chosen to be maintained as such and presented in Sections 5.1 - 5.4. As a follow up, in Section 5.5, the performance of the non-local method in predicting the low-frequency, in-situ effective stiffness was investigated. As expected, the non-local 1D model more closely matches the 3D model. Nevertheless, as the 3D model behaves stiffer than the effective local 1D model, the non-local 1D model overestimates the in-situ stiffness to a higher degree than the local model; a γ of 0.6 best matches the observed response. However, that optimized non-local model yields a lower mismatch with the measured transmissibilities and a better visual fit of the strains and displacements than obtained with the optimized local model.

Finally, in line with feedback obtained from DNV GL in qualifying the Effective stiffness method, a re-evaluation of the in-situ C_s profile was considered. In directly incorporating

the C_s values as found after inversion (Fig. 2.18), one attributes a 100% certainty to the measured (inverted) values. It is better practice to incorporate some engineering judgement in establishing the profile, creating a smoother, more averaged C_s profile. The non-local effective model that is based on the updated, smoother C_s profile (i.e., on the updated 3D model) was shown to overestimate the low-frequency stiffness with 20%; a stiffness correction factor γ of only 0.8 was needed to best fit the observed response. The obtained misfit in transmissibilities and the visual fit with the measured strains and displacements of the latter model are even better than previously obtained with the original 3D model and the related local 1D effective model.

Despite the improved match with the field measurements, the in-situ stiffness is still overestimated using the presented effective stiffness method. The remaining errors are likely related to either the, inherently uncertain, soil-characterisation step or the 3D modelling step. The 3D model can be improved by incorporating nonlinearities related to the soil modulus and the interface between the pile and soil. A straightforward 20% degradation of the Young's modulus profile that is based on the smooth C_s profile resulted in a spot-on match with the measured pile response.

6.2. RECOMMENDATIONS FOR FUTURE RESEARCH

Despite the author's endeavor, the work leaves behind some research for future efforts. Some directions are listed below.

- This work presented a method to improve the accuracy in simulating SSI, and handled the characterisation of soil in a rather deterministic way. Due to the highly variable nature of both its spatial distribution and its properties, it is better practice to apply a probabilistic approach in characterising the soil, similar as for instance [143]. The increased accuracy yielded by incorporating seismic measurements and 3D modelling can be overshadowed by the error made in identifying the soil properties.

- In the current analyses, the soil profile was idealized to consist of horizontal homogeneous layers; this was the assumption in both the SCPT and MASW inversion methods, and also in the 3D SSI model. The (site-dependent) error caused by such a simplification should be assessed for the large horizontal scale involved in the MASW, but also the soil around the currently applied ~10 m diameter monopiles might not be adequately probed by merely the ~ 4 cm diameter CPT cone. Adding horizontal variability would make the design methods for the symmetrically-assumed structures more cumbersome, making the incorporation of 3D effects yet more indispensable.

- The stress-strain relationship of soils is nonlinear. Nevertheless, the current work exploits the often applied assumption that the initial, small-strain reaction can be modelled in a linear elastic way. Other than for a lab test on a soil sample, it is very challenging to assess what stress-strains behaviour occurs in the SSI of a specific structure and load case. Nevertheless, the presented methods can be extended to incorporate strain-dependent moduli of the soil. In doing so,

one has to choose the appropriate shear modulus degradation curves published in literature, of which the shape, as discussed in Section 2.1, depends on many condition factors. Note however that, by employing more advanced models to increase the accuracy, the uncertainty does not necessarily decrease due to the many added input parameters that need to be defined. Extending the non-local effective stiffness method towards incorporating soil nonlinearity is the topic of an ongoing MSc thesis which the author is currently supervising.

- Besides assuming linear stress-strain soil behaviour, also the interface condition between the pile wall and the soil was assumed linear; the nodes of the soil and steel elements in the 3D FE models were fully 'glued', meaning that no slip or gap formation was allowed. Moreover, the compressional properties of the soil elements were assumed equal to the tensional properties. The extent of these modelling simplifications for the SSI of interest should be investigated.

- 'The' stiffness of an SSI system does not exist; due to the discussed nonlinear behaviour and memory effects of soil, the stiffness that the MP foundation actually experiences is dependent on the magnitude and history of the loading. Both the stiffness evolution and permanent displacements need to be incorporated. If we can establish the relation between the initial, virgin stiffness and the unloading-reloading stiffness for specific soils, the methods of this thesis can be applied in a similar way to derive an effective 1D model that incorporates cyclic effects.

- Analyses of the other data collected in the validation measurement campaign: the tests performed on the monopile of turbine W24, and the data of the sensors installed in the soil next to W27 (MP45). Although the response of the foundation pile of W24 was only recorded with accelerometers on the pile head and on the shaker, and no SCPT was performed at that location, the test could serve as a secondary validation. The shear modulus profile can be established by calibrating an empiric relation based on the CPT parameters. Additionally, the data recorded by the accelerometers and piezometers of the subsoil cones installed next to MP45 have not yet been sufficiently analyzed. Hopefully that data will allow for a better, more detailed understanding of the soil reaction mechanisms occurring in the recorded SSI.

- As explained in Section 2.3, many valuable steps were taken in developing a method to identify the in-situ small-strain material damping. Hopefully that research track will soon give conclusive results (the author is currently guiding another MSc thesis on this topic). Then the procedure for deriving the 1D model that mimics also the 3D SSI complex-valued response described in Section 4.3.5 can be used to derive a proper damping estimate for the design models. The MASW is deemed a more appropriate method for deriving the small-strain damping characteristics of the undisturbed in-situ soil than the most often employed laboratory tests - we note, however, that such lab tests are useful for determining the damping at larger strain levels.

- The presented methods allow for identifying steady-state 1D effective damping. However, the frequency dependence of this low-frequency damping should be investigated for it to be applied in the foreseen time-domain OWT simulations. Nevertheless, similar as was assumed for the stiffness (Section 5.4.1), the damping of MP structures is not expected to show highly frequency dependent behaviour between frequencies of 0 and 1 Hz. If this nonetheless proves to be the case, most likely equivalent frequency-dependent dashpots can be found that mimic such damping behaviour.

A

SUPPLEMENTARY INFORMATION TO THE EXPERIMENTAL VALIDATION

This appendix provides some supplementary information to Chapter 5.

Table A.1 lists the used model parameters, which, together with the values given for the point masses, dashpot tuning coefficients α and stiffness correction factors γ listed in Section 5.3.1, are given for the purpose of repeatability of some of the presented results.

Symbol	Description	Value	Symbol	Description	Value
t	pile wall thickness [mm]	50	κ	Timoshenko shear coefficient [-]	0.53
E	Young's modulus steel [N/m^2]	$2.10 \cdot 10^{11}$	ρ	mass density steel [kg/m^3]	7850
G	shear modulus steel [N/m^2]	$8.08 \cdot 10^{10}$	$\rho_{s.plug}$	mass density soil plug [kg/m^3]	1500
D	diameter [m]	5	η	added soil mass factor [-]	3.4
L	embedded length [m]	24	M_s	soil resonator mass factor [-]	8.6
k_{eff} **pol.**	4th order polynomial values for k_{eff}, z=0..24 m	$9.3757 \cdot 10^5$, $-1.0308 \cdot 10^7$, $7.4008 \cdot 10^6$, $1.1771 \cdot 10^8$, $1.3055 \cdot 10^8$			

Table A.1: Model parameters. The top 4 and lowest 2 m of the pile have a 60 mm wall thickness for pile driving purposes.

As a reference to the site characterisation (Chapter 2 and Section 5.1), Fig. A.2 shows the CPT profile captured by SCPT45.

Fig. A.1, showing an example of the steady-state (filtered) accelerometer response, is given as supplementary information to Section 5.2.

Figs. A.3, A.4 and A.5, show the modelled and measured strains for a few higher frequencies. They are given as supplementary information to Section 5.3.1. The mismatch for the strains at higher frequencies between 10 and 15 m below mudline (shown in Figs. A.4 and A.5) are apparent. This is related to an incorrect modelling of the inertia (or stiffness) at that location.

Fig. A.6 shows the time trace and corresponding power spectral density (PSD) of a recorded excitation decay after the boat landing of MP45 was hit by a service boat. It serves as a reference Section 5.4.2.

Fig. A.7 shows the measured and modelled transfer function for the strain gauges along the pile for the Light weight setup. It serves as supplementary information to Section 5.4.5.

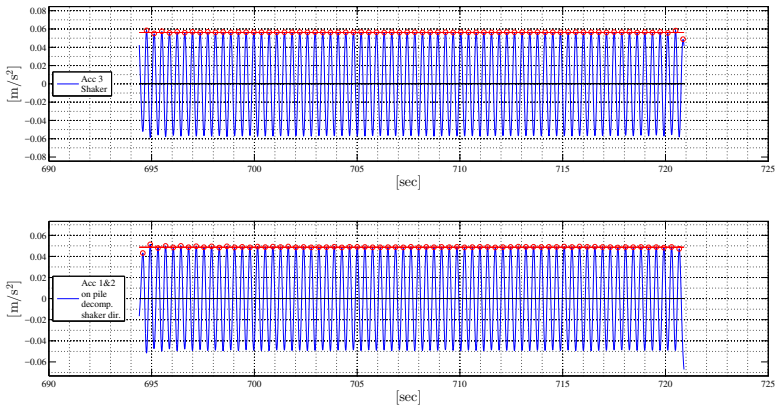

Figure A.1: Accelerometer responses after filtering for frequency plateau 2.68 Hz, Middle weight setup. The red circles indicate the picked peaks, of which the mean was taken over the selected cycles (red line). The signals of accelerometers 1 and 2, which were attached to the pile at 0.95 m below the shaker accelerometer (nr. 3), were combined to get the decomposed signal in the direction of the shaker excitation.

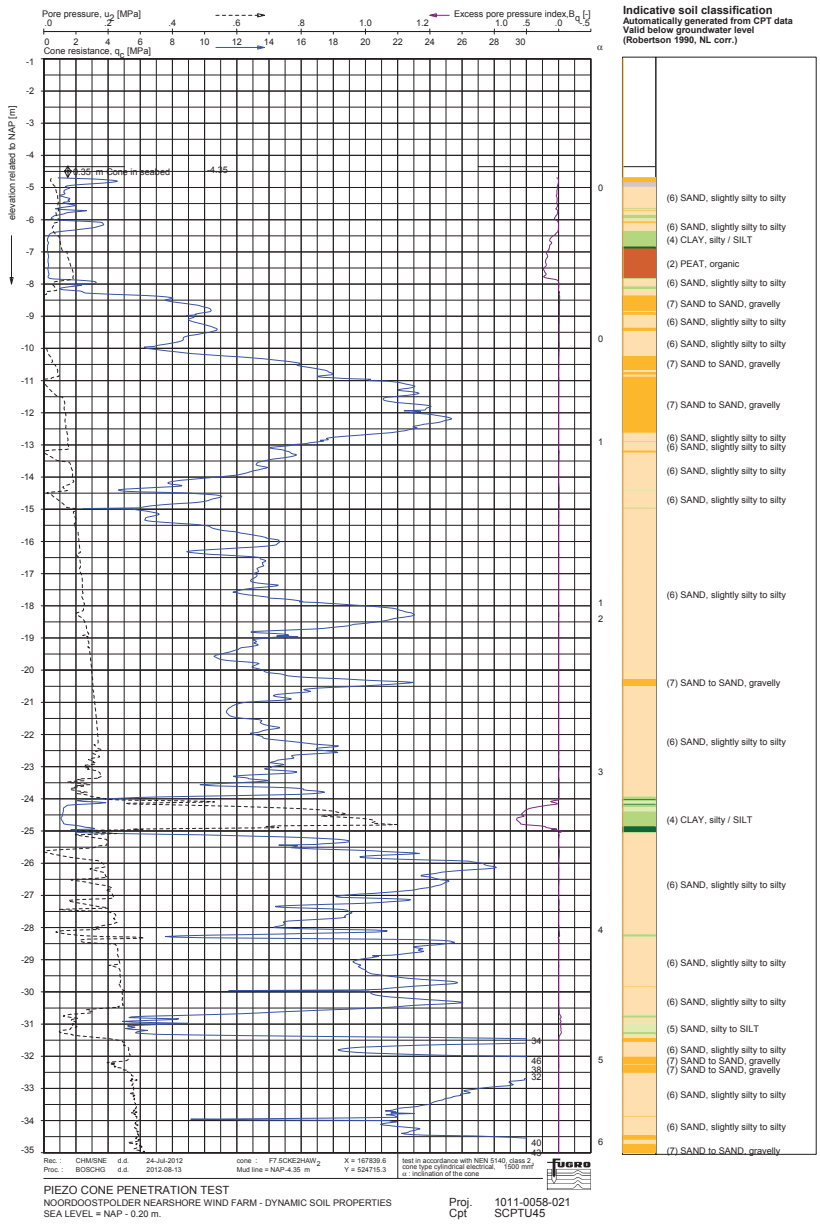

Figure A.2: CPT output (cone resistance q_c, pore pressure behind cone u_2, pore pressure index B_q and Robertson soil classification) from SCPT45 (location of turbine W27) measured in 2012. Note that the depth is given in relation to NAP, the Dutch equivalent of Mean Sea Level.

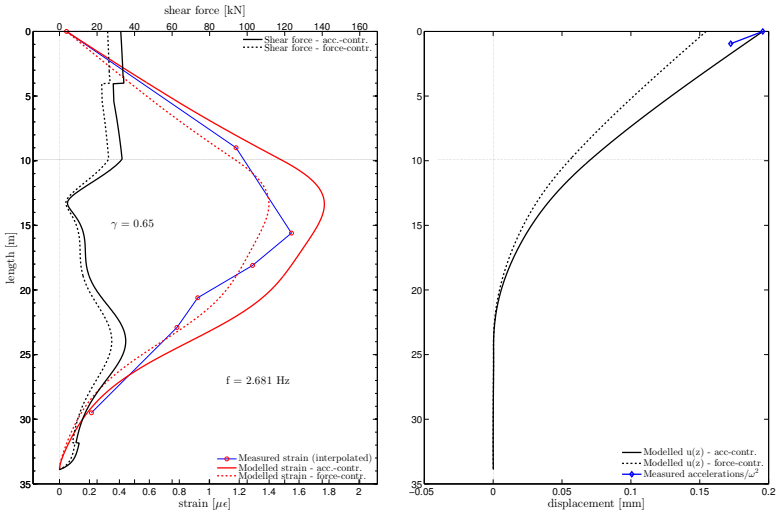

Figure A.3: Match in strains with a stiffness correction factor retrieved by optimizing for the internal transmissibility (Figure 5.12), for the Middle weight setup, exciting at a frequency of 2.68 Hz. The absolute values of both the acceleration- and force- controlled modelled responses are shown in terms of shear force and strain (left panel) and displacements (right panel).

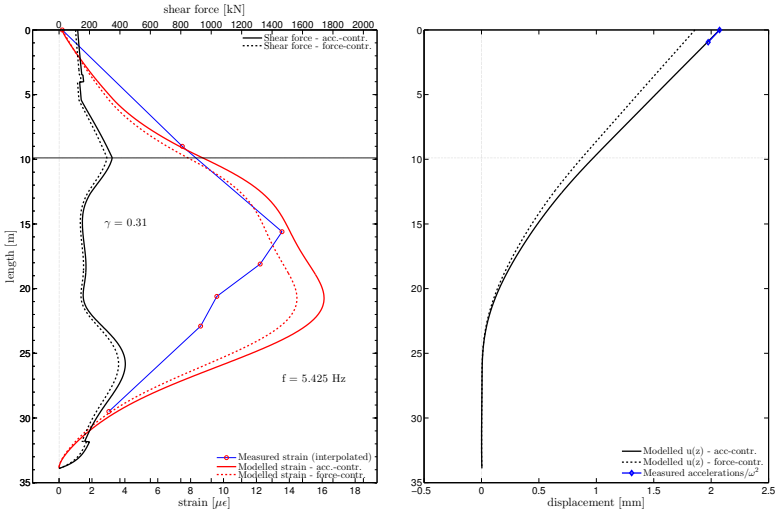

Figure A.4: Match in strains with a stiffness correction factor retrieved by optimizing for the internal transmissibility (Figure 5.12), for the Middle weight setup, exciting at a frequency of 5.42 Hz (resonance frequency). The absolute values of both the acceleration- and force- controlled modelled responses are shown in terms of shear force and strain (left panel) and displacements (right panel).

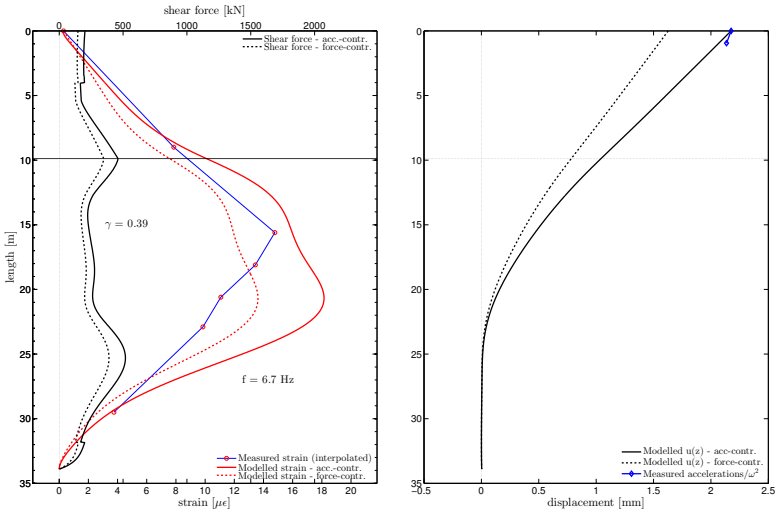

Figure A.5: Match in strains with a stiffness correction factor retrieved by optimizing for the internal transmissibility (Figure 5.12), for the Middle weight setup, exciting at a frequency of 6.70 Hz. The absolute values of both the acceleration- and force- controlled modelled responses are shown in terms of shear force and strain (left panel) and displacements (right panel).

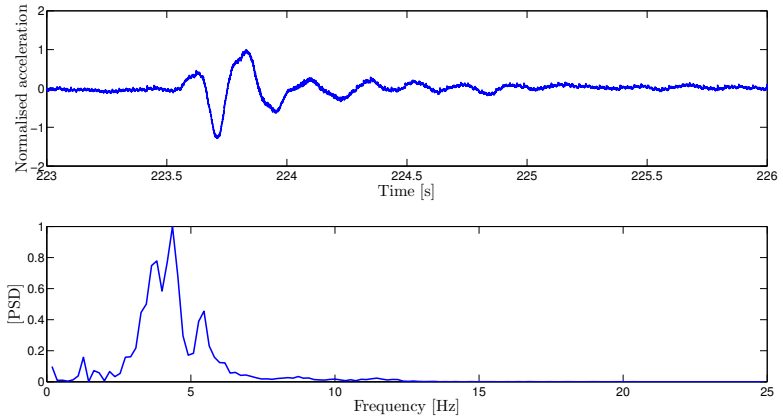

Figure A.6: Measured accelerations (normalised) at the head of MP45 after an impact of a service boat on the boat landing. The time domain of the excitation decay is shown in the upper panel and the lower panel shows the corresponding normalised PSD. Other than during the shaker measurements, the concrete main platform was installed during these measurements.

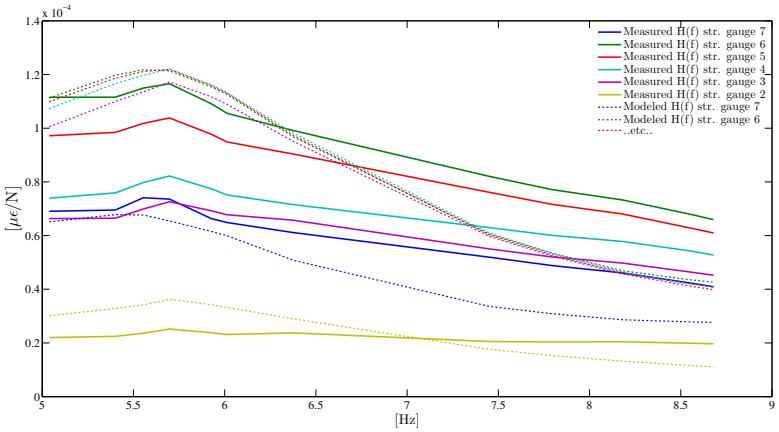

Figure A.7: Measured (continuous lines) and modelled (dotted lines) transfer functions for the strain gauges along the pile for the Light weight setup. For the modeled response, the factors on stiffness as given by the thick black line given in Figure 5.12 (optimization for transmissibilities: Equation 5.17) were applied to the effective 1D soil stiffness profile retrieved in Section 4.2.2. The dashpot coefficients were tuned for the transfer functions of the Middle weight setup (Figure 5.14) to a value of $c(z) = 1.56e^{-2}k_{eff}(z)$. As can be seen, the resonance peak has shifted from 5.4Hz (Middle weight setup) to 5.7Hz for this Light weight setup.

CURRICULUM VITÆ

Willem Geert Versteijlen was born on February 14^{th}, 1984 in Brussels, Belgium and was nicknamed Pim. After having received his baccalaureate at the European school of Woluwe in 2002, he took a gap year during which he traveled through New Zealand and learned Spanish in Costa Rica and Spain. He started his BSc Civil Engineering at the TU Delft (TUD) in 2003, followed by a MSc Offshore Engineering. During his studies he was in the board of sailing school 'De Brielse Zeilschool' for which he was granted another gap year sponsored by the university. Towards the end of his MSc he performed his internship at the Panama Canal in 2010.

Having graduated cum laude on the topic of soil damping for offshore wind turbines at Siemens Wind Power (SWP) in The Hague under the guidance of Prof. Andrei Metrikine, he continued with a PhD study on the track of soil-structure interaction for monopile foundations in combination with a job as a Load Engineer at SWP at the end of 2011. Together with Sven Voormeeren, he wrote a research proposal to increase the effort and the chance of obtaining useable results. This 4-year 'DISSTINCT' project (started January 2014) was a collaboration between SWP, Fugro, TUD, DNV GL and BMO Offshore and comprised amongst others a second PhD position at the TUD and the execution of in-situ MASW, shaker and impact-hammer measurements.

The main contribution of his work is the development of a new design method for the lateral stiffness of rigidly behaving piles, which was validated to predict the measured response of an in-situ monopile much better than the current design practice. The developed 'Effective Stiffness method' was qualified by DNV GL in November 2017, and the Dutch government is now including SCPT measurements as part of the environmental conditioning scope in their offshore wind farm tenders.

List of Publications

Journal publication

4. E. Kementzetzidis, S. Corciulo, W.G. Versteijlen, F. Pisanò , Geotechnical aspects of offshore wind turbine dynamics from 3D soil-structure non-linear FE simulations, Soil Dynamics and Earthquake Engineering (2018) *Submitted.*

3. W.G. Versteijlen, J.M. de Oliveira Barbosa, K.N. van Dalen, A.V. Metrikine, Dynamic soil stiffness for foundation piles: Capturing 3D continuum effects in an effective, non-local 1D model, International Journal of Solids and Structures 134 (2018) 272-282. doi:10.1016/j.ijsolstr.2017.11.007.

2. W.G. Versteijlen, F.W. Renting, P.L.C. van der Valk, J. Bongers, K.N. van Dalen, A.V. Metrikine, Effective soil-stiffness validation: Shaker excitation of an in-situ monopile foundation, Soil Dynamics and Earthquake Engineering 102 (2017) 241-262. doi:10.1016/j.soildyn.2017.08.003.

1. W.G. Versteijlen, A.V. Metrikine, K.N. van Dalen, A method for identification of an effective Winkler foundation for large-diameter offshore wind turbine support structures based on in-situ measured small-strain soil response and 3D modelling, Engineering Structures 124 (2016) 221-236. doi:10.1016/j.engstruct.2016.06.007.

Conference publication

5. W. G. Versteijlen, et al., Effective stiffness method for rigid monopile foundations of offshore wind turbines and in-situ validation, X international conference on recent advances in structural dynamics, EURODYN, 2017.

4. W.G. Versteijlen, J.M. De Oliveira Barbosa, K.N. Van Dalen, A.V. Metrikine, Method for extracting an equivalent Winkler model of the 3D dynamic soil-structure interaction of large-diameter offshore monopile foundations, in: Proceedings of 43 rd International Summer School-Conference Advanced Problems in Mechanics (APM), St. Petersburg, Russia, 22-27 June 2015, Institute for Problems in Mechanical Engineering of RAS, IPME RAS, 2015.

3. W.G. Versteijlen, K.N. van Dalen, A.V. Metrikine, L. Hamre, Assessing the small-strain soil stiffness for offshore wind turbines based on in situ seismic measurements, in: J. Phys. Conf. Ser., Vol. 524, IOP Publishing, 2014, p. 012088. doi:10.1088/1742-6596/524/1/012088.

2. W.G. Versteijlen, K.N. van Dalen, A.V. Metrikine, L. Hamre, Assessing the small-strain soil stiffness for offshore wind turbines based on in situ seismic measurements, in: Proceedings of the 9th International Conference on Structural Dynamics, EURODYN , 2014. link.

1. W.G. Versteijlen, A.V. Metrikine, J.S. Hoving, E. Smid, W.E. de Vries, Estimation of the vibration decrement of an offshore wind turbine support structure caused by its interaction with soil, in: Proceedings of the EWEA Offshore 2011 Conference, Amsterdam, The Netherlands, European Wind Energy Association, 2011.

INDEX

BIBLIOGRAPHY

[1] S. Gössling, F. Fichert, P. Forsyth, Subsidies in aviation, Sustainability 9 (8) (2017) 1295.

[2] A. Neslen, Shell lobbied to undermine EU renewables targets, documents reveal, https://www.theguardian.com/environment/2015/apr/27/shell-lobbied-to-undermine-eu-renewables-targets-documents-reveal, accessed: 2017-10-30 (2015).

[3] L. Myllyvirta, Smoke & Mirrors - How Europe's biggest polluters became their own regulators, Tech. rep., Greenpeace (2015).

[4] G. Pearse, et al., Quarry vision: coal, climate change and the end of the resources boom, Quarterly Essay (33) (2009) 1.

[5] J. Murray, IEA accused of "deliberately" undermining global renewables industry, https://www.businessgreen.com/bg/news/1806340/iea-accused-deliberately-undermining-global-renewables-industry, accessed: 2017-10-30 (2009).

[6] K. Drum, In 2002, the IEA Predicted Solar Was Going Nowhere. And in 2003. And 2004. And 2005..., http://www.motherjones.com/kevin-drum/2017/05/2002-iea-predicted-solar-was-going-nowhere-and-2003-and-2004-and-2005/, accessed: 2017-10-30 (2017).

[7] United Nations - Framework Convention on Climate Change, The paris agreement, http://unfccc.int/paris_agreement/items/9485.php (December 2015).

[8] Frankfurt School - UNEP Collaborating Centre, Global trends in renewable energy investment 2017, Tech. rep., Bloomberg & UN Environment (2017).
URL http://fs-unep-centre.org/publications/global-trends-renewable-energy-investment-2017

[9] J. Hansen, M. Sato, G. Russell, P. Kharecha, Climate sensitivity, sea level and atmospheric carbon dioxide, Philosophical Transactions of the Royal Society of London A: Mathematical, Physical and Engineering Sciences 371 (2001). doi:10.1098/rsta.2012.0294.
URL http://rsta.royalsocietypublishing.org/content/371/2001/20120294

[10] J. Englander, High Tide on Main Street, Boca Raton, FL: The Science Bookshelf, 2013.

[11] J. Hansen, M. Sato, P. Hearty, R. Ruedy, M. Kelley, V. Masson-Delmotte, G. Russell, G. Tselioudis, J. Cao, E. Rignot, et al., Ice melt, sea level rise and superstorms: evidence from paleoclimate data, climate modeling, and modern observations that 2 °c global warming could be dangerous, Atmospheric Chemistry and Physics 16 (6) (2016) 3761–3812.

[12] H. Kan, B. Chen, Particulate air pollution in urban areas of Shanghai, China: health-based economic assessment, Science of the Total Environment 322 (1) (2004) 71–79.

[13] S. Ji, C. R. Cherry, M. J. Bechle, Y. Wu, J. D. Marshall, Electric vehicles in China: emissions and health impacts, Environmental science & technology 46 (4) (2012) 2018–2024.

[14] G. Muttitt, The Sky's Limit - Why the Paris climate goals require a managed decline of fossil fuel production, Tech. rep., Oil Change International (September 2016).

[15] A. Doukas, Talk is Cheap: how G20 governments are financing climate disaster, Tech. rep., Oil Change International (July 2017).
URL http://priceofoil.org/content/uploads/2017/07/talk_is_cheap_G20_report_July2017.pdf

[16] Ernst & Young, Analysis of the value creation potential of wind energy policies, Tech. rep. (2012).
URL http://www.ey.com/Publication/vwLUAssets/Informe_wind/$FILE/Value_creation_wind_policies.pdf

[17] Siemens, What is the real cost of offshore wind?, Tech. rep. (2014).
URL https://www.energy.siemens.com/br/pool/hq/power-generation/renewables/wind-power/SCOE/Infoblatt-what-is-the-real-cost-of-offshore.pdf

[18] Roland Berger, Think Act beyond mainstream - Offshore wind power, takeaways from the Borssele wind farm, Tech. rep. (2016).

[19] A. de Pee, K. F, S. A, Winds of change? why offshore wind might be the next big thing, https://www.mckinsey.com/business-functions/sustainability-and-resource-productivity/our-insights/winds-of-change-why-offshore-wind-might-be-the-next-big-thing?cid=other-eml-alt-mip-mck-oth-1705&hlkid=809e645e8f284280a626c383d0292f32&hctky=2598927&hdpid=6a0f5e28-71b2-443a-b049-ab5b5dab37b1, accessed: 2017-11-01 (May 2017).

[20] A. Ho, A. Mbistrova, The European offshore wind industry - Key trends and statistics 2016 (2017).

[21] Offshore wind project cost outlook, http://www.cleanenergypipeline.com/Resources/CE/ResearchReports/ (2014).

[22] Offshore developments, https://www.wind-energy-the-facts.org/development-and-investment-costs-of-offshore-wind-power.html, accessed: 2017-11-03.

[23] M. Seidel, S. Voormeeren, J.-B. van der Steen, State-of-the-art design processes for offshore wind turbine support structures, Stahlbau 85 (9) (2016) 583–590.

[24] C. LeBlanc, G. T. Houlsby, B. W. Byrne, Response of stiff piles in sand to long-term cyclic lateral loading, Géotechnique 60 (2) (2010) 79–90.

[25] M. Heidari, H. El Naggar, M. Jahanandish, A. Ghahramani, Generalized cyclic p-y curve modeling for analysis of laterally loaded piles, Soil Dynamics and Earthquake Engineering 63 (2014) 138–149.

[26] M. Achmus, Y. S. Kuo, K. Abdel-Rahman, Behavior of monopile foundations under cyclic lateral load, Comput. and Geotech. 36 (5) (2009) 725–735.

[27] G. T. Houlsby, C. N. Abadie, W. J. A. P. Beuckelaers, B. W. Byrne, A model for nonlinear hysteretic and ratcheting behaviour, International Journal of Solids and Structures 120 (2017) 67–80.

[28] B. Byrne, et al., PISA: New design methods for offshore wind turbine monopiles, in: Proceedings of the 8th International Conference 12-14 September 2017 Royal Geographical Society, London, UK, Offshore Site Investigation and Geotechnics, Society for Underwater Technology, 2017, pp. 142–161.

[29] M. Achmus, K. Abdel-Rahman, P. Peralta, On the design of monopile foundations with respect to static and quasi-static cyclic loading, Proceedings of the Offshore Wind Energy Conference, Copenhagen, 2005.

[30] A. H. Augustesen, S. P. H. Sørensen, L. B. Ibsen, L. Andersen, M. Møller, K. T. Brødbæk, Comparison of calculation approaches for monopiles for offshore wind turbines, in: The European Conference on Numerical Methods in Geotechnical Engineering, CRC Press LLC, 2010, pp. 901–906.

[31] K. Thieken, M. Achmus, K. Lemke, A new static p-y approach for piles with arbitrary dimensions in sand, Geotechnik 38 (4) (2015) 267–288.

[32] B. W. Byrne, et al., New design methods for large diameter piles under lateral loading for offshore wind applications, in: 3rd International Symposium on Frontiers in Offshore Geotechnics (ISFOG 2015), Oslo, Norway, June, 2015, pp. 10–12.

[33] D. Kallehave, B. W. Byrne, C. L. Thilsted, K. K. Mikkelsen, Optimization of monopiles for offshore wind turbines, Philos. Tr. Roy. S.-A 373 (2035) (2015) 20140100.

[34] F. Vorpahl, H. Schwarze, T. Fischer, M. Seidel, J. Jonkman, Offshore wind turbine environment, loads, simulation, and design, Wiley Interdisciplinary Reviews: Energy and Environment 2 (5) (2013) 548–570.

[35] N. J. Tarp-Johansen, L. Andersen, E. D. Christensen, C. Mørch, S. Frandsen, B. Kallesøe, Comparing sources of damping of cross-wind motion, in: European Offshore Wind 2009: Conference & Exhibition, The European Wind Energy Association, 2009.

[36] W. G. Versteijlen, A. V. Metrikine, J. S. Hoving, E. Smid, W. E. de Vries, Estimation of the vibration decrement of an offshore wind turbine support structure caused by its interaction with soil, in: Proceedings of the EWEA Offshore 2011 Conference, Amsterdam, The Netherlands, European Wind Energy Association, 2011.

[37] O. Rhersellah, Validity of identified modal parameters based on rotor-stop tests of offshore wind turbines (2013).

[38] M. Damgaard, L. B. Ibsen, L. V. Andersen, J. K. F. Andersen, Cross-wind modal properties of offshore wind turbines identified by full scale testing, Journal of Wind Engineering and Industrial Aerodynamics 116 (2013) 94–108.

[39] P. L. C. van der Valk, M. G. L. Ogno, Identifying Structural Parameters of an Idling Offshore Wind Turbine Using Operational Modal Analysis, in: F. N. Catbas (Ed.), Dynamics of Civil Structures, Volume 4, Conference Proceedings of the Society for Experimental Mechanics Series, Springer International Publishing, 2014, pp. 271–281. doi:10.1007/978-3-319-04546-7_31.

[40] H. C. Kramers, P. L. C. van der Valk, J. W. van Wingerden, Statistical evaluation of the identified structural parameters of an idling offshore wind turbine, in: Journal of Physics: Conference Series, Vol. 753, IOP Publishing, 2016, p. 052006.
URL http://stacks.iop.org/1742-6596/753/i=5/a=052006

[41] W. Weijtjens, R. Shirzadeh, G. De Sitter, C. Devriendt, Classifying Resonant Frequencies and Damping Values of an Offshore Wind Turbine on a Monopile Foundation for Different Operational Conditions, Ewea 2014 (2014) 83–87doi:10.1049/iet-rpg.2013.0229.

[42] C. Koukoura, A. Natarajan, A. Vesth, Identification of support structure damping of a full scale offshore wind turbine in normal operation, Renewable Energy 81 (2015) 882–895. doi:10.1016/j.renene.2015.03.079.
URL http://linkinghub.elsevier.com/retrieve/pii/S0960148115002700

[43] H. Matlock, Correlations for design of laterally loaded piles in soft clay, in: Offshore Technology in Civil Engineering: Hall of Fame Papers from the Early Years, ASCE, 1970, pp. 77–94.

[44] L. C. Reese, W. R. Cox, F. D. Koop, Analysis of laterally loaded piles in sand, Proceedings of the 6th Annual Offshore Technology Conference, Houston, Texas, USA, (OTC 2080) (1974) 473–484.

[45] M. W. O'Neill, J. M. Murchinson, Fan Evaluation of p-y Relationships in Sands, Tech. rep., A report to the American Petroleum Institute (1983).

[46] I. P. Lam, G. R. Martin, Seismic design for highway bridge foundations, in: Lifeline Earthquake Engineering: Performance, Design and Construction, ASCE, 1986, p. 21.

[47] K. T. Brødbæk, M. Møller, S. P. H. Sørensen, A. H. Augustesen, Review of p-y relationships in cohesionless soil, Tech. Rep. 57, Aalborg University (2009).

[48] Varun, D. Assimaki, G. Gazetas, A simplified model for lateral response of large diameter caisson foundations - linear elastic formulation, Soil Dyn. Earthq. Eng. 29 (2) (2009) 268–291.

[49] Standard DNVGL-ST-0126 Support structures for wind turbine (April 2016).

[50] K. Terzaghi, Evaluation of coefficients of subgrade reaction, Geotechnique 5 (4) (1955) 297–326.

[51] C. Leth, S. P. H. Sørensen, R. T. Klinkvort, A. Augustesen, O. Hededal, L. B. Ibsen, A snapshot of present research at AAU and DTU of large-diameter piles in coarse-grained materials, in: The Nordic Geotechnical Meeting, 2012, pp. 491–498.

[52] J. Stevens, J. Audibert, et al., Re-examination of p-y curve formulations, in: Offshore Technology Conference, Offshore Technology Conference, 1979.

[53] D. L. Pradhan, Development of P-Y curves for monopiles in clay using finite element model Plaxis 3D Foundation, Master's thesis, NTNU - Trondheim (2012).

[54] S. Soerensen, L. Ibsen, A. Augustesen, Effects of diameter on initial stiffness of p-y curves for large-diameter piles in sand, numerical methods in geotechnical engineering, in: Proc. of the 7th European Conference, Trondheim/Norway, Vol. 2, 2010.

[55] K. Abdel-Rahman, M. Achmus, Finite element modelling of horizontally loaded monopile foundations for offshore wind energy converters in germany, in: International Symposium on Frontiers in Offshore Geotechnics (ISFOG), Perth, Australia, Taylor & Francis London, 2005, pp. 309–396.

[56] K. Lesny, J. Wiemann, Finite-element-modelling of large diameter monopiles for offshore wind energy converters, in: Proceedings of the GeoCongress, Atlanta, Georgia, USA, 2006.

[57] D. Kallehave, C. L. Thilsted, M. A. Liingaard, Modification of the API p-y formulation of initial stiffness of sand, in: Offshore Site Investigation and Geotechnics: Integrated Geotechnologies-Present and Future. Proceedings of the 7th International Conference on Offshore Site Investigations and Geotechnics, London, Society of Underwater Technology, 2012, pp. 465–472.

[58] G. Gazetas, R. Dobry, Horizontal Response of Piles in Layered Soils, J. Geotech. Eng. 110 (1) (1984) 20–40. doi:10.1061/(ASCE)0733-9410(1984)110:1(20).

[59] D. Badoni, N. Makris, Nonlinear response of single piles under lateral inertial and seismic loads, Soil Dynamics and Earthquake Engineering 15 (1) (1996) 29–43. doi:10.1016/0267-7261(95)00027-5.

[60] J. P. Wolf, Simple physical models for foundation dynamics, Developments in geotechnical engineering 83 (1998) 1–70.

[61] T. Nogami, M. Novak, Resistance of soil to a horizontally vibrating pile, Earthquake Engineering & Structural Dynamics (3) 249–261. doi:10.1002/eqe.4290050304.

[62] M. Novak, T. Nogami, Soil-pile interaction in horizontal vibration, Earthquake Engineering & Structural Dynamics 5 (1977) 263–281. doi:10.1002/eqe.4290050305.
URL http://doi.wiley.com/10.1002/eqe.4290050305

[63] L. M. Kagawa, Takaaki and Kraft, Dynamic characteristics of lateral load-deflection relationships of flexible piles, Earthq. Eng. Struct. Dyn. (1) 53–68. doi:10.1002/eqe.4290090105.

[64] K. Lesny, J. Wiemann, Design aspects of monopiles in german offshore wind farms, in: Proceedings of the International Symposium on Frontiers in Offshore Geotechnics, AA Balkema Publishing, 2005, pp. 383–389.

[65] M. F. Cook, J. K. Vandiver, Measured and predicted dynamic response of a single pile platform to random wave excitation, in: Offshore Technology Conference, 1982.

[66] M. Damgaard, V. Zania, L. V. Andersen, L. B. Ibsen, Effects of soil–structure interaction on real time dynamic response of offshore wind turbines on monopiles, Engineering Structures 75 (2014) 388–401. doi:10.1016/j.engstruct.2014.06.006.

[67] M. Damgaard, M. Bayat, L. V. Andersen, L. B. Ibsen, Assessment of the dynamic behaviour of saturated soil subjected to cyclic loading from offshore monopile wind turbine foundations, Comput. Geotech. 61 (2014) 116–126.

[68] E. Kementzetzidis, S. Corciulo, W. G. Versteijlen, F. Pisanò, Geotechnical aspects of offshore wind turbine dynamics from 3D soil-structure non-linear FE simulations, Soil Dynamics and Earthquake Engineering *Submitted*.

[69] G. Masing, Eigenspannungen und Verfestigung beim Messing, in: Proceedings, second international congress of applied mechanics, 1926, pp. 332–335.

[70] C. N. Abadie, Cyclic Lateral Loading of Monopile Foundations in Cohesionless Soils, Ph.D. thesis, University of Oxford (2015).

[71] W. Beuckelaers, Fatigue life calculation of monopiles for offshore wind turbines using a kinematic hardening soil model, Ground Engineering.

[72] D. Lombardi, S. Bhattacharya, D. M. Wood, Dynamic soil-structure interaction of monopile supported wind turbines in cohesive soil, Soil Dynamics and Earthquake Engineering 49 (2013) 165–180.

[73] T. De Blaeij, On the modelling of installation effects on laterally cyclic loaded monopiles, Master's thesis, Delft University of Technology (2013).

[74] G. W. Blaney, M. W. O'Neill, Measured lateral response of mass on single pile in clay, Journal of geotechnical engineering 112 (4) (1986) 443–457.

[75] C. B. Crouse, S. L. Kramer, R. Mitchell, B. Hushmand, Dynamic tests of pipe pile in saturated peat, Journal of geotechnical engineering 119 (10) (1993) 1550–1567.

[76] R. Osgood, G. Bir, H. Mutha, B. Peeters, M. Luczak, G. Sablon, Full-scale modal wind turbine tests: comparing shaker excitation with wind excitation, in: Structural Dynamics and Renewable Energy, Volume 1, Springer, 2011, pp. 113–124.

[77] B. W. Byrne, et al., Field testing of large diameter piles under lateral loading for offshore wind applications, in: Proceedings of the 16th European Conference on Soil Mechanics and Geotechnical Engineering, Edinburgh, UK, 2015.

[78] W. G. Versteijlen, A. V. Metrikine, K. N. van Dalen, A method for identification of an effective Winkler foundation for large-diameter offshore wind turbine support structures based on in-situ measured small-strain soil response and 3D modelling, Engineering Structures 124 (2016) 221–236. doi:10.1016/j.engstruct.2016.06.007.

[79] W. G. Versteijlen, J. M. de Oliveira Barbosa, K. N. van Dalen, A. V. Metrikine, Dynamic soil stiffness for foundation piles: Capturing 3D continuum effects in an effective, non-local 1D model, International Journal of Solids and Structures 134 (2018) 272 – 282. doi:10.1016/j.ijsolstr.2017.11.007.

[80] W. G. Versteijlen, K. N. van Dalen, A. V. Metrikine, L. Hamre, Assessing the small-strain soil stiffness for offshore wind turbines based on in situ seismic measurements, in: J. Phys. Conf. Ser., Vol. 524, IOP Publishing, 2014, p. 012088. doi:10.1088/1742-6596/524/1/012088.

[81] A. de Groot, Determination of dynamic soil properties from in-situ offshore low-frequency seismic measurements, MSc. thesis Delft University of Technology (2014).

[82] C. de Winter, Inversion of near-surface seismic measurements to estimate soil stiffness relevant for offshore wind turbines, MSc. thesis Delft University of Technology (2014).

[83] I. Bolderink, Identification of dynamic soil properties relavant for offshore wind turbines through full waveform inversion of in-situ measured seismic data, MSc. thesis Delft University of Technology (2015).

[84] M. Armstrong, Seismic Inversion for Identification of Soil Stiffness and Damping for Offshore Wind Turbines, MSc. thesis Delft University of Technology (2016).

[85] Versteijlen W.G. and Renting F, Westermeerwind Measurement campaign: Validation phase DISSTINCT research project, e W OF COE MEC LOADS-40-A454-05, Rev 8.

[86] DNV GL, Technology Certificate - Effective Stiffness Method for small strain soil reactions (November 2017).

[87] DNV GL, Disstinct Technology Qualification, Effective Stiffness Method, report No.17-1418, Rev. 0.

[88] W. G. Versteijlen, Technology Qualification Basis - The Effective Stiffness method, Tech. Rep. Doc. ID. WP OF EN ES SUS FO-40-2161-00, Siemens Gamesa Renewable Energy - DNV GL (2017).

[89] S. L. Kramer, Geotechnical Earthquake Engineering Prentice Hall, Prentice-Hall, Inc, 1996.

[90] L. Karl, Dynamic Soil Properties out of SCPT and Bender Element Tests with Emphasis on Material Damping, Ph.D. thesis, Ghent University (2005).

[91] J. H. Atkinson, G. Sallfors, Experimental determination of stress-strain-time characteristic in laboratory and in situ tests, in: B. A A (Ed.), X ECSMFE, Vol. III, Firenze Associazione Geotecnica Italiana, Italy, 1991, pp. 915–956.

[92] B. Seed, H., I. Idriss, Soil moduli and damping factors for dynamic response analysis, Tech. rep., Earthquake Engineering Research Centre, University of California, Berkeley, report No. EERC 70-10 (1970).

[93] J. M. Llambias, D. J. Shepherd, M. D. Rodwell, Sensitivity of seismic structural response to interpretation of soils data, Soil Dynamics and Earthquake Engineering 12 (6) (1993) 337–342.

[94] A. Sawangsuriya, Wave processes in Classical and New solids, INTECH Open Access Publisher, 2012, Ch. 7, Wave Propagation Methods for Determining Stiffness of Geomaterials.

[95] J. A. Studer, M. G. Koller, Bodendynamik Grundlagen, Kennziffern, Probleme (1997).

[96] R. J. Jardine, D. M. Potts, A. B. Fourie, J. B. Burland, Studies of the influence of non-linear stress–strain characteristics in soil–structure interaction, Geotechnique 36 (3) (1986) 377–396.

[97] S. Foti, C. G. Lai, G. J. Rix, C. Strobbia, Surface Wave Methods for Near Surface Site Characterization, CRC Press, 2015.

[98] R. G. Stockwell, L. Mansinha, R. Lowe, Localization of the complex spectrum: the S-transform, IEEE T. Signal Proces. 44 (4) (1996) 998–1001.

[99] P. K. Robertson, K. Cabal, Estimating soil unit weight from CPT, in: 2nd International Symposium on Cone Penetration Testing, 2010, pp. 2–40.

[100] T. Kokusho, Cyclic triaxial test of dynamic soil properties for wide strain range, Soils Found. 20 (2) (1980) 45–60.

[101] J. E. Bowles, Foundation Analysis and Design, McGraw-Hill, New York, 1996.

[102] K. N. van Dalen, Multi-component Acoustic Characterization of Porous Media, Springer, 2013.

[103] J. J. M. Carcione, Wave fields in real media: Wave Propagation in Anisotropic, Anelastic, Porous and Electromagnetic Media, Vol. 38 of Handbook of Geophysical Exploration: Seismic Exploration, 2007.

[104] E. L. Hamilton, Elastic properties of marine sediments, J. Geophys. Res. 76 (2) (1971) 579–604.

[105] E. L. Hamilton, Vp/Vs and Poisson's ratios in marine sediments and rocks, J. Acoust. Soc. Am. 66 (4) (1979) 1093–1101.

[106] Offshore Standard DNV-OS-J101 Design of offshore wind turbine structures (October 2010).

[107] L. Paoletti, Y. Hegazy, S. Monaco, R. Piva, Prediction of shear wave velocity for offshore sands using CPT data–Adriatic Sea, in: Proc. of 2nd International Symposium on Cone Penetration Testing (CPT'10), Vol. 2, 2010, pp. 361–368.

[108] S. Badsar, In situ determination of material damping in the soil at small deformation ratios, Ph.D. thesis, KU Leuven (2012).

[109] M. Maraschini, F. Ernst, S. Foti, L. V. Socco, A new misfit function for multimodal inversion of surface waves, Geophysics 75 (4) (2010) 31–43.

[110] R. Noorlandt, et al., Characterisation of ground motion recording stations in the groningen gas field, Journal of Seismology 22 (3) (2018) 605–623. doi:10.1007/s10950-017-9725-6.

[111] M. Vanneste, C. Madshus, V. L. Socco, M. Maraschini, P. M. Sparrevik, H. Westerdahl, K. Duffaut, E. Skomedal, T. I. Bjørnarå, On the use of the Norwegian Geotechnical Institute's prototype seabed-coupled shear wave vibrator for shallow soil characterization–I. Acquisition and processing of multimodal surface waves, Geophysical Journal International 185 (1) (2011) 221–236.

[112] V. L. Socco, D. Boiero, M. Maraschini, M. Vanneste, C. Madshus, H. Westerdahl, K. Duffaut, E. Skomedal, On the use of the Norwegian Geotechnical Institute's prototype seabed-coupled shear wave vibrator for shallow soil characterization-II. Joint inversion of multimodal Love and Scholte surface waves, Geophysical Journal International 185 (1) (2011) 237–252.

[113] S. Badsar, M. Schevenels, W. Haegeman, G. Degrande, Determination of the material damping ratio in the soil from SASW tests using the half-power bandwidth method, Geophysical Journal International 182 (3) (2010) 1493–1508.

[114] A. S. Misbah, C. L. Strobbia, Joint estimation of modal attenuation and velocity from multichannel surface wave data, Geophysics 79 (3) (2014) EN25–EN38.

[115] J. M. Carcione, D. Kosloff, R. Kosloff, Wave propagation simulation in a linear viscoelastic medium, Geophysical Journal International 95 (3) (1988) 597–611.

[116] A. Lichtl, S. Jones, Full scale simulation of spacex's mars rocket engine, 16:00-21:00 min (2015).
URL http://on-demand.gputechconf.com/gtc/2015/video/S5398.html

[117] W. G. Versteijlen, J. M. De Oliveira Barbosa, K. N. Van Dalen, A. V. Metrikine, Method for extracting an equivalent Winkler model of the 3D dynamic soil-structure interaction of large-diameter offshore monopile foundations, in: Proceedings of 43rd International Summer School-Conference Advanced Problems in Mechanics (APM), St. Petersburg, Russia, 22-27 June 2015, Institute for Problems in Mechanical Engineering of RAS, IPME RAS, 2015.

[118] E. Kausel, J. M. Oliveira Barbosa, PMLs: A direct approach, International Journal for Numerical Methods in Engineering 90 (3) (2012) 343–352.

[119] M. Damgaard, L. V. Andersen, L. B. Ibsen, Dynamic response sensitivity of an offshore wind turbine for varying subsoil conditions, Ocean Engineering 101 (2015) 227–234.

[120] M. Damgaard, L. V. Andersen, L. B. Ibsen, H. S. Toft, J. D. Sørensen, A probabilistic analysis of the dynamic response of monopile foundations: Soil variability and its consequences, Probabilist. Eng. Mech. 41 (2015) 46–59. doi:http://dx.doi.org/10.1016/j.probengmech.2015.05.001.

[121] O. C. Zienkiewicz, R. L. Taylor, The Finite Element Method for Solid and Structural Mechanics, Butterworth-Heinemann, 2005.

[122] J. D. Achenbach, Wave Propagation in Elastic Solids, Vol. 16, North-Holland Publishing Company - Amsterdam, 1973.

[123] L. Andersen, J. Clausen, Impedance of surface footings on layered ground, Computers & structures 86 (1) (2008) 72–87.

[124] Y. He, B. Byrne, H. Burd, Application of numerical-based design method for laterally loaded monopiles in layered soils, in: OSIG 8th International Conference, London, SUT, 2017.

[125] H. G. Poulos, T. S. Hull, The role of analytical geomechanics in foundation engineering, in: Foundation engineering: Current principles and practices, ASCE, 1989, pp. 1578–1606.

[126] W. G. Versteijlen, F. W. Renting, P. L. C. van der Valk, J. Bongers, K. N. van Dalen, A. V. Metrikine, Effective soil-stiffness validation: Shaker excitation of an in-situ monopile foundation, Soil Dyn Earthq Eng 102 (2017) 241–262. doi:10.1016/j.soildyn.2017.08.003.

[127] R. Weijermars, Principles of Rock Mechanics, Alboran Science Publishing, 1997.

[128] D. W. Wilson, Soil-pile-superstructure interaction in liquefying sand and soft clay, Ph.D. thesis, University of California, Davis (1998).

[129] K. F. Graff, Wave Motion in Elastic Solids, Oxford University Press, 1975.

[130] A. T. de Hoop, Handbook of Radiation and Scattering of Waves: Acoustic Waves in Fluids, Elastic Waves in Solids, Electromagnetic Waves, Academic Press, 1995.

[131] J. van Kan, A. Segal, F. Vermolen, Numerical Methods in Scientific Computing, VSSD, 2005.

[132] M. Jamiolkowski, D. C. F. Lo Presti, M. Manassero, Evaluation of relative density and shear strength of sands from cpt and dmt, in: Soil behavior and soft ground construction, ASCE, 2003, pp. 201–238.

[133] American Petroleum Institute (API), Recommended Practice for Planning, Designing and Constructing Fixed Offshore Platforms-Working Stress Design (RP 2A-WSD) (2000).

[134] R. Greeuw, Preliminary analysis of experimental data in offshore shaker tests, Tech. rep., Delft University of Technology, internship report (2016).

[135] F. W. Renting, K. N. van Dalen, A. V. Metrikine, Exact analytical expression for the added mass for offshore monopile foundations, In Preparation.

[136] A. K. Chopra, Dynamics of Structures: Theory and Applications to Earthquake Engineering. (2007).

[137] A. Verruijt, An Introduction to Soil Dynamics, volume 24 of Theory and Applications of Transport in Porous Media (2010).

[138] J. K. Lim, B. Lehane, Interpretation difficulties of pile set-up in sand, in: Frontiers in Offshore Geotechnics III, CRC Press, 2015.

[139] F. Dezi, F. Gara, D. Roia, Dynamic response of a near-shore pile to lateral impact load, Soil Dyn Earthq Eng 40 (2012) 34–47.

[140] V. E. Komurka, A. B. Wagner, T. B. Edil, Estimating soil/pile set-up, Tech. rep., Wisconsin Highway Research Program (2003).

[141] M. Gerrits, A study on the natural frequency discrepancies in offshore wind turbines, Tech. rep., Delft University of Technology, internship report (2015).

[142] K. Pozorska, Investigation of the results of soil mechanics sensors at the shaker test on monopile W27 in the wind farm Westermeerwind in The Netherlands (2015).

[143] L. V. Andersen, M. Vahdatirad, M. T. Sichani, J. D. Sørensen, Natural frequencies of wind turbines on monopile foundations in clayey soils - a probabilistic approach, Computers and Geotechnics 43 (2012) 1–11.